Universitat Autònoma de Barcelona

# FERROMAGNETIC INSULATOR THIN FILMS BASED ON Ni/Mn DOUBLE PEROVSKITES

**Mónica Emperatriz Bernal Salamanca**

# FERROMAGNETIC INSULATOR THIN FILMS BASED ON Ni/Mn DOUBLE PEROVSKITES

Mónica Emperatriz Bernal Salamanca
Advanced Characterization and Nanostructured Materials
Institut de Ciència de Materials de Barcelona

Supervisors:
Dr. Lluís Balcells Argemí
Dra. Zorica Konstantinović

Tutor:
Prof. Vassil Hristov Skumryev

Universitat Autònoma de Barcelona
Departament de Física

A thesis submitted for the degree of Doctor of
*Philosophy in Physics*

Bellaterra, September 2021

*"Lo que sabemos es una gota, lo que ignoramos es un inmenso océano. La admirable disposición y armonía del universo, no ha podido sino salir del plan de un ser omnisciente y omnipotente".*
*Isaac Newton*

# *Abstract*

Double perovskite oxides of the $R_2NiMnO_6$ family (RNMO, where R is a rare earth element) have received considerable attention as ferromagnetic insulators (FM-Is). Their multifunctional physical properties make them potential candidates for technological applications in spintronic devices, such as magnetodielectric capacitors and spin filters tunnel barriers. In this family, $La_2NiMnO_6$ (LNMO; R = La) has attracted much more attention for its near-room-temperature ferromagnetic transition ($T_C \approx 280$ K). Consequently, RNMO systems show a gradual structural change with the substitution of La by another rare-earth element R with smaller ionic radius, thus affecting its physical properties. In these materials, one of the greatest challenges is to control the ordering of the B-sites cations. In spite of their great interest, high-quality RNMO epitaxial thin films with double perovskite structure, usually obtained by pulsed laser deposition, are still very scarce. It is worth emphasizing that, at the beginning of this thesis work, no study or related report was published on RNMO (R = La and Pr) thin films grown by magnetron sputtering deposition technique.

In this work, we present a detailed study on the epitaxial growth of $La_2NiMnO_6$ and $Pr_2NiMnO_6$ double perovskite thin films by RF (radio frequency) magnetron sputtering. The influence of growth parameters (i.e., oxygen pressure, growth temperature and annealing) on the structural properties, microstructure, stoichiometry, and magnetic and transport properties of the films is thoroughly investigated. In addition, the nature of the ferromagnetic interaction between Ni and Mn ions in RNMO compounds is elucidated by X-ray absorption spectroscopy. After optimization of the growth conditions, we demonstrate that high-quality epitaxial, insulating and ferromagnetic thin films of LNMO and PNMO, with good B-site cationic ordering (i.e., $T_C$ and Ms very close to the bulk value), can be prepared despite a certain degree of non-stoichiometry by RF sputtering technique. Additionally, as ultrathin RNMO films (~ 3 nm thick) are required for applications as spin filter in tunnel barriers, we have deposited films with different thicknesses under the optimized growth conditions and evaluated the influence of strain state using two kinds of substrates (STO and LAO). Structural and magnetic properties of the films have shown a strong dependence on film thickness. In particular, the thinnest films showed a loss of ferromagnetism at the (film-substrate) interface.

Finally, a detailed morphological characterization of the LNMO and PNMO thin films reveals that the film surface shows very low roughness. At the same time, we show that annealing process at high temperature under high oxygen pressure, commonly employed to improve the magnetic properties of the films, promotes the spontaneous formation of surface nanostructures. In this regard, the evolution of the structural and magnetic properties of the films is studied as a function of the annealing treatment at different temperatures. It is shown that the formation of NiOx nanocuboids leads to a nanostructured film surface with regions of locally different electrical transport characteristics.

# *Resumen*

Los óxidos de dobles perovskita de la familia $R_2NiMnO_6$ (RNMO, donde R es un elemento de tierras raras) han recibido una atención considerable como aislantes ferromagnéticos (FM-Is). Sus propiedades físicas multifuncionales los convierten en candidatos potenciales para aplicaciones tecnológicas en dispositivos espintrónicos, como condensadores magnetodieléctricos y barreras de túnel de filtros de espín. En esta familia, $La_2NiMnO_6$ (LNMO; R = La) ha llamado mucha más la atención por su transición ferromagnética cercana a la temperatura ambiente ($T_C \approx 280$ K). En consecuencia, los sistemas RNMO muestran un cambio estructural gradual con la sustitución del La por otro elemento de las tierras raras R con menor radio iónico, afectando así sus propiedades físicas. En estos materiales, uno de los mayores desafíos es controlar el orden de los cationes de los sitios B. A pesar de su gran interés, las películas delgadas epitaxiales de RNMO de alta calidad con estructura de doble perovskita, generalmente obtenidas por deposición con láser pulsado, siguen siendo muy escasas. Vale la pena enfatizar que, al comienzo de este trabajo de tesis, no se publicó ningún estudio o informe relacionado sobre películas delgadas RNMO (R = La y Pr) preparadas mediante la técnica de deposición catódica con magnetrón.

En este trabajo, presentamos un estudio detallado sobre el crecimiento epitaxial de películas delgadas de doble perovskita de $La_2NiMnO_6$ y $Pr_2NiMnO_6$ por pulverización catódica con magnetrón de RF (radio frecuencia). Se investiga a fondo la influencia de los parámetros de crecimiento (es decir, presión de oxígeno, temperatura de crecimiento y recocido) sobre las propiedades estructurales, la microestructura, la estequiometría y las propiedades magnéticas y de transporte de las películas. Además, la naturaleza de la interacción ferromagnética entre los iones Ni y Mn en compuestos RNMO se elucida mediante espectroscopía de absorción de rayos X. Después de la optimización de las condiciones de crecimiento, nosotros demostramos que se pueden preparar películas delgadas epitaxiales, aislantes y ferromagnéticas de alta calidad de LNMO y PNMO, con un buen orden catiónico en el sitio B (es decir, $T_C$ y Ms muy cerca del valor en volumen) a pesar de un cierto grado de no estequiometría mediante la técnica de pulverización catódica de RF. Adicionalmente, dado que se requieren películas ultrafinas de RNMO (~ 3 nm de espesor) para aplicaciones como filtros de espín en barreras túnel, nosotros hemos depositado películas con diferentes espesores en las condiciones de crecimiento optimizadas y hemos evaluado la influencia del estado de tensión utilizando dos tipos de sustratos (STO y LAO). Las propiedades estructurales y magnéticas de las películas han mostrado una fuerte dependencia del espesor de la película. En particular, las películas más delgadas mostraron una pérdida de ferromagnetismo en la interfaz (película-sustrato).

Finalmente, una caracterización morfológica detallada de las películas delgadas LNMO y PNMO revela que la superficie de la película muestra una rugosidad muy baja. Al

mismo tiempo, mostramos que el proceso de recocido a alta temperatura bajo alta presión de oxígeno, comúnmente empleado para mejorar las propiedades magnéticas de las películas, promueve la formación espontánea de nanoestructuras superficiales. En este respecto, se estudia la evolución de las propiedades estructurales y magnéticas de las películas en función del tratamiento de recocido a diferentes temperaturas. Se muestra que la formación de nanocubos de $NiO_x$ conduce a una superficie de película nanoestructurada con regiones de características de transporte eléctrico localmente diferentes.

# *Acknowledgements*

En primer lugar deseo expresar mis agradecimientos a Benjamín Martínez por brindarme la oportunidad de realizar esta tesis doctoral en su grupo. Muy especialmente también deseo agradecer a mis directores de tesis Lluís Balcells y Zorika Konstantinović, quienes con su conocimiento científico, apoyo y paciencia hicieron un aporte invaluable durante el desarrollo de esta tesis. Gracias por los conocimientos que me han permitido adquirir y por la confianza depositada en la realización de esta tesis doctoral bajo su dirección. De la misma manera quiero agradecer por la ayuda prestada en el laboratorio y por la disposición en la discusión de resultados. A Lluís por brindarme toda la confianza en el manejo del sputtering y por resolver cualquier problema que pudiera haber surgido en el momento.

También quiero agradecer a Carlos Frontera por su paciencia y tiempo en resolver mis preguntas. Por la disponibilidad en discutir resultados, a pesar de lo ocupado que siempre estaba. Gracias Carlos por ser como un tercer director de tesis para mí y por participar en parte de las correcciones de la tesis.

También quiero dar mis agradecimientos a los otros miembros del grupo, Alberto, Bernat, Narcís... por esos momentos en las reuniones de grupo. A mis compañeros Sergi y Víctor, por esas horas compartidas durante los almuerzos, de reír y hablar cualquier tema que se nos ocurriese en el momento. A mis compañeros del despacho por compartir cualquier discusión, también por las chocolatas y dulces que nos venían muy bien para alegrar el día y cambiar un poco la rutina.

Por supuesto, también quiero agradecer al soporte técnico del ICMAB, del ICN2 y CCiTUB. A Bernat por su colaboración con el PPMS y SQUID. A Sergio Valencia por los experimentos desarrollados en BESSY II. A Javier Herrero por los experimentos en el sincrotrón ALBA y por encaminarme en el proceso de simulación de los espectros XAS, también en la comprensión de los resultados.

Mis más profundos agradecimientos a mi familia, por la motivación, por el constante apoyo, por esas palabras de aliento que siempre me fortalecieron en este camino y así no desfallecer en esos momentos críticos.

El desarrollo de esta tesis doctoral se facilitó gracias a una beca de Colciencias doctorado exterior (Colombia), así como al apoyo financiero del Ministerio de Economía y Competitividad de España a través del Programa “Severo Ochoa” para Centros de Excelencia en I + D + i (SEV-2015-0496), y Proyecto MAT2015-71664-R. También gracias a la financiación del Programa de Investigación e Innovación Horizonte 2020 de la Unión Europea en virtud del Acuerdo de subvención Marie Sklodowska-Curie No. 645658 (Proyecto DAFNEOX).

# Contents

# List of Abbreviations

| | |
|---|---|
| **AF** | Antiferromagnetic |
| **AFM** | Atomic force microscopy |
| **APB** | Antiphase boundary |
| **ASD** | Anti-site disorder |
| **C-AFM** | Conductive atomic force microscopy |
| **CF** | Crystal field |
| **CFT** | Crystal field theory |
| **DP** | Double perovskite |
| **EDAX** | Energy dispersive X-ray analysis |
| **EPMA** | Electron probe micro-analysis |
| **FC** | Field-cooled |
| **FM** | Ferromagnetic |
| **FM-I** | Ferromagnetic insulator |
| **f.u.** | Unit formula |
| **GKA** | Goodenough-Kanamori-Anderson |
| **$H_C$** | Coercive field |
| **HS** | High spin |
| **IP** | In-plane |
| **JT** | Jahn-Teller |
| **LAO** | $LaAlO_3$ |
| **LNMO** | $La_2NiMnO_6$ |
| **LS** | Low spin |
| **MPMS** | Magnetic properties measurement system |
| **Ms** | Saturation magnetization |
| **MTJ** | Magnetic tunnel junctions |
| **OP** | Out-of-plane |
| **PNMO** | $Pr_2NiMnO_6$ |
| **$PO_2$** | Oxygen Pressure |

| | |
|---|---|
| **PPMS** | Physical properties measurement system |
| **RNMO** | $R_2NiMnO_6$ |
| **RF** | Radio-frequency |
| **RT** | Room temperature |
| **rms** | Root mean square |
| **RSM** | Reciprocal space map |
| **SQUID** | Superconducting quantum interference device |
| **SEM** | Scanning electron microscopy |
| **STEM** | Scanning transmission electron microscopy |
| **STO** | $SrTiO_3$ |
| **$T_C$** | Curie temperature |
| **TEM** | Transmission electron microscopy |
| **TEY** | Total electron yield |
| **TFY** | Total fluorescence yield |
| **TMO** | Transition metal oxide |
| **VRH** | Variable range hopping |
| **XAS** | X-ray absorption spectroscopy |
| **XMCD** | X-ray magnetic circular dichroism |
| **XRD** | X-ray diffraction |
| **XRR** | X- ray reflectivity |
| **ZFC** | zero field cooled |

# Chapter 1

# Introduction

## 1.1 Motivation

The technology that combines electronics with magnetism through the manipulation of electron spins and which is considered as a replacement technology for conventional electronics is called spintronics (neologism coming from the contraction of spin and electronics). In conventional electronics, information is encoded by the electron charge, while in spintronics the electron spin is used as an additional degree of freedom. Spintronics offers the potential for nonvolatile memories, faster data processing speeds with less power usage, larger storage densities and additional functionalities, such as quantum computation, which are not yet possible with conventional semiconductor devices [1] [2].

The first widely studied spintronics effect was giant magnetoresistance (GMR), observed in thin film structures composed of alternating ferromagnetic and nonmagnetic layers (e.g. Fe/Cr or Co/Cu superlattices) in the 1980's [3] [4] [5]. This effect consists in a significant decrease (typically 10–80%) in electrical resistance in the presence of a magnetic field [6]. Another spintronic effect that has given rise to a large number of experimental and theoretical studies is tunnel magnetoresistance (TMR). Conventional magnetic tunnel junctions (MTJs) consist of two ferromagnetic electrodes separated by a thin insulating barrier (i.e. FM/I/FM heterostructure). In this type of devices, the resistance of the tunnel current changes with the relative orientation of the magnetization of the two magnetic layers [7].

Large TMR effects can be obtained if specific magnetic materials, typically the so-called half-metals, are used. Among the materials that have been predicted to be half-metals, many are oxides [8] [9]. In this regard, this triggered an important activity on magnetic oxide thin films, with the main objective of making oxide MTJs and eventually measuring large TMR response [7]. In addition, with the development of metal-based spintronics in the late 1980's and 1990's, important advances were made on the growth of high-quality oxide thin films and heterostructures. This technological breakthrough was soon expanded to the transition metal oxides (TMOs) having perovskite ($ABO_3$) structure [10]. Perovskite oxides are fascinating materials that exhibit many intriguing physical properties. In particular, strongly correlated

electron oxides display complex interactions between charge, spin, and lattice degrees of freedom, and various order parameters compete with each other, resulting in a complex phase diagram [11].

The tendency towards device miniaturization has emphasized the need for multifunctional materials, i.e. materials that can perform more than one task or that can be manipulated by several independent stimuli. The physical properties exhibited by transition metal oxides with perovskite structure (ferroelectricity, ferromagnetism, antiferromagnetism, metallicity, superconductivity, optical properties, etc.) thus provide tremendous advantages for spintronics by bringing additional functionalities that do not exist in more conventionally used materials [7]. Among them, rare earth manganites (e.g. $LaMnO_3$) and their chemically doped derivatives are the most widely studied perovskites due to many useful properties and behaviors, including colossal magnetoresistance (CMR), half-metallicity, metal-insulator transitions (MITs), multiferroic behaviour and magnetoelectric coupling [12]. The discovery of CMR in mixed-valence manganite films, in the 90s, triggered intense research activities on these materials. The first notable impact of magnetic oxides in the field of spintronics was the use of such manganites as electrodes in MTJs [13], yielding TMR ratios one order of magnitude larger than what had been obtained with transition metal electrodes [7]. This development of the field of oxides was accompanied by enormous progress in thin film deposition technology over the last two decades [14].Thereby, the growth of high quality oxide thin films and heterostructures showed important advances concerning sample quality [15]. Since then, research on oxide spintronics has been intense, and it has been focused on half-metallic material systems such as doped manganites, magnetite and double perovskites [13].

First discovered by Ward et al. in 1961[16], double perovskites (DPs) are a broad class of compounds with a general chemical formula of $A_2BB'O_6$, with two different transition metal (TM) elements at B sites (B, B') and the possible presence of different rare-earth and alkaline earth elements at A sites. DPs offer a wide range of magnetic and transport properties, ranging from ionic conductivity [17], superconductivity [18], ferromagnetism [19] [20] ferroelectricity [21] and multiferroic behavior [22] [23] etc. Therefore, the urgent need to solve the problems of energetic efficiency, data storage, and processing speed of current microelectronic devices has boosted the search for new materials and paradigms capable of circumvent those problems. Spintronics has been pointed out as a potential alternative technology to develop a multifunctional electronics that combines logic operations, data storage and transmission with an improved energetic efficiency. The development of spintronic devices requires the generation and control of highly spin-polarized currents [15] or pure spin currents [2]. A way of obtaining a highly spin-polarized current is by using spin filtering effects through FM/I/FM tunnel barriers [24] [25]. A simpler way to obtain the same effect can be done by using a ferromagnetic insulating barrier [26] [27]. Nevertheless, ferromagnetic-insulators (FM-Is) are very scarce. In this context, DPs of the $R_2NiMnO_6$ family (with R a rare-earth atom) are amongst the few FM-Is known and they may play a promising role in the next generation spintronic industry [28] [29] [30].

Recently, FM-Is, by combining ferromagnetic and insulator characteristics, have attracted great attention as they can achieve great performances in the fields of spintronics and multiferroics [31] [32]. The MTJ, one of the most important spintronic devices, requires high spin (HS)-polarized materials to enhance the performance of TMR, and FM-Is have a potential to increase the magnitude of TMR as spin-filtering barriers [33]. The spin filtering effect of FM-I barriers is caused by the spin-sensitive conductance induced by spin-dependent potentials in FM-Is [34] [35]. These complex physical properties arise from competing interactions between magnetic (spins), structural (phonons) and polarization (charges) order parameters [35].

Among DP oxides, $La_2NiMnO_6$ (LNMO) is a FM-I that has attracted considerable attention due to its high Curie temperature ($T_C$), very close to RT ($T_C$ = 280K) [1], and magnetodielectric properties [35] [36]. It has been observed that properties of LNMO change considerably by substitution of La cation by other rare earth elements with smaller ionic radius. Moreover, the entire series of these oxides, $R_2NiMnO_6$ (where R is a rare-earth), has been reported to be ferromagnetic with a decrease in their Curie temperature due to large deviation of Ni–O–Mn bond angle (from $180^o$) with the substitution of the rare earth elements [30] [37]. The ferromagnetic (FM) ordering in RNMO compounds is explained by superexchange interaction between $Mn^{4+}$ and $Ni^{2+}$ according to the Goodenough-Kanamori rules [38], and is very sensitive to the ordered distribution of cations in the B sublattice of the DP structure [39]. In LNMO, the rare combination of FM-I state originates from the virtual hopping of the electrons from half-filled $e_g$ orbitals of $Ni^{2+}$ to empty $e_g$ orbitals of $Mn^{+4}$ leading to TM($e_g^2$)– O–TM($e_g^0$) super exchange interaction which is FM in $180^o$ geometry [40]. However, disordering of Ni and Mn cations of the DP structure, as well as oxygen vacancies, may strongly suppress the FM superexchange interaction [41]. In fact, cationic disorder reduces the saturation magnetization from 5 $\mu_B$/f.u. (the maximum expected for the FM contribution of $Ni^{2+}$ and $Mn^{4+}$) since, according to the Goodenough-Kanamori rules, disordering introduces antiferromagnetic (AF) $Mn^{4+}$−O−$Mn^{4+}$ and $Ni^{2+}$−O−$Ni^{2+}$ interactions [28] [42] [43].

In this thesis, we focus our attention on exploring two types of ferromagnetic TMOs with double perovskite structure $R_2NiMnO_6$, where R = La, or Pr (i.e. $La_2NiMnO_6$ and $Pr_2NiMnO_6$). These materials are indeed ferromagnetic insulators (FM-Is) and, as such, could be good candidates for magnetically active insulating barriers in spin filters. Although there have been many studies on the synthesis and properties of RNMO (especially for R = La) in bulk form [44] [28], there are few reports of thin films of these materials. In this regard, our study will focus on the growth optimization and the study of the physical properties of RNMO thin films deposited by R.F. magnetron sputtering technique.

## 1.2 Objectives

The main goal of the present thesis is to grow ferromagnetic insulators in thin film form for applications in spintronic devices, such as spin filters tunnel barriers. For this purpose, we have chosen two types of double perovskite of the form $R_2NiMnO_6$ obtained by substitution of Mn by Ni, specifically $La_2NiMnO_6$ and $Pr_2NiMnO_6$. The technique used for the growth of the films has been through a sputtering source, which is known to be suitable for large scale deposition. The growth conditions to obtain high quality thin films must be optimized and carefully studied through the different physical characterization techniques. After achieving optimal growth conditions and thus thin films with good ferromagnetic behavior, the magnetic properties and B-site cationic ordering will be studied in detail.

## 1.3 Outlook of the Thesis

This work is divided into four chapters. Here, in chapter 1, we start with a general introduction of RNMO (R = La, Pr) thin films with double perovskite structure. Additionally, we present the most relevant general concepts used throughout this thesis. The main physical concepts of $A_2BB'O6$ compounds such as their crystalline and electronic structure, factors that affect the crystalline structure and magnetic interactions of these materials, are briefly explained. Finally, the main factors and growth modes of thin films are mentioned. Chapter 2 focuses on describing the different steps that were carried out for the RNMO thin film deposition, such as the synthesis of the target material and the surface optimization of the substrates. In addition, the methodology that was carried out for the optimization of the growth conditions of the films (by RF magnetron sputtering technique) is explained.

Chapters 3 and 4 are focused on the growth and physical characterization of thin films of insulating ferromagnetic RNMO thin films. In this regard, a detailed study of the optimization of the growth parameters (i.e. chamber oxygen pressure, growth temperature and annealing) in order to obtain high-quality of RNMO thin films with good ferromagnetic properties is presented. At the same time, to determine the films with good crystalline quality, the morphological and structural properties are examined and discussed in detail along with the transport properties and magnetic characterization of the films. On the other hand, as the stoichiometry of the RNMO films crucially affects their functional properties, we discuss the influence of growth parameters on the stoichiometry and B-site cationic ordering of the films. Additionally, in chapter 3, a detailed study of the evolution of the morphological, structural and magnetic properties of the films as a function of the annealing temperature is presented.

In chapter 4 too, the structural and magnetic properties of PNMO films varying thickness deposited on two different substrates are explored, in order to study the role of the structural mismatch and strain state in the films. Finally, we examine the nature of the ferromagnetic interaction in the RNMO films by X-ray absorption spectroscopy (XAS) and X-ray magnetic circular dichroism (XMCD) measurements, which are also compared to theoretical simulation.

The experimental techniques used in the course of this thesis are briefly described in Appendix A. Deposition technique and growth conditions of the RNMO samples are described, as well as structural, transport and magnetic characterization techniques. Finally, X-ray absorption spectroscopy (XAS) and X-ray magnetic circular dichroism (XMCD) techniques are briefly explained.

# 1.4 General concepts

## 1.4.1 Transition metal oxides

Transition metal oxides (TMOs) [45], as strongly correlated systems, exhibit a large variety of electronic and magnetic phases with remarkably diverse functional properties, including ferromagnetism, superconductivity, ferroelectricity, colossal magnetoresistance (CMR), metal-insulator transitions (MIT) and other charge- and spin-ordered states, with potential applications to novel electronic devices. Such phenomena arise as a consequence of the strong interactions of the transition metal *d* orbitals (outermost electrons) with the oxygen *p* orbitals, and to the coupling between the charge, spin, orbital, and lattice degrees of freedom, that are inherent to many TMOs [45]. These functional properties of TMOs can be exploited for practical applications such as spintronic devices, resistance random access memory (ReRAM), solid oxide fuel cells (SOFCs) to mention a few [46] [47]. Among TMOs, perovskites have received ample attention because they exhibit a great variety of functional properties including those mentioned above in a particularly simple structure [48].

This chapter focuses on briefly explaining the most general physical concepts TMOs with double perovskite structure ($A_2BB'O_6$). We will explore aspects such as their crystalline and electronic structure, factors that affect the crystalline structure, cationic ordering and magnetic interactions, which are important for the understanding and fabrication of these materials. In particular, in this thesis, we explore two ferromagnetic TMOs with double perovskite structure, namely $La_2NiMnO_6$ and $Pr_2NiMnO_6$, as their ferromagnetic insulating character makes them promising candidates for spintronic devices. Hence, their main physical properties will be discussed below.

## 1.4.2 Crystalline Structure: Perovskite Oxides

Perovskites constitute a large family of inorganic crystalline compounds and one of the most extensively studied structures in materials science. The perovskite structure, whose basic chemical formula is $ABO_3$ (where A and B are cations) is depicted in Fig 1.1. The crystal structure of $ABO_3$ represents an ideal simple perovskite cell has cubic symmetry (space group $Pm\bar{3}m$). In Fig. 1.1, B cations, typically transition metals (Mn, Fe, Co, Ni, etc.) are at the center of an octahedron, surrounded by 6 first-neighbour oxygen anions, thus forming the characteristic $BO_6$ octahedron; whereas A cations, often a rare earth element (La, Pr, Nd etc) are surrounded by 12 oxygen anions [49]. As mentioned before, the ideal structure of perovskite is a cubic lattice; nevertheless few compounds have this ideal cubic structure. Generally, many perovskite oxides have slightly distorted variants with lower symmetry (e.g., hexagonal or orthorhombic) [50].

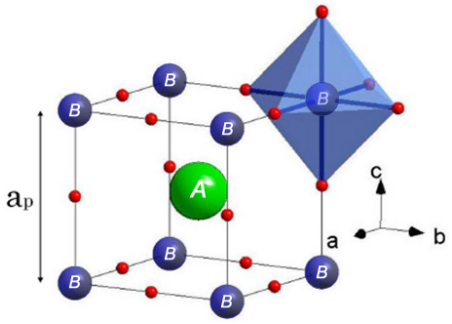


Figure 1.1. Representation of the $ABO_3$ ideal perovskite structure. The A, B cations and oxygens are shown as green, blue and red spheres.

The perovskite structure is highly adaptive and the majority of elements in the periodic table can be somehow inserted into it [49]. In this regard, due to the strong correlation between structure and physical properties, perovskite oxides present a variety of physical properties and they have been intensely studied over the last few decades. The manganites [51], cuprates [51], vanadates [52] etc, are a few examples.

The perovskite structure enables chemical doping and substitution on both A-site ($A_{1-x}A'_xBO_3$) and B-site ($AB_xB'_{1-x}O_3$). For example, starting from the $LaMnO_3$ as parent compound, A-site cation doping, e.g. by Sr ($La^{3+}/Sr^{2+}$), gives rise to $La_{1-x}Sr_xMnO_3$. This substitution may alter the properties of the compound. For instance, while $LaMnO_3$ [53] is an antiferromagnetic insulator, $La_{1-x}Sr_xMnO_3$ [54] is ferromagnetic. On the other hand, the substitution of the B-site Mn cation by Ni gives rise to $La_2NiMnO_6$ (LNMO), also called $LaNi_{0.5}Mn_{0.5}O_3$. Thus, $Mn^{4+}/Ni^{2+}$ take place for half the B sites, thereby when B-sites are occupied in an ordered manner by two different cations with a B/B' (Ni/Mn) inside the structure (ratio 1:1 for Ni:Mn), it becomes the so-called "double perovskite" with the sum

formula $A_2BB'O_6$ [55]. It results that LNMO is a ferromagnetic insulator (FM-I). Our study focuses on RNMO compounds, namely $La_2NiMnO_6$ and $Pr_2NiMnO_6$, which will be explained later.

### 1.4.3 Double Perovskite Oxides

The double perovskite structure can be derived out of the simple perovskite structure of general formula $ABO_3$. The unit cell is doubled with alternate perovskite units $ABO_3$ and $AB'O_3$ along the three crystallographic axes [55]. In this regard, materials of the form $ABO_3.AB'O_3 \equiv A_2BB'O_6$ (where A is a rare-earth metal, alkali, or alkaline earth metal and B/B' are typically transition metal ions) are called double perovskites (DP) [49]. The corners of the DP structure are occupied by the transition metal atoms B and B' with oxygen atoms located in between, forming alternating $BO_6$ and $B'O_6$ octahedra. The large alkaline-earth metal or rare-earth metal atom A occupies the body-centered site with a 12-fold oxygen coordination in each unit (see Fig. 1.2) [56]. An ideal double perovskite $A_2BB'O_6$ crystallizes in the cubic crystal structure with rock-salt ordering of B and B' cations. Nevertheless, the two different B and B' cations may remain disordered at the B site, or they can order with a B:B' ratio of 1:1, forming a so-called B-site ordered double-perovskite $A_2BB'O_6$ with rock-salt type order (see Fig. 1.2) [55]. In addition to the rock salt ordering, cations can order into columns or layers. The most symmetric and the most widely observed pattern in double perovskites is called rock salt ordering because the pattern of B and B' (or A and A') cations is equivalent to the anion and cation positions in the rock salt structure [57] [58]. The rock salt type configuration has alternate B and B' cationic arrangements in all three dimensions, creating a rock-salt-type arrangement. Cubic (space group: $Fm\bar{3}m$) and monoclinic (space group: $P2_1/n$) lattices are the few examples of rock salt configurations [59].

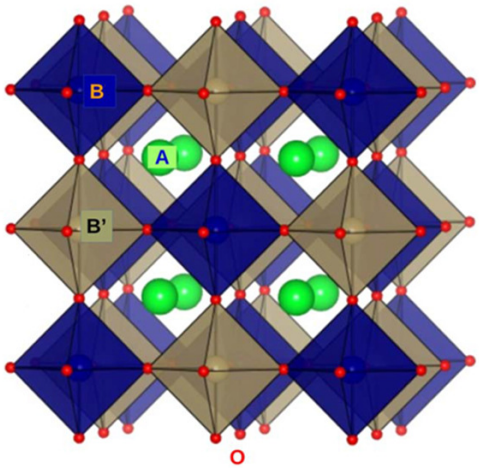


Figure 1.2 Schematic illustration of double perovskite $A_2BB'O_6$ with rock-salt type order. Fig taken from Ref. [55]

Accordingly, the DP structure presents additional features. The atomic combination is highly flexible by adjusting different A, B, and B' elements, giving rise to intriguing physical properties such as charge disproportionation [60], high-temperature spin ordering [61], half metallicity [62], ferroelectricity [63], and giant dielectric constant [64]. In $A_2BB'O_6$ double perovskites, the degree of B-site ordering determines the crystal structure and magnetic exchange interactions between the respective magnetic B (B')-cations. Compared to simpler $ABO_3$ perovskites, the presence of chemical order of B and B' cations influences considerably both magnetic and electronic properties [65]. On the other hand, the $A_2BB'O_6$ structure can be distorted by tilt or distortion of the $BO_6$ octahedra or by cationic displacements in order to optimize the cation bonding with different A, B, and B' atomic combinations. As a result, a variety of crystal structures are formed, ranging from tetragonal, monoclinic to rhombohedral structures [66].

## 1.4.4 Crystal distortions in $A_2BB'O_6$

In $A_2BB'O_6$ double perovskites, the topology is thermodynamically stable, nevertheless, the crystal structure may distort, as a result of the competing bonding preferences of the A, B and B' species, being often unstable [67]. A variety of factors can influence both the phase formation and the resulting behaviour of these compounds. As an example, the material may be oxygen deficient, or alternatively may display so-called anti-site disorder, i.e. imperfect segregation of the B and B' site cations, both of which affect the crystal structure and may interfere with the physical properties [59]. Moreover, due to the numerous combinations of cations with different ionic radius, the ideal cubic rock-salt ordered $A_2BB'O_6$ double perovskite structure can also be distorted by cationic displacements, distortion and/or tilt/rotation of the $BO_6$ octahedra, in order to optimize the cation bonding with different A, B, and B' atomic combinations. These modifications can occur independently or, as often, in combination with each other. Moreover, the resulting changes may be cooperative in the sense that they affect all octahedra in a similar way, or non-cooperative, in which case the distortions may cancel out at a macroscopic level although they may still influence microscopic properties [68]. The amount of distortion is generally small and is readily influenced by external factors. Thus, changes in temperature, pressure, crystallite size or form may alter the type and degree of distortion present [66]. As a result, a variety of crystal structures are formed as the temperature or pressure is changed.

### 1.4.4.1 Cationic displacements

Cation displacements occur when the $BO_6$ octahedra remain perfect (or nearly so) and the cations are simply displaced away from the center of the octahedron. This change is usually associated with cations that are "too small" for the octahedral site. Therefore, the crystal structure undergoes a series of symmetry changes; it becomes tetragonal, trigonal or orthorhombic, depending on the direction of cation displacement and the magnitude of the displacements occurring [68].

### 1.4.4.2 Distortions of the $BO_6$ octahedra

Distortion of the $BO_6$ octahedra occur when the $BO_6$ octahedron itself can distort to give elongated or flattened octahedra, which, in extreme cases can lead to square planar or square pyramidal coordination. These distortions are a result of interactions between the cation electronic orbitals and the surrounding anions, typified by the Jahn–Teller (JT) effect. Octahedral distortion can also be caused by cation valence changes [68]. The JT effect occurs in systems in which there are several degenerate energy levels and not fully occupied. In this case, the JT theorem predicts that the system will experience a distortion of the ideal octahedral geometry that will lower the symmetry, remove the degeneration, and decrease the energy. Thus an energetic stabilization will happen by removing the electronic degeneracy of the highest occupied molecular orbital [69].With respect to perovskite structures, the JT theorem applies to octahedrally coordinated transition metal B-site cations. It implies that perovskites containing ions with certain *d*-electron configurations (so-called Jahn–Teller ions) will have an enhanced stability when located in a distorted octahedral environment compared to an undistorted one [68]. Therefore, distortion of the $BO_6$ octahedra due to electronic instabilities, such as the JT effect, can affect the crystal structure of the $A_2BB'O_6$ double perovskite [70].

### 1.4.4.3 Octahedral tilt or rotation of the $BO_6$ octahedra

The tilt or rotation of the octahedra is the most common distortion mechanism. Similar to the case of cationic displacement, octahedral tilt or rotation occur when the $BO_6$ octahedra remain perfect (or nearly perfect). Thus, to accommodate the cations size, the octahedra are tilted in order to improve packing and decrease the energy of the crystal. In many cases, slight tilting of the octahedra, to enhance the crystal stability, is mostly associated with A cations that are

too small [70]. Thereby, the $BO_6$ octahedra twist to effectively reduce the cavity dimensions, again allowing the structure to accommodate values of tolerance factor (t) less than 1. As with cation displacement, rotation also lowers the symmetry of the crystal and has a profound influence on the physical properties [68]. In case of an ideal cubic rock-salt ordered $A_2BB'O_6$ double perovskite, the unit cell is doubled in all three crystallographic directions compared to a single perovskite, resulting in a space group *Fm-3m*. However, although many cubic ordered double perovskites are known, the majority of compositions crystallize in lower symmetry space groups due to the occurrence of an octahedral tilting distortion in their structures [65]. Similar octahedral tilting as with single perovskites is possible, but the resulting space groups differ [59]. Thus, structures with reduced symmetry are more common. These octahedral tilting distortions can be described using the Glazer's notation [71].

The octahedral tilting takes place mainly to optimize the A-site cation bonding in case of non-ideal ionic radius ratio. For $R_2NiMnO_6$ compounds, the size mismatch among R, Ni and Mn ions results in tilting of the octahedra. The Goldschmidt [72] tolerance factor (t) is a common way of expressing the cation size mismatch and, is an estimate of the stability of the structure. For $A_2BB'O_6$ double perovskites with two different B-site cations, an average of the B-cation radii is used. Therefore, for RNMO systems, $t$ is expressed as $t = (r_R + r_O)/\sqrt{2}\left[\frac{r_{Ni}+r_{Mn}}{2} + r_O\right]$, where $r_R$, $r_{Ni}$, $r_{Mn}$ and ro are the ionic radii of R, Ni, Mn and O ions, respectively. With decreasing $r_R{}^{3+}$, the value of $t$ decreases, which indicates a tilting of the octahedra and thus a bending of the Ni-O-Mn bonds [37] [73] [74].

On the other hand, in the ideal case of fully matched A- and B (B')-cations, t=1 and the undistorted *F*m-3m cubic structure would be realized. In the most relevant cases, when the tolerance factors are smaller (t < 1), the A-site cation radius is smaller than ideal, and the perovskite structure compensates for the cation size mismatch by tilting the $BO_6$ octahedra. In this case, stress can be released by a change of bond length, instead of an octahedral tilting. One possibility is for the A–O bonds to stretch beyond their ideal lengths, making the A-site cation underbonded, while the B–O and/or B'–O bonds contract, making one or both of these cations overbonded. Both octahedral tilting and bond length change may take place simultaneously [75] [76]. In this regard, the crystal symmetry is reduced to the tetragonal *I4/m* or monoclinic $P2_1/n$ space group. In contrast, the disordered double perovskites often crystallize in an orthorhombic *Pnma* structure [77]. When t > 1, the A-site cation is too large and the strain caused by the radius mismatch cannot be relieved by octahedral tilting. Typically various hexagonal structures are formed instead of a perovskite structure [59].

Therefore, based on the tolerance factor the double perovskite compounds have different structures, i.e., cubic for 1.05 > t > 1.00, tetragonal for 1.00 > t > 0.97, and monoclinic/orthorhombic for t < 0.9 [62]. In case of the rock-salt ordered $A_2BB'O_6$ double perovskites, a typical progress of octahedral tilting with decreasing tolerance factor has been found as $a^0a^0a^0$ (*F* m-3m) → $a^0a^0c^-$ (*I* 4/m) or $a^-a^-a^-$ (*R* -3) → $a^0b^-b^-$ (*I* 2/m) → $a^+b^-b^-$ (*P* $2_1$/n) [78] [79]. Comparing similar "fixed B-cation families" can show this progress of octahedral tilting [79]. Disordered $A_2BB'O_6$ double perovskites are described by the same space groups

as single perovskites. The most common tilt system is $a^-b^+a^-$ (*P nma*) followed by $a^0a^0a^0$ (*P* m-3m). In addition, there are few compounds reported with $a^-a^-a^-$ (*R*-3c) and $a^0a^0c^-$ (*I* 4/mcm) tiltings, and one compound each with $a^0b^-b^-$ (*I mma* or *I bmm*) and $a^+b^-c^-$ (*P* $2_1/m$) [59]. Compared with a study by Lufaso et al.,[80] the frequency of these space groups is quite similar to $ABO_3$ single perovskites. In case of $La_2NiMnO_6$ double perovskite the rock-salt ordering between the Ni and Mn ions at the B-site of the system have been reported in various studies [1] [19] [81]. The lowest energy structure crystallizes in the B-site rock-salt ferromagnetic (FM) monoclinic *P* $2_1/n$ structure exhibiting a $a-a-c+$ rotational pattern in agreement with experimental observations [82] [83].

Additionally, these tilts and rotations are extremely sensitive to external conditions, including temperature, pressure and strain. Changes in temperature and pressure may induce structural phase transitions and subsequently changes in physical properties in ordered double perovskites [84] [85]. Pressure has an influence on the octahedral tilt angles and the associated *B*-O-*B′* bond angles. In all cases, an increase in temperature decreases octahedral tilt and thus increases the crystal symmetry. Transition to a cubic structure is most commonly observed [86] [87] [59]. In RNMO double perovskites, local atomic structure around Ni and Mn ions is a key factor in determining various physical properties such as magnetic ordering and electronic properties. Thus, the magnetic exchange interaction is associated with the deviation in octahedral tilting, Ni/Mn-O bond lengths, and Ni–O–Mn bond angles [37]. Previous reports argue that the saturation moment increases with increasing oxygen pressure. Low saturation magnetic moment at low oxygen pressure has been explained by the increased structural distortions involving the $B(B')O_6$ octahedra as well as other interatomic structural features [41].

Finally, strain is an important factor to take into account. This condition (strain) is particularly important in the case of thin films which are epitaxially grown onto a substrate. Tensile or compressive strain in the film often arises because of mismatch between the lattice parameters of the substrate and those of the film. Such effects can cause considerable changes in the physical properties of the film itself or of the interface region. In addition, chemical substitution at A- and B(B')-sites in a double perovskite may significantly alter the tilt and rotation of the linked octahedral [68].

## 1.4.5 Factors affecting the crystal structure

The crystal structure can be affected by several factors such as cation ionic radii, B-site cation ordering, electronic instabilities, bond angles, bond length, bond covalency and other bonding preferences, and synthesis conditions [49]. Among the most important are the synthesis conditions and this may be one reason why for some compounds several different space groups have been assigned [88]. For example, the electronic and magnetic properties

of $R_2NiMnO_6$ double perovskites, such as the saturation magnetization, magnetic ordering temperature (Curie temperature, $T_C$), and the electronic band gap vary considerably from one report to the other [89] [30] [37].These differences may result from the various synthesis routes and growth conditions (such as pressure, temperature, annealing atmosphere/ temperature, cooling rate and deposition time) which significantly influence the crystallographic structure and the extent of the antisite disorder at the Ni/Mn sites [29] [42] [90] Oxygen vacancies can also affect the crystal structure and symmetry. The growth of $La_2NiMnO_6$ thin films under different oxygen pressures can result in variations of the defect concentration such as oxygen vacancies [41]. When oxygen vacancies exist in the sample, they induce transfer of an electron from the $e$ band of $Ni^{2+}$ ions to that of neighboring $Mn^{4+}$ ions, creating intermediate-spin $Ni^{3+}$ $\left(t_{2g}^6 e_g^1\right)$ and $Mn^{3+}$ JT cations, which cause local JT distortions of the octahedral sites. The JT distortions would inhibit long-range ordering of Ni and Mn on different lattice sites, stabilizing vibronic ferromagnetic $Mn^{3+}$–O–$Mn^{3+}$, $Ni^{3+}$–O–$Mn^{3+}$, and $Ni^{3+}$–O–$Ni^{3+}$ superexchange interactions in an atomically disordered volume [41]. In this regard, such a vibronic superexchange gives a small stabilization as compared to the static ferromagnetic $Mn^{4+}$–O–$Ni^{2+}$ superexchange, and thus the magnetization is decreased [91]. Previous reports on $La_2CoMnO_{6-\delta}$ compounds by Dass and Goodenough, argued that oxygen vacancies introduce $Mn^{3+}$ ions and tend to trap a second $Mn^{3+}$ near neighbor in an antisite position, thus lowering the atomic order and the saturation magnetization [91].

### 1.4.5.1 B-site cation ordering

The structure and space group of the $A_2BB'O_6$ perovskites depend on the B-site cation ordering. What truly separates the complex $A_2BB'O_6$ perovskite from the $ABO_3$ single perovskites is the possibility for the two B-site cations to order [49] [92] [93]. The B cations generally determine the physical properties of double perovskites. Different types of B-site cation ordering are possible [49]. Nevertheless, the compounds are usually either rock-salt ordered or disordered, followed by a much larger number of disordered compounds [23]. The stability of the B-site rock-salt-ordering increases with a corresponding increase in the difference in the oxidation state of the B and B' cations [65]. Therefore, the factors that control B-cation arrangement in $A_2BB'O_6$ double perovskites are the differences in oxidation state, ionic radius, cation coordination geometry, and A-cation/B-cation size ratio. The oxidation state, and to some extent, the cation radius differences are the major factors affecting the B-site cation order [65]. Such order-disorder phenomena are of fundamental interest, but the ordering also affects many of the physical properties of these compounds [67] [94]. For instance, the half-metallicity and magnetoresistance properties of $Sr_2FeMoO_6$ are strongly affected by the degree of B-site cation order [95]. Reports on $La_2NiMnO_6$ thin films have established that B-site ordering can play a key role in finding the physicochemical

behaviors of double perovskites, especially the coincidence of strong magnetoelectric response and magnetic transition [96] [97].

As mentioned before, the synthesis conditions could affect the crystal structure and physical properties of the $R_2NiMnO_6$ thin films. Ordering of B-site cations (Ni/Mn) could be influenced by oxygen partial pressure and growth temperature. In particular, for $La_2NiMnO_6$ (LNMO) compounds, ordering of B-site cations affects the crystal structure. It was reported that orthorhombic LNMO (*Pbnm*) is B-site disordered and monoclinic LNMO ($P2_1/n$) exhibits a long-range B-site ordering [98] [99]. Previous studies by Farheen et al., [90] have indeed indicated how variations in annealing temperature and atmosphere affect the crystallinity and magnetic properties of LNMO films. Such an ordering process takes place by a thermally activated diffusion of cations. The process is kinetically controlled and higher temperatures and longer annealing times tend to increase order. At equilibrium, high order would be expected [100]. For example, $La_2CoMnO_6$ has a high degree of order when annealed at 1060 K, and which lowers when annealed at 1640 K [101]. At the same time, studies by Kyômen et al.,[102] have shown that the B-site order of this compound freezes around 1400 K, and that the order parameter of quenched samples changes quite abruptly around this temperature.

### 1.4.5.2 Degree of order and types of disorder

The choice of A-site cation can also affect a double perovskite material as its oxidation state influences the average oxidation state of the B/B' cations. For instance, an $A^{3+}$ cation (La, Pr, Nd, etc.) requires that B/B' cations have an average valence of 3+, making possible the following options: $B^{3+}/B'^{3+}$, $B^{2+}/B'^{4+}$, and $B^{1+}/B'^{5+}$. In this regard, the degree of B sites order that is finally produced depends not only on the valence distribution but also on the choice of elements as cations as each element can have its preferred individual valence state according to the applied growth conditions, e.g., growth temperature and oxygen partial pressure [77]. Therefore, the degree of B-site cation order can be quantified as a first approximation by a simple long-range order parameter, defined as:

$$S = 2g_B - 1 \tag{1.1}$$

where $g_B$ is the occupancy of a B-site cation at its correct site. The completely ordered double perovskite corresponds to S = 1, which means that all sites are fully occupied by the correct cations and the so-called anti-site disorder, ASD = 0. The completely disordered double perovskite will have a value of S = 0. However, an intermediate ordering between these two extreme partial cation ordering is also possible, with a degree of ordering at $0 < S < 1$. The range of cation order in a single compound can vary widely due to different synthesis conditions, which can be a way of controlling the cation order in some of the $A_2BB'O_6$ compounds [59].

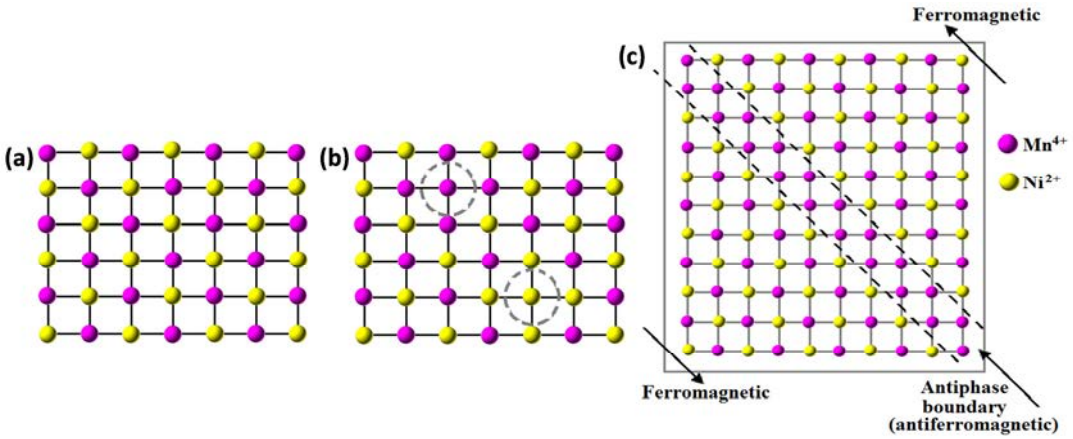


Figure 1.5. B-site cation disorder schemes: (a) completely ordered, (b) anti-site disorder and (c) antiphase boundary in a (001) plane of $La_2NiMnO_6$. Fig reproduced from Ref.[103].

The disorder of the B-site cations can take place in different ways, as presented in Fig. 1.5. The simplest case is the anti-site disorder (ASD), where B and B' cations simply switch places. Small amount of such ASD point-like defects are always expected to be present due to configurational entropy (see Fig.1.5 (b)) [59]. This type of ASD naturally occurs in double perovskites, and strongly affects their magnetic and electronic properties. Recent reports by Pal et al. [104] reported that ASD in the $La_2NiMnO_6$ system leads to the introduction of antiferromagnetic interaction through $Ni^{2+}$-$O^{2-}$-$Ni^{2+}$ and $Mn^{4+}$-$O^{2-}$-$Mn^{4+}$ superexchange, thereby reducing the saturation magnetization $M_s$. Another common type of defects is called antiphase boundary (APB). First suggested by Goodenough, [103] APBs consist in the out-of-phase of crystal domain periodicity, which separates two ordered domains with reversed B and B' site occupancies (see Fig.1.5 (c)). In a way, this can be considered as an accumulation of ASD at one place, resulting in the correct periodicity of the ordered phase, but in reverse order [105]. For example, in $Sr_2FeMoO_6$ double perovskite, cation ordering has been studied quite extensively, as the physical properties are very sensitive to ordering, and it appears that APBs are favored over ASD [105]. On the other hand, Nasir et al. [37] indicates that APBs in $R_2NiMnO_6$ compounds may contain Ni and Mn interactions, which are antiferromagnetic in nature, and often result in spin-glass state and additional magnetic transitions. The magnetic exchange interaction is associated with deviations in octahedral tilting, Ni/Mn−O bond lengths, and Ni−O−Mn bond angles. Thus, in the absence of a magnetic field, two ferromagnetic domains couple antiferromagnetically across the APB. It should also be noted that the neighboring spins couple antiferromagnetically at the anti-site disorders of an ordered matrix [37] [106]. On the other hand, the formation of ASD in $R_2NiMnO_6$ systems can be prevented by optimization of the synthesis conditions and annealing temperatures [106]. Dass et al. [28], argued that, in case of $La_2NiMnO_6$, prolonged annealing may lower the amount of antisite defects, but the APBs are not affected.

# 1.5 Crystal field splitting

In transition metal perovskites, the crystalline field theory is focused on the interaction between the *d* orbitals of the central ion and the donor atoms of the ligands. Thus, the crystal field emphasizes the energy split-up due to *p* - *d* hybridization between transition metal ions and O atoms. The highly localized *d*− orbitals and their interactions with the spin, orbital and lattice degrees of freedom can be modelled by the crystal field theory [107]. In transition metals, the Hund intra-atomic coupling which tends to line up spins, gives rises to two different energy bands, one for each spin orientation (spin up and spin down). In the case of manganites, the central transition metal Mn ion is surrounded by the oxygen octahedral, the degeneration of the five *d*-orbitals is broken due to the octahedral crystal field originating from the Coulomb repulsion with the $O^2$ ligands [107]. As shown schematically in Fig. 1.6 (a) the *d* states of a transition metal ion, which are five-fold degenerate for a free standing atom, tend to split into two groups: the $e_g$ doublet ( $d_{x^2-y^2}$ and $d_{z^2}$ ($d_{3z^2-r^2}$) orbitals), lying higher in energy (since these states point directly towards the O atoms and hence feel more electrostatic repulsion from the O electrons) and the $t_{2g}$ triplet ($d_{zx}$, $d_{yz}$ and $d_{xy}$ orbitals) which are lower in energy (since they point away from the O atoms) [10].

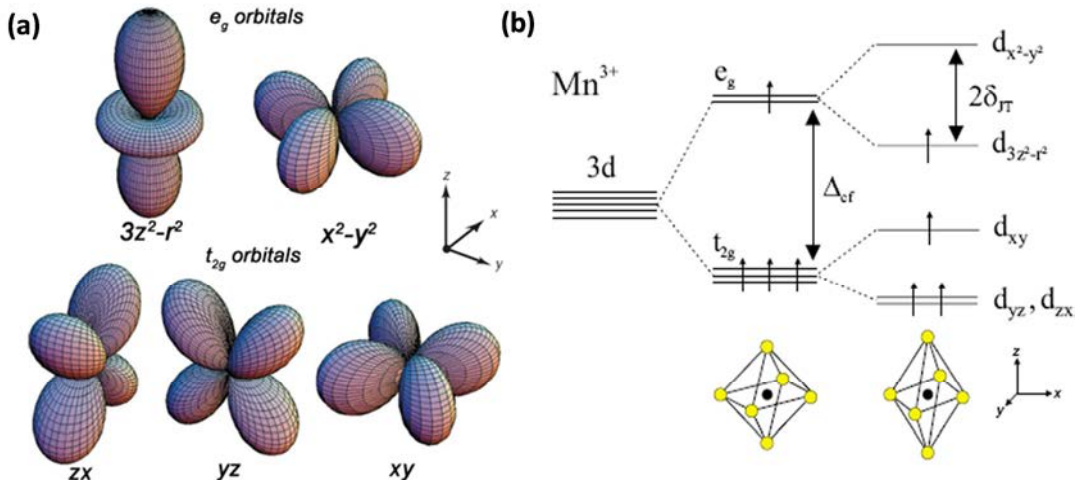


Figure 1.6. (a) Five *d* orbitals. In the cubic crystal field, this fivefold degeneracy is lifted to two $e_g$ orbitals ($(x^2-y^2)$ and $(3z^2-r^2)$) and three $t_{2g}$ orbitals ((*xy*), (*yz*) and (*zx*)). (b) Lifting of the degeneracy of 3d orbitals in $Mn^{3+}$ ions by the Jahn–Teller distortion. The crystal field splitting (CFS), $\Delta_{cf}$, is around 1.5 eV, while the energy difference $2\delta_{JT}$ between the $e_g$ states is about 1 eV. Fig reproduced from refs [107] [10].

The case of $Mn^{3+}$ ([Ar] $3d^4$) has a $d^4$ electronic configuration in a high spin state, with three electrons in its $t_{2g}$ and one electron in its $e_g$ orbitals $\left(t_{2g}^3 e_g^1\right)$, and total spin S = 2. It has a

partially occupied $e_g$ state being sensitive to JT distortion [108], which is due to the lowering of electronic energy by distortions of the $BO_6$ octahedra, as shown in Fig 1.6 (b). The case of $Mn^{4+}$ ([Ar]$3d^3$ electronic configuration) would not show this effect because there is no net lowering of the electronic energy by a distortion. In manganites, such distortions have a significant impact on the electronic and magnetic properties [108] [109] .On the other hand, the energy difference between the $e_g$ and $t_{2g}$ orbitals is usually referred to as the crystal-field splitting ($\Delta_{CF}$) which depends on the nature of the transition metal, its valence and its distance to the oxygen anions. This splitting is typically $\Delta_{CF}$~1.5 eV in the case of manganites [110] [10].

As a particular case, the electronic structure for the two magnetic ions that compose our $R_2NiMnO_6$ materials, $Ni^{2+}$ and $Mn^{4+}$, is displayed in Fig 1.7. Their electronic configurations are given as: [Ar] $3d^8$ for $Ni^{2+}$, and [Ar] $3d^3$ for $Mn^{4+}$. Therefore, for $Ni^{2+}$ ($3d^8, t_{2g}^6 e_{g,}^2 S = 1$), the three $t_{2g}$ levels are completely filled having half-filled $e_g$ orbitals, whereas for the $Mn^{4+}$ ($3d^3, t_{2g}^3 e_g^0, S = 3/2$), the three $t_{2g}$ levels are half-filled having empty $e_g$ orbitals, spins are parallel and coupled to $S$ = 3/2 following Hund's rules interaction. The electrons in each $t_{2g}$ and $e_g$ determine the relative size of ferromagnetic and antiferromagnetic interactions, which would give rise to the magnetic order of the whole $R_2NiMnO_6$ systems [111].

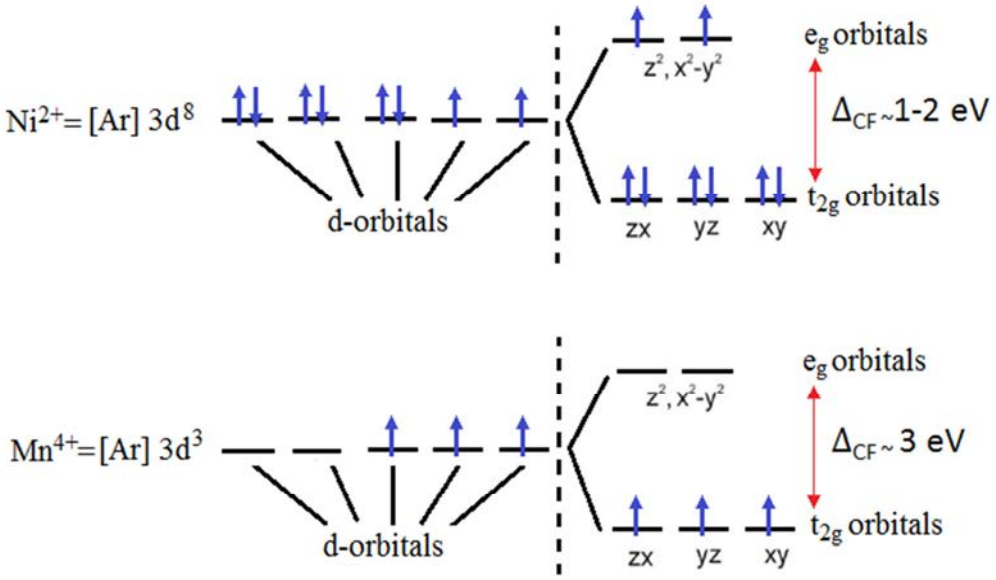


Figure 1.7. Crystal field splitting of the *d*-orbitals of $Ni^{2+}$ and $Mn^{+4}$ in $BO_6$ octahedron of perovskite oxides.

According to Goodenough–Kanamori–Anderson (GKA) rules [111] ordering of $Mn^{4+}$ and $Ni^{2+}$ ions in $R_2NiMnO_6$ materials leads to long-range ferromagnetic coupling superexchange interactions, in the case of half-filled $e_g$ orbital to empty $e_g$ orbital virtual spin transfer, such as $Ni^{2+}(e^2)$–O–$Mn^{4+}(e^0)$ [111] [81] [112]. The energy splitting between $t_{2g}$ and $e_g$ states, $\Delta_{CF}$, is about 3 eV for Mn, and about 1–2 eV for Ni. Both $Mn^{4+}$ and $Ni^{2+}$ are in high-spin (HS)

configuration [113] (see Fig. 1.7). Note that antiferromagnetic (AFM) coupling arises in the case of half-filled to half-filled virtual change transfer, as in $Ni^{2+}(e^2)$–O–$Ni^{2+}(e^2)$ and $Mn^{4+}(t^3)$–O–$Mn^{4+}(t^3)$. In addition, Jahn-Teller ions have a single electron in twofold-degenerate fluctuating $e_g$-orbital occupation as in $Ni^{3+}(e^1)$–O–$Mn^{3+}(e^1)$, $Mn^{3+}(e^1)$–O–$Mn^{3+}(e^1)$ and $Ni^{3+}(e^1)$–O–$Ni^{3+}(e^1)$, giving a three-dimensional ferromagnetic vibronic superexchange interaction [111] [41].

# 1.5.1 Magnetic interactions

In a perovskite structure the exchange interactions depend on the overlap of the wave functions of the magnetic ions. Therefore, the magnetic ground state in TMOs is almost always determined by indirect magnetic exchange interactions of transition-metal (TM) cations which are separated by an $O_2-$ anion in between. For $R_2NiMnO_6$ systems the magnetic interaction that is important and responsible for the ordering of individual magnetic moments is the superexchange interaction [13].

## 1.5.1.1 Superexchange interaction

Superexchange interaction in oxides takes place between neighboring magnetic cations through the intermediate O 2*p* states forming a semicovalent bond. The degree of covalence arises from the sharing of valence electrons between the transition metal atoms and the oxygen atoms that surround them. In this way, the interaction between neighboring transition-metal ions through the jointly shared oxygen atoms results in long-range magnetic ordering [114]. In 180° superexchange, the cation–anion–cation bond is more of less linear, depending on the degree of octahedral tilt and distortion. In this geometry, the GKA rules indicate that the two paramagnetic cations will have a strong tendency to align in an antiferromagnetic fashion. In the case of 90° superexchange, the bond angle is square, and the GKA rules indicate that magnetic moment alignment is ferromagnetic, but the tendency is much weaker than in the previous case [68]. Therefore, as *d*-orbitals can have different orientations and configurations, may give rise to different types of ferromagnetic (FM, sign positive) or antiferromagnetic (AF, sign negative) superexchange interactions.

The exact nature of the coupling due to superexchange interactions can be determined accurately for a majority of 3*d* TMOs using the Goodenough [114], Kanamori [115] and Anderson rules [116], ('GKA' rules). For octahedral-site cations in perovskite structures, these rules enable to determine the sign of the exchange integral and the type of interaction depending on the orbital configuration of the two magnetic metal ions involved in the

interaction via the oxygen atoms. For this, one has to keep in mind that (i) the Pauli exclusion principle forces two electrons in the same $e_g$ orbital to have antiparallel spins whereas (ii) Hund's rule favours electrons with parallel spins in different orbitals ($t_{2g}$ and $e_g$) of the same 3d shell [13]. For angles of 180° between the cation-anion-cation bond, three different cases are considered [117]:

1. $e_g$-$e_g$: two half- filled $e_g$ cation orbitals overlapping oxygen $p_\sigma$ orbital, giving rise to weak and strong AF interaction. (Figure 1.8 (a)),

2. $t_{2g}$-$t_{2g}$: two half-filled $t_{2g}$ orbitals of cations directed towards the intermediate $p_\pi$ anion orbital and produce the AF interaction between the transition-metal cations, and is weaker than 1 (Figure 1.8 (b)),

3. $e_g$-$e_g$ : in order to give rise to an intrinsic strong ferromagnetic interaction in a double perovskite structure, as $La_2NiMnO_6$, two transition-metal ions are needed; one with $e_g$ electrons (M) and another without $e_g$ electrons (M'), in an M-O-M' linear arrangement, i.e., (180° bond angle) (Figure 1.8(c)). Such a linear arrangement is achieved in a double perovskite structure, in which M and M' are ordered in a rock-salt manner at the B site of the perovskite structure [117]. On the other hand, the interactions coming from $t_{2g}$ orbitals must be considered in cooperation with the angle dependence of the Ni –O–Mn bond [111].

In this regard, $La_2NiMnO_6$ [81] and $Pr_2NiMnO_6$ [29] double perovskites are examples of FM insulators, resulting from ferromagnetic superexchange interaction between $Ni^{2+}$ (half-filled $e_g$ orbitals) and $Mn^{4+}$ (empty $e_g$ orbitals), i.e. $Ni^{2+}$–O–$Mn^{4+}$ ($e^2$–$2p$–$e^0$) [81] [112]. Some manganites, such as $LaMnO_3$ and $PrMnO_3$, are examples of AF insulators due to superexchange interaction between $Mn^{3+}$–O–$Mn^{3+}$ ($e_g$–$2p$–$e_g$).

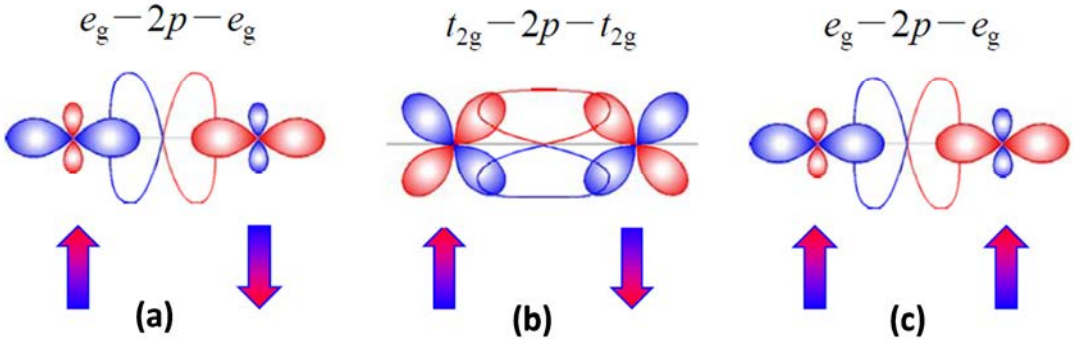


Figure 1.8. Magnetic interaction between octahedral site transition-metal ions via an oxygen ion according to the Kanamori-Goodenough rules (180° cation-anion-cation interactions). (a) AF interaction of M'($e_g$)–O–M'($e_g$). Half-filled $e_g$ orbitals of M' cations overlapping oxygen $p_\sigma$ mediate the strong AF interaction; (b) AF interaction of M($t_{2g}$)–O–M($t_{2g}$). Half-filled $t_{2g}$ orbitals of M cations overlapping oxygen $p_\pi$ produce the AF interaction; (c) FM interaction of M($e_g$)–O–M'($e_g$) one with $e_g$ electrons (M) and another without $e_g$ electrons (M'). Figure taken from ref. [117]

# 1.6 Double perovskites: $R_2NiMnO_6$ (R= La, Pr)

Double perovskites $R_2NiMnO_6$ (R = La, Pr) have been of great interest in the scientific community due to their diverse physical properties and the wide prospect of technological applications. These materials can be widely used for fabricating novel magnetic, electronic, and multiferroic superlattices/systems because their properties can be tailored by changing the radius ($r_R^{3+}$) of the $R^{3+}$ ion [37]. Multifunctional properties of these perovskites include colossal magnetoresistance, magneto-capacitance and dielectric properties [1] [118] [119]. Such properties of $R_2NiMnO_6$ compounds result from spin-phonon coupling, which strongly depends on the R and Ni/Mn-site ordering [42] [120] [37]. As previously mentioned in the introduction, in this thesis, we focus our attention on exploring two kinds of ferromagnetic TMOs: $La_2NiMnO_6$ and $Pr_2NiMnO_6$. These materials are characterized by being ferromagnetic insulators and due to their complex physical properties they are promising candidates for spintronic devices [19] [29]. Recent work on this class of ($R_2NiMnO_6$) compounds has been primarily focused on $La_2NiMnO_6$, while other $R_2NiMnO_6$ ($R \neq La$) compounds have been less investigated.

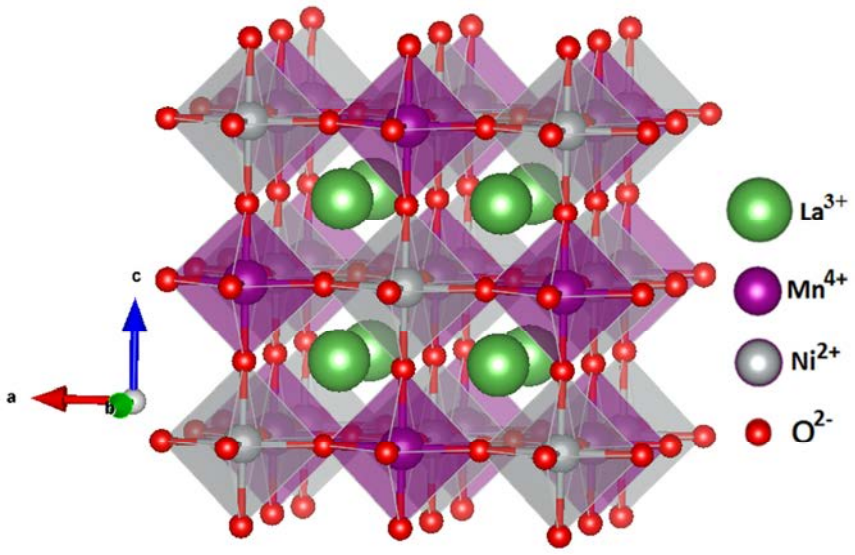


Figure 1.9. Crystallographic structure of $La_2NiMnO_6$ ($P2_1/n$).

$La_2NiMnO_6$ has received considerable interest because of its high magnetic transition temperature ($T_C \approx$ 280 K) [28], insulating characteristics, magneto-dielectric effect and the possibility of preparing high quality LNMO thin films [96] [41]. This is also due to its multifunctional nature that can be promoted by manipulating the coupling between

its electronic, magnetic, and phonon order parameters [1]. Over the years, the magnetic properties of bulk LNMO have been widely studied in order to gain better understanding of the nature of the magnetic exchange interactions in this compound [44] [99] [28]. On the other hand, apart from $La_2NiMnO_6$, the physical properties of $Pr_2NiMnO_6$ in bulk and thin film forms have been less investigated; [120] [29] although some studies on bulk $Pr_2NiMnO_6$ samples have reported a single ferromagnetic-to-paramagnetic transition at 228 K [120].

Previous studies on $R_2NiMnO_6$ compounds, by Booth et al., [30] and Nasir et al.,[37] have demonstrated that substitution of $La^{3+}$ by a smaller rare earth ionic radius $R^{3+}$ induces significant modifications in the Ni–O–Mn bond angle directly involved in the superexchange mechanism. The decrease in bond angle reduces the degree of overlap of Mn−O and Ni−O orbitals. Therefore, rare-earth ion size greatly influences the electronic and magnetic ground states. The orbital overlap within the B−O−B' bond is key in this aspect [30] [37]. Consequently, compared to that of $La_2NiMnO_6$, the magnetic transition temperature, $T_C$, decreases with decreasing the $r_R{}^{3+}$ radius (see Fig. 1.10 (c)). Polycrystalline $R_2NiMnO_6$ samples prepared by sol−gel method revealed that by decreasing $r_R{}^{3+}$, the ferromagnetic transition temperature $T_C$ decreased monotonously from 270 K for R=La to 80 K for R=Ho. Therefore, $T_C$ is controlled by the nature and size of rare-earth ion (see Fig. 1.10 (c)) [37].

On the other hand, as mentioned before the origin of ferromagnetism in $R_2NiMnO_6$ compounds, is mainly governed by superexchange interaction and GKA rules [111]. The superexchange coupling arises from the virtual hopping between half-filled $Ni^{2+}$ and empty $Mn^{4+}$ orbitals through the oxygen. Therefore, this monotonic decrease of $T_C$ with decreasing $r_R{}^{3+}$ indicates that the magnetic behaviour of these materials is correlated not only to the Ni−O−Mn bond angle, but also by the variation of covalency/ionicity of the Ni/Mn−O bond length (see Fig. 1.10 (a) and (b)) [30] [37] [121] [122]. Extended X-Ray Absorption Fine Structure (EXAFS) and X-ray diffraction (XRD) studies revealed that the reduction in Ni-O-Mn bond angles and increase of average Mn/Ni-O bond distances with reducing $r_R{}^{3+}$ reduce the overlap between orbitals, i.e., the Mn/Ni−O covalent character. In turm, this lowers the strength of the superexchange interaction between the $Ni^{2+}$ and $Mn^{4+}$ ions. Consequently, the Curie temperature $T_C$ decreases and the octahedral tilting increases [37].

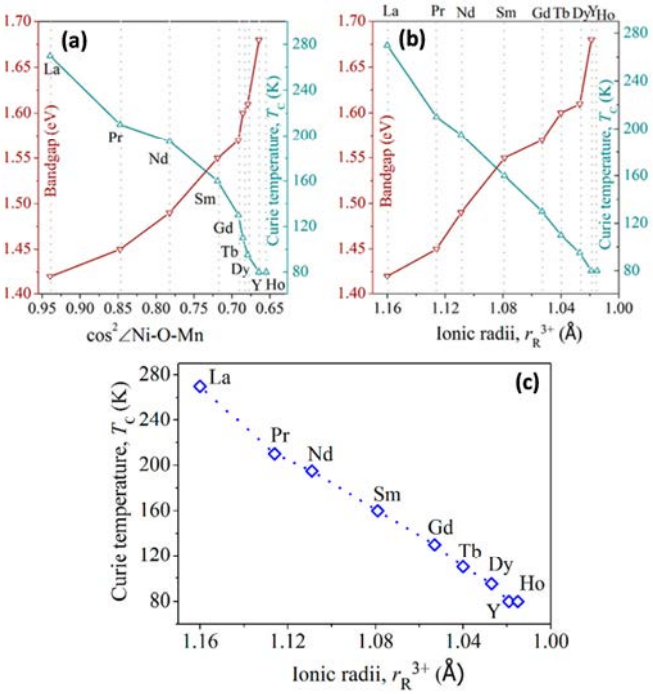


Figure 1.10. Electronic band gap and Curie temperature $T_C$ of $R_2NiMnO_6$ compounds as a function of (a) superexchange angle ∠Ni−O−Mn, and (b) ionic radii $r_R^{3+}$. (c) Variation of the magnetic ordering temperature $T_C$ as a function of rare-earth ion size, $r_R^{3+}$. Figs were reproduced from ref [37].

On the other hand, $RMnO_3$ has an orthorhombic perovskite structure, whereas $RNiO_3$ is rhombohedral. The structure of $R_2NiMnO_6$ (R= La, Pr) exists at high temperature in rhombohedral phase ($R\bar{3}$ *or* $R\bar{3}c$), whereas it transforms at room temperature to monoclinic ($P2_1/n$) or orthorhombic (*Pbnm*) [28] [30] [120]. Studies have demonstrated that well-ordered $La_2NiMnO_6$ and $Pr_2NiMnO_6$ in bulk or film form may be arranged in rhombohedral $R\bar{3}$ and monoclinic $P2_1/n$ space groups with $Ni^{2+}$ and $Mn^{4+}$ cations alternatively arranged at the B sites [123] [124]. Fig. 1.9 shows the ordered monoclinic structure in a bulk $La_2NiMnO_6$ sample.

For $R_2NiMnO_6$ compounds there are two main issues: (i) the valence states of the Ni and Mn ions, and (ii) the mechanism of ferromagnetic exchange interaction between Ni and Mn magnetic moments. As for the valence states, there are two possibilities, $Ni^{3+}$– $Mn^{3+}$ and $Ni^{2+}$– $Mn^{4+}$. As for the exchange interaction, it is actually connected to the valence states because the sign of the superexchange interaction, which is the plausible magnetic mechanism in this system, is determined by the valence states of Ni and Mn ions through the GKA rules [111].

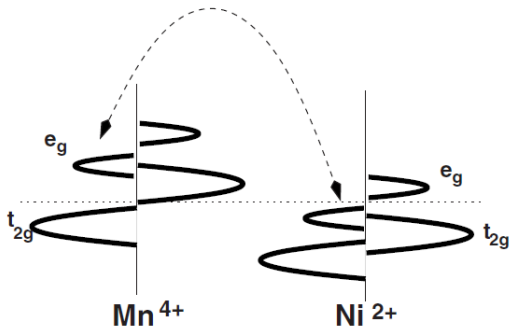


Figure 1.11. The superexchange interaction between $e_g$-$e_g$ gives rise to a ferromagnetic order according to the GKA rules. Figure taken from ref. [111]

In addition, the changes in the valence states and size of Ni/Mn cations provoke modifications in their electronic and magnetic states. Thereby, a large difference in size and valence of the B-B' sites cations promotes high degree of B-sites order [77]. Thus, depending on the magnetic properties, $R_2NiMnO_6$ (R= La, Pr) may be classified as:

(i) A long range ordered $Ni^{2+}/Mn^{4+}$ phase, due to the difference in valence states and ionic radii (0.690 Å and 0.530 Å in octahedral symmetry), showing a single transition ferromagnetic at about 280 K for LNMO [28] and 228 K for PNMO [120]. Moreover, the theoretic magnetic moments of $Ni^{2+}$ (S=1) and $Mn^{+4}$ (S=3/2) are $2\mu_B$ and $3\mu_B$, respectively. Therefore, for a configuration $Ni^{2+}/Mn^{4+}$ and long-range B-site order, a saturation magnetization of $5\mu_B$/f.u is expected. In this regard, it is due to the ferromagnetic superexchange interaction $Ni^{2+}$–O–$Mn^{4+}$, that in the octahedral symmetry, $Ni^{2+}$–O–$Mn^{4+}$ valence states form the electron configuration of $d^8\left(t_{2g}^6 e_g^2\right) - O(2p) - d^3(t_{2g}^3 e_g^0)$. Thus, assuming that the interaction between two $t_{2g}$ orbitals is smaller than the interaction between $e_g$ orbitals, the ferromagnetic ordering in $R_2NiMnO_6$ is governed by the 180° superexchange from the bond between oxygen and the occupied Ni ($e_g^2$) and unoccupied Mn($e_g^0$) ions, respectively (see Fig.1.11 and Fig 1.7) [111] [81] [112]. On the other hand, in RNMO systems the disordering of B-sites easily occurs, since ionic radii difference of $Ni^{2+}$ (0.69 Å) and $Mn^{4+}$ (0.53 Å) ions is 0.16 Å and the charge difference is 2. In the case of an ionic radii difference smaller than 0.2 Å or a charge difference smaller than 3, B-site disordering easily occurs [125] [65].

(ii) A cation disordered phase with random ordering of the Ni/Mn cations, showing a single transition ferromagnetic around 100-150 K due to the super-exchange interaction of $Ni^{3+}$-O–$Mn^{3+}$ with the electron configuration of low-spin and high-spin $d^7\left(t_{2g}^6 e_g^1\right) - O(2p) - d^4\left(t_{2g}^3 e_g^1\right)$.

(iii) An admixture phase, showing two paramagnetic-to-ferromagnetic transitions owing to the above mentioned exchange interactions [126].

## 1.6.1 Non-stoichiometry and oxygen content

In an ordered compound, the degree of ordering is a characterization of preferential occupation of different atoms on respective sites of an unit cell. An ideal crystal structure of $La_2NiMnO_6$ has the general formula of $A_2BB'O_6$, with an ordered arrangement of Ni cation at B site, Mn cation at B' site, and La cation at A site [49]. In the non-stoichiometric $La_2Ni_{1-x}Mn_{1+x}O_6$ compounds, Ni and Mn alternatively occupy the B and B' sites in a double perovskite $A_2BB'O_6$. The alteration of the relative chemical composition between Ni and Mn in the $La_2Ni_{1-x}Mn_{1+x}O_6$ compounds exhibits a significant effect on the crystal structure, physical properties and ionic ordering. Appropriate synthesis conditions are necessary to stabilize the double perovskite structure. In fact, the oxygen content and the degree of cations site ordering affect the final properties of the material, which are mainly controlled by the synthesis route, heat treatment, and atmosphere. Moreover, the change in valence states affects the ferromagnetic superexchange interaction between Ni and Mn ions via oxygen

Previous reports by J. Blasco et al, [99] [85] [127] investigate the crystallographic structure, ferromagnetic ordering and electronic states in non-stoichiometric $LaNi_{1-x}Mn_xO_{3+\delta}$ (x = 0.1, 0.25, 0.5, 0.75, 0.9) samples with different oxygen content prepared by sol-gel method following a citrate route. Different sintering conditions were used to obtain samples with different degree of oxidation. At the same time, in order to study the effects of the oxygen content several thermal treatments were carried out to the samples with $x \geq 0.5$. In this series of samples, as the Ni content goes up to x = 0.5 for $LaNi_{0.5}Mn_{0.5}O_{3.05}$, $LaNi_{0.5}Mn_{0.5}O_{3.06}$, and $LaNi_{0.5}Mn_{0.5}O_{3.08}$, $T_C$ increases in a ranging from 267-280 K. The highest $T_C$ (≈ 280 K) corresponded to the most oxidized sample. The Ni-rich samples ($x < 0.5$), as $LaNi_{0.75}Mn_{0.25}O_{3.0}$ and $LaNi_{0.9}Mn_{0.1}O_{3.02}$, showed a similar $T_C$, around 260 K. Nevertheless, in this series of $LaNi_{1-x}Mn_xO_{3+\delta}$ (x= 0.5, 0.25 and 0.1) samples, a strong reduction of the magnetization (from 1.85-0.13 $\mu_B$/f.u.) is observed with the increase of the Ni content. This result was related with two effects: a higher transition metal vacancy and high degree of transition-metal oxidation (higher amounts of $Mn^{4+}$ and/or $Ni^{3+}$). The Ni atom is in mixed-valence (2+ and 3+ states) in samples of the Ni-rich region. Therefore, a possible explanation of their magnetic properties is that the Ni subband is not localized in the Ni-rich region of the samples, as it occurs for $LaNiO_3$.

On the other hand, in the set of $LaNi_{1-x}Mn_xO_{3+\delta}$ samples with ($x > 0.5$), i.e. $LaNi_{0.25}Mn_{0.75}O_{3+\delta}$ and $LaNi_{0.1}Mn_{0.9}O_{3+\delta}$, the magnetic ordering begins at around 180 K and 150 K with magnetic anomalies below $T_C$. The oxidized samples show a lower value of magnetic moment and this difference seems to increase with increasing the Mn content of the sample. For instance, $LaNi_{0.1}Mn_{0.9}O_{3.13}$ and $LaNi_{0.1}Mn_{0.9}O_{3.0.2}$ samples showed a Ms of 3.15 and 3.55 $\mu_B$/f.u., respectively. This difference is higher than between $LaNi_{0.25}Mn_{0.75}O_{3.09}$ and $LaNi_{0.25}Mn_{0.75}O_{3.0}$ samples with a Ms of 2.95 and 3.0 $\mu_B$/f.u., respectively. In the oxidized samples, ferromagnetic ordering does not seem to be completely achieved. Consequently, the

magnetic state may be more affected by the presence of vacancies at the Mn/Ni sites that are strongly disruptive for the magnetic exchange.

Neutron-diffraction experiments showed that the crystallographic structure of $LaNi_{1-x}Mn_xO_{3+\delta}$ depends on both the Ni/Mn ratio and the oxygen content. The unit cell of stoichiometric samples ($\delta = 0$) in the Ni-rich region for $LaNi_{0.75}Mn_{0.25}O_{3.0}$ ($x < 0.5$) is rhombohedral (space group, $R\bar{3}c$), while in the Mn-rich region for $LaNi_{0.25}Mn_{0.75}O_{3.0}$ ($x > 0.5$) it is orthorhombic (space group, *P*bnm). Both $LaNi_{0.5}Mn_{0.5}O_3$ ($x = 0.5$) phases coexist at room temperature because this compound undergoes a structural phase transition just at room temperature. At the same time, the unit cell volume increased in stoichiometric samples (Mn-rich region) i.e., $LaNi_{0.25}Mn_{0.75}O_{2.97}$ and $LaNi_{0.1}Mn_{0.9}O_{3.0}$ while the oxidized samples as $LaNi_{0.5}Mn_{0.5}O_{3.08}$, $LaNi_{0.25}Mn_{0.75}O_{3.09}$ and $LaNi_{0.1}Mn_{0.9}O_{3.13}$ showed a smaller unit cell due to the presence of cationic vacancies. On the other hand, neutron diffraction patterns indicated that ferromagnetic long-range ordering for $LaNi_{1-x}Mn_xO_{3+\delta}$ samples was only achieved for $x \geq 0.5$ ($x = 0.5$, 0.75, 0.9) that is, in this case, for the samples with higher Mn content. Then, the $Ni^{2+}$–O–$Mn^{4+}$ ferromagnetic interaction and ordered arrangement of $Ni^{2+}$ and $Mn^{4+}$ ions was found for $LaNi_{0.5}Mn_{0.5}O_{3+\delta}$ ($x = 0.5$) samples, while for the rest of the samples Ni and Mn atoms are randomly distributed. Therefore, $LaNi_{0.5}Mn_{0.5}O_{3+\delta}$ samples can be considered as a double perovskite, i.e, $La_2NiMnO_6$ [99] [85] [127].

According to these previous results, we have observed in our RNMO films good ferromagnetic properties for non-stoichiometric samples. Particularly, $La_2Ni_{1-x}Mn_{1+x}O_6$ samples with a remarkable Ni deficiency show good magnetic properties, in contrast stoichiometric samples exhibit values of $T_C$ and Ms far from the optimum ones. The Ni/Mn ratio strongly depends on the oxygen content used in the growth process. A detailed description of the stoichiometry of our samples will be discussed in Chapters 3 and 4.

# 1.7 Magnetic Anisotropy

The physical origin of magnetic anisotropy can be attributed to dipole-dipole interaction and the spin-orbit coupling (SOC). Dipole-dipole interaction is responsible for shape anisotropy, and spin-orbit coupling is the origin of many other type of magnetic anisotropies such as magneto-crystalline anisotropy and magnetoelastic anisotropy [128]. One factor which may strongly affect the shape of the M, H (or B, H) curve, or the shape of the hysteresis loop, the coercivity and remanence is magnetic anisotropy. This term simply means that the magnetic properties depend on the direction in which they are measured. It is an experimental fact that ferromagnetic single crystals exhibit ‘easy’ and ‘hard’ directions of the magnetization; i.e. the energy required to magnetize a crystal depends on the direction of the applied field relative to the crystal axes. Thereby depending on the orientation of the field with respect to the crystal lattice one would need a lower or higher magnetic field to reach the saturation magnetization [129].

On an M(H) curve, easy axis is the direction inside a crystal, along which small applied magnetic field is sufficient to reach the saturation magnetization. A magnetic easy axis is characterized by a large remanence and a large coercive field. Hard axis is the direction inside a crystal; along which large applied magnetic field is needed to reach the saturation magnetization. Both magnetic remanence and coercive field are smaller than in magnetic easy direction. On the other hand, from the technological viewpoint this magnetic anisotropy is one of the most important properties of magnetic materials. Depending on the type of application, material with high, medium or low magnetic anisotropy will be required, for respective application as, for example, permanent magnets, information storage media or magnetic cores in transformers and magnetic recording heads [129]. There are many types of magnetic anisotropy as magnetocrystalline anisotropy, shape anisotropy and magnetoelastic anisotropy. Magnetic anisotropy constant $K$ is a measure of the strength of the anisotropy and can be expressed as [130]:

$$E_a = K_1 V sin^2\theta \tag{1.2}$$

$K_1$ the first-order uniaxial anisotropy constant, $V$ is the volume of the magnet and θ is the angle between the magnetization and the film normal. This expression only is useful for uniaxial magnetic anisotropy, because it is very limited and excludes any higher order term, However, for low-dimensional systems like thin films, this expression enables to interpret anisotropy direction [131]. There can also be a contribution to the interface anisotropy that is magnetoelastic in origin. This is related to stress relief by defect formation at interfaces. It is inversely related to the layer thickness and may therefore be significant at small thicknesses [132]. Surface magnetic anisotropy, with also of technological use, arises when $K_s$ favors the alignement of magnetization along the normal to a thin film:

$$E_s = K_s cos^2(\theta) \tag{1.3}$$

Where $K_s$ ($K_s$<0) is the surface anisotropy constant, θ the angle between magnetization and the normal to the film [132].

## 1.7.1 Magnetocrystalline anisotropy

Magnetocrystalline anisotropy is a phenomenon in which the internal energy (magnetic anisotropy energy) varies by the direction of magnetization in the material. The magnetic anisotropy energy which is affected by the symmetry of the crystal structure of the material is called magnetocrystalline anisotropy energy, $K_1$, which is an intrinsic value for each material [133]. The microscopic origin of the magnetocrystalline anisotropy is the spin-orbit coupling (SOC) interaction. In principle, also the exchange interaction and the dipolar interaction could contribute to the magnetocrystalline anisotropy. The exchange interaction, however, cannot give rise to anisotropy since it is proportional to the scalar product of the spin vectors and is

therefore independent of the angle between the spins and the crystal axes. The dipolar interaction energy, on the other hand, does depend on the orientation of the magnetization relative to the crystal axes. In principle it results, apart from the shape contribution in a magnetocrystalline contribution [129]. Intrinsically, the existence of magnetocrystalline anisotropy implies a corresponding anisotropy in the magnetization [134]. It occurs in all crystalline ferro- and ferrimagnetic materials. Consequently, the spin–orbit interaction will be primarily responsible for the magnetocrystalline anisotropy in Fe, Ni (both cubic) and Co [135] [129].

# 1.8 Thin film growth

## 1.8.1 Strained or relaxed epitaxial thin films

Thin films with lattice parameters showing a fixed relation to those of the substrate are called epitaxial. They form an extended single crystalline film which grows in a pseudomorphic way on top of the respective substrate. In contrast, textured thin films are polycrystalline but with a certain lattice plane oriented preferentially parallel to the respective substrate plane. Whether or not a film grows epitaxially over some range of thickness sensitively depends on the lattice mismatch f between the two materials [13]. It is defined as:

$$f = \frac{a_f - a_s}{a_s} \tag{1.4}$$

where $a_f, a_s$ denote the in-plane lattice constants $a$ of the film and the substrate [13].

As illustrated in Figure 1.12 (a), $f < 0$ results in a tensile (compressive) strain of the film in the in-plane (out-of plane) direction, whereas $f > 0$ results in a compressive (tensile) strain of the film in the in-plane (out-of plane) direction (Figure 1.12(b)). In both the cases, the total volume of the unit-cell almost and always remains constant. When the film grows on matched or nearly lattice matched substrates, the film grows defect free. Note that $f$ usually is a function of temperature as the thermal expansion coefficients of the film and the substrate may be different. On the other hand, if the thickness of the film exceeds a critical value $d_c$ the lattice of the thin film will relax to its bulk lattice parameters, accompanied with the formation of defects at the interface between film and substrate in form of dislocations, oxygen vacancies and intermixing of cations etc. (Figure 1.12(c)) [13]. Moreover, substrate-induced lattice strain has been reported to change a wide variety of properties, such as including the crystal symmetry, transport and magnetic anisotropies, the magnitude of ferromagnetic ($T_C$) and charge ordering melting field and the tendency towards phase

separation, etc. In most cases, these changes are interpreted in terms of substrate-induced strain, which relaxes with increase in thickness [10].

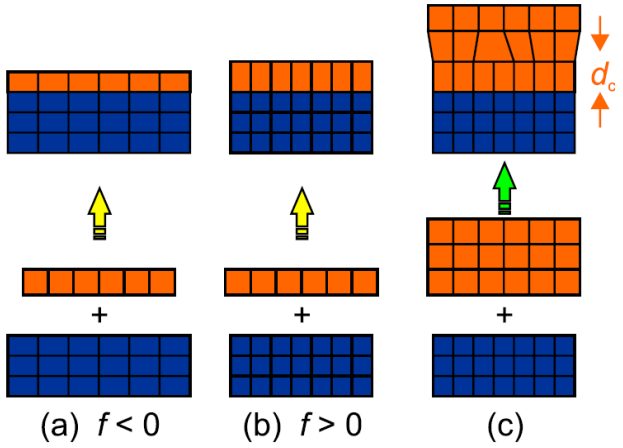


Figure 1.12. Heteroepitaxial thin film growth can result in strain as a result of the lattice mismatch *f*. (*a*) In-plane (ip) tensile and out-of-plane (op) compressive strain, (*b*) ip compressive and op tensile strain, (*c*) relaxed thin film growth for a thickness > $d_c$ [13].

## 1.8.2 Growth modes

The growth modes that occur in thin layer growth processes may be summarized as consisting of a statistical process of nucleation, surface-diffusion controlled growth of the three-dimensional nuclei, and formation of a network structure and its subsequent filling to give a continuous film [136]. Depending on the thermodynamic parameters of the deposit and the substrate surface, the initial nucleation and growth stages the thin films grow in one of three major thermodynamic growth modes and may be described as the Frank–van der Merwe (FM) growth mode, the Volmer–Weber (VW) growth mode and The Stranski–Krastanov (SK) growth mode [136] [137]. Each of the three scenarios is observed, thus the three schools complement each other. Unification of the three historical approaches to epitaxy and prediction of the growth mode were achieved by Bauer [138] in considering the thermodynamic quantities involved in epitaxy, namely, the three macroscopic surface tensions: $\gamma_o$, $\gamma_i$, and $\gamma_s$ – the free energy per unit area at the overlayer/vacuum interface, the overlayer/substrate interface, and the substrate/vacuum interface, respectively [136].

On the other hand, if $\gamma_o$ and $\gamma_i$ are small compared to $\gamma_s$, the system gains energy when being totally covered by the overlayer (the FM growth mode), whereas, if not, it will only partly be covered (the VW growth mode). For a film composed of *n* layers, the criterion of the FM growth mode is:

$$\gamma_{o(n)} + \gamma_{i(n)} \leq \gamma_s \tag{1.5}$$

The *n* dependence of $\gamma_o$ reflects surface free energy changes caused by possible changes in lattice constant and/or structure at the overlayer surface. The thickness dependence of $\gamma_i$ has its origins in (i) the true interface energy caused by the generally different crystallographic structure and/or lattice constant of overlayer and substrate and by the electronic hybridization at the interface and (ii) the volume strain accumulated in a pseudomorphic overlayer that is conveniently incorporated into $\gamma_{i(n)}$ [136]. A description overview of the three growth modes will take place next.

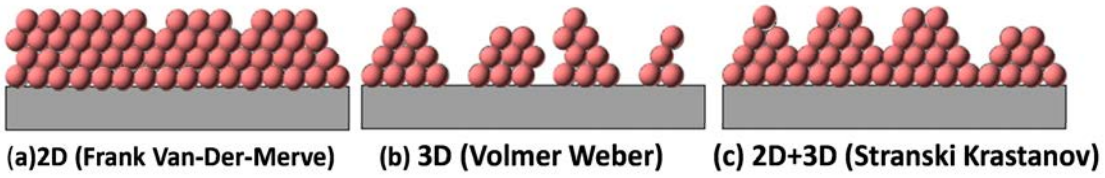


Figure 1.13 Schematic representations of different growth modes in thin films.

(a) **'Frank-van der Merwe (FM)' (2D morphology, layer-by-layer or step-flow growth)**

Frank and van der Merwe used elasticity theory to derive the concept of a critical misfit below which monolayer-by- monolayer growth appears [139]. In general, layer growth, considered as 2D growth (Fig 1.13(a)), occurs if the depositing atoms or molecules are more strongly bonded to the substrate than to each other, and each layer is progressively less strongly bonded than the previous one. Until the bulk bond strength is reached, the thin film forms planar, two-dimensional sheets and grows in a layer-by-layer fashion. The entire field of oxide thin films deposition has developed based on the ability to control materials through this growth mode and similar growth modes. The equality in equation (1.5) holds for the trivial case of homoepitaxy that thus displays the FM growth mode, if grown under conditions close to thermodynamic equilibrium. In the heteroepitaxial case, the obvious condition for the FM mode is that $\gamma_{o(n)} \ll \gamma_s$ [136] [13].

(b) **'Volmer–Weber' (3D morphology, island growth)**

Volmer and Weber, applying nucleation theory, assumed that crystalline films grew from 3D nuclei on the substrate and that their relative number and growth rate were determined by interfacial and surface free energies [140]. Island growth, considered as 3D growth (Fig 1.13(b)), occurs when the deposited atoms or molecules are bonded more strongly to each other than to the substrate. Then, the smallest stable clusters nucleate on the substrate and grow in the vertical direction forming three-dimensional islands. This is often the case when film and substrate are dissimilar materials such as metals or semiconductors on oxide substrates. The VW mode results if $\gamma_{o(n)} > \gamma_s$ [136] [13].

(c) **'Stranski–Krastanov' (initially 2D, after critical thickness, 3D morphology, layer + island growth)**

Stranski and Krastanov was based on atomistic calculations and assumed that initially a few pseudomorphic 2D layers are formed, on top of which 3D crystals with their natural lattice constant will grow [141]. Therefore, this growth mode combines the features of layer-by-layer growth and discrete three-dimensional nucleation, i.e., 2D growth and then converts to 3D growth (Fig 1.13(c)). If, for a given misfit, the influence of the substrate is increased, one passes from the VW to the SK mode, where a few 2D layers become thermodynamically stable. Lattice mismatch of over layer and substrate leads to a monotonic increase in volume strain energy in a 2D pseudomorphic film with increasing thickness $n$. Equation (1.5) implies an instability at a critical thickness $n$c, where $\gamma_{o(n)} + \gamma_{i(n)} > \gamma_s$, and the system switches from 2D to 3D growth morphology [136].

There are two possible reasons for the transition from 2D to 3D morphology in the SK growth mode. First, the film material can grow in the first few monolayers in a crystallographic structure that differs appreciably from its own bulk. In this case, the SK mode will be accompanied by the crystallographic change to the film's bulk lattice structure taking place at $n$c. This induces an abrupt increase in free energy at the interface between the two crystal structures and shifts the energy balance in favor of 3D growth. The second possible reason is strain relief by the formation of ''mounds.'' mounds can adopt very efficiently to their bulk lattice constant in case of compressive strain. When the strain energy is high, the increase in surface area is more than counterbalanced. The S-K nucleation is common with metal-on-metal deposition and at low temperatures where the surface mobility is low [136].

# Chapter 2

# Thin film growth process

This chapter is focused on the processes that were carried out during the preparation of $R_2NiMnO_6$ (RNMO) thin films, where R= La, Pr. It is organized into two main blocks. The first block details the synthesis of the target material used for the RNMO film deposition, the requirements and surface optimization of the substrates. Then, the second block focusses on the optimization of growth conditions of films deposited by RF magnetron sputtering technique.

Perovskite thin films have been frequently grown by magnetron sputtering technique [142], but few work has been reported on growth of thin films with double perovskite structure. Double perovskite systems have been more often grown by pulsed laser deposition (PLD) as it is usually adopted for precise thin film growth of various transition metal oxides [143] [144] [29]. Nevertheless, synthetic conditions of double perovskite lead to a wide range of reported properties but there is usually a small growth window for epitaxial thin films [145] [143]. Molecular beam epitaxy (MBE) has also been used for the growth of high-quality epitaxial double perovskite thin films. However, this technique is constrained by a rather low oxygen pressure during growth and few publications have been reported [146]. Moreover, chemical methods such as sol-gel synthesis [147], solid-state reaction method [28], metalorganic aerosol deposition [148] and polymer-assisted deposition [149], have some advantages as, for instance, a precise control of the film stoichiometry over a large substrate area. On the other hand, magnetron sputtering technique allows the preparation of excellent thin films under high oxygen pressure, but has few limitations regarding to the material [150] [151] [152].The principal advantages of R.F magnetron sputtering are the production of homogeneous, uniform and high quality thin films with good adhesion and stability, allowing large-area samples, multilayer structures [153], simple processing at low cost, etc. For this reason, magnetron sputtering deposit on has become the most widely used technique in the industry, such as [154] metallization in integrated circuits [155], large area coatings of architectural glass [156], protective optical system [157], photovoltaic solar cells [158], etc. In the field of thin film research, this technique has been oriented toward understanding the main

physical mechanisms, such as the influence of the deposition parameters (see section 2.4 in this chapter), adherence between substrate and deposited material, and chemical reactions near the substrate [154]. Nevertheless, the physical and chemical properties of the resulting thin films are strongly dependent upon the deposition parameters.

Therefore, in this thesis work thin films with double perovskite structure were grown by R.F magnetron sputtering. It is worth noticing that at the beginning of this thesis work, no previous study on RNMO thin films grown by this technique had been reported. Thereby, all $La_2NiMnO_6$ (LNMO) and $Pr_2NiMnO_6$ (PNMO) thin films used in this thesis have been grown at the ICMAB laboratory using homemade sputtering system (see details of the technique in appendix A.1).

# 2.1 Targets and substrates

Before the deposition of thin films by magnetron sputtering, there are two essential aspects that we must take into account. On the one side, the preparation of a stable and stoichiometric target that allows adequate and continuous growth of the films. On the other side, the surface quality of the substrates is required to grow homogeneous and reproducible thin films. These aspects will be described below.

## 2.1.1 Target preparation

The target is a pressed and sintered polycrystalline pellet having the desired stoichiometry composition. Stoichiometric targets of RNMO (R= La, Pr) of diameter d=1.3" (3.3cm), prepared by solid state reaction were used for the growth of LNMO and PNMO thin films, respectively. At the same time, a stoichiometric ceramic LNMO target was also prepared by sol-gel method. Target synthesis was carried out in the Instituto de Ciència de Materials de Barcelona (ICMAB, CSIC).

## 2.1.1.1 Target preparation by solid state reaction method

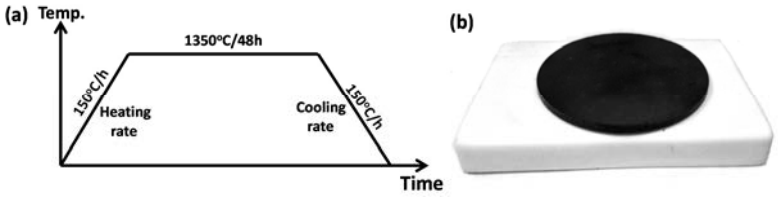


Figure 2.1. (a) Typical heating ramp for the powder sintering and (b) finished target of $Pr_2NiMnO_6$ (d=1.3") prepared by solid state-reaction.

Prior to RNMO thin film deposition, stoichiometric targets prepared by solid-state reaction of $La_2NiMnO_6$ and $Pr_2NiMnO_6$ were synthesized by mixing stoichiometric powders of commercially available oxides, as summarized in table 2.1.

Table 2.1 Stoichiometric reactions by solid state reaction.

| |
|---|
| $La_2O_3 + NiO + MnO_2 \rightarrow La_2NiMnO_6$ |
| $Pr_2O_3 + NiO + MnO_2 \rightarrow Pr_2NiMnO_6$ |

The pellets were produced from mixing the primary oxide powders, i.e. $La_2O_3$ (99.99 % pure), $Pr_2O_3$ (99.99 % pure), $MnO_2$ (99.99 % pure) and NiO (99.99 % pure). The process consists in several steps:

1) The powders are mixed and grinded manually, usually for one hour in an agate mortar, in order to increase homogenization of the different oxides in the posterior thermal treatment.

2) The mixture is hydraulically pressed in a slow continuous process, in order to compress the pellet (at a maximum pressure of twenty tons) and thus increase its density.

3) The pressed pellet is thermally treated, i.e. it is heated inside an alumina crucible up to 1100ºC-1200ºC for 24 hours in air (with increasing and decreasing ramps of about 150ºC/h).

4) The target composition (phase identification) is controlled by powder XRD analysis (see details of this technique in appendix A.4).After this step, the pellet is again homogenized in the mortar and steps 1-3 are repeated until one can discard the presence of other spurious phases.

5) At the end, the thermal treatment is applied up to 1400ºC for 48 hours in air. This process ensures to achieve a homogeneous and dense target (an example of target is shown in Fig 2.1(b)).

X-ray powder diffraction pattern analysis of the final target of $Pr_2NiMnO_6$ with no additional spurious phase present is shown in Fig.2.2. The XRD peaks are indexed on the basis of monoclinic $P2_1/n$ (single cell) according to the Rietveld refinement. A similar procedure was carried out for $La_2NiMnO_6$ target.

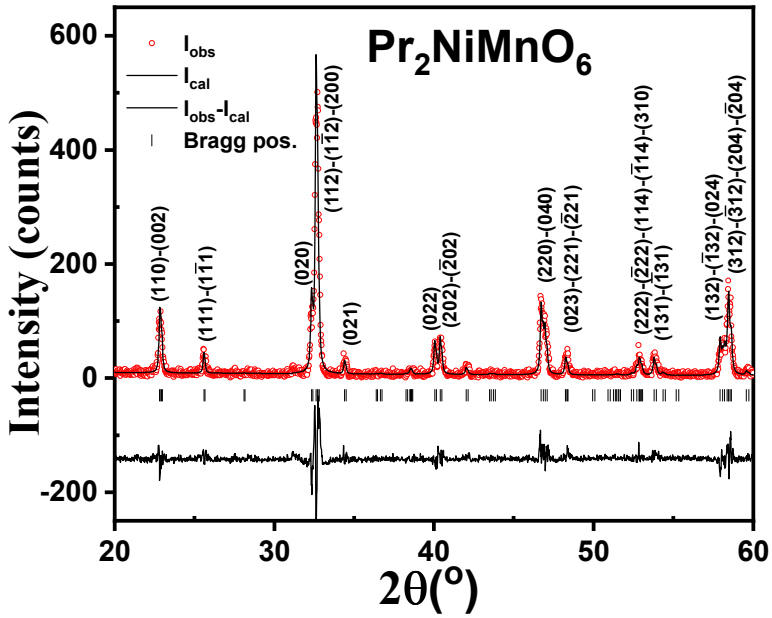


Figure. 2.2 XRD pattern of the final target of $Pr_2NiMnO_6$ prepared by solid state reaction method. The peaks clearly show the primary contribution of the PNMO phase. $I_{obs}$, $I_{cal}$ represent XRD of the observed and calculated intensities, respectively, and (|) the Bragg position.

### 2.1.1.2 Target preparation of $La_2NiMnO_6$ by sol-gel method

Stoichiometric target of $La_2NiMnO_6$ prepared by sol-gel method consisted of several steps: Metal nitrides were dissolved in a 1M solution of citric acid, in a 6:1 citrate-metal ratio (twice the necessary amount to completely complex the cations). Solutions were heated and stirred until gel formation. Heating proceeded until combustion and dehydration was complete. The resulting brownish ashes were calcined in two stages of 6 hours each, first at 300ºC, followed by another cycle at 600ºC. The heating rate was 5°C/min. The powder was then ground with a few drops of of 4% polyvinyl alcohol (PVA) solution as binder, and pressed into circular pellets of 1.3" of diameter. The pellets were sintered twice (two cycles of 6 hours at 1350ºC) in order to improve the homogeneity and density of the target. The resulting materials were examined using X-ray diffraction (see Fig. 2.3). The XRD peaks are indexed on the basis of monoclinic $P2_1/n$ (majority cell) according to the Rietveld refinement, which confirms that they have a perovskite structure with no additional phase present.

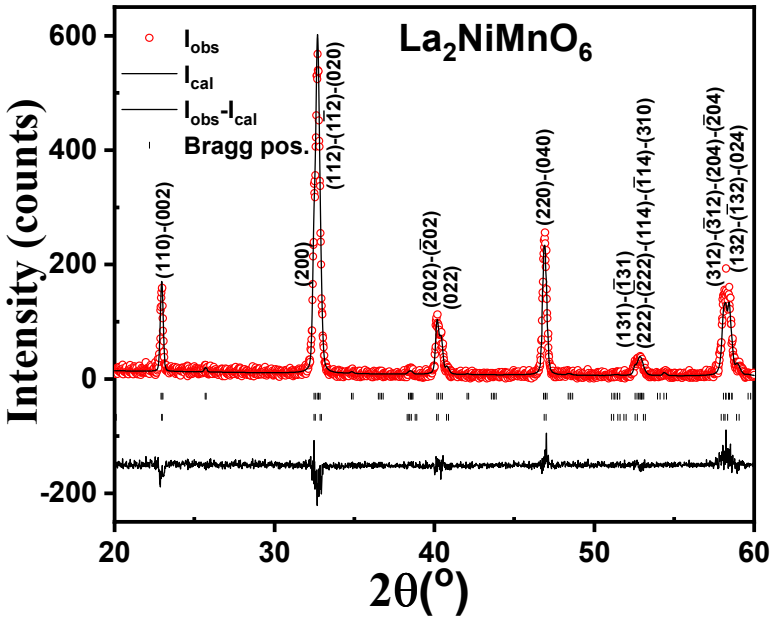


Figure. 2.3 XRD pattern of the final target of $La_2NiMnO_6$ prepared by sol-gel method, the peaks clearly show the primary contribution of LNMO. $I_{obs}$ and $I_{cal}$ represent the observed intensity and calculated intensity respectively, and (ı) the Bragg position.

In summary, during this thesis work we have prepared different stoichiometric targets of LNMO and PNMO. The targets are 1.3" in diameter, 0.5 cm-thick, and have a density of approximately 4.2 g/cm$^3$.

## 2.1.2 Substrate requirements

The structure and the surface quality of the substrates on which the thin films are grown represent a fundamental parameter that has a strong influence on the growth process and the subsequent thin film quality (crystallographic structure, surface roughness, etc.). An inhomogeneous substrate can induce heterogeneous nucleation centers during thin film formation, preventing layer-by-layer growth [139], thus favoring the Volmer-Weber growth type [140] (see chapter 1, section 1.8.2). Substrates are much more than just a chemically inert mechanical support for thin films; they are functional elements in thin film technology**.**

For the development of a reliable deposition technology for high-quality films, the optimal substrate has to meet the following conditions:

(a) High crystallographic lattice match between the film and the substrate to avoid strain-induced defect generation;

(b) Similar thermal expansion coefficients of the film and the substrate to avoid the appearance of cracks;

(c) No chemical interaction at the interface between the film and the substrate to avoid interdiffusion.

Generally, we can distinguish between two kinds of substrates:

(i) Those compatible with the oxide thin film deposition technique without additional buffer layer(s), and

(ii) Those where a buffer layer is required to accommodate a large lattice mismatch or prevent chemical interaction between the substrate and the oxide thin film.

Typical candidates of the first category are $SrTiO_3$ and $LaAlO_3$ for manganite thin film deposition [159]. For the growth of high quality epitaxial thin films with atomically controlled interface, substrates with an atomically flat and chemically homogeneous surface, i.e. a surface with the step-terrace structure of one-unit cell step height and also of single chemical termination, are fundamental. The interface interaction between an overlying thin film and the underlying substrate surface critically controls the growth and subsequent properties of transition metal oxides (TMOs) thin films [160] [161] [162]. As purchased, $SrTiO_3$ (STO) and $LaAlO_3$ (LAO) substrates have a high structural quality and low surface roughness, but they do not guarantee the existence of a single atomic termination. The surface of these commercially available oxide substrates in as-received state (i.e., without thermal treatment) is usually composed of a mixture of AO and $BO_2$ layers of the perovskite structure $ABO_3$.

Moreover, they do not exhibit the step-terrace structure of one-unit cell step height that is expected for single-terminated atomically flat surfaces (see Fig. 2.6 (a)) [163].

In this thesis, the substrates used for the epitaxial growth of oxide perovskite systems were 5x5 $mm^2$ (001)-oriented single crystals of $SrTiO_3$ (STO) and (001)-oriented $LaAlO_3$ (LAO) (commercially purchased from CrysTec GmbH). These substrates are widely used for the deposition of diverse perovskite oxides because they present similar crystallographic characteristics as $R_2NiMn0_6$ (R = La, Pr) thin films, such as compatibility of lattice constants, chemical and composition stability; and they also permit depositions at high temperature [19]. They will be presented separately below.

### 2.1.2.1 $SrTiO_3$ (001) substrate

STO is an insulator with $ABO_3$ cubic perovskite structure (space group *Pm3m*) at room temperature (lattice parameter $a_{STO}$=3.905 Å). The crystal structure is sketched in Fig. 2.4 (a), where the $Ti^{4+}$ cations are six-fold coordinated by $O^{2-}$ anions, whereas each of the $Sr^{2+}$ cation is surrounded by eight $TiO_6$ octahedra (coordinated by 12 $O^{2-}$ anions). Within the $TiO_6$ octahedra, a hybridization of the O-*2p* states with the Ti-*3d* states leads to a pronounced covalent bonding, while $Sr^{2+}$ and $O^{2-}$ ions exhibit ionic bonding character [163]. For any given planar direction (h, k, l) of a perovskite structure, there are always two distinct types of alternating, equally spaced atomic planes, having different areal densities of the three constituent elements (Sr, Ti and O). For instance, the (100) $SrTiO_3$ surface can exhibit two different types of atomic termination, one is formed by a SrO (AO, A-site) plane and the other by a $TiO_2$ ($BO_2$, B-site) plane [164] separated by a half unit cell (see Fig. 2.4 (a) and (b)). Nevertheless, considering the nominal chemical valences, $SrTiO_3$ (001) consists of two nonpolar atomic layers of SrO and $TiO_2$ (see Fig. 2.4 (b)).

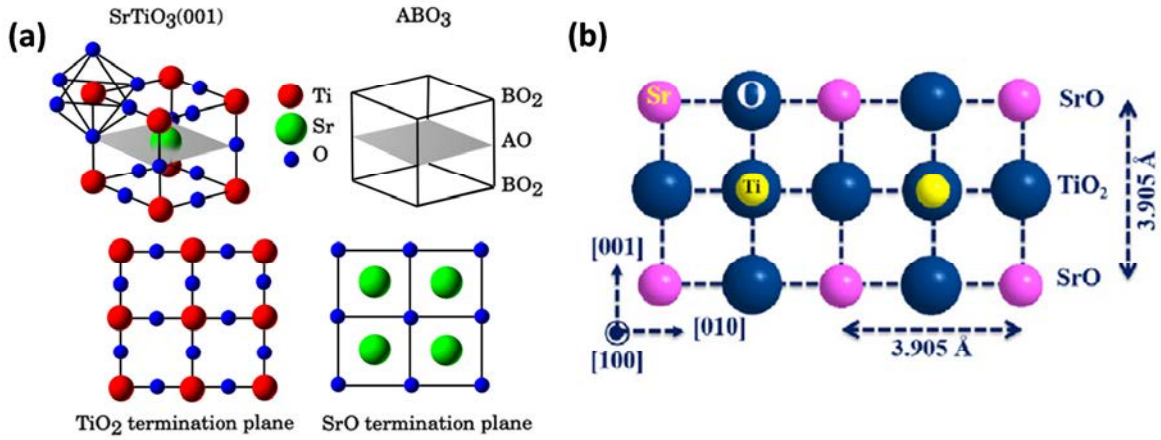


Figure. 2.4 (a) $ABO_3$ crystal structure and possible terminating planes of a (001) $SrTiO_3$ surface. (b) Schematic side view of $SrTiO_3$ (001) surface showing alternating neutral SrO and $TiO_2$ layers [162].

In the case of RNMO (R = La, Pr) thin films on STO substrates, two different adatom incorporations are possible: (R, Ni)O on $TiO_2$ or $MnO_2$ on SrO. In the growth of thin films with perovskite structure, the substrate surface has to be single terminated to impose one possible stacking sequence and a smooth morphology [164]. By a thermal treatment of the substrate, a single termination can be obtained.

### 2.1.2.2 $LaAlO_3$ (001) substrate

$LaAlO_3$ (LAO) is an insulator with rhombohedral perovskite structure (space group *R3mR*) at room temperature (pseudo-cubic lattice constant of $a_{LAO}$=3.789 Å). In the structure unit cell (see Fig 2.5 (a)), the $La^{3+}$ cation locates at (000), the $Al^{3+}$ cation at (1/2 1/2 1/2), and the $O^{2-}$ anions at the face-centers {1/2 1/2 0} [165]. Consequently, the formal charges of $La^{+3}$ , $Al^{3+}$ and $O^{2-}$ produce two terminations differing in nominal charges of $(La\text{-}O)^{+}$ and $(Al\text{-}O_2)^{-}$ (see Fig 2.5 (b)). It should be noted that the layers are not neutrally charged and an excess of charge of half of the electron (or hole) charge exists per unit interface cell. Thus, this perovskite structure consists of alternating polar planes of LaO and $AlO_2$ stacked in the <001> cubic direction which is equivalent to the $< 11\bar{1} >$ rhombohedral direction (see Fig 2.5 (a)). In this regard, the LAO (001) surface would consist purely of either $LaO^+$ or $AlO_2^-$ termination. The distance between the adjacent $LaO^+$ and $AlO_2^-$ layers is the half of a unit cell [162], as shown in Fig. 2.5(b). Therefore, a thermal annealing treatment is necessary to control the substrates surface morphology and achieve a smooth, single terminated surface [162].

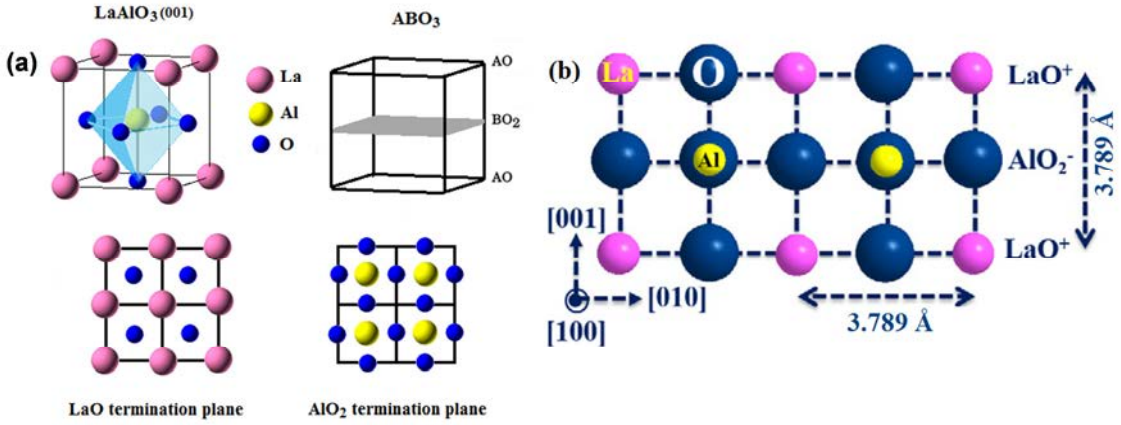


Figure 2.5. (a) $ABO_3$ crystal structure and possible terminating planes of a (001) $LaAlO_3$ surface. (b) Schematic side view of $LaAlO_3$ (001) unit cell showing the alternating stacking of $LaO^+$and $AlO_2^-$ layers [166]

## 2.1.2.3 Selective thermal treatment of the substrate

As mentioned above, the (pseudo) cubic cell, oriented in the (001) direction, is represented by a simplified stack of alternating AO and $BO_2$ layers of the perovskite structure ($ABO_3$). As received substrates have polished mixed-terminated surfaces, with nearly equal proportion of AO and $BO_2$ terminations. The pristine substrate surface is very flat with low roughness, rms ≈ 0.2 nm (see profile lines in Fig. 2.6 (a) and Fig 2.7(a)). Nonetheless, single termination, with only 0.4 nm high steps (Fig. 2.6 (b) ans Fig.2.7 (b)), is desirable for controlled growth at an atomic level. Therefore, it is crucial to thermally treat the surface before depositing complex oxide heterostructures [167].

The first method for the surface treatment of $SrTiO_3$ (001) substrates was developed by Kawasaki et al. [168] [169]. The method is based on chemical treatments to distinguish SrO and $TiO_2$ chemically and make the surface chemically homogeneous. After etching in hydrofluoric acid solution with pH = 4.5 for 30 s, the substrates are thermally treated at 1000$^{o}$C in $O_2$ gas flow for 2–3 h. The annealing temperature is kept below 1000$^{o}$C to avoid Sr diffusion from the bulk to surface. Step-terrace structure of STO (001) surface after the treatments was predominantly composed of $TiO_2$, as confirmed by low energy ion scattering spectroscopy (ISS) measurements [168]. Raisch et al., [170] using the same method proposed by Kawasaki et al. [168] [169], confirmed by means of x-ray photoelectron spectroscopy (XPS) the $TiO_2$ surface termination (with negligible amount of SrO termination). A simpler method to produce an atomically flat surface was developed by Connell et al. [171]. The treatment procedure includes first thermal annealing (at 1000°C for 1 h) of a substrate to induce SrO segregation at the surface and then dissolving Sr oxides into de-ionized water (DI-water leaching) [171]. A further annealing of the substrate at 1000$^{o}$C for 1 h in air produces an atomically flat surface with $TiO_2$-rich termination, as revealed by XPS measurements [172] [173] [162].

Finally, K. Iwahori et al., [174] reported the simplest but effective method to obtain a single-terminated $SrTiO_3$ (001) surface. The method consists in cleaning and rinsing with organic solvents and distilled water the STO (001) surface. Then, in order to remove the distorted and stressed layers on the surface, the samples are subjected to ultrasonic agitation in distilled water for 1 min. After the ultrasonic agitation, samples are annealed in air at 1000°C for 2 h. As a result, the $SrTiO_3$ (001) surface becomes extremely flat, composed of atomically flat terraces with single atomic-layer sharp steps. Surface analysis by atomic force microscopy (AFM), friction force microscopy (FFM), and collision ion-scattering spectroscopy (CAICISS) revealed that the atomically flat $SrTiO_3$ (001) surface was predominantly terminated with $TiO_2$ atomic planes. According to these previous reports, the $TiO_2$ surface is more dominant after thermal treatment. Therefore, a $TiO_2$-terminated surface is expected in our thermally-treated $SrTiO_3$ (001) substrates.

On the other hand, some experiments on bulk crystals have indicated that the $LaAlO_3$ surface is terminated on either LaO or $AlO_2$ planes, depending on the annealing temperature [175] [176] while others have suggested that both terminations are present simultaneously [177] [178]. Kim et al., [176] reported a method to prepare single-terminated $LaAlO_3$ (001) substrates. The method consisted of annealing LAO (001) single-crystal substrates at high temperatures (1000–1100$^{o}$C) for 10 h in oxygen flow. After this process, LAO substrates are transferred to a growth chamber and heated at 750°C under $10^{-6}$ Torr of $O_2$ for 1 h, in order to remove surface contaminants such as carbonates. In situ reflection high-energy electron diffraction (RHEED) and ex-situ atomic force microscope (AFM) measurements show that the substrates have very clean and atomically flat surfaces with dominantly $AlO_2$ terminated surfaces. Gunnarsson et al., [179] reported another method to obtain single-terminated $LaAlO_3$ (001) substrates. They reported that a chemical etching of the surface with HCl, followed by an annealing in oxygen at the relatively low-temperature of 800◦C, lead to a single termination. Atomic force microscope (AFM) and lateral friction force microscopy (LFM) measurements confirm the predominant $AlO_2$ termination. On the other hand, by annealing $LaAlO_3$ (001) substrates between 1100◦C and 1500◦C in air (3 h) and using a combination of transmission electron diffraction measurements and density functional calculations, Lanier et al., [180] observed that LAO single crystals terminate in the LaO surface with one lanthanum vacancy per surface unit cell to compensate for the charged nature of the surface. Another study on $LaAlO_3$ (001) substrates annealed at 1150$^{o}$C either in UHV or in air, using low-energy electron diffraction (LEED), revealed a mixed termination layer on the surface, where LaO terminated regions are well reconstructed and $AlO_2$ terminated regions are unreconstructed, being LaO-plane termination most stable [181]. Taking into account these previous reports, by performing a thermal treatment in air at high temperature in our $LaAlO_3$ (001) substrates a predominant A-site (LaO) termination is expected in our $LaAlO_3$ (001) substrates.

In order to obtain atomically flat surfaces with single termination in our substrates, we have carried out the method proposed by K. Iwahori et al., [174] described above. Firstly, we have cleaned the substrates as detailed in the following steps:

- Cleaning with acetone with ultrasound (10 min)
- Cleaning with ethanol with ultrasound (10 min)
- Cleaning with pure milli-Q water with ultrasound (10 min)

The ultrasonic agitation process, as mentioned above, allows to remove the distorted and stressed layers on the surface. Secondly, these substrates were dried in argon gas and thermally treated at 1000$^{o}$C for 2h in air with heating/cooling rates of 300$^{o}$C/h. This process allows to obtain unique termination in both STO and LAO substrates (see below Figs 2.6 and 2.7). After the thermal treatment of substrates, the surface is usually characterized by atomic force microscopy (AFM). In Fig. 2.6 (a), the surface of an as-received (001)-STO substrate

although being flat, is lacking the step-terrace structure on the surface. After thermal treatment, the substrate surface turns into a step-terrace structure as clearly revealed by the AFM image (Fig. 2.6(b)). The majority height of the steps is 0.4 nm which corresponds approximately to one-unit cell of the STO (0.395 nm), (see profile line in Fig. 2.6(b)).

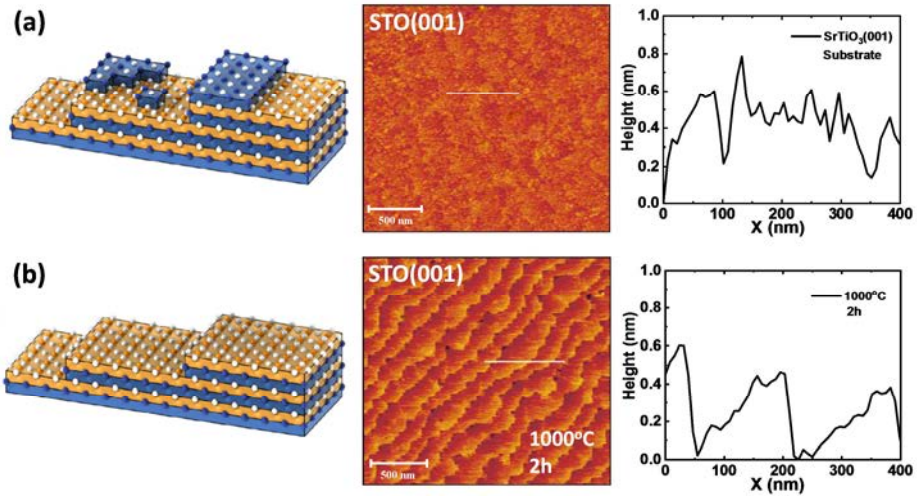


Figure 2.6. (a) Atomic structure, AFM topography ($2x2\mu m^2$) and line profile along the white line of an as-received STO(001) substrate and (b) Atomic structure, AFM topography of a STO (001) substrate after thermal treatment and thus with single-termination, line profile with typical one-unit cell step height of h~0.4nm. Schematic figures, representing AO and $BO_2$ layers were reproduced from ref [162].

The same procedure performed on STO substrates, has been carried out on LAO substrates. After thermal treatment, the LAO surface turns homogeneous into a step-terrace structure with step height around one unit cell (h~0.4 nm), as can be seen in corresponding AFM image (Fig. 2.7(b)).

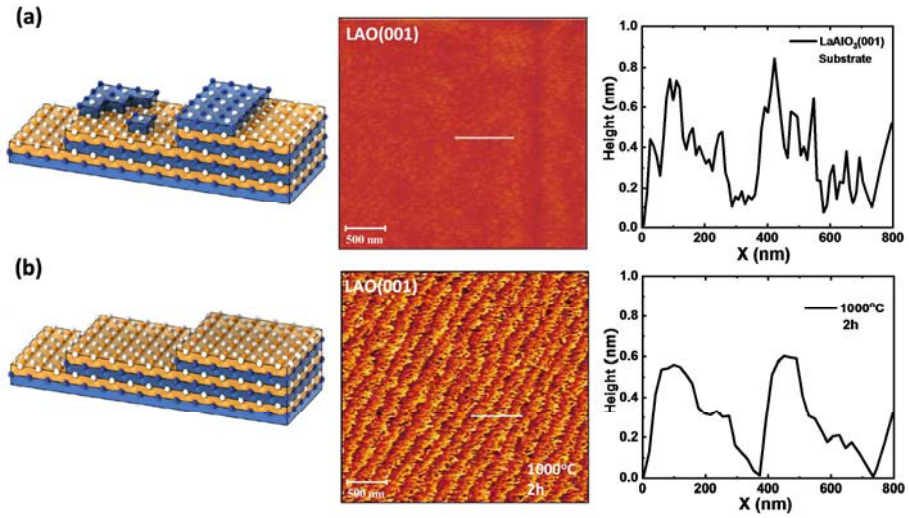


Figure 2.7. (a) Atomic structure, AFM topography ($2x2\mu m^2$) and line profile along the white line of an as-received LAO(001) substrate and (b) Atomic structure, AFM topography of a LAO(001) substrate after thermal treatment with single-termination, line profile with typical one-unit cell step height of h~0.4nm. Schematic figures, representing AO and $BO_2$ layers were reproduced from ref [162].

### 2.1.2.4 Miscut angle (θ) of the substrate

In addition to the thermal treatment conditions, the final step-terrace morphology of substrates depends on the mechanical polishing process. Actually, commercially available substrates come with mechanically polished surfaces and therefore with some miscut angle [162].

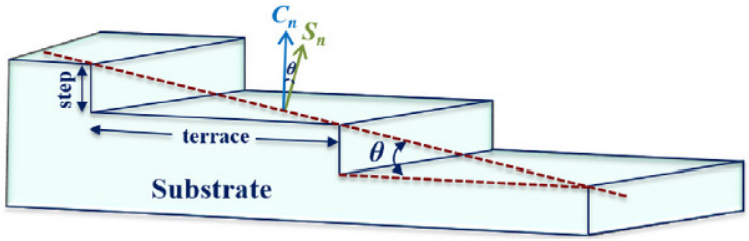


Figure. 2.8 Schematic representation of a substrate taken from ref [162]. Miscut angle (θ) of a substrate, defined as the angle between surface normal ($S_n$) and the crystal plane normal ($C_n$), determines terrace width.

The miscut angle (θ) of a substrate is defined as the angle between the polished surface (red dashed line) with surface normal ($S_n$) and the crystal plane (001) ($C_n$) [182], as drawn in Fig. 2.8. As-polished surfaces, characterized by a certain miscut angle, crucially determine the terrace width and finale step-terrace morphology after thermal treatment [164]. In particular, a low miscut angle (θ ~0.02°) leads to a wider terrace width d≈1250 nm (see Fig 2.9(b)).

AFM measurements (5x5μm$^2$ areas) of two (001)-oriented STO substrates after thermal treatment are shown in Fig.2.9 (a)-(b). AFM images reveal a morphology of terraces and steps with unit cell height ~0.4 nm and terrace widths of 110 nm and 1250 nm corresponding to approximatively to a miscut angle of 0.2$^o$ and 0.02$^o$ respectively (see Fig.2.9 (a)-(b)).

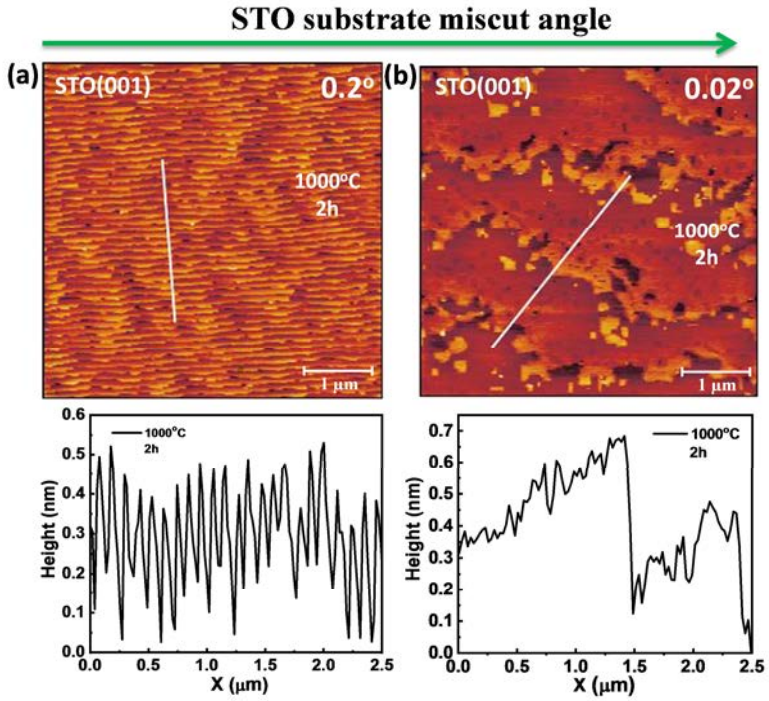


Figure. 2.9. AFM images (after thermal treatment) of the surfaces (5x5μm$^2$ areas) of: (a) 0.2° and (b) 0.02$^o$ miscut STO substrate. The different surface morphologies are clearly visible. Bottom panels show the line profile of its corresponding AFM image.

# 2.2 RNMO thin films by magnetron sputtering

Magnetron sputtering technique is based on bombardment and/or ejection of material from a source called target with ions from a plasma and depositing it on a substrate. Fig. 2.10 (a) shows the photograph of the sputtering equipment used in this thesis work. The film growth shown in inset of Fig. 2.10 (b) is on-axis (where the normal axis of the center of the target coincides with the normal axis of the substrate). Ionic bombardment of the target is obtained by a flux of gas (oxygen in our case), which is ionized due to the potential difference in the ion gun. Therefore, a highly ionized plasma is created in the region between the magnetron sputtering cathode target and the anode outer crown where the discharge process occurs [137].

On the other hand, a strong magnetic field near the target area forces electrons to travel in spiral trajectory along magnetic flux lines. This arrangement confines the plasma near the target area (see inset Fig. 2.10 (c)) thus preventing it to damage the thin film being formed on the substrate [156] [137].

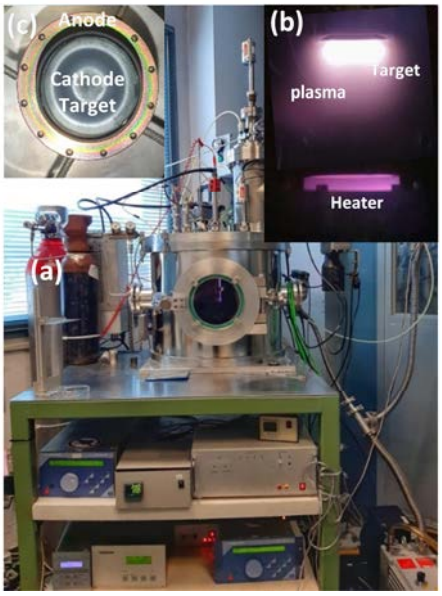


Figure 2.10. Magnetron Sputtering setup used for the growth of RNMO (R = La, Pr) thin films, located at the ICMAB.

The operating parameters of magnetron sputtering are the gas pressure, power, substrate temperature and target-to-substrate distance. On the other hand, we have to specify that the power supply for the magnetron is RF (radio frequency) type because the target is an insulator. In this regard, to avoid the accumulation of positive charge on its surface and the stop of the sputtering process, a radio frequency (RF) AC signal is added to the DC voltage; to compensate for the number of positive and negative ions that reach the surface of the target. Thereby, RF-sputtering enables the use of insulating targets [183]. (For more details of this technique see appendix A1). As mentioned before, in order to grow $R_2NiMnO_6$ (R = La, Pr) epitaxial thin films and with the least amount of structural defects, we have selected $SrTiO_3$ (STO) and $LaAlO_3$ (LAO) substrates, due their perovskite crystal structure as well as the low structural mismatch between RNMO and substrate, promoting the deposition of thin films of high structural quality. Structural mismatch $\delta$ is defined by $\delta = (a_{bulk} - a_{substrate})/ a_{substrate} * 100\%$, where $a_{bulk}$ and $a_{substrate}$ are lattice constants of RNMO and substrate, respectively. It should be noted that we will mostly refer to the value of cell parameters in pseudocubic notation ($a_{LNMO}$= 3.876 Å [41] and $a_{PNMO}$=3.848 Å [30]), although the cell parameters of RNMO are a= $\sqrt{2}a_p$, b= $\sqrt{2}a_p$ and c= $2a_p$, respectively.

Table 2.2 Lattice parameters in-plane and structural mismatch of bulk LNMO and PNMO and the different substrates.

| Material | Lattice constant (Å) | Structural mismatch δ (%) |
|---|---|---|
| **LNMO** | **3.876** | |
| STO | 3.905 | -0.74 |
| LAO | 3.789 | 2.29 |
| **PNMO** | **3.848** | |
| STO | 3.905 | -1.46 |
| LAO | 3.789 | 1.55 |

Therefore, in table 2.2, it can be observed that the lattice parameter of bulk LNMO and PNMO is smaller than the STO one (negative structural mismatch), leading to a tensile strain during thin film growth. On the other hand, the lattice parameters are larger than the LAO one (positive structural mismatch), leading to a compressive strain.

## 2.2.1 General effect of growth conditions

Optimization of thin films growth by magnetron sputtering is challenging, due to huge number of operating parameters leading to different growth modes, thus affecting the film quality and its physical properties. The main parameters to take into account in the RNMO (R = La, Pr) film growth are: RF power, target-to-substrate distance, substrate temperature, sputtering gas pressure and gas mixture that affect growth rate, the diffusion of the adatoms on the surface, re-sputtering process, and the thin film growth mode (which affects crystallinity, texture and roughness of the samples). In addition, annealing process after film growth and cooling rate could affect the oxygen stoichiometry, surface morphology, crystal structure, and thus modify the functional properties of the films. In our growth protocol, all films were deposited by keeping fixed RF power (40 W) and target-to-substrate distance (5 cm), while changing oxygen pressure, growth temperature and annealing conditions. In this section, we will give the protocol that has been followed in this thesis to optimize the film properties, mainly their magnetic properties. In this regard, we will focus in LNMO films grown on STO substrates. A detailed study on this topic will be carried out in Chapter 3.

### 2.2.1.1 Methodology used to optimize thin film growth

The crystal structure and B-site cation ordering [49] [92] [93] in double perovskites $A_2BB'O_6$ is strongly affected by the synthesis conditions, where the temperature plays an essential role. It has been found that the synthesis of the perovskite phase begins with relatively fast formation of a partially ordered phase, which then orders during annealing [101] [28]. Higher temperatures and longer annealing times tend to increase order, affecting the morphology, the structural and physical properties of the films. However, the optimal growth temperature and annealing thermal process depends on the desired composition. Besides temperature, the oxygen pressure during synthesis may also affect the degree of cationic ordering, and thus the thin film structure and magnetic properties. It has been shown that the pressure can induce a phase transition and changes in the octahedral tilting in the ordered double perovskites $A_2BB'O_6$ [86]. At low pressures, the dominant compression mechanism is often bond shortening, whereas at high pressures octahedral tilting becomes increasingly important [86] [184]. On the other hand, RNMO thin films grown by PLD have reported high degree of B-site cationic ordering using high growth temperatures (750-900$^{o}$C) and high oxygen pressures (100-1000 mTorr) [185] [144] [42]. Therefore, taking into account these previous reports, in order to optimize and evaluate the effect of oxygen pressure on the structural and magnetic properties of our LNMO films, we have started the optimization of the growth conditions by keeping a fixed growth temperature of 850$^{o}$C while the oxygen pressure was varied. On the other hand, a second optimization process has been carried out by keeping a constant oxygen pressure while the growth temperature was varied. In this section, the initial optimization process of LNMO films using a target prepared by sol-gel method is present. Additionally, a more detailed study of these films will be presented in depth in Chapter 3.

Therefore, Fig. 2.11 shows a series of LNMO thin films on (001)-oriented $SrTiO_3$ (STO) substrates grown by keeping a fixed growth temperature of 850$^{o}$C under different oxygen pressures (ranging from 120 to 350 mTorr) for 1h. After film deposition, all samples were annealed (in-situ) at the same growth temperature (1h under 420 Torr $O_2$) with a cooling rate of 10$^{o}$C/min.

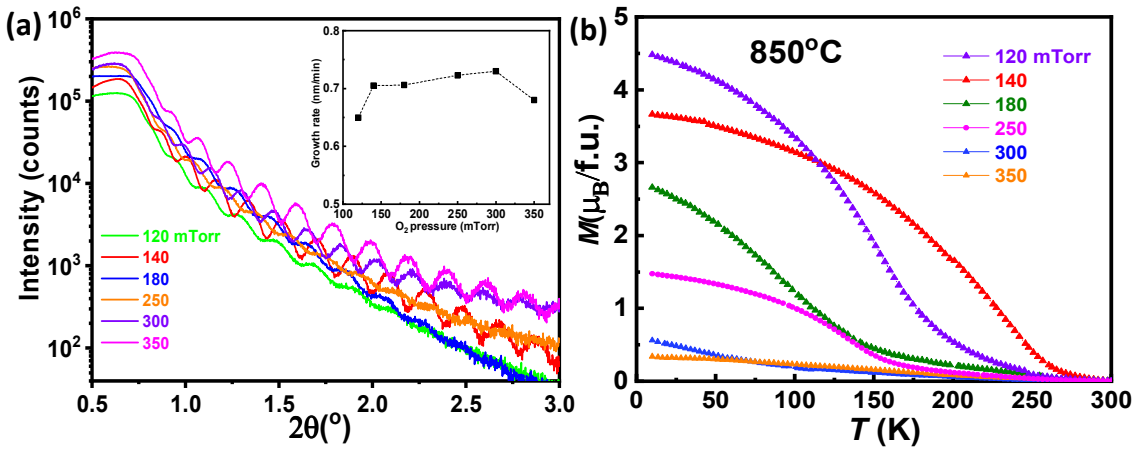


Figure. 2.11 (a) XRR data and (b) in-plane magnetization as a function of temperature under an applied field of 5 KOe ($\mu_0$H =0.5 T) of LNMO thin films grown under different oxygen pressures (ranging from 120 to 350 mTorr) at 850°C for 1h.

The X-ray diffraction technique extensively used for the work of this thesis was X-ray reflectivity (XRR). XRR measurements allow determining the thickness of the samples (see appendix A.4.5 for more details on this technique). Fig 2.11 (a) shows θ/2θ scan carried out at low angles (0.5 to 3°) of the samples under study. The thickness is obtained from position of minima in the XRR curve, allowing extracting the growth rate of the samples and control reproducibility (see inset Fig 2.11). In this regard, XRR analysis (Fig 2.11 (a)) indicated similar thickness values t~40±5 nm with a growth rate around v~0.7 nm/min (see inset Fig.2.11 (a)). It can be observed, that the growth rate does not show a strong dependence with the oxygen pressure, which is not an usual case. The opposite behavior, i.e. growth rate variations with oxygen pressure, was observed during PNMO films growth, which will be discussed later (see chapter 4). On the other hand, in-plane magnetization as a function of temperature under an applied field of 5 KOe of LNMO thin films grown at 850°C under different oxygen pressures are shown in Fig 2.11 (b). M(T) curves exhibit strong dependence on the oxygen pressure. Samples deposited at high oxygen pressure ($PO_2$ > 180 mTorr) show very deficient magnetic properties with a Curie temperature Tc below 120 K (estimated from inflection point). With decreasing oxygen pressure, $T_C$ rises up to ~ 240 K ($PO_2$=140 mTorr). Further decrease of pressure ($PO_2$ < 100 mTorr) leads again to degradation of the magnetic transition. Therefore, from this series of samples LNMO thin films grown/annealed at high growth temperatures (850°C) under low oxygen pressures ($PO_2$~140 mTorr) show optimal growth conditions and seem to favor B-site cationic ordering. However, these results are in contrast with previous results reported for LNMO samples prepared by PLD [185] [144] [42] which will be discussed later (see chapter 3, section 3.1.2). The analysis of this series of samples, including a deeper characterization of their morphology, structure, stoichiometry and physical properties, will be carried out later (see chapter 3)

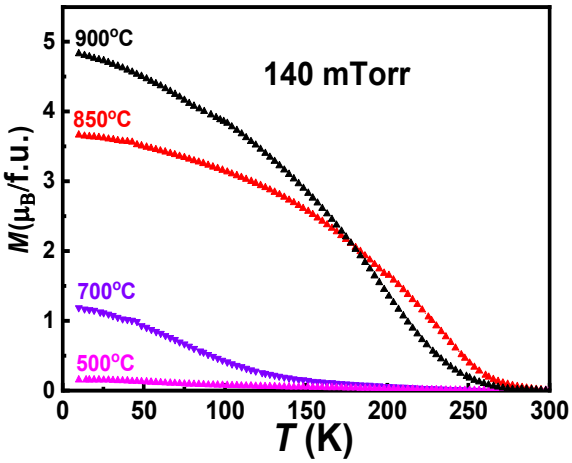


Figure. 2.12 In-plane magnetization as a function of temperature under an applied field of 5 KOe ($\mu_0$H =0.5 T) of LNMO thin films grown under 140 mTorr $O_2$ and deposited at different growth temperatures (ranging from 500°C to 900°C for 1h).

Once the oxygen pressure during LNMO growth was optimized, we have studied the influence of the substrate temperature. Fig 2.12 shows in-plane magnetization as a function of temperature under an applied field of 5 KOe of LNMO thin films grown by keeping a fixed oxygen pressure of 140 mTorr and deposited at different growth temperatures. After film deposition, as-grown samples were annealed (in-situ) at the same growth temperature (1h under 420 Torr $O_2$) with the cooling rate of 10°C/min. It can be appreciated that all films reveal a single ferromagnetic transition $T_C$. Nevertheless, ferromagnetic properties of LNMO films strongly depend on growth temperature. Samples deposited at lower temperatures ($T \leq 700$°C) show very deficient magnetic properties ($T_C < 100$ K) and low magnetization values. By increasing the growth temperature up 850°C, the ferromagnetic transition increases ($T_C \sim 240$ K) and then slightly decreases for 900°C. The improvement of $T_C$ in samples grown/annealed at higher growth temperatures (850°C) might be caused by the degree of $Ni^{2+}$ and $Mn^{4+}$ ions ordering in LNMO system [96], while the existence of $Ni^{3+}$ and $Mn^{3+}$ would promote the degradation of ferromagnetism (low-$T_C$) in our samples [96] (see chapter 3 for details).

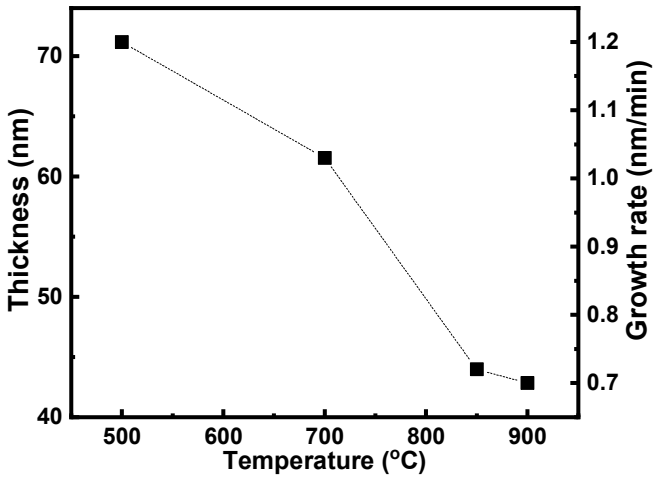


Figure 2.13 Thickness and growth rate as a function of temperature of LNMO thin films grown under 140 mTorr $O_2$ and deposited at different growth temperatures ranging from 500°C to 900°C for 1h.

In this set of samples, XRR analysis revealed that the sample thickness is highly dependent on growth temperature. In Fig 2.13, samples deposited below 700°C are much thicker (t > 60 nm) than samples deposited above 800°C (t <45 nm). Therefore, the deposition rate decreases by increasing the growth temperature (from 1.2 nm/min for 500 °C to 0.7 nm/min for 900 °C). This gradual change in film thickness with temperature can only be explained by the phenomenon of resputtering, where the deposited material is removed, due to a re-emission process during the deposition by ion or atom bombardment [186]. During film growth by magnetron sputtering, a target (or source) material is bombarded by energetic particles, generated by the plasma, to be deposited onto a substrate where the film is growing. In the resputtering processes, these energetic particles produce the reemission of the film ad-atoms, reducing this way their sticking. The resputtering effects can be enhanced by increasing the substrate temperature. In this case, the reevaporation and resputtering of atoms from the substrate surface occur more easily [187]. When the temperature is increased, the mobility of the ad-atoms also increases, which results in a decrease of the surface residence time, for the atoms arriving to the substrate surface. This increase in mobility decreases the binding energy of the ad-atoms, reducing the threshold of energy necessary for their reemission [187]. Consequently, resputtering can decrease the film growth rate and, in some cases, lead to a complete suppression of the film growth. On the other hand, this phenomenon of resputtering could also lead to a variation of the film stoichiometry. Studies by electron probe microanalysis (EPMA) revealed that films deposited at higher growth temperatures display Ni deficiency, while samples deposited at low temperatures have a Ni/Mn ratio close to 1 (see more details in chapter 3).

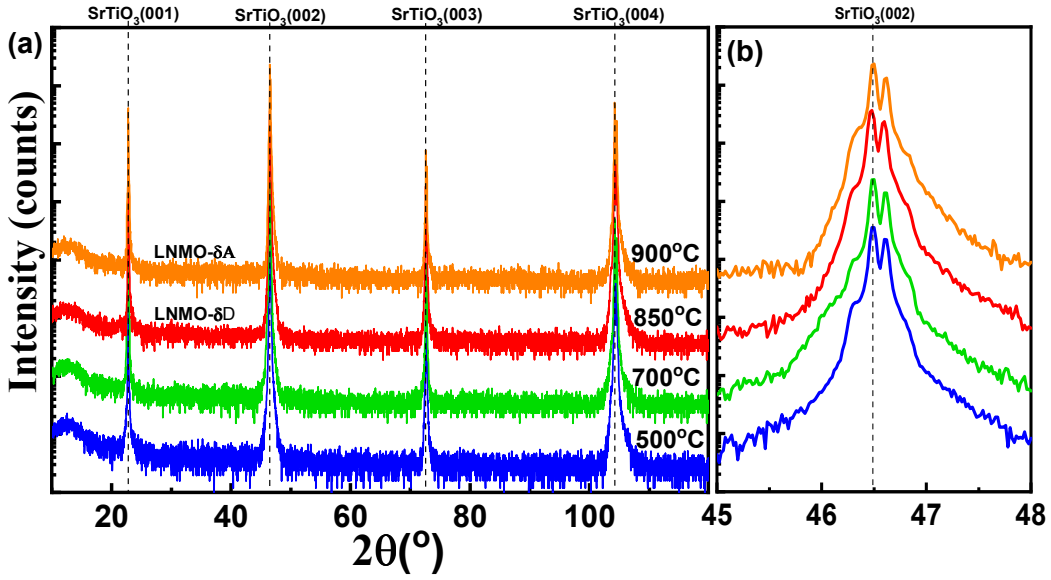


Figure 2.14 (a) θ/2θ XRD scans of LNMO thin films grown under 140 mTorr $O_2$ at different substrate temperatures (ranging from 500°C to 900°C). After film deposition, as-grown samples were annealing (in-situ) at the same growth temperature (1h under 420 Torr $O_2$). (b) Zoom of the $(002)_{STO}$ reflection.

In order to determine the structural properties of the films, X-ray diffraction (XRD) θ/2θ scans allow us to obtain information on the phase and crystalline quality of the material under study. Fig 2.14 shows the x-ray patterns to optimize the crystalline quality of the LNMO films as a function of the deposition temperature. All XRD patterns show only the peaks of the STO substrate (see dashed vertical line). The (00*l*) reflections of the LNMO phase were not appreciated, indicating that the layer peaks probably overlap with the substrate peaks (see also dashed black line (002) reflection of STO substrate in Fig. 2.14 (b)). Therefore, in order to determine the in-plane and out-of-plane lattice parameters high-resolution θ/2θ XRD scans of the (002) reflections and RMS around (103) reflections were carried out. Samples deposited at 850°C and 900°C (labeled as LNMO-δD and LNMO-δA respectively) were used for their corresponding study (see chapter 3, section 3.2.2).

## 2.2.1.2 Effects of annealing and cooling rate

The annealing treatments after film growth can lead to a modification of oxygen stoichiometry and increase the degree of long-range cationic order in perovskite oxides, and thus improve the magnetic and transport properties. For $R_2NiMnO_6$ (R= La, Pr) materials, chemical ordering of B-site cations (Ni/Mn) strongly affects the physical properties, particularly magnetic properties [188] [49] [59]. Therefore, the ordering of B-site in bulk RNMO (R= La, Pr) or thin films could be improved by changing the thermal annealing

parameters [146]. In our thin film growth protocol, in addition to oxygen pressure during growth, another way to introduce oxygen into the $R_2NiMnO_6$ (R= La, Pr) structure is through annealing processes. Standard growth conditions in our films include high (in-situ) annealing temperatures (800°C-900°C) under high oxygen pressure (420 Torr $O_2$) after film growth, with an annealing time of around 1h. A high oxygen pressure during annealing is required, as it contributes to improving the physical properties of the films, while longer annealing times have no significant effect. For the annealing, the oxygen pressure was adjusted (below atmospheric pressure) right after deposition, by keeping the chamber closed to prevent contamination of the film.

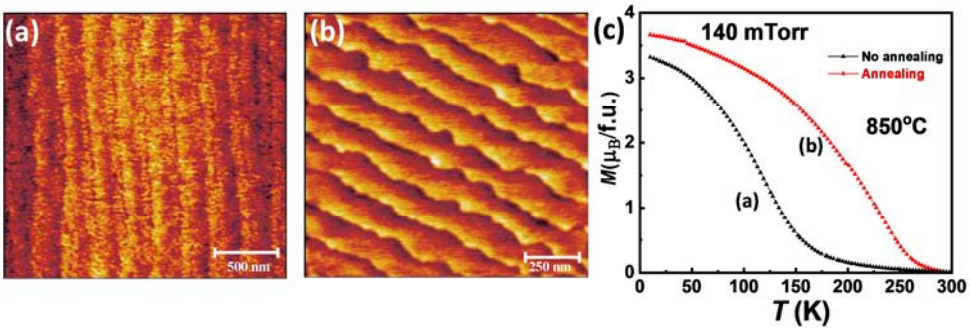


Figure 2.15. AFM topography images of LNMO thin films deposited at 850°C under $PO_2$=140 mTorr (a) without annealing and (b) in-situ annealed at the same temperature (850°C) under $PO_2$=420 Torr (for 1h). (c) Corresponding in-plane magnetization as a function of temperature under $\mu_0H$ =0.5 T.

AFM images and magnetization of two samples grown at the same growth conditions (850°C under 140 mTorr for 1h) without and with annealing process are shown in Fig.2.15. After annealing treatment, films were cooled down to room temperature with a rate of 10°C/min. Both samples, as-grown sample (no annealing) in Fig 2.15 (a) and in-situ annealed sample in Fig 2.15(b), have very flat surface with step-terrace morphology. However, it can be appreciated that the morphology of the as-grown film has clearly less defined contours than annealed film. Hence, the surface morphology clearly improves with the annealing process. In addition, the annealing treatment also improves the ferromagnetic properties (see Fig. 2.15 (c)). While the as-grown film shows indeed deficient magnetic properties ( $T_C$ < 150 K), the annealed film has a ferromagnetic transition close to the optimal Curie temperature of LNMO bulk (Tc≈ 280 K) [125]. Annealing at high temperature corresponds to a higher effective oxygen chemical potential, thus promoting cation ordering in the matrix, thereby increasing the overall magnetic moment. At the same time, it facilitates interdiffusion of Ni and Mn, homogenizing the composition and the structure [145] [143]. In previous work, Singh et al., [189] have reported the role of annealing temperature and atmosphere in controlling cation ordering and magnetic properties of $La_2NiMnO_6$ thin films. On the other hand, some studies on the similar double perovskite with composition $La_2CoMnO_6$ (in bulk or

thin films) also indicate that the annealing conditions affect the magnetic and structural properties [91] [145]. In our RNMO (R= La, Pr) systems, while the non-annealed samples present poor magnetic properties, the annealing process is found to significantly improve both $T_C$ and the magnetization.

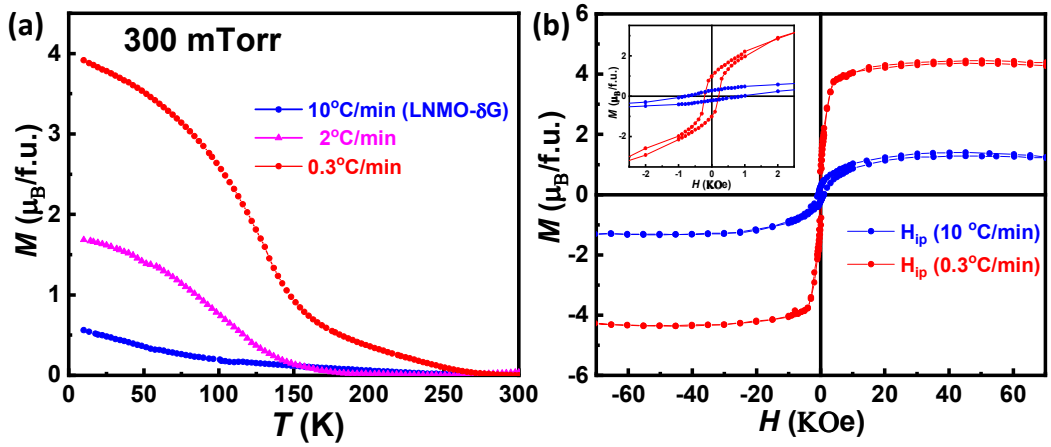


Figure 2.16. (a) In-plane magnetization as a function of temperature under $\mu_0 H$ =0.5 T of LNMO thin films with different cooling rate. Films were grown at 850°C under 350 mTorr $O_2$ for 1h, with in-situ annealing at the same growth temperature (1h under 420 Torr $O_2$). (b) M(H) hysteresis loops for the field applied in-plane at 10K of LNMO samples with the highest and lowest cooling rate (10°C/min and 0.3°C/min, respectively). The inset shows in detail the low field region.

Finally, beside the annealing process, cooling rate can also play a significant role in the functional properties of thin films. In our protocol growth optimization of RNMO (R = La, Pr) thin film (see appendix A.1.1), we usually use cooling rate of 10°C/min. Here, we have tried to improve the magnetic properties of the samples, applying slower cooling rates after annealing treatment of different LNMO samples (growth/annealing at 850°C under 300 mTorr $O_2$). In this regard, besides of the LNMO sample with usual cooling rate of 10°C/min (labeled as LNMO-δG, see chapter 3 for more details), we have grown two additional LNMO samples under the same growth conditions, applying two slower cooling rate (2°C/min and 0.3°C/min). M(T) curves of these three samples are shown in Fig 2.16 (a). It can be observed a monotonous improvement of $T_C$, from $T_C$-100 K to ~138 K (estimated from the inflection point), when lowering the cooling rate from 10°C/min to 0.3°C/min, respectively. At the same time, in-plane M(H) hysteresis loops measured at 10K for two samples with the highest and lowest cooling rate (10°C/min and 0.3°C/min) are shown in Fig. 2.16 (b). The thickness of these samples was found to be ~ 44 nm (10°C/min), and ~ 49 nm (0.3°C/min) respectively, therefore very similar. It can be appreciated that the sample with the highest cooling rate (10°C/min) has a coercive field $Hc \approx 800$ Oe, while in the sample with the lowest cooling rate (0.3°C/min) $Hc \approx 200$ Oe (see inset in Fig. 2.16 (b)). By decreasing the cooling rate the

remanent magnetization increases from $M_r \approx 0.27\ \mu_B$/f.u. ($10^oC$/min) to $M_r \approx 0.99\ \mu_B$/f.u. ($0.3^oC$/min), as well as the saturation magnetization from $Ms \approx 1.4\ \mu_B$/f.u. ($10^oC$/min) to $Ms \approx 4.4\ \mu_B$/f.u. ($0.3^oC$/min). This improved saturation magnetization value was found to be very close to that reported for the LNMO bulk value of $5\mu_B$/f.u [1]. Nevertheless, the $T_C$ value is still very low with respect to the bulk properties of LNMO with $T_C$~280K [125]. In this regard, annealing process at $850^oC$ under 420 Torr $O_2$ was not enough to increase the $T_C$ of samples grown at high oxygen pressures ($PO_2 \geq 150$ mTorr $O_2$) and high growth temperatures ($850^oC$), indicating oxygen deficiency inside the film (see Fig. 2.11 (b)). Therefore, an increase of $T_C$ as a result of a slower cooling process after annealing can be explained by the longer time in which the film was exposed to high temperatures (slowly cooled from $850^oC$). In conclusion, these results indicate better oxygen absorption during slow annealing, improving the B-site cationic ordering and therefore the magnetic properties of the films [190]. On the other hand, low oxygenation of samples can induce changes in the Ni spin state, which could explain the smaller saturation magnetization in the sample with low $T_C$. Finally, in spite of a slow cooling rate after annealing treatment, the magnetic properties of LNMO samples (growth/annealing, $850^oC$ at 300 mTorr $O_2$) are still very deficient.

Previous reports in double perovskite systems of similar composition to $La_2NiMnO_6$, such as $La_2CoMnO_6$ [102], reveal an orthorhombic-to rhombohedral phase transition temperature that seems to depend on the cooling rate during the synthesis. In a slow-cooled sample the oxidation states appear to be near to $Co^{2+}$ and $Mn^{4+}$, while in quenched samples the balance is moved towards $Co^{3+}$ and $Mn^{3+}$ [102]. A similar behavior may happen in our LNMO thin films, where the ordering of the oxidation states at the *B* sites appear to be near $Ni^{2+}$ and $Mn^{4+}$ in slow-cooled samples, which improves the magnetic properties of the films (see Fig. 2.16). This change in the oxidation states in double perovskite systems modifies the tolerance factor of the compound, which then influences the phase transition temperature [102].

# Summary

In this chapter, we have presented a detailed explanation of the growth procedure of RNMO thin films by R.F magnetron sputtering technique. Previous to film deposition, stoichiometric targets of $La_2NiMnO_6$ and $Pr_2NiMnO_6$ with double perovskite structure have been prepared. In addition, for the growth of high quality thin films with atomically controlled interface, a subsequent thermal treatment was carried out on the substrates ($SrTiO_3$ and $LaAlO_3$ single crystals). As a growth protocol, all films were deposited by keeping fixed RF power (40 W) and target-to-substrate distance (5cm), while changing oxygen pressure, growth temperature and annealing conditions. In order to obtain high quality thin films, we have explored and optimized the impact of oxygen pressure and growth temperature on their physical properties. In addition, the annealing process and cooling rate has been found to have a great influence

on the crystallization and magnetic properties of films. In this optimization process, we have determined the narrow window of growth conditions that allow obtaining good ferromagnetic LNMO thin films. For more details, the specific optimization and study of the physical properties of our films will be carried out in the next two chapters.

# Chapter 3

# Growth and physical properties of $La_2Ni_{1-x}Mn_{1+x}O_6$ thin films

In this chapter, we report on the growth and physical characterization of $La_2Ni_{1-x}Mn_{1+x}O_6$ (LNMO) thin films with double perovskite structure on top of (001)-oriented $SrTiO_3$ substrates by RF magnetron sputtering. It is worth mentioning that when we started this thesis work, no report was found of LNMO thin films deposited by magnetron sputtering technique. The influence of oxygen pressure ($PO_2$), growth temperature and annealing on the microstructure, stoichiometry, and magnetic and transport properties of the films is thoroughly investigated. In particular, special attention has been given to addressing two issues. Firstly, high annealing temperature treatments (800°C-900°C) under high oxygen pressures (420 Torr) have a great influence on the progress of crystallization and the magnetic properties of LNMO films. Nevertheless, these high temperature treatments after film growth seem to be responsible of the formation of nanocomposites at the film surface. Second, the magnetic properties of bulk LNMO have been widely studied over the years in order to gain better understanding of the nature of the magnetic exchange interactions in this compound [1] [39] [191] [44]. There are few reports of thin films of this material and they usually concern deposition by Pulser Laser Deposition (PLD) technique. Those studies have concluded that ordered double perovskites are only stable within a very narrow growth window [145] [189]. Outside of this window, the studies on thin films have evidently depicted that there is either a short-range-ordered phase or coexistence of multiple phases like the polycrystalline bulk samples in thin films of $La_2NiMnO_6$ [192] [19] [41]. On the other hand, electron probe microanalysis (EPMA) measurements have revealed that high oxygen pressure promotes the growth of stoichiometric films, with a Ni/Mn ratio almost equal to 1. Nevertheless, these films exhibit poor ferromagnetic properties with respect to the expected optimum values corresponding to ferromagnetic ordering mediated by superexchange interaction between $Ni^{2+}$ and $Mn^{4+}$ according to the Goodenough-Kanamori rules. Most interestingly, films grown at low $PO_2$ exhibit Ni/Mn ratios below 1, but ferromagnetic properties close to the optimal ones. In this regard, the valence balance between Ni and Mn ions in nonstoichiometric sample has been elucidated by X-ray absorption spectroscopy. The results indicate that Ni deficiency

plays a crucial role in the puzzling insulating ferromagnetic behavior observed in nonstoichiometric samples. Therefore, we report a detailed study of structural, magnetic and transport properties and composition of two characteristic types of samples.

This chapter is divided into three main parts. In the first part, we present the optimization of the growth parameters (i.e. chamber oxygen pressure, growth temperature and annealing). In the second part the influence of stoichiometry on ferromagnetic properties in the LNMO thin films. Finally, in the third part, the spontaneous formation of the nanostructures at the surface is presented.

.

# 3.1 Optimization of growth conditions

In literature, $La_2NiMnO_6$ thin films have been mainly grown by PLD technique. Previous studies report that a high degree of cationic ordering is achieved in films grown under high oxygen pressure (100-1000 mTorr) and high growth temperature (700-900$^o$C) [185] [144] [42]. In this section, the optimization of growth conditions of LNMO thin films on $SrTiO_3$ (001) substrates deposited by RF sputtering is presented in detail (although already briefly introduced in chapter 2). On the other hand, in this study LNMO thin films were deposited using two different targets, one prepared by the sol-gel method and one by the solid-state reaction route (see chapter 2, section 2.1). Thereby, in this section, only the LNMO thin films grown at 900$^o$C under different oxygen pressures were grown using the target prepared by the solid-state method. We have not observed significant differences in terms of film quality and physical properties.

## 3.1.1 Structural and morphological properties under different oxygen pressures and growth temperatures

Understanding the influence of growth conditions on the structural and morphological properties of LNMO thin films allows us to determine the film with good crystalline quality. Moreover, the surface morphology of the films plays an essential role in applications such as tunnel junctions, spin valves, etc. A layer-by-layer growth with step-terrace morphology is indeed very important to ensure the continuity of the layer for very thin films, and their eventual integration in heterostructures.

### 3.1.1.1 Thin films grown at 850°C

To evaluate the influence of oxygen pressure on structural and morphological properties of the films, a set of LNMO thin films on (001)-oriented $SrTiO_3$ (STO) substrates were grown using a target prepared by sol-gel method. Films were grown under different oxygen pressures (ranging from 120 to 350 mTorr) keeping the fixed growth temperature (850°C for 1h). After thin film deposition, as-grown samples were annealed (in-situ) at the same growth temperature (1h under 420 Torr $O_2$). The cooling rate was 10°C/min. The sample thickness, determined by XRR measurements, was found to be very similar in all samples, with values around ~39-44 nm (see chapter 2, Fig. 2.11 (a)).

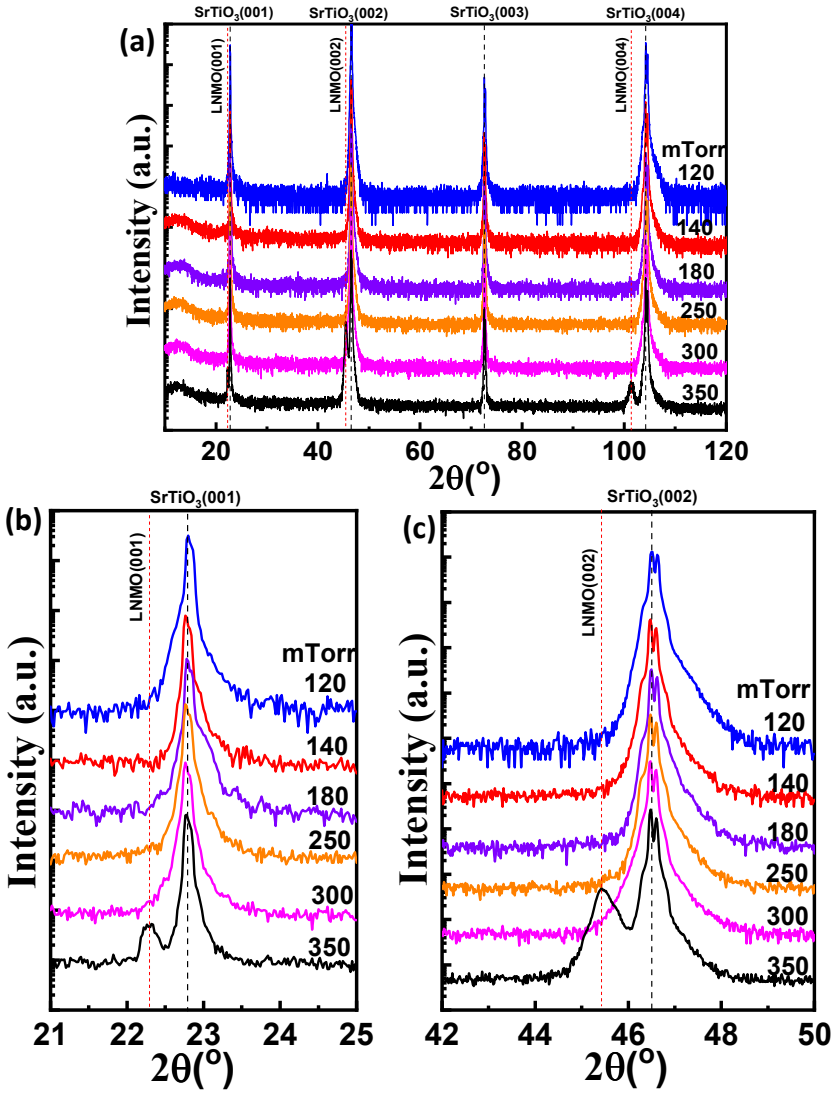


Figure 3.1 (a) θ/2θ XRD scans of LNMO thin films grown under different oxygen pressures at 850°C. (b) Scans around the (001) reflection and (c) scans around the (002) reflection of both STO substrate and LNMO film.

X-ray diffraction measurements were carried out to evaluate the crystalline quality of the samples. θ/2θ XRD scans of LNMO thin films grown at 850°C under various oxygen pressures are shown in Fig. 3.1 (a). As mentioned in chapter 1 (see section 2.2), for simplicity, and also for easier comparison between film and substrate, the indexing of cell parameters will be referred to the pseudocubic notation. The epitaxial LNMO film ($a_{p\ \text{bulk-LNMO}} \approx 3.876$ Å) [41] on STO substrate ($a_{p\ \text{STO}} \approx 3.905$ Å) grows under a tensile in-plane strain.

In XRD patterns, the most intense peaks correspond to (00*l*) reflections of the STO substrate (see dashed black line). The (00*l*) reflections of the LNMO phase cannot be clearly appreciated, which could indicate that the layer peaks overlap with the substrate peaks, with exception of the sample deposited at higher oxygen pressure (350 mTorr). For more details, scans around (001) and (002) reflections are shown in Fig. 3.1 (b) and (c). The XRD patterns of the sample grown at 350 mTorr $O_2$ shows clearly the (00*l*) peaks of the LNMO phase which take place at 2θ values slightly lower than the ones of STO substrate (see dashed red line). The out-of-plane *c* lattice parameter for this sample was found to be 3.830Å, very close to the LNMO bulk value (3.876 Å) [41]. To detect LNMO phase in other films, high-resolution θ/2θ XRD was performed (see section 3.2). In addition, XRD patterns do not show traces of spurious phase, supposing single-phase LNMO films and thus with good crystalline quality.

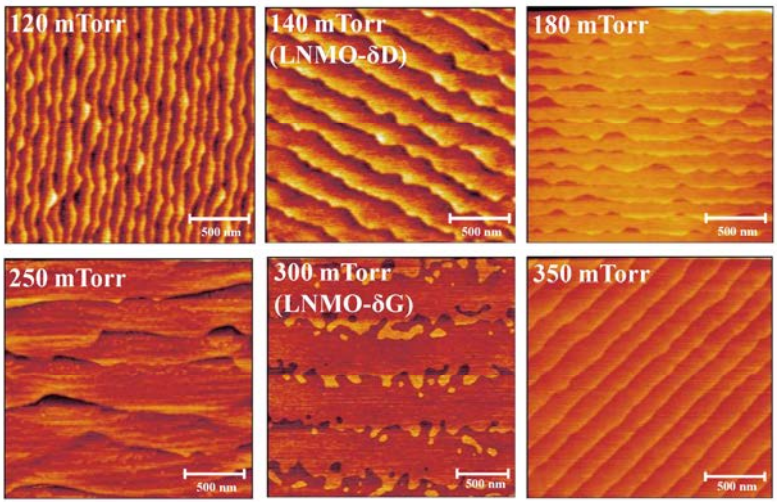


Figure. 3.2 AFM topography images of LNMO thin films grown under different oxygen pressures at 850°C. Samples grown at 140 and 300 mTorr were labeled as LNMO-δD and LNMO-δG, respectively (detailed respective studies are shown below, in section 3.2).

To evaluate the surface morphology and growth mechanisms, atomic force microscopy (AFM) and scanning electron microscopy (SEM) measurements were carried out on the LNMO films (Fig. 3.2 and Fig 3.3). AFM images in tapping mode show a flat surface for all samples. These high-quality surfaces with a very low roughness of rms < 0.4 nm (in the order of the perovskite unit cell length) indicate a 2D growth mode.

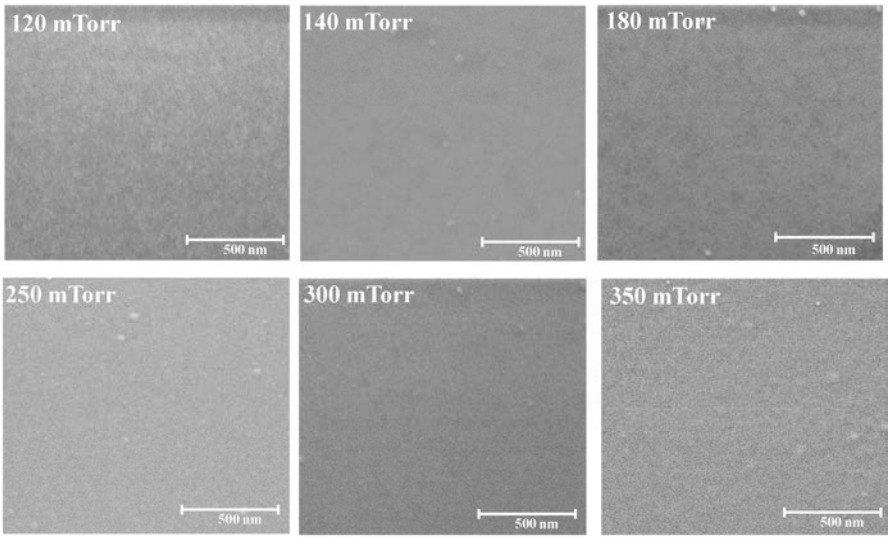


Figure. 3.3 SEM micrographs of the corresponding AFM images (see Fig.3.2) of LNMO films grown under different oxygen pressures at 850°C.

In Fig. 3.3, SEM micrographs of the corresponding AFM images (shown in Fig. 3.2) confirm a very flat surface. Nevertheless, in some regions of the samples the presence of small nanoparticles, randomly distributed, can be observed. The grain size and composition will be studied later (see section 3.3.2).

## 3.1.1.2 Thin films grown at 900°C

In this section, the structural and surface properties were explored in a series of LNMO samples grown using a target prepared by solid-state reaction method (see chapter 2, section 2.1). Samples were grown under different oxygen pressures (ranging from 70 to 600 mTorr) keeping the substrate temperature fixed (900º for 1h). As before, after film deposition, as-grown samples were annealed (in-situ) at the same growth temperature (for 1h under 420 Torr $O_2$) and a cooling rate of 10°C/min. It should be noted that any change in the target (or sputtering conditions) requires a new optimization of the growth conditions (principally oxygen partial pressure values and growth temperature). Nevertheless, the general tendency with different growth conditions remains similar.

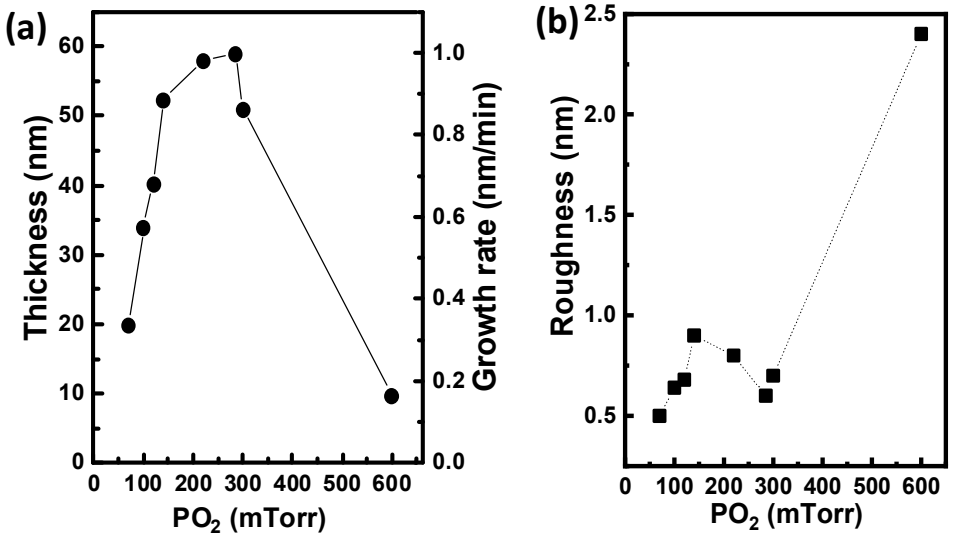


Figure 3.4 (a) Thickness (left axis) and growth rate (right axis) and (b) roughness of LNMO thin films grown at 900°C under different oxygen pressures.

XRR analysis revealed that the thickness of the samples is dependent of the oxygen pressure conditions. By increasing the oxygen pressure from 70 to 285 mTorr $O_2$, the film thickness increases from 20 to 60 nm. Nevertheless, for the sample deposited under 300 mTorr $O_2$, a slight decrease in the thickness was found (t~51 nm). Finally, the thickness of sample grown under 600 mTorr $O_2$ decreases considerably (t~10 nm). Thus, the growth rate shows strong non-monotonous oxygen pressure dependence (Fig.3.4 (a)), contrary to the samples grown at 850°C where the growth rate was almost constant (see chapter 2, Fig 2.11). This strong decrease of the thickness in LNMO films deposited at high pressures (600 mTorr) could be associated to the phenomenon of resputtering [193]. This effect was very notable in PNMO films deposited under similar growth conditions (from which a detailed description is given in chapter 4, section 4.1.1), where the thickness of the samples decreased monotonically from 95 to 28.5 nm as the oxygen pressure increases.

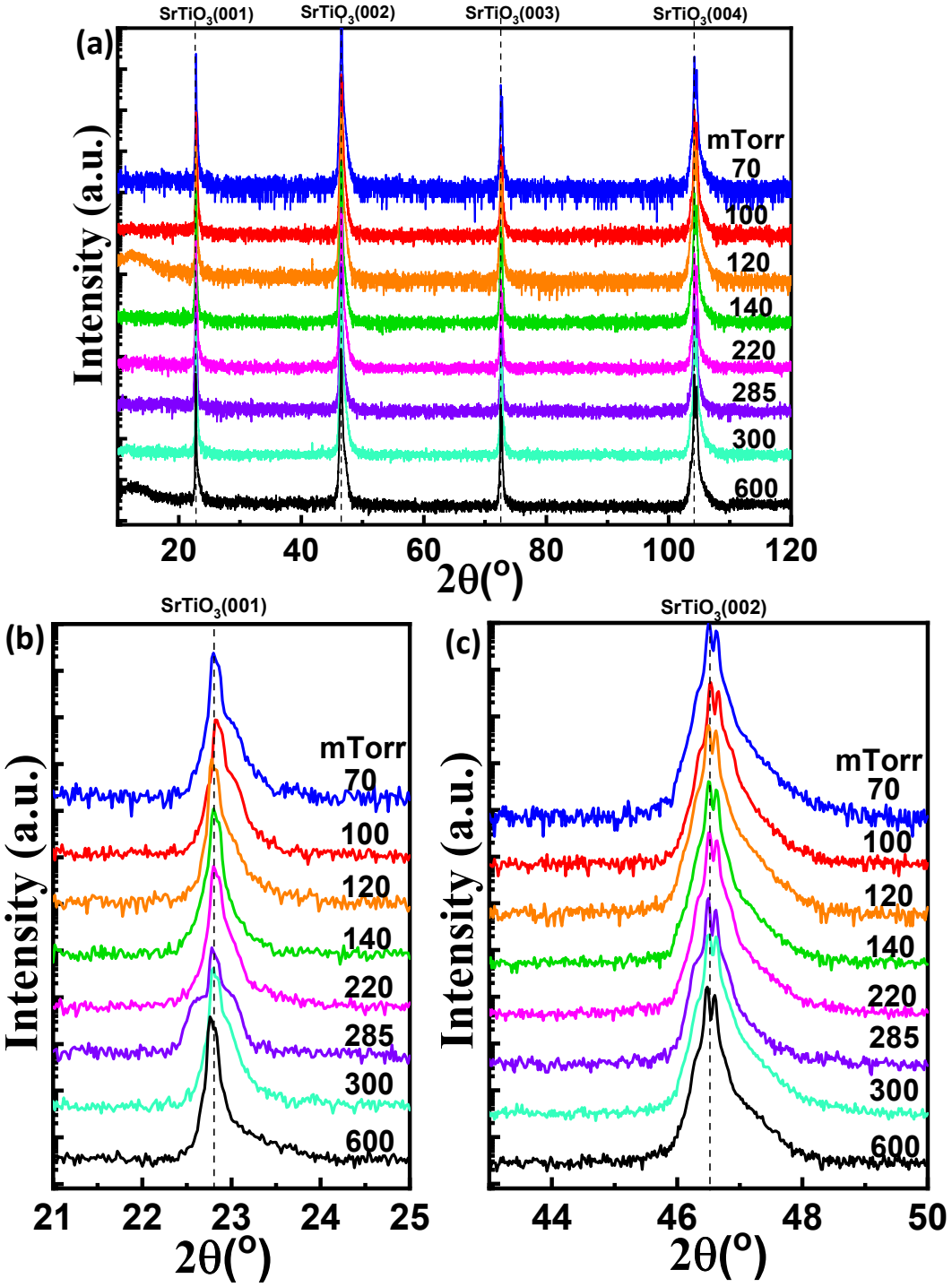


Figure 3.5 (a) θ/2θ XRD scans of LNMO thin films grown under different oxygen pressures at 900°C. (b) Scans around the (001) reflection and (c) scans around the (002) reflection of both STO substrate and LNMO film.

The crystal structure of the samples was evaluated by X-ray diffraction measurements (see Fig. 3.5 (a)). As previously, only the peaks corresponding to the STO substrate (see dashed black line) in all XRD patterns can be clearly observed, while the (00*l*) LNMO reflections are

difficult to detect. For more details, a scan around the (001) and (002) reflection of STO substrate is shown in Fig. 3.5 (b) and (c). It can be appreciated that the film peaks are not visible. Nevertheless, by performing Reciprocal Space Maps (RSMs) measurements, the in-plane and out-of-plane parameters can be accurately determined.

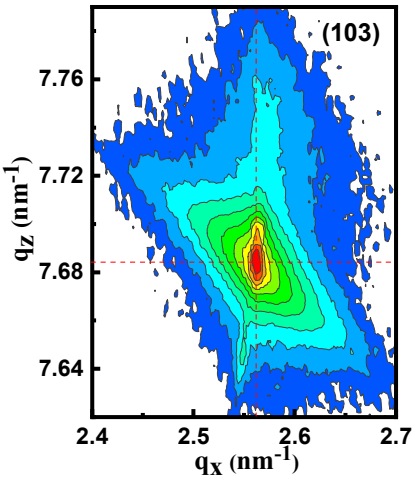


Figure 3.6 Reciprocal Space Map (RSM) around (103) reflection of an illustrative LNMO film (thickness, t=34 nm) grown/annealed at 900°C under 100 mTorr $O_2$. Red dashed lines indicate the center of the STO substrate reflection.

In order to determine both lattice parameters (i.e. out-of-plane and in-plane), reciprocal space maps (RSMs) were carried out on LNMO samples. Therefore, with the RSMs and using the equations in appendix (see section A.4.4), the values of both in-plane ($a_{||}$) and out-of-plane ($a_{\perp}$) lattice parameters can be extracted and the epitaxial strain state of the film can be studied. Fig 3.6 shows the RSM around $(103)_{STO}$ reflection of a LNMO film (thickness t=34 nm) grown/annealed at 900°C under 100 mTorr $O_2$ and with good ferromagnetic properties (see Fig 3.10 (b) in section 3.1.2). The in-plane cell parameter of LNMO film is equal to that of the STO substrate ($a_{STO}$= 3.905Å), indicating that it grows fully strained. On the other side, the out-of-plane lattice parameter is estimated to be $a_{\perp}$=3.880 Å, giving rise to the unit cell volume of V~59.2 Å$^3$. According to these results, the evolution of the structural and magnetic properties of a same LNMO film grown at 900°C, with a successive (ex-situ) annealing at high temperatures (800°C and 900°C), is studied later in this chapter (for more details see section 3.3.2.2). The results, after successive annealing, reveal a shrinkage of the out-of-plane lattice parameter down to the LNMO bulk value, 3.876 Å [41]. The same film grown/annealed at 900°C shows a reduction of the unit cell volume (see Fig 3.33 and Fig. 3.34) with values similar to those reported for this sample here (grown/annealed at 900°C under 100 mTorr $O_2$), resulting in improved magnetic properties (see Fig 3.10 (b)). Similarly as in this study, these results can be associated with the incorporation of oxygen inside the

structure and the formation of $Mn^{4+}$. On the other hand, the lattice parameters considering the monoclinic ($P2_1/n$) structure of double perovskite LNMO lead to cell parameters a=b=5.519 Å and c=7.759 Å. These values are found to be close to the values reported in the literature [28] [145] [194].

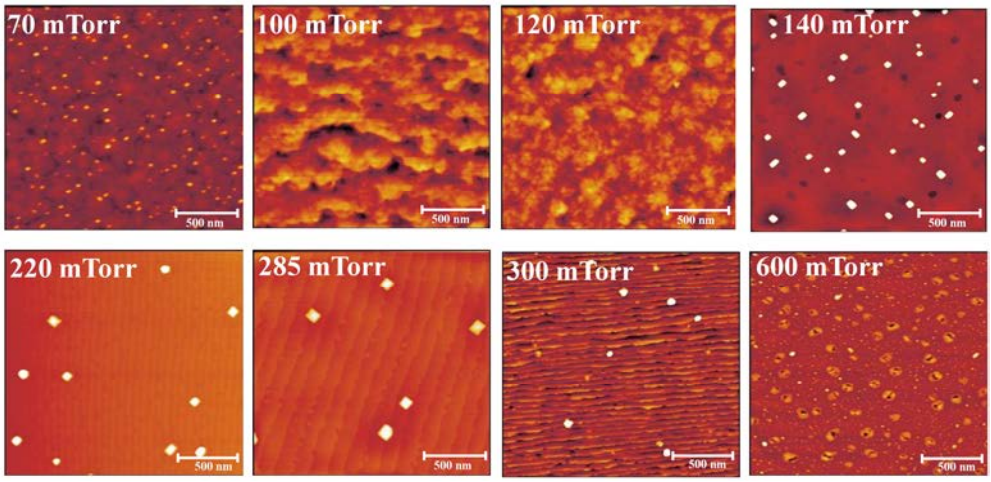


Figure 3.7. AFM topography images of LNMO thin films grown under different oxygen pressures at 900°C.

In Fig 3.7, atomic force microscopy (AFM) images in tapping mode show the evolution of the surface topography as a function of oxygen pressure. In the case of samples deposited at low pressures ($PO_2$<140 mTorr), the step-terrace-morphology is not observed. Nevertheless, some mounds evenly distributed over surface of the films can be appreciated, as well as small holes. On the other hand, samples grown at high oxygen pressures ($PO_2 \geq$ 220 mTorr), show a steps-terraces morphology, indicating a 2D growth mode. Additionally, some randomly distributed 3D structures (nanometric cubes) appear as bright spots over the film terraces. Particularly, the sample deposited at the highest oxygen pressure (600 mTorr) shows a morphology without step-terraces and only the formation of nanostructures is appreciated. Similarly, these nanoparticles were also observed on the surface of LNMO films by SEM measurements (see Fig.3.8). The formation of these nanostructures as a function of the growth temperature and the annealing process will be studied below (see section 3.3.2).

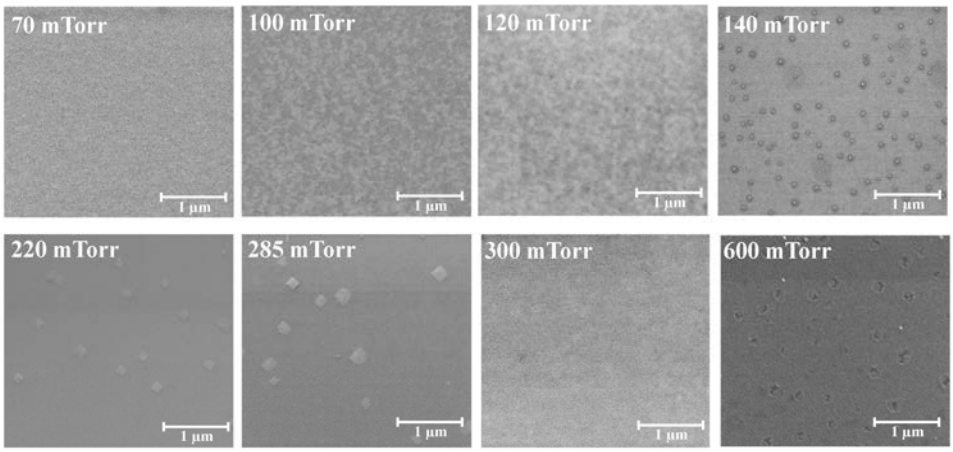


Figure 3.8 SEM micrographs of the corresponding AFM images (see Fig.3.7) of LNMO films grown at 900°C under different oxygen pressures**.**

The evolution of the roughness of the films as a function of the oxygen pressure is shown in Fig. 3.4 (b). One can observe low roughness values (rms < 1 nm) for almost all films. For the samples deposited at high oxygen pressures (from 220 to 300 mTorr) with step-terrace morphology, the roughness values were found to be around the unit cell value (rms ~ 0.5 nm). For the sample deposited at 600 mTorr $O_2$, the roughness value was high (rms ~ 2.4 nm), most probably related to the presence of 3D nanostructures at the surface.

## 3.1.1.3 Thin films grown under 140 mTorr $O_2$

In this section, we study the evolution of the structural properties and surface morphology as a function of the deposition temperature under a fixed oxygen pressure during film growth. This series of LNMO samples on STO (001) substrates were grown using a target prepared by sol-gel method. For this study, a low oxygen pressure was selected, because good ferromagnetic properties were found in this pressure range, i.e. $PO_2$ < 150 mTorr (see section 3.1.2 below). In this regard, samples were deposited under a fixed oxygen pressure of $PO_2$=140 mTorr, at different substrate temperatures, ranging from 500 to 900°C for 1h. As before, after film deposition, samples were annealed (in-situ) at the same growth temperature (for 1h under 420 Torr $O_2$) and a cooling rate of 10°C/min. The thickness of these samples (see Fig 3.9), determined by XRR analysis is found to be dependent of the growth temperature. The samples deposited at low temperatures (T ≤ 700°C) were significantly thicker (t~70 nm) than the ones deposited at high growth temperature (T ≥ 800°C) (t~40 nm). The gradual decrease in thickness of the samples with the growth temperature can be explained by the phenomenon of resputtering (see Chapter 2, Fig 2.13). Similarly to the samples deposited at different pressures, θ/2θ XRD diffraction did not allow determining

correctly the structure of the films, as only the peaks corresponding to the STO substrate are clearly observed (see chapter 2, Fig 2.14). In this case, as we mentioned before, reciprocal space maps (RSMs) allow studying the structure of the films, as in-plane and out-of-plane parameters can be precisely determined (see section 3.2.1 and 3.3.2.1). Therefore, this section will only focus on describing the morphology of the LNMO films deposited at different growth temperatures.

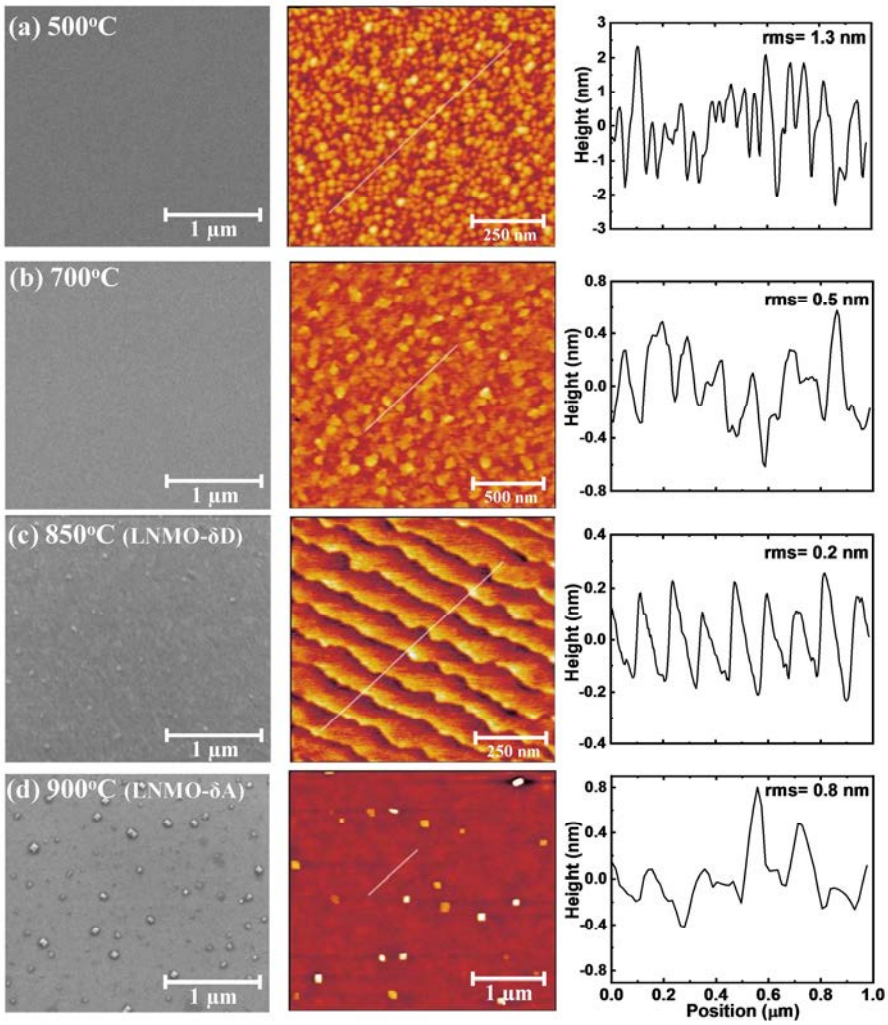


Figure 3.9 SEM micrographs (left), AFM topography (middle) and corresponding profile lines (right) of LNMO samples grown under 140 mTorr $O_2$ at different growth temperatures: (a) 500°C, (b) 700 °C, (c) 850 °C, and (d) 900°C.

AFM and SEM measurements were used to study the effect of the deposition temperature on the surface morphology of the LNMO films. Fig. 3.9 depicts four LNMO samples deposited at different growth temperature ranging from 500°C to 900°C. Samples grown/annealed at 850°C and 900°C were labelled as LNMO-δD and LNMO-δA, respectively (for their respective study in section 3.2). SEM micrographs (left column) of samples grown at low

temperatures (≤ 700°C) show a flat surface, without any presence of segregations (see Fig 3.9 (a) and (b)). At the same time, AFM images (middle column) of the same samples reveal a granular morphology with a tendency to a 3D growth mode. At higher temperatures (850°C and 900°C), SEM images show a homogeneous surface with the presence of nanoparticles randomly distributed on the film surface (Fig. 3.9 (c)). The corresponding AFM image at 850°C shows a flat surface with step-terrace morphology, indicating a 2D growth mode. The nanoparticles were not appreciated in this area of the sample. The corresponding AFM image at 900°C corroborates the morphology seen by SEM. A flat morphology and some nanoparticles randomly distributed on the film surface can be seen clearly in Fig. 3.9 (d). The grain analysis of this sample was studied later (see section 3.3.2). Additionally, profile lines (right column) corresponding to the marked lines in the AFM image confirm a smooth surface with a root-mean-square (RMS) surface roughness of rms~0.2 nm and 0.8 nm for samples grown at 850 °C and 900°C, respectively. For the thickest films grown at low temperature (≤ 700°C), the roughness values are still low (rms ≤ 1.3 nm). Therefore, it should be noted that the LNMO films grown on $SrTiO_3$ can be obtained with smooth surfaces up to large values of thickness.

## 3.1.2 Magnetic properties

Growth conditions, especially growth temperature and oxygen pressure during film growth, in LNMO systems have a large influence on magnetic properties, as mentioned in chapter 1. Previous results on LNMO films, deposited on STO substrates by pulsed laser deposition (PLD) [19] [144] [192] [125], report that magnetic properties depend on film thickness and growth conditions. The optimal growth conditions allow to achieve a ferromagnetic transition near room temperature and a high saturation magnetization (i.e. $T_C$~280 K, Ms~ 5$\mu_B$/f.u.) [1] [185]. The origin of ferromagnetism in LNMO compounds is governed by the super-exchange interaction between $Ni^{2+}$ and $Mn^{4+}$ through oxygen. The presence of defects, cation vacancies and/or the arrangement of *B*-site ions, significantly depend on synthesis conditions and strongly influence the magnetic properties [191] [19] [41]. Therefore, to obtain qualitative information about the Ni/Mn cation ordering at the B sites in our films, in-plane magnetization measurements were carried out. In this section, the magnetic properties have been studied as a function of growth temperature and oxygen pressure.

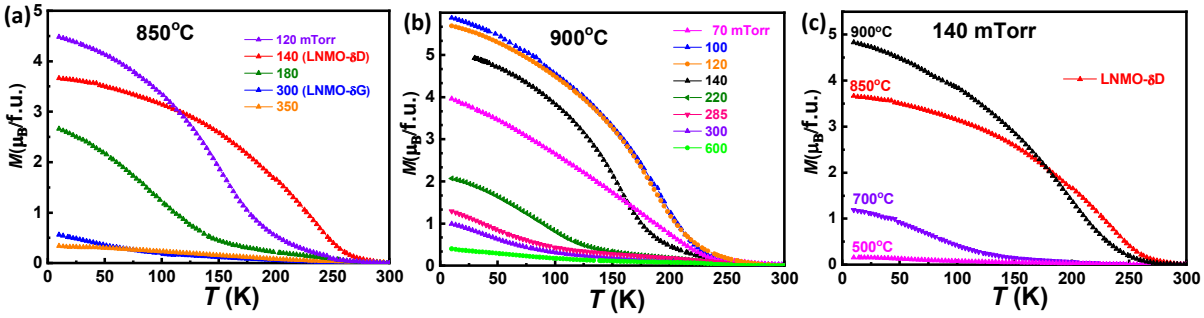


Figure 3.10. In-plane magnetization as a function of temperature under an applied field of 5 kOe ($\mu_0 H$ = 0.5 T) of LNMO thin films grown under: (a) different oxygen pressure ranging from 120 to 350 mTorr, and keeping a fixed growth temperature of 850°C for 1h, (b) different oxygen pressure ranging from 70 to 600 mTorr at fixed temperature of 900°C, and (c) different growth temperatures under fixed 140 mTorr $O_2$.

Figs. 3.10 shows in-plane magnetization of LNMO thin films grown under different oxygen pressures (70 mTorr < $PO_2$ < 600 mTorr) and different growth temperatures (500°C < T < 900°C) under an applied magnetic field of 5 kOe. It can be appreciated that the magnetization exhibits a strong dependence on the growth conditions. Samples grown under a high oxygen pressure ($PO_2$ > 180 mTorr) and high growth temperatures (850°C and 900 °C) (Fig. 3.10 (a) and (b)) show very deficient magnetic properties with $T_C$ < 150 K (estimated from the inflexion point). With decreasing oxygen pressure $T_C$ improves significantly, rising up to $T_C \approx 240$ K for the samples deposited under $PO_2$ = 140 mTorr at 850°C (Fig.3.10(a)) and Tc ≈ 200 K for $PO_2$ = 100 mTorr at 900°C (Fig. 3.10(b)). With further decreasing the oxygen pressure ($PO_2$ < 70 mTorr), the magnetization transition decreases again. We have also observed a non-monotonous dependence of $T_C$ on the deposition temperature under an oxygen pressure of 140 mTorr (Fig. 3.10(c)). When the growth temperature decreases from 900°C to 850°C, $T_C$ increases from $T_C$ ~160 K to ~240 K, respectively. On the other side, thin films grown at low growth temperatures (T ≤ 700°C) show deficient magnetic properties with low magnetic transition ($T_C$ < 100 K). The later suggests that the films might contain Ni–O–Ni and Mn–O–Mn arrangements because low growth temperatures would not be high enough to promote *B*-sites cation ordering, as observed in Ref. [143]. Oxygen vacancies could also appear under low oxygen pressure growth at low temperature, thus causing the degradation of ferromagnetism in these samples [145]. Therefore, the optimum growth conditions of LNMO thin films with ferromagnetic transition near room temperature ($T_C$ ~ 240K), very close to the bulk counterpart [1] [185], have been obtained in samples grown/annealed at 850°C under oxygen pressure of $PO_2$ = 140 mTorr (sample labeled as LNMO-δD).

The different $T_C$ values for samples grown under $PO_2$ = 140 mTorr at 900°C (black curve in Fig. 3.10 (b) and (c)) could be related to the different targets used (targets prepared by solid state reaction and by sol gel method). By comparing the growth of LNMO films using the two targets, we have observed that films deposited using the target prepared by the solid state

method require low oxygen pressures during film growth than when the sol-gel target is used. Good growth conditions have been obtained under a narrow range of pressures, around 100-120 mTorr (see Fig. 3.10 (b)). However, as mentioned before, any change of target requires a new optimization of the growth conditions.

According to previous results reported for LNMO samples prepared by PLD, good ferromagnetic properties (i.e. $T_C \approx 260K$ and $M_S \sim 5\mu_B$/f.u. at low temperature) and good stoichiometry are obtained in LNMO films prepared at high oxygen pressures (i.e. 300mTorr [19] or even 800mTorr [41]) and high growth temperatures (around 750-800$^o$C). After film growth, (in-situ) annealing treatments under high oxygen pressure (760 Torr $O_2$) have been carried out to promote B site cationic ordering and minimize the oxygen deficiency [144] [42]. In general, samples grown under low oxygen pressure ($PO_2$ < 500 mTorr $O_2$) present a low saturation magnetization [41] [143]. An exception is reported in Ref. [19], where films prepared under $PO_2$ > 180 mTorr have magnetic saturation value close to the theoretical value ($M_S \sim 5\mu_B$/f.u). These results are in contrast with our own observations, as we have obtained LNMO samples with good ferromagnetic properties (i.e., Tc ≈ 240 K and Ms ≈ 5.3 $\mu_B$/fu at 10 K) using low oxygen pressures ($PO_2$ < 150 mTorr $O_2$) and high growth temperature (850$^o$C). In addition, samples grown under high oxygen pressures ($PO_2 \geq$ 180 mTorr) and at the same growth temperature show poor ferromagnetic properties (see section 3.2). Therefore, to clarify the origin of these discrepancies, we have carefully analyzed the stoichiometry (using EPMA) of our samples in the next section.

## 3.1.3 Chemical composition

The physical properties of the films are directly determined by their stoichiometry. Therefore, the composition of the samples is an essential information on the material under study. In this section, we present the influence of oxygen pressure and growth temperature on the chemical composition and stoichiometry ratio of LNMO thin films, whose structural, morphological and magnetic properties have been presented in the previous section.

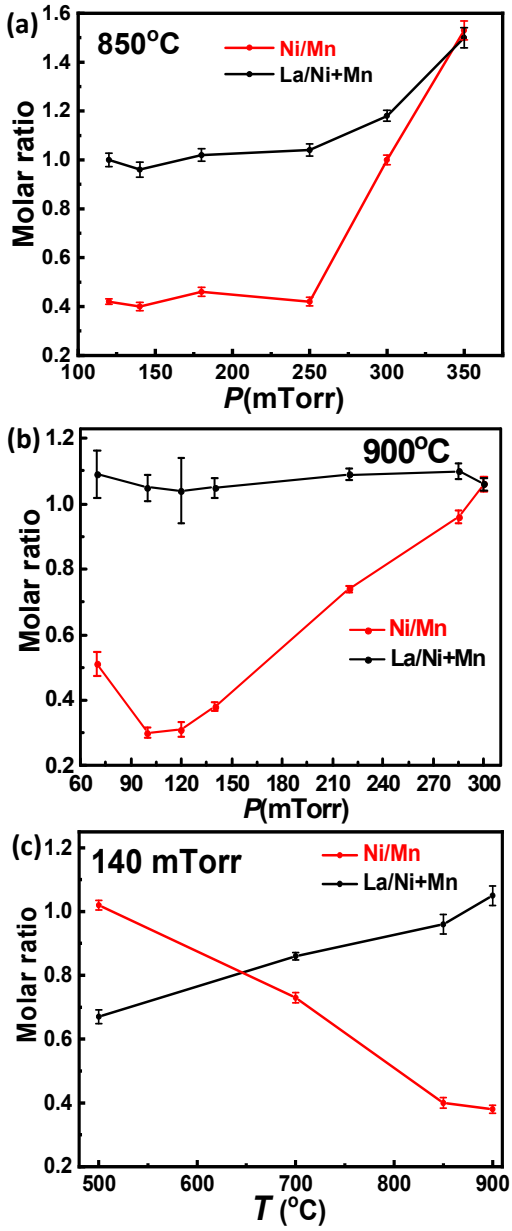


Figure 3.11 Stoichiometry ratio (obtained by EPMA) of LNMO thin films grown on STO (001) substrates: (a) at a growth temperature of 850°C under different oxygen pressures (ranging from 120 to 350 mTorr), (b) at a growth temperature of 900°C under different oxygen pressures (ranging from 70 to 300 mTorr), and (c) at different growth temperatures under 140 mTorr $O_2$ for 1h. Error bars have been estimated from the dispersion of the EPMA results at different points of the sample surface.

The chemical composition and stoichiometry ratio of LNMO thin films grown on STO substrates have been analyzed by electron probe microanalysis (EPMA). Fig. 3.11 (a) and (b) show the stoichiometry ratio of LNMO films grown at 850°C and 900°C under different oxygen pressures, while the stoichiometry ratio of LNMO films grown under 140 mTorr $O_2$ at different growth temperatures is depicted in Fig. 3.11 (c). The quantitative compositional

data for all elements are shown in Tables 3.1, 3.2 and 3.3. Tables show for each oxygen pressure/growth temperature (1st column) the atomic percent of each element (2nd-5th columns), La for unit formula f.u. (6th column), the Ni:Mn ratio (7th column) and the value of x (8th column). Due to the presence of oxygen in both film and substrate, oxygen concentration is not computed due to the presence of the relatively large O background signal from the substrate, which is difficult to separate from the one coming from the film. Therefore, a nominal stoichiometry is imposed for oxygen, in the composition of the samples expressed as $La_2Ni_{1-x}Mn_{1+x}O_6$.

**Table 3.1:** Chemical composition and stoichiometry ratio of $La_2Ni_{1-x}Mn_{1+x}O_6$ thin films grown under different oxygen pressures (ranging from 120 to 300 mTorr) at 850°C. Samples were grown using the target prepared by sol-gel method.

| ***P*O$_2$ (mTorr)** | **La (atom %)** | **Ni (atom %)** | **Mn (atom %)** | **O (atom %)** | **La (per f.u.)** | **Ni:Mn** | **x** |
|---|---|---|---|---|---|---|---|
| 120 | 19.2 (2) | 6.3 (1) | 13.2(2) | 67.2 (4) | 1.98 (3) | 0.48 (1) | 0.35 (1) |
| 140 (LNMO-δD) | 19.2 (2) | 6.0 (1) | 14.0 (2) | 67.1 (5) | 1.92 (3) | 0.43 (2) | 0.40 (2) |
| 180 | 19.0 (2) | 6.0 (2) | 12.3 (1) | 67.0 (3) | 2.08 (2) | 0.49 (2) | 0.34 (1) |
| 250 | 20.0 (1) | 6.1(2) | 14.0 (1) | 66.3 (2) | 1.99 (2) | 0.44 (2) | 0.39(1) |
| 300 (LNMO-δG) | 20.0 (2) | 9.0 (1) | 9.0 (1) | 66.1 (3) | 2.22 (2) | 1.00 (1) | 0.00 |
| 350 | 20.3 (3) | 8.2 (1) | 5.2 (1) | 61.0 (3) | 1.94 (4) | 1.60 (3) | -0.23 (1) |

**Table 3.2:** Chemical composition and stoichiometry ratio of $La_2Ni_{1-x}Mn_{1+x}O_6$ thin films grown under different oxygen pressures (ranging from 70 to 300 mTorr) at 900°C. Samples were grown using the target prepared by solid state reaction method.

| ***P*O$_2$ (mTorr)** | **La (atom %)** | **Ni (atom %)** | **Mn (atom %)** | **O (atom %)** | **La (per f.u.)** | **Ni:Mn** | **x** |
|---|---|---|---|---|---|---|---|
| 70 | 20.1 (6) | 6.3 (2) | 12.2 (5) | 61.2 (1.1) | 2.18 (7) | 0.52 (3) | 0.32 (2) |
| 100 | 20.0 (4) | 3.9 (2) | 13.3 (1) | 66.3 (6) | 2.37 (4) | 0.30 (2) | 0.54 (1) |
| 120 | 20.3 (1.0) | 5.2 (1) | 14.2 (9) | 59.2 (1.9) | 1.98 (9) | 0.34 (2) | 0.49(1) |
| 140 | 20.0 (2) | 5.1 (1) | 14.0 (2) | 64.1 (4) | 2.08 (3) | 0.36 (1) | 0.47 (1) |
| 220 | 20.1 (2) | 7.1 (4) | 11.2 (1) | 64.3 (2) | 2.19 (2) | 0.63 (1) | 0.23(1) |
| 285 | 20.2 (3) | 9.1 (1) | 9.2 (1) | 59.1 (3) | 2.21(3) | 0.99 (2) | 0.01 (2) |
| 300 | 20.3 (1) | 10.2 (1) | 9.1 (1) | 65.0 (1) | 2.10 (2) | 1.12 (2) | -0.06 (2) |

**Table 3.3:** Chemical composition and stoichiometry ratio of $La_2Ni_{1-x}Mn_{1+x}O_6$ thin films deposited at different growth temperatures (ranging from 500°C to 900°C) at 140 mTorr $O_2$. Samples were grown using the target prepared by sol gel method.

| T(°C) | La (atom %) | Ni (atom %) | Mn (atom %) | O (atom %) | La (per f.u.) | Ni:Mn | x |
|---|---|---|---|---|---|---|---|
| 500 | 13.1 (3) | 10.0 (1) | 10.0 (1) | 67.2 (2) | 1.30 (2) | 1.00 (2) | 0.00 |
| 700 | 17.2 (1) | 8.1 (2) | 12.2 (1) | 65.3 (2) | 1.67 (1) | 0.66 (1) | 0.20 (1) |
| 850 | 19.2 (2) | 6.0 (1) | 14.0 (2) | 67.1 (5) | 1.92 (3) | 0.43 (2) | 0.40 (2) |
| 900 | 20.0 (2) | 5.0 (1) | 14.0 (2) | 65.0 (4) | 2.08 (3) | 0.36 (1) | 0.47(1) |

It can be observed that the film stoichiometry shows a strong dependence on oxygen pressure (Fig. 3.11 (a) and (b)). All films grown at high temperatures (850°C and 900°C) under different oxygen pressures present a La:(Ni+Mn) atomic ratio very near 1 (see black line), while the Ni/Mn ratio (see red line) strongly depends on $PO_2$ used in the growth process. Nevertheless, LNMO samples deposited at low temperatures 500°C and 700°C (Fig. 3.11 (c)) under the same oxygen pressure (140 mTorr $O_2$) show a La:(Ni + Mn) atomic ratio clearly below 1 (see black line), while the Ni/Mn ratio is near 1 (see red line). That indicates that LNMO samples deposited at low growth temperatures ($T \leq 700$°C) have a certain degree of La deficiency (see table 3.3), which has a strong impact on ferromagnetic properties (with $T_C$ < 100 K; see Fig 3.10 (c)). On the other hand, samples grown at high oxygen pressure ($PO_2$ > 200 mTorr) present a Ni/Mn ratio close to 1 (and thus good stoichiometry), while samples grown at low pressures ($PO_2 \leq 180$ mTorr) show a Ni/Mn ratio far from 1 (see table 3.1 and 3.2). Therefore, according to these results, at low pressures samples become Ni-deficient, reaching values of a Ni/Mn ratio of about 0.3 (x ~ 0.54, $La_2Ni_{0.46}Mn_{1.54}O_6$) as shown in Table 3.2. At the same time, it can also be appreciated that samples grown at highest temperatures, i.e., 900°C (Fig. 3.11 (b)), have little effect on the stoichiometry of the films which are still Ni deficient (see table 3.2). In contrast to this remarkable Ni deficiency, samples exhibit excellent FM properties. In particular, the film grown at 850°C under 140 mTorr $O_2$ has good ferromagnetic properties (i.e., Tc ≈240 K and Ms≈5.3 $\mu_B$/fu at 10 K)) with a Ni/Mn ~0.43 (x≈0.40, $La_{1.9}Ni_{0.6}Mn_{1.4}O_6$).

In this regard, it should be remarked that similar results were reported by Blasco et al. [85]. They found a ferromagnetic behavior in Ni-deficient samples with $T_C$ = 200 K and $M_S$ = 2.75 $\mu_B$/f.u. (equivalent to 5.5 $\mu_B$/f.u. in double perovskite notation) for bulk $LaNi_{0.25}Mn_{0.75}O_3$, sintered in oxygen-poor (Ar) atmosphere (see chapter 1, section 1.6.1 for more details). In addition, a very detailed local study of LNMO films grown by molecular beam epitaxy (at very low oxygen pressure) has shown a spontaneous segregation of the stoichiometric $La_2NiMnO_6$ into a $La_2Ni_{1-x}Mn_{1+x}O_6$ (x ≈ 0.2) matrix and NiO inclusions [146]. According to these results, $NiO_x$ segregations at the LNMO film surface will be discussed later (see section 3.3.2).

On the other hand, taking into account the influence of stoichiometry on ferromagnetic properties, we will focus on two characteristic samples prepared at same growth temperature (850°C) but different oxygen pressure: 140 mTorr (LNMO-δD) and 300 mTorr $O_2$ (LNMO-δG). The first sample has good ferromagnetic properties but Ni deficiency, while the second sample has nearly the nominal Ni/Mn=1 stoichiometry but poor ferromagnetic properties (see section 3.2).

## 3.1.4 Transport properties

In order to obtain information on the ohmic regime of the LNMO films, current-voltage (I-V) characteristics were measured at room temperature. Fig. 3.12 (a) shows the I-V characteristics for three LNMO films deposited at 900°C under different oxygen pressures (140, 220 and 300 mTorr).

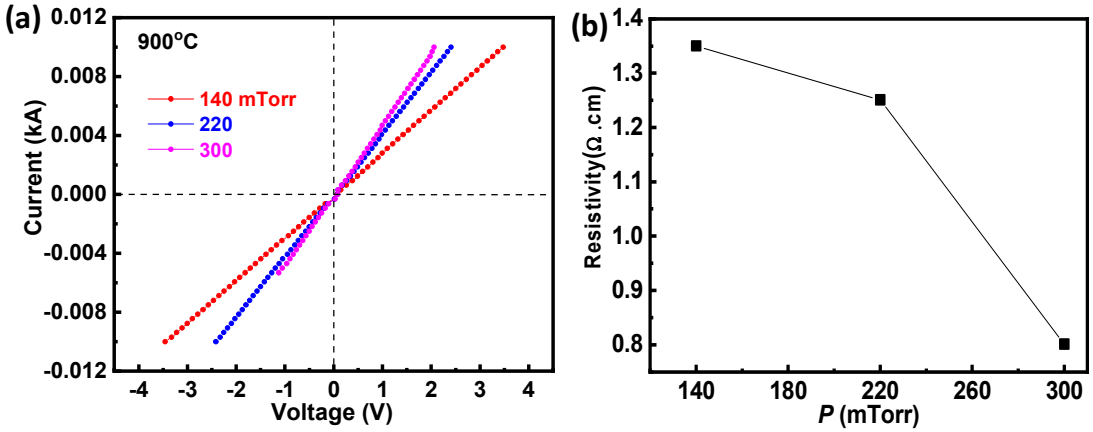


Figure 3.12 (a) I-V characteristics (at RT) of LNMO thin films and (b) RT-resistivity as a function of oxygen pressure for the same films.

From the linear shape of the I-Vcharacteristics, one can deduce an ohmic behavior (with the probed voltage range) for all samples. It can be appreciated in Fig 3.12 (b) that the film resistivity decreases slightly when increasing the oxygen pressure. A value of $\rho$ = 1.4 Ω.cm was obtained for the sample grown at 140 mTorr $O_2$, while for the samples deposited at 220 and 300 mTorr $O_2$ the $\rho$ values were found to be ~1.3 Ω.cm and 0.8 Ω.cm, respectively.

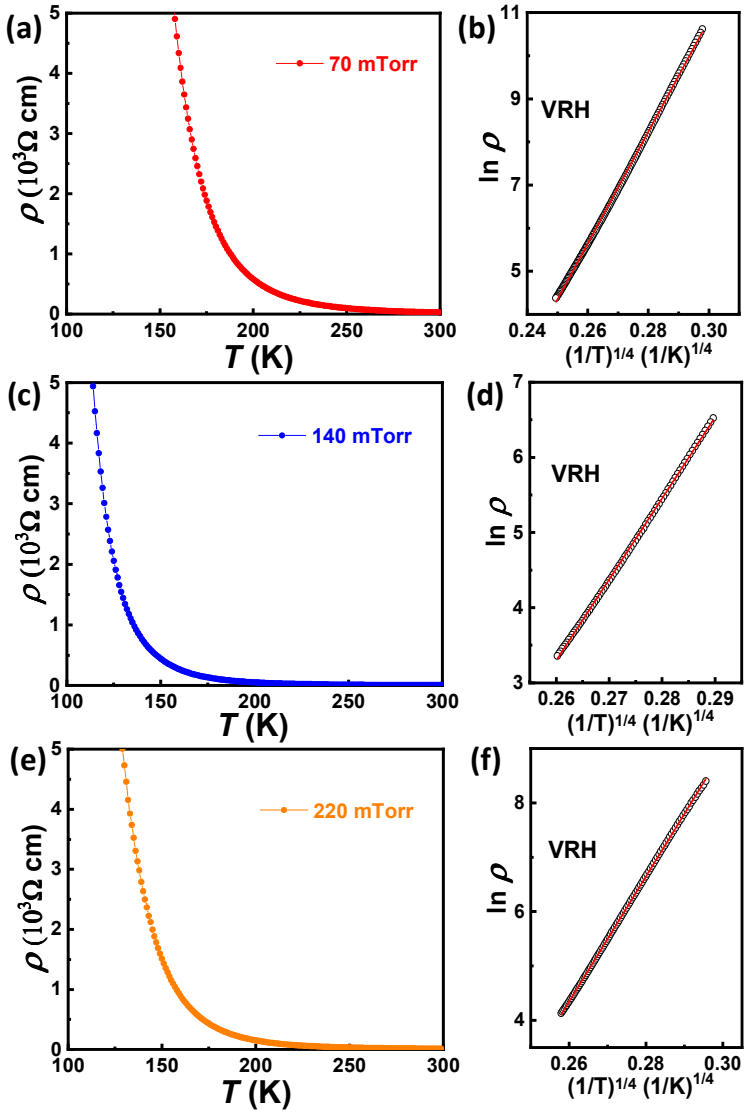


Figure 3.13 [(a),(c)-(e)] Temperature-dependent resistivity of LNMO thin films grown/annealed at 900°C and at an oxygen pressure of 70, 140 and 220 mTorr, under zero magnetic field. [(b),(d)-(f)] Corresponding ln $\rho$ *vs.* $(1/T)^{1/4}$ plot. The red line represents the fitting of the experimental data.

LNMO films, with their potential applications in spintronic devices such as magnetodielectric capacitors and spin filtering tunnel junctions [1] [19] [144] [192] require an insulating behavior. Therefore, the transport properties were measured as a function of temperature. Fig 3.13 depicts the resistivity as a function of temperature of LNMO films grown/annealed at 900°C under different oxygen pressures (70, 140 and 220 mTorr $O_2$). The temperature-dependent resistivity $\rho$(T) measured under zero magnetic field shows that resistivity increases with decreasing temperature without any anomaly near the magnetic ordering temperature [195] [1], indicating an insulating behavior over the whole temperature range measured (100 K ≤ T ≤ 300 K) in all films (see Fig 3.13 [(a),(c)-(e)]). At lower temperatures (T < 100 K), the

high resistance of the films did not allow a reliable measurement. On the other hand, the temperature dependence can be well described by a three-dimensional (3D) variable-range hopping (VRH) model:

$$\rho(T) = \rho_0 \, exp \, (T_0/T)^{1/4} \tag{3.1}$$

where $\rho_0$ is the pre-factor and $T_0$ is the characteristic hopping temperature, related to the electron hopping probability $P$ of the material, i.e., $T_0 \, \alpha \, 1/P$ [196] [195]. The 3D VRH fitting can be directly appreciated in the Fig 3.13 [(b),(d)-(f)] where the ln $\rho$ versus $(1/T)^{1/4}$ plots are shown, with values of fitting parameter $T_0$ such as: $T_0 \approx 2.8 \times 10^8$ K (for 70 mTorr) $T_0 \approx 1.4 \times 10^8$ K (for 140 mTorr) and $T_0 \approx 1.6 \times 10^8$ K (for 220 mTorr). These values are found to be similar to those of $La_2NiMnO_6$ [36], and other transition metal oxides [197]showing similar behaviour.

Finally, it should be noted that the dependence of $\rho$(T) at high temperature does not allow to rule out the thermal activation mechanisms, described by Arrhenius law [198] [199] $\rho(T) = \rho_0^{'} \exp(E_0/K_B T)$, where $\rho_0^{'}$ is a constant, $E_0$ is the required activation energy for the conduction process and $K_B$ is the Boltzmann constant. The extracted values of the activation energy $E_0$ were found to be very similar for the three LNMO samples ($E_0 \approx 0.3 \pm 0.1$ eV), and close to the energy required to transfer an electron from $Ni^{2+}$ to $Mn^{4+}$ [28] [200]. These values are comparable to that reported in $La_2NiMnO_6$ [200] [195], $La_2MRuO_6$ (M = Mg; Co; Ni and Zn ; $E_0 \sim 0.07$-$0.17$ eV) [201] and RNMO compounds [73]

## 3.1.5. Influence of thickness on magnetic properties

In order to explore the dependence of thickness on the magnetic properties, LNMO films of different thickness (t) have been deposited onto STO (001) substrates and their magnetic properties were measured. Samples were grown at 850°C under 140 mTorr $O_2$ varying the deposition time of the film (i.e., 60, 30, 15 and 5 min). After film deposition, as-grown samples were annealed (in-situ) at the same growth temperature (1h under 420 Torr $O_2$). These samples were grown using a target prepared by solid-state reaction method (see chapter 2, section 2.1.1).

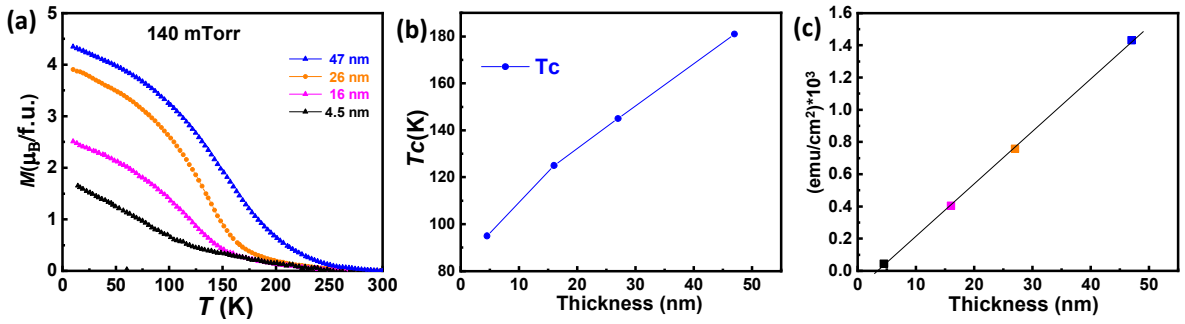


Figure 3.14 (a) In-plane magnetization of LNMO/STO thin films of different thickness as a function of temperature under $\mu_0 H$ = 0.5 T. (b) Curie temperature $T_C$ of the same samples as a function of thickness. (c) Magnetization (emu/cm$^2$)*10$^3$ at 60K as a function of thickness.

In-plane magnetization as a function of temperature under an applied magnetic field of 5 kOe of LNMO thin films of different thicknesses are shown in Fig 3.14 (a). It can be appreciated that the magnetization (Fig. 3.14 (a) and (c)) and the Curie temperature $T_C$ (Fig. 3.14 (b)) reach lower values as the film thickness decreases. Therefore, a notable degradation of the magnetic properties takes place as the film becomes thinner. In fact, the absence of a ferromagnetic character has been reported in ultrathin films (t < 4 nm) [202] [203] [204].This can be attributed, as a first approximation, to the existence of an interface dead layer that modifies the magnetic and structural properties. Some factors that contribute to a dead layer effect on very thin films could be: a chemically and/or structurally altered film-substrate interface, as well as a discontinuous film coverage over the substrate surface during the initial film growth [205]. Fig. 3.14 (c) depicts the magnetization (emu/cm$^2$)*10$^3$ at 60K as a function of thickness. In this figure, by extrapolation to zero, the thickness of the dead layer was found to be ~3.7 nm. The origin of the dead layer has been fewly explored in LNMO compounds. Nevertheless, in perovskite systems, scanning tunneling spectroscopy [206] and magnetic-resonance measurements [207] [208] have shown that the existence of a dead layer in highly strained thin films is connected to a phase separation phenomenon at the interface or to the presence of structural inhomogeneities localized at the interface between film and substrate [209] [210] [211].

On the other hand, previous results of RMSs around (103) reflection of LNMO films grown on STO substrates (tensile strain), with similar thicknesses around t ~ 40-48 nm, have confirmed that LNMO films are fully strained. The in-plane pseudocubic cell parameter of LNMO films mimics that of the STO substrate ($a_{STO}$= 3.905Å) (see section 3.2.1 and 3.3.2.2 for more details). Reports on the film thickness dependence of lattice parameters have shown that the lattice parameters for the thinnest films present in-plane values near or equal to those of the substrates and that a lattice relaxation takes place when the film thickness increases [202] [212] [213] [214]. Thus, our LNMO films seem to be fully strained and do not experience in-plane relaxation up to a thickness of t ~ 50 nm. On the other hand, the out-of-plane lattice parameters remain elongated with respect to LNMO bulk value of 3.876Å [41]

(see section 3.3.2.2), in contrast to the expected contraction of out-of-plane lattice parameter due to tensile strain. As a result, a higher unit cell volume arises in the perovskite structure of our LNMO films, suggesting the presence of oxygen deficiency and $Mn^{3+}$ ions which could lead to the degradation of the magnetic properties. In this regard, the degradation of magnetization and $T_C$ for thinner films could be associated with the formation of antisite disorders, oxygen defect, cationic vacancies and/or inhomogeneities in the film, which disrupts the ferromagnetic long-range order of the B-sites and results in a reduction of the magnetic properties [19] [123] [41].

# 3.2 Influence of stoichiometry on ferromagnetic properties

Growth conditions, such as temperature, annealing and oxygen partial pressure, have been optimized in order to obtain LNMO thin films with good ferromagnetic properties. Nevertheless, it is found that good stoichiometric samples always exhibit values of *T*c and *M*s far from the optimum ones. In contrast, samples with a remarkable Ni deficiency show excellent magnetic properties. In this section, we report a detailed study on the structure, microstructure and magnetic properties of two characteristic types of samples: a non-stoichiometric sample with good ferromagnetic properties (high $T_C$) and a stoichiometric sample with poor ferromagnetic properties (low $T_C$); whose stoichiometric analysis by EPMA was studied above (see sections 3.1.2 and 3.1.3). At the same time, to understand the ferromagnetic character in Ni-deficient samples, the analysis of the valence states of Ni and Mn ions was carried out by X-ray absorption spectroscopy (XAS) and X-ray magnetic circular dichroism (XMCD) measurements. More specifically, the first sample chosen was grown at 140 mTorr $O_2$ (high Tc) with a Ni/Mn ~ 0.43 ($x \approx 0.4$, $La_{1.9}Ni_{0.6}Mn_{1.4}O_{6.0}$) labeled as LNMO-δD, while the second sample was grown under 300 mTorr $O_2$ (low Tc) with a Ni/Mn ~1.0 ($x \approx 0.0$, $La_{2.0}Ni_{0.9}Mn_{0.9}O_{6.0}$) labeled as LNMO-δG, respectively.

## 3.2.1 Structural properties

XRR curves of non-stoichiometric (LNMO-δD) and stoichiometric (LNMO-δG) samples are depicted in Figs. 3.15 (a) and (b), which correspond to the highest and lowest $T_C$ obtained, the fitting to these data (black lines) has been done using XRay utilities library [215]. Thickness values found for both samples are very similar (42 and 44 nm). The root mean square (rms)

value of surface roughness for these two samples was found to be very small, about of 0.2 nm and steps height of about 0.4 nm, corresponding to the perovskite unit cell (see Fig. 3.2).

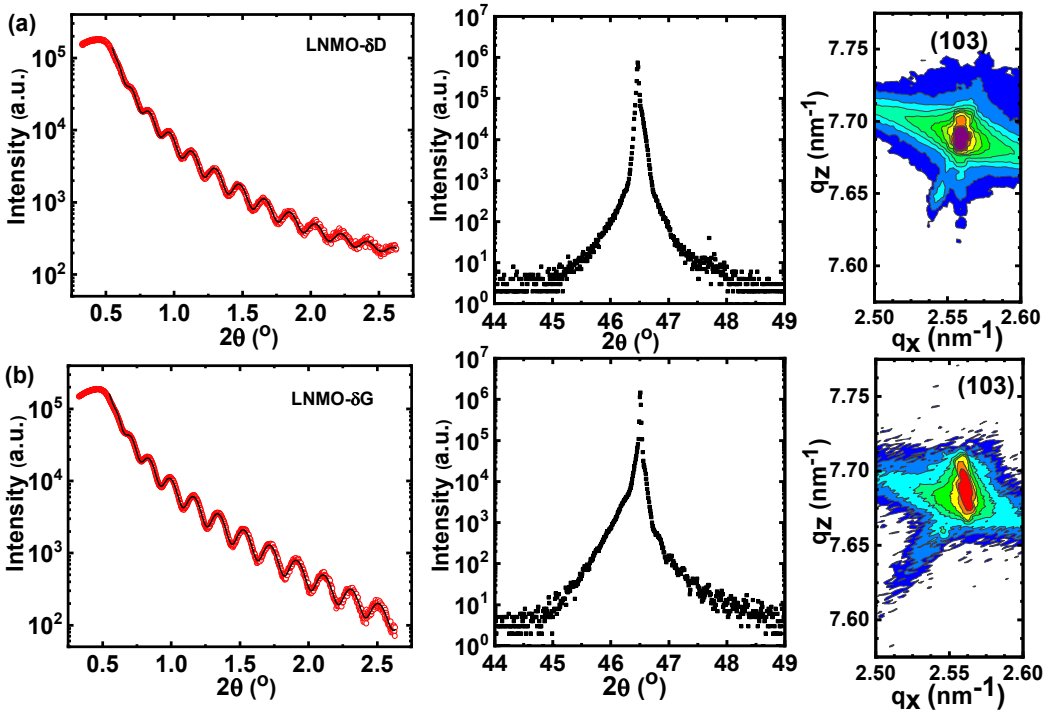


Figure 3.15. XRR data (left), high resolution θ/2θ XRD scans of the (002) reflections (middle) and RSM around (103) reflections (right) for: (a) LNMO-δD (140 mTorr $O_2$) and (b) LNMO-δG (300 mTorr $O_2$) thin films grown on STO (001) substrate, with thickness values of 42 and 44 nm.

In addition, structural properties have been investigated by high resolution θ/2θ X-ray diffraction (XRD), Figs. 3.15 (middle), show scans around $(002)_{STO}$ reflection using Cu-$K_{\alpha 1}$ monochromatic radiation of LNMO-δD and LNMO-δG samples, respectively. From these θ/2θ XRD scans the corresponding out-of-plane lattice parameters are determined: $c$=3.895Å for LNMO-δD and $c$=3.908Å LNMO-δG, which are slightly higher than the pseudocubic perovskite lattice parameter of bulk LNMO, namely 3.876 Å [41] and this difference may be caused by the presence of $Mn^{3+}$. It is also worth mentioning here that Laue fringes can only be seen in LNMO-δG sample but not in LNMO-δD one, indicating good crystalline quality as corroborated by HRTEM measurements (see below). Reciprocal space maps, around $(103)_{STO}$ reflection of the same samples are shown in Figs. 3.15 (right). Measures evidence that the films grown fully strained. In fact, for LNMO-δD sample, a small peak coming from the LNMO film can be seen just above the substrate peak. For LNMO-δG sample, both peaks are fully overlapped due to the high similarity between the out of plane lattice parameters.

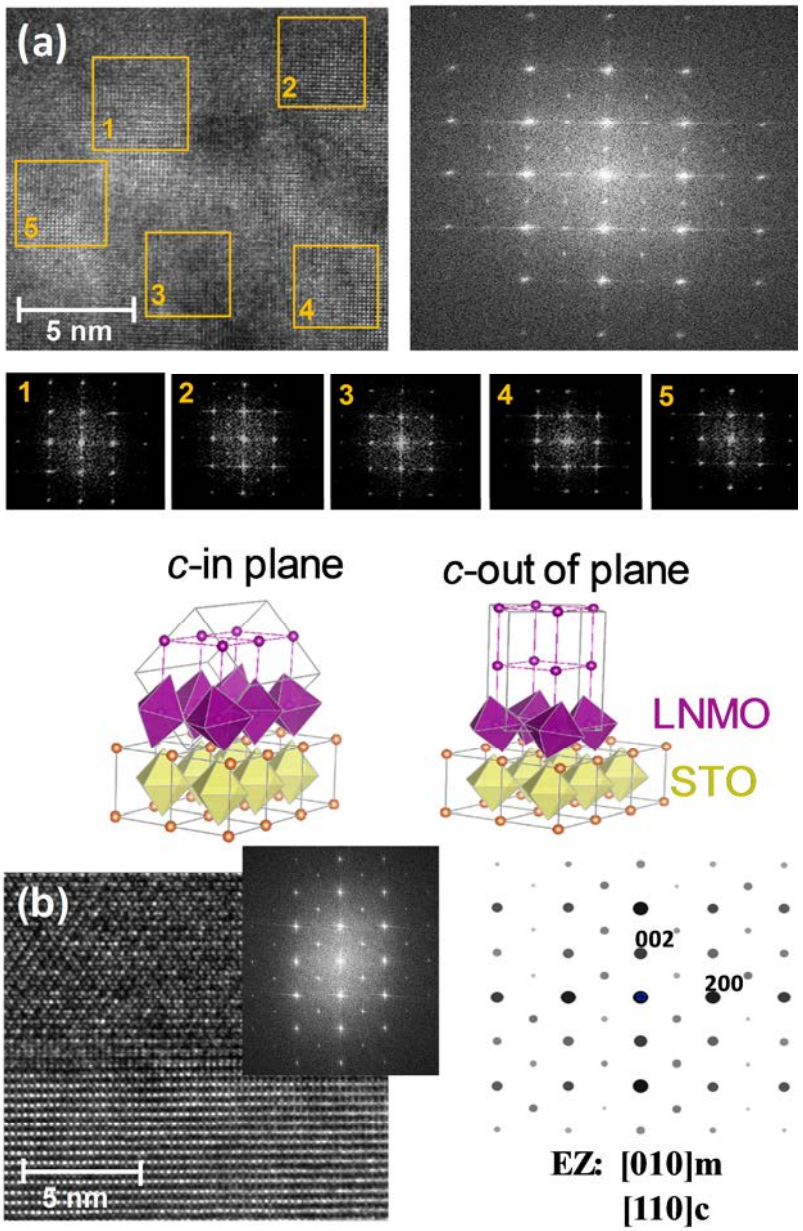


Figure.3.16 (a) Cross-section HRTEM image of the LNMO-δD (140 mTorr) film viewed along the STO [100] zone axis and corresponding Fourier filtered image emphasizing the strain state of the film and the coexistence of nanodomains with different orientations. Bottom panels show, from left to right, an FFT of the whole image exhibiting superlattice spots at (0 0 l/2), (0 k/2 l/2), and (0 k/2 0) (indexed according to STO orientation), and FFT patterns obtained from windows 1, 2 and 3, respectively, revealing the orientations of different nanodomains: In 1 the c-axis of the film is in-plane and parallel to the image, in 2 the c-axis is in-plane and perpendicular to the image, and in 3 it is oriented out-of-plane. In 1, 2, and 3, peaks and zone axes are referred to the pseudocubic unit cell of LNMO. (b) Schematic models for the observed epitaxial relationships. (c) Cross-section HRTEM image and corresponding FFT pattern of the LNMO-δG (300 mTorr) film viewed along the [110] zone axis, exhibiting high crystalline quality and an in-plane orientation of the monoclinic $c_{LNMO}$ axis. The encircled spot corresponds to the (h/2 h/2 −l/2) superlattice. Indices are referred to the pseudocubic unit cell of LNMO.

A deeper insight into the microstructural features can be obtained by using high resolution transmission electron microscopy (HRTEM) (see Figs. 3.16 (a), (b)). For HRTEM observations in Fig. 3.16 (a) sample LNMO-δD was cut along the (100) direction of STO. HRTEM images show the coexistence of domains with different orientations as can be appreciated in the Fourier transform (FT) of the image. The FT of a large area shows different spots corresponding to the enlargement of the LNMO lattice with respect to STO (LNMO cell parameters are of the type $a \approx b \approx \sqrt{2}a_p$, $c \approx 2a_p$ where $a_p$ is the primitive perovskite cell parameter). These spots can be indexed as (0 k/2 l ) (k odd), (0 k l/2) (l odd) and (0 k/2 l/2) (k and l odd) and indicate different orientations of the LNMO cell in the film. This is better illustrated by FT of small regions. For some regions only spots corresponding to (0 k/2 l) (k odd) are found thus in those regions $c_{LNMO}$ is parallel to (010)-STO substrate direction; in other zones only spots of the type (0 k l/2) (l odd) can be seen, which correspond to $c_{LNMO}$ parallel to (001)-STO; and finally a third type of regions where spots of the type (0 k/2 l/2) (k and l odd) are present corresponds to $c_{LNMO}$ parallel to (100)-STO. Indices are referred to the pseudocubic unit cell of LNMO. On the other hand, in Fig. 3.16 (b) sample LNMO-δG was cut along (110)-STO direction. In this case, the sample is more homogenous and only one type of spots corresponding to the larger cell of LNMO are observed and superstructure spots are indexed as (h/2 -h/2 l/2) (h and l odd). This indicates that the orientation of $c_{LNMO}$ axis is parallel to (100) or (010) (in the plane of the film). Therefore, HRTEM observations confirm that domains with in-plane and out-of-plane orientations of $c_{LNMO}$ coexist in LNMO-δD sample, while only in-plane orientation of $c_{LNMO}$ is stabilized for LNMO-δG sample. This multiple orientations of c-axis in LNMO-δD must be related to the absence of Laue fringes in the θ/2θ scans, as previously mentioned.

## 3.2.2 Magnetic properties

The ferromagnetic character of non-stoichiometric (LNMO-δD) and stoichiometric (LNMO-δG) samples has been studied in detail. In this regard, zero field cooling-field cooling (ZFC-FC) magnetization curves of both, LNMO-δD and LNMO-δG, samples measured using a field of H≈ 0.1T, are depicted in Fig. 3.17 (a). This figure evidences the strong dependence of the magnetic behaviour on the oxygen pressure during the growth process. M(T) curves of LNMO-δG sample do not show evidences of ferromagnetic ordering. At lower temperatures a small magnetic character can be observed, since the ZFC-FC curves are separated by a very small magnetic moment. On the other hand, M(T) curves of LNMO-δD display the expected temperature dependence of a FM with no signal of double transition, and a Curie temperature of about 240K. Here, the ZFC-FC curves are 1 kOe apart, which is indicative of a strong hysteresis loop. Therefore, to study this behavior in more detail, M(H) measurements were carried out at low temperature.

The field dependence of the magnetization, *M(H),* after correcting the diamagnetic contribution from substrate and other instrumental contributions [216] is shown in Fig.3.17 (b). *M(H)* loops corresponding to sample LNMO-δD at T=10 K exhibit the expected hysteretic behaviour with a coercive field of about 1.4 kOe and 1.2 kOe for the field applied in-plane (IP) and out-of-plane (OP) configurations respectively. Accordingly, magnetization remanence for the IP configuration ($M_r$ ~3.1$\mu_B$/f.u) is larger than that found for the OP ($M_r$~1.7$\mu_B$/f.u). On the other hand, according to Fig. 3.17 (b) the easy magnetization direction lies in the film plane. Although this is the usual behaviour in thin films since shape anisotropy tends to place magnetization in plane, the large remanence and coercive field of the out-of-plane magnetization curve cannot be understood by considering only shape anisotropy and indicates that magnetocrystalline anisotropy also plays an important role. Furthermore, HRTEM characterization has shown that domains with different crystallographic orientations coexist. Consequently, magnetocrystalline anisotropy would contribute to both in-plane and out-of-plane directions, in accordance with the observed behaviour.

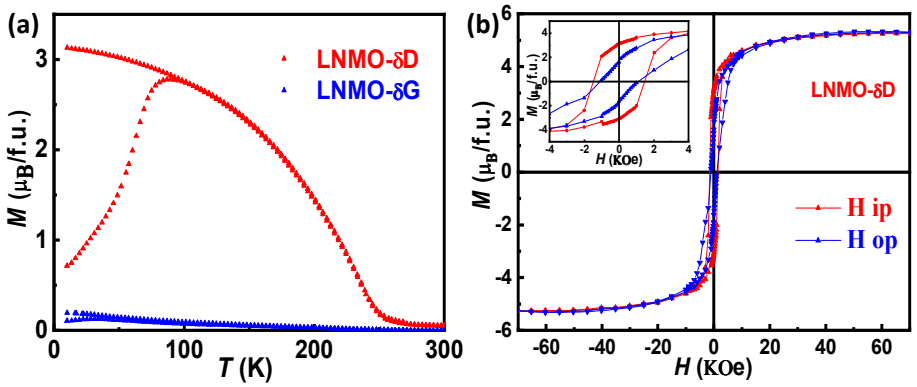


Figure 3.17 (a) Magnetization measured after ZFC and FC as a function of temperature under an applied field of 1 kOe (in the plane of the film) of LNMO-δD (140 mTorr $O_2$, red curve) and LNMO-δG (300 mTorr $O_2$, blue curve). (b) M(H) hysteresis loops of LNMO-δD at 10 K for H applied in-plane and out-of-plane, the inset shows in detail the low field region.

On the other hand, a saturation magnetization of $M_s$~5.3$\mu_B$/f.u, is found, i.e. somewhat larger than the expected theoretical value (~5$\mu_B$/f.u.) for perfectly ordered stoichiometric $La_2Ni^{2+}Mn^{4+}O_6$ [1] and also larger than the experimental bulk value (~4.96$\mu_B$/f.u.). At this point it is worth mentioning that non-stoichiometry enhances the maximum value achievable for the magnetization for full FM ordering. For the stoichiometry (Ni/Mn ratio) found in our case $M_s$ should be around 5.9 $\mu_B$/f.u., as 2 $\mu_B$/Ni (x 0.57 Ni/f.u.) are attributed to $Ni^{2+}$ and 3.30 $\mu_B$/Mn (x 1.43 Mn/f.u. ) to $Mn^{3.66+}$ (as a fraction of $Mn^{4+}$ must reduce to $Mn^{3+}$ to compensate Ni deficiency).

### 3.2.3 Transport properties

The temperature and field-dependence of the resistivity of the LNMO-δD film under 0 and 9 T magnetic field is plotted in Fig. 3.18 (a).The measurements show that the resistivity values increase when cooling, thus exhibiting insulating behaviour in the whole temperature range. At lower temperatures about T < 220 K, R(T) curves did not show any signal due to their high resistance below this region. Almost no magnetic field dependence of the resistivity is detected even when crossing $T_C$ (~240K).

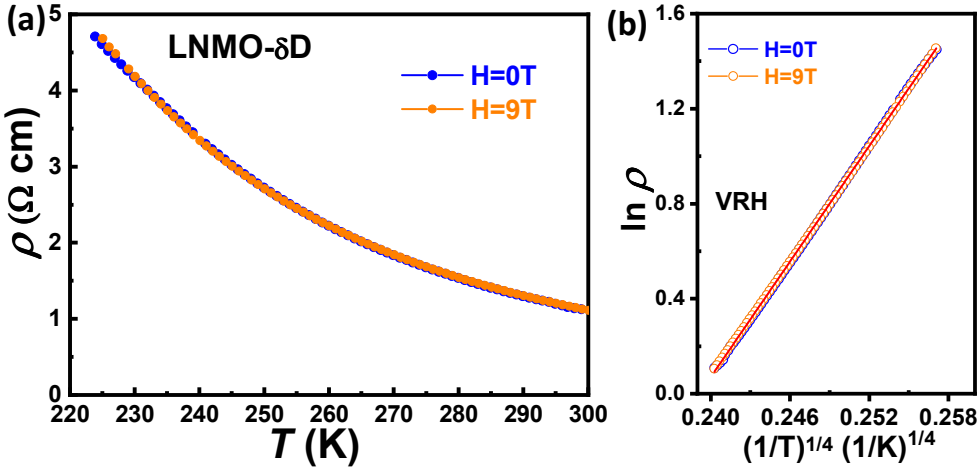


Figure 3.18 (a) Temperature dependent resistivity of LNMO-δD thin film under zero and 9T magnetic field, (b) Plot of ln $\rho$ *vs.* $(1/T)^{1/4}$. The red line represents the fitting of the experimental data.

On the other hand, by using a three-dimensional (3D) variable-range hopping (VRH) as described in the equation (3.1) in section 3.1.4, the 3-D VRH fitting can be directly seen in the plot of ln $\rho$ versus $(1/T)^{1/4}$ as shown in Fig. 3.18(b). Therefore, it can be appreciated that by decreasing the temperature below $T_C$ (~ 240K) a linear evolution of the resistance is observed without variation with the magnetic field (see fitting red line). The slope of the curve corresponds to $T_0^{1/4}$, in this case, we have obtained a value of $T_0 \approx 0.4 \times 10^8$ K which is similar to the values reported for other transition metal oxides [197] [200].

## 3.2.4 X-ray absorption spectroscopy (XAS)

As mentioned in chapter 1, the FM character of $La_2NiMnO_6$ is understood in terms of the superexchange interactions between $Ni^{2+}$ and $Mn^{4+}$ according to the Goodenough-Kanamori rules. Nevertheless, the large Ni deficiency found in LNMO-δD sample puts a question mark over this interpretation. To determine the valence states of Ni and Mn ions in Ni-deficient samples X-ray absorption spectroscopy (XAS) and X-ray magnetic circular dichroism (XMCD) measurements were carried out at Ni $L_{2,3}$ and Mn $L_{2,3}$ edges in LNMO-δD (x≈0.40) sample. The Mn- $L_{2,3}$ spectra were measured in both the total electron yield (TEY) and total fluorescence yield (TFY) modes, while the Ni- $L_{2,3}$ spectra were measured by the total electron yield (TEY) mode at two different temperatures 20 and 300K, under ultrahigh vacuum conditions ($2 \cdot 10^{-10}$ mbar). The applied magnetic field (parallel to the X-ray beam) was 4T. As explained in appendix (see section A.7), the total electron yield (TEY) mode is a technique extremely surface-sensitive of the sample with a probing depth of 2-5 nm. This method does not suffer from the "selfabsorption" effects as it happens for the fluorescence mode. The total fluorescence yield (TFY) mode is mainly sensitive to an inner region of the sample with a large probing depth (> 1000Å in the soft x-ray region), thus is particularly suitable for studying bulk electronic structures. However, TFY measurements in thin films suffer from the "selfabsorption" effects, thus it is important to apply correction procedures to the spectra to recover the real signal of absorption coefficient [217].

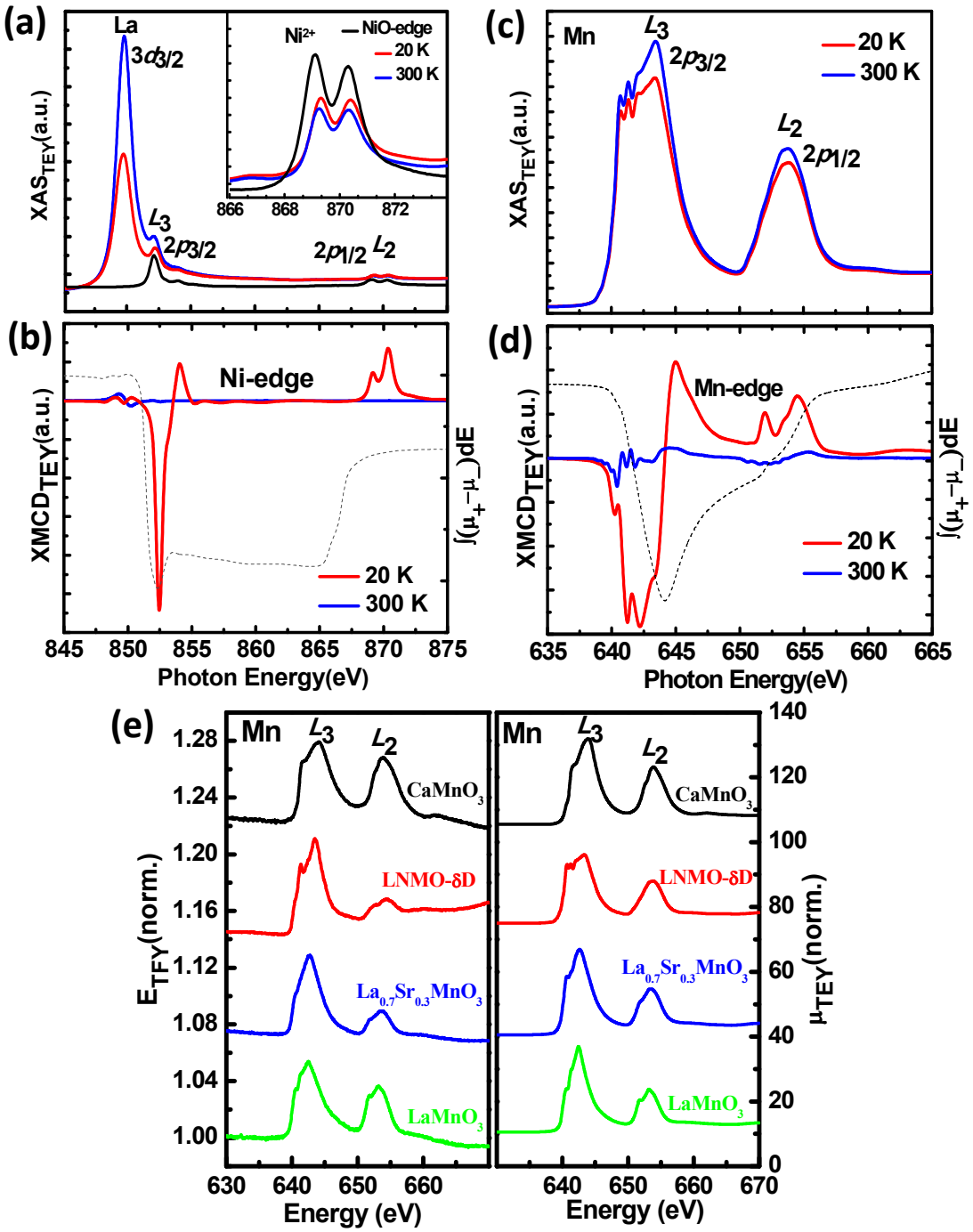


Figure 3.19. XAS spectra for an epitaxial LNMO-δD thin film. (a) Ni $L_{2,3}$ and (c) Mn $L_{2,3,}$ the inset shows the Ni $2p_{1/2}$ absorption peak, absorption spectrum of NiO is also plotted for comparison (black curve). XMCD of (b) Ni $L_{2,3}$ and (d) Mn $L_{2,3}$, measured at 20K (red curves) and room temperature (RT) (blue curves); the dashed line shows the corresponding integral at 20K (right axis, note that dashed lines start at zero value). (e) Absorption-corrected FY (left) and TEY(right) Mn $L_{2,3}$ XAS edge of LNMO-δD film compared with reference spectra such as: $LaMnO_3$, LSMO and $CaMnO_3$ at 300K respectively.

The $L_{2,3}$ ($2p \rightarrow 3d$ transition) XAS spectra, measured by using the TEY technique, corresponding to Ni and Mn are shown in Fig. 3.19 (a) and (c). The features of the Ni- $L_{2,3}$ spectra correspond to transitions of the form $2p^6 3d^n \rightarrow 2p^5 3d^{n+1}$ which splits the spectrum in two main Ni $2p$ peaks XAS, that represent the $2p_{3/2} \rightarrow 3d$, $L_3$ edge ($h\upsilon \approx$ 850-855 eV ) and $2p_{1/2} \rightarrow 3d$, $L_2$ edge ($h\upsilon \approx$ 865-875 eV) transitions, separated by the spin-orbit splitting of the $2p$ core level [83]. The line shape of the spectra depends strongly on the multiplet structure given by the Ni $3d$-$3d$ and $2p$-$3d$ Coulomb and exchange interactions, as well as the local crystal field effects generated by O $2p$ ligands and the hybridization with them [83].

In results, the Ni $L_3$ edge (see Fig. 3.19 (a)) is overlapped with the La $M$ ($3d_{3/2} \rightarrow 4f$) absorption peak and is hard to analyze. In contrast, the Ni $L_2$ edge ($\hbar\upsilon \approx$ 865-875 eV) absorption peak (shown in the inset) can be easily compared with that of NiO ($Ni^{2+}$) also shown in the inset. All three edges present a double peak feature that is quite similar to all Ni-divalent compounds, and is well understood in terms of a covalent ground state of mainly $Ni^{2+}$ ($3d^8$) character plus an anion-dependent fraction of the $3d^9\underline{L}$ and $3d^{10}\,\underline{L}$ configurations, where $\underline{L}$ stands for an anion (ligand) hole [218]. This double peak is also displayed by $L_2$ edge of a stoichiometric (and with almost full cationic ordering) sample of $La_2NiMnO_6$, and very different from the $L_2$ peak of $PrNiO_3$ and $NdNiO_3$ corresponding to ($Ni^{3+}$) [83] [127]. Therefore, we can concluded that the oxidation states of Ni ions in our Ni-deficient sample is 2+. It is worth mentioning that a XANES study in a bulk sample of $LaNi_{1-x}Mn_xO_3$ has concluded that for $x \geq 0.5$ the valence of Ni stabilizes to 2+ [83].

In order to determine the valence of Mn, we have also measured the $L_{2,3}$ edges of reference samples $LaMnO_3$ ($Mn^{3+}$), $La_{0.7}Sr_{0.3}MnO_3$ ($Mn^{3.3+}$) and $CaMnO_3$ ($Mn^{4+}$). Spectra measured in both TEY and FY detection modes at room temperature are compared in Fig. 3.19 (e). The features of the Mn- $L_{2,3}$ spectra correspond to transitions of the form $2p^6 3d^n \rightarrow 2p^5 3d^{n+1}$ which splits the spectrum in two main Mn $2p$ peaks XAS, that represent the $2p_{3/2} \rightarrow 3d$, $L_3$ edge ($h\upsilon \approx$ 641-645 eV ) and $2p_{1/2} \rightarrow 3d$, $L_2$ edge ($h\upsilon \approx$ 652-656 eV) transitions, separated by the spin-orbit splitting of the $2p$ core level [83]. In Fig. 3.19 (e) a shift of the Mn $L_3$ peak toward higher energies for all XAS spectra in the series of samples is detected. By comparing $L_3$ absorption peaks of $LaMnO_3$ at 642.5eV ($Mn^{3+}$) and $CaMnO_3$ located at 644.1 eV ($Mn^{4+}$), with that of LNMO-δD centered between both compounds at 643.5 eV, the valence of the latter can be estimated to be around +3.6. Therefore, assuming a 2+ valence for Ni, and recovering sample stoichiometry values determined by EPMA, a mixed-valence of 3.64+ is obtained for Mn. Thus, XAS measurements lead us to conclude that Ni-deficient samples (LNMO-δD) contain a certain quantity of $Mn^{3+}$ and therefore, Mn must be in a mixed-valence $Mn^{3+}/Mn^{4+}$ oxidation state. For that reason, since $Mn^{3+}$ ions have a larger magnetic moment that $Mn^{4+}$ ones, larger values of the saturation magnetization might be observed in Ni-deficient samples.

On the other hand, X-ray magnetic circular dichroism (XMCD) has been used to investigate the specific magnetic properties of Ni and Mn ions in the LNMO-δD sample. All the XMCD spectra (see Figs. 3.19 (b) and (d)) have been normalized to the integrated area of the corresponding XAS spectra [113]. These spectra were measured by TEY method at 20K and

300K. It is found that $L_3$ absorption peak show a strong negative XMCD signal at both Ni and the Mn edges (at 20K), which indicate that the $Ni^{2+}$ and $Mn^{3.6+}$ ions are aligned ferromagnetically. XMCD signal nearly disappears at room temperature (above $T_C$).

Finally, in order to extract quantitative information about orbital magnetic moment $\mu_{orb}$ and spin magnetic moment $\mu_{spin}$ contributions to the magnetic moment of Ni 3*d* and Mn 3*d* states, we apply the so-called sum-rules in the XMCD spectra, assuming that the border between the $2p_{3/2}$ and $2p_{1/2}$ regions is 865 eV for the Ni *L* edge and 650 eV for the Mn *L* edge and neglecting the contribution of the magnetic dipole operator <Tz> [83] [219] [220]. In this regard, the corresponding integral of the XMCD signal is also depicted in Figs 3.19 (b) and (d) (see dashed black line). Therefore, using the equations in appendix (see section A.7.2) in the case of Mn ions from the integral of XMCD signal it is found that $\mu_L^{Mn} \approx 0$. In contrast we obtained $\mu_L^{Ni}/\mu_S^{Ni} = 0.32$ at 20K for Ni. Thus, XMCD study reveals that orbital moment of Ni is not quenched. Worth to mention that this orbital contribution is necessary for spin-orbit interactions giving rise to magnetocrystalline anisotropy, and reinforces the interpretation that this must be the origin of the magnetic anisotropy evidenced in Fig. 3.17 (b).

In summary, assuming that FM ordering in LNMO systems comes from superexchange interactions between $Ni^{2+}$ and $Mn^{4+}$, the values of Tc and Ms obtained for stoichiometric samples clearly indicate that Ni/Mn cationic ordering in the B-sublattice is absent in the LNMO-δG sample and there is practically no magnetic signal. On the other hand, XAS measurements allow concluding that Ni ions are stabilized as $Ni^{2+}$ even in nonstoichiometric samples, while Mn ions are in a mixed-valence $Mn^{3+}$-$^{4+}$ state with an effective valence of +3.6. Nevertheless, samples exhibit insulating behavior, and therefore double-exchange interaction cannot be invoked to explain the observed FM ordering. In this regard, to explain the excellent magnetic properties found in Ni-deficient samples some kind of cationic ordering between $Ni^{2+}$, $Mn^{3+}$, and $Mn^{4+}$ in the B sublattice has to be assumed, and thus, the question of whether a Ni deficiency can favor Ni/Mn ordering arises.

# 3.3. Nanostructure formation on LNMO film surface

In this section, structural and magnetic properties of non-stoichiometric $La_2Ni_{1-x}Mn_{1+x}O_6$ thin films, prepared at high temperature (T = 800-900 $^oC$) and low oxygen pressure ($P_{O2}$ = 130-150 mTorr), are studied as a function of annealing conditions. Independently to the growth conditions used, the surface morphology (studied by Scanning Electron Microscopy, SEM) shows the formation of the crystalline organic polymer (OP) islands, randomly distributed over the film surface. The modification of the manganese valence state due to the presence of organic polymer islands is studied by means of X-ray photoemission microscopy (X-PEEM).

On the other side, high temperature annealing treatment (T = 800-900$^{o}$C), typically used to improve magnetic properties, promotes the spontaneous formation of nanometric ($NiO_x$) cubes, as previously reported [146].

## 3.3.1 $Mn^{2+}$ Formation

By studying the surface morphology of the samples by SEM, the formation of organic nanostructures with fractal-like geometry has been observed over LNMO surface. These nanostructures have been observed in LNMO samples independently of the growth conditions using a $La_2NiMnO_6$ target prepared by sol-gel method (see chapter 2, section 2.1.1.2).

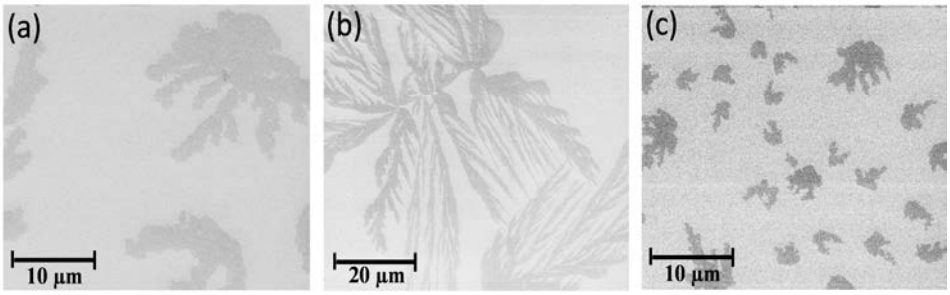


Figure 3.20 SEM micrographs of LNMO/STO thin films grown at a growth temperature of 850$^{o}$C at different oxygen pressures: (a) 140 mTorr, (b) 250 mTorr and (c) 300 mTorr; with in-situ annealing at 850$^{o}$C (1h under 420 Torr $O_2$)

Fig. 3.20 shows SEM images of LNMO samples grown on STO (001) substrates at a growth temperature of 850$^{o}$C under different oxygen pressures (ranging from 140 to 300 mTorr). After film deposition, as-grown samples were in-situ annealed at 850$^{o}$C (1h under 420 Torr $O_2$) to optimize the film magnetic properties. These SEM images show the formation of organic nanostructures with fractal-like geometry (dark areas) over the film surface, irrespectively of the growth conditions.

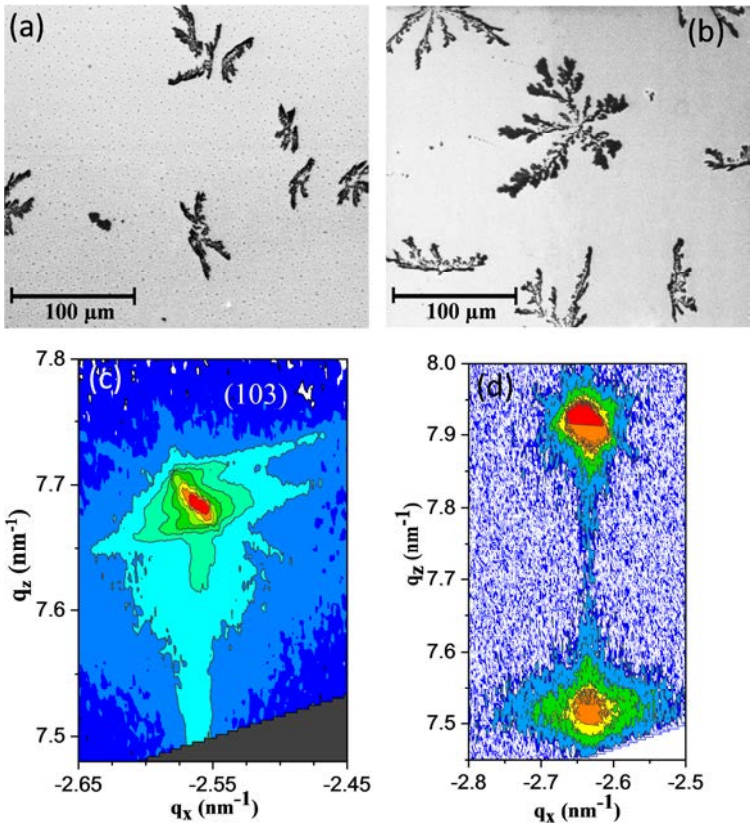


Figure 3.21 SEM micrographs of organic nanostructures with a magnification of 400x over $La_2Ni_{0.57}Mn_{1.43}O_6$ films grown on the surface of (a) $SrTiO_3$ (001) and (b) $LaAlO_3$ (001) substrates. The panels (c) and (d) show RSM around (103) reflection for the corresponding thin films.

Fig. 3.21 shows the formation of nanostructured islands with dendritic morphologies over of LNMO thin films growth on $SrTiO_3$ (a) and $LaAlO_3$ (b) substrates. Samples were grown/annealed at 850$^o$C under oxygen partial pressure of 140 mTorr for 1h. In both cases random ramified islands are observed exhibiting a fractal-like geometry typically observed in systems with very low edge diffusion. The islands have mostly several branches with high up to several tens of nanometers. The structural strain of the underlying LNMO thin films grown on top of STO and LAO substrates was analyzed by means of Reciprocal Space Maps (RSM). RSM around (103) reflection of the corresponding thin films (Fig. 3.21 (c)-(d)), evidenced that the underlying 40nm-thick LNMO films are fully strained, indicating that the in-plane pseudocubic cell parameter of the film is equal to that of the STO ($a_{STO}$= 3.905Å) and LAO ($a_{LAO}$=3.789 Å) substrates. As previously observed in LNMO films on STO (001) substrates (tensile strain) deposited under similar growth conditions (see section 3.2.1 and 3.3.2).

The estimated in-plane and out-of-plane parameters in pseudo cubic perovskite notation are $a_{||=}$ 3.905Å and $a_{\perp}$=3.941Å in LNMO/STO and $a_{||}$ =3.789Å and $a_{\perp}$=3.978Å in LNMO/LAO thin films, giving rise to LNMO cell parameters a=b=5.522Å, c=7.868Å and a=b=5.358Å, c=7.956 Å, respectively. These values are in close agreement with previous reports [145]

[194] and with LNMO samples deposited with similar growth conditions, using the target prepared by the solid-state reaction method (see section 3.3.2.1). Therefore, the formation of organic nanostructures does not affect the structure of the film, because these formations are over LNMO film surface.

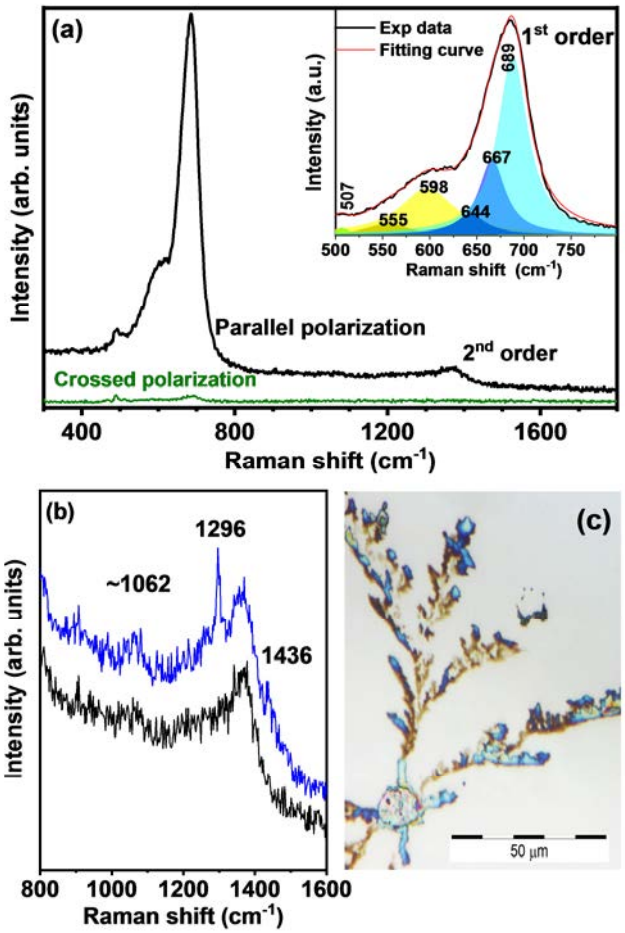


Figure 3.22 (a) Polarized Raman spectra of LNMO/LAO thin film at 300 K. Inset shows the fit of the spectral profile obtained in parallel polarization by a sum of Lorentzians ascribed to 1st order LNMO Raman modes. (b) Raman spectra in the range of 800–2000 $cm^{-1}$ measured on blue part of fractal-like island (blue line) and clean film surface (black line). (c) Micrograph of fractal-like islands seen under the 50 × objective of optical microscope coupled to the Raman spectrometer.

Since X-ray diffraction could not detect any additional secondary phase, the composition of fractal-like islands was investigated by Raman spectroscopy (Fig. 3.22). These measurements were carried out in Belgrade, Serbia with the collaboration of M. Šćepanović. Raman scattering measurements were performed at room temperature using a TriVista 557 Raman spectrometer in backscattering micro-Raman configuration with a 300/300/500 groves/mm diffraction gratings combination. A Coherent VerdiG solid-state laser with a wavelength of $\lambda = 532$ nm was used as an excitation source. Laser beam focusing was accomplished by a microscope objective with 100×magnification. The laser power at the sample surface was

varied from <1 to 5 mW (the output laser power between 20 and 100 mW). Low laser powers, applied during the collection of Raman spectra of dendritic structures formed at the LNMO/LAO film surface was carefully chosen to avoid photochemical or thermal decomposition of these nanostructures.

Fig. 3.22(a) shows Raman spectra of LNMO thin film on top of LAO, recorded in parallel and crossed polarizations of incident and scattered light. Beside the LAO Raman peaks detected below 500 $cm^{-1}$, two broad Raman features dominate the parallel-polarized spectrum. The feature located around 598 $cm^{-1}$ could be related to antisymmetric stretching (AS), whereas the feature at about 685 $cm^{-1}$ could be assigned to symmetric stretching (S) vibrations of $(Ni/Mn)O_6$ octahedra characteristic for LNMO structure [41] [190] [221]. The decomposition of the spectral structure between 500 and 800 $cm^{-1}$ according to the procedure proposed by Iliev et al. [190] reveals Raman bands at about 507, 555, 598, 644, 667 and 689 $cm^{-1}$ (see the inset in Fig. 3.22 (a)). Note that the frequencies of both AS and S modes of the film are appreciably higher than the corresponding phonon frequencies in the LNMO single crystal [190]. Pronounced blueshifts [222] could be related to compressive stress in the LNMO thin films, due to the lattice mismatch between the film and the substrate (see Fig. 3.21(d)). Also, significantly higher Mn amount in the film under investigation than in the stoichiometric LNMO could be partly responsible for the observed blueshift of the Raman modes (knowing that the atomic mass of Mn (54.938) is lower than that of Ni (58.693) [221]. To identify the subtle changes between the surface with/without fractal-like island the optical microscope coupled to the Raman spectrometer was used (Fig. 3.22(c)). It is worth noticing, that these islands are very sensitive to the irradiation by a focused laser beam. Thus, soon after the exposure to the laser beam (even with a power of <1 mW) brown parts of ramified branches began to fade and disappear, leaving only a clean surface of the film. Only structures of intense blue colour proved to be more resistant to the laser irradiation, which enabled measurement of their Raman spectra. These spectra show some subtle differences above 1000 $cm^{-1}$ in comparison to the spectra recorded on the clean film surfaces, as shown in the Fig. 3.22(b). Additional peaks detected in the spectra of blue parts of branches at about 1062, 1296 and 1436 $cm^{-1}$ could be related to the C–C symmetric stretching, the $CH_2$ twisting and $CH_2$ bending modes, respectively, usually attributed to vibrational bonds of alkyl groups $C_nH_{2n+1}$ [223]. In spite of the low signal-to- noise intensity ratio and the appearance of the LMNO second order mode in the spectral range of interest, the relatively narrow band at about 1296 $cm^{-1}$ may be an indication of the polyethylene rotator (semi- crystalline) or crystalline phases [224].

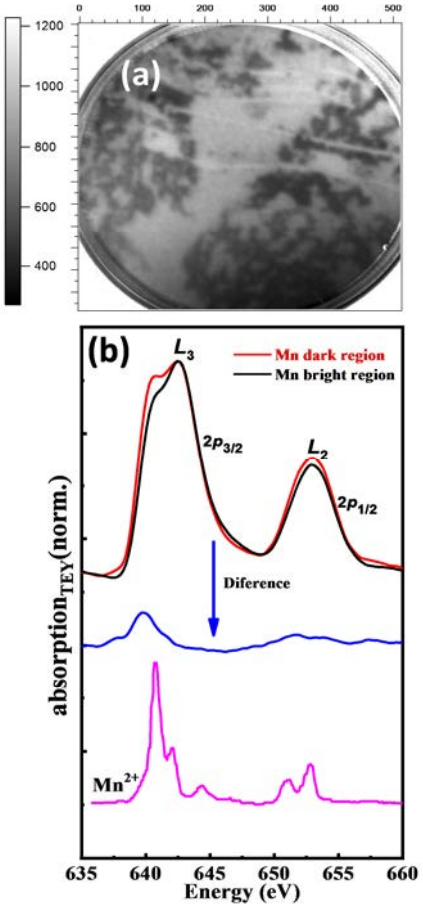


Figure 3.23 (a) X-PEEM images computed from the sum of images obtained across the Mn $L_{2,3}$ edge (0.2 eV step size) for samples annealed under oxygen pressure at Tann=800°C. Field of view 20 um. (b) Corresponding XAS Mn $L_{2,3}$ spectra obtained from dark (red curve) and bright (black curve) regions for (a) respectively. Blue curve is obtained as the difference of XAS spectra for dark and bright areas after proper normalization (see text). Magenta curve is a digitalized version of a theoretical $Mn^{2+}$ spectra reported in [225].

In order to investigate whether the oxidation state of Mn is affected by the presence of OP islands over LNMO films surface, the space-resolved X-ray absorption spectroscopy (XAS) experiments have been carried out on the OP/LNMO thin films annealed at 800°C. The spectra were measured by the total electron yield (TEY) mode at room temperature. As mentioned before (see appendix A.7.1), the total electron yield (TEY) mode is a technique extremely surface-sensitive of the sample, just few nanometers (2-5 nm), which allows us to determine the above. Xray photoemission electron microscopy (X-PEEM) experiments were performed at the UE49PGM beam line of BESSY II [226], the synchrotron radiation source of the Helmholtz-Zentrum Berlin, Germany. X-PEEM technique renders space resolved spectroscopic information and enables different working modes such as XAS and XPS. X-PEEM images were recorded for incoming photon energies across the Mn $L_{2,3}$-edge i.e. Mn

$L_3$ (641.8 eV) and $L_2$ edges (652.8 eV) (0.2 eV step size) with linearly polarized radiation. All images were normalized to a background image and drift corrected.

In Fig 3.23 (a), OP islands imaged by X-PEEM show a dark contrast as compared to the bright one for LNMO regions with no OP on top. Mn $L_{2,3}$ XAS spectra have been extracted from dark (OP on top of LNMO) and bright (bare LNMO) regions, red and black curves, respectively in Fig. 3.23(b). Note that the XAS spectra obtained from regions with OP islands present an increase of the spectral weight at the low energy side of the $L_3$ peak, at 640.8 eV, as compared to that of pure LNMO regions. In order to reveal the origin of such difference we normalize the spectra following the procedure described in [227] and plot their difference (blue curve in Figs. 3.23(b)). The difference spectrum mimics spectral features typical of divalent Mn [225]. We hypothesize that the presence of carbon in organic nanoestructure is at the heart of the formation of $Mn^{2+}$ in agreement with [228] and leads to the deviation of the nominal mixed $Mn^{3+}/Mn^{4+}$ state, observed previously [229]. To account for this unexpected organic material, we believe that the most plausible scenario is to assume that, during target preparation by the citrate decomposition method; a nanocomposite between PVA and oxide (LNMO) was formed that modifies the thermal decomposition of PVA. PVA has been used for binder in ceramic pellets as it is a very good agglutinant that it is later destroyed during the thermal treatment. However, when PVA is part of a nanocomposite, its thermal decomposition may be significantly modified to higher temperatures as previously reported [230]. Thus, we believe that this could be the scenario of our experiments, i.e., organic material observed in the island is the result of the modified decomposition of PVA during target preparation that remains during film deposition. Nevertheless, this organic compound is not absorbed into the structure, so it is only detected on the surface of the films promoting the formation of $Mn^{2+}$.

## 3.3.2 $NiO_x$ nanocuboids

In this section, we report on the spontaneous formation of nickel-oxide nanocuboids at the surface of $La_2Ni_{1-x}Mn_{1+x}O_6$ (x = 0.47) thin films. Annealing treatments (in-situ or ex-situ) in oxygen at high temperature (800-900$^o$C) after thin film growth promote the spontaneous formation of NiO nanocuboids, giving place to the formation of a nanostructured surface. The control of the spontaneous formation of nanostructures at the film surface is of strong interest in many different fields, from catalysts to microelectronics, since surface and interfacial properties may be substantially enhanced. For this purpose, the study of the formation of NiO nanocuboids at the surface of LNMO samples grown on $SrTiO_3$ (001) substrates have been carried out on two characteristic samples. The first one is a LNMO sample deposited at a growth temperature of 900$^o$C under 140 mTorr $O_2$ with (in-situ) annealing at the same growth temperature (for 1h under 420 Torr $O_2$), this sample has been labeled as LNMO-δA. The second one is a LNMO sample deposited at the same growth temperature and oxygen pressure

as the previous one (900°C, 140 mTorr $O_2$) but, after film growth, the evolution of the physical and structural properties was followed by repeated ex-situ annealings at 800°C (Annealed-800°C) and 900 °C (Annealed-900°C) for 1h under 420 Torr $O_2$ of the same LNMO thin film. After the annealing process, the cooling rate was 10°C/min. As determined by X-ray reflectivity, the thickness *t* of the different LNMO films presented in this study was ranging as 40 nm < t < 50 nm. Our results indicate that the post-annealing processes improve the magnetic properties as well as the structural properties. Nevertheless, high annealing temperatures (800-900°C) produce the formation of $NiO_x$ segregates, while modifying significantly the local transport properties at the film surface.

### 3.3.2.1 In-situ annealed thin film

In Fig.3.24 the surface morphology of a LNMO film, after usual annealing in-situ process at 900°C, reveals the existence of a nanostructured surface. The SEM image (Fig.3.24 (a)) detects uniformly distributed nanocuboids throughout the film surface, with nearly square-based, sub-100 nm in size. AFM topography in Fig. 3.24 (b) confirms the presence of nanocuboids, distributed on top of a flat LNMO surface with low roughness (rms~0.3 nm). The estimated occupation of the surface is below 15%. The inset of Figure 3.24(b) reveals a nanocuboids with a typical height of ~12 nm. An interesting observation is that nanocuboids' edges are mainly oriented along the [100] direction of the substrate (note that SEM and AFM images are rotated around 45° respect to the substrate edge during observation).

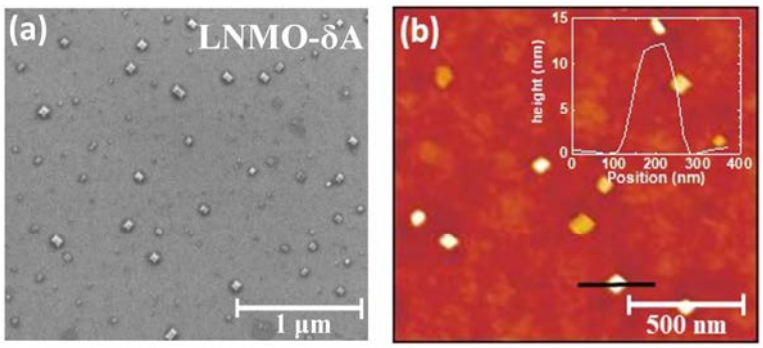


Figure 3.24 a) SEM micrographs and b) AFM image of LNMO-δA thin film (thickness,t=42 nm) with in-situ annealing at 900° C with the height profile of one nanocuboid in the inset.

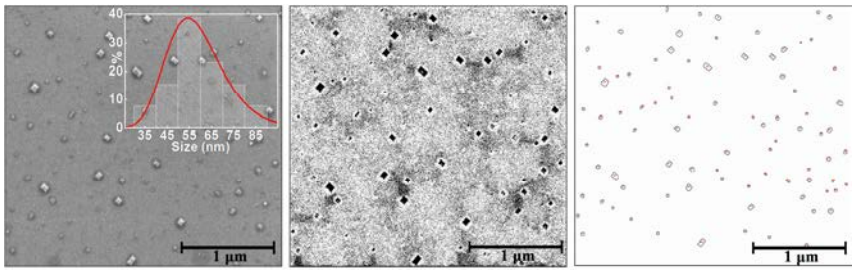


Figure 3.25 SEM micrograph with a magnification of 50000x of LNMO-δA thin film (thickness, t=42 nm, in-situ annealing at 900°C). Filtered image of its corresponding SEM image (medium) and automated grains counting with ImageJ software (right).

The size of nanocuboids was determined from SEM micrographs using image analysis (ImageJ software [231]) averaging measurements of a large number of particles at different regions of the film surface. The distribution of nanoparticle size is well described by the log-normal function $f(S) = \frac{1}{\sqrt{2\pi}\sigma S}\exp\left[-\frac{ln^2\left(\frac{S}{S_0}\right)}{2\sigma^2}\right]$, where the fitting parameters $S_0$ and σ are the most probable nanoparticle size and the width of the distribution, respectively.

The distribution of nanocuboids size is well described by the log-normal function with the most probable size of around $S_0$~58 nm and the distribution width of σ~0.23 (see image in Fig.3.25). The average nanoparticle size $S_M$ is determined from the most probable nanoparticle size ($S_M = S_0 \exp(\sigma^2/2)$). Summary of the obtained values for the surface density and average nanoparticle volume is presented in table 3.4 .

Table 3.4. Surface density, average nanoparticle volume, total volume of the nanoparticles ($NiO_X$) per unit surface (1µm$^2$) and nanoparticle fraction volume of LNMO-δA thin film (determined from Figure 3.25)

| Annealing T (in-situ) | Density (NP/µm²) | NP volume (nm³) | NPs volume (nm³)/µm² | NP fraction volume |
|---|---|---|---|---|
| 900°C | ~$1.04*10^{-1}$ | ~ $4.2\ 10^4$ | ~ $4.4\ 10^5$ | ~0.011 |

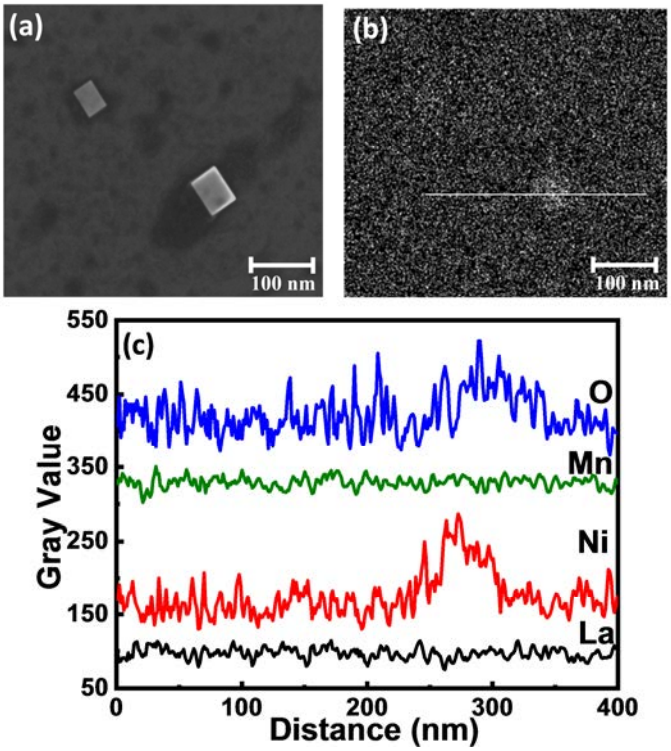


Figure 3.26 (a)-(b) Small area SEM and EDX map at energy of E=15eV with the corresponding profile spectra of different elements by X-ray spectroscopy analysis in (c).

Information regarding the chemical composition of the nanometric cuboids was obtained from Energy Dispersive X-Ray (EDX) analysis. A small area SEM image of a single nanocuboid and the corresponding EDX map obtained at 15 KeV are shown in Fig. 3.26 (a)-(b). The profile spectra of constituent elements (La $L_{\alpha 1}$, Ni, Mn and O $K_{\alpha 1}$) in a single nanocuboid are shown in Fig. 3.26 (c), indicating the presence of nickel and oxygen. The presence of La and Mn have been excluded due to the very low detection percentage (no difference observed along the baseline in Fig. 3.26 (b). Therefore, semi-quantitative, EDX analysis indicates that the nanometric cuboids formed on top of the LNMO films surface are Ni-rich phase, most probably NiOx phases, in agreement with recent reports of the formation of NiOx segregates in LNMO double perovskites [146] [232]. In those works, it is proposed that oxygen deficiency in LNMO films could favors the formation of antisite defects [41] and NiOx phase segregations [146] [232]. The coexistence of double perovskite and NiO secondary phase is supported by first principles modeling of growth in oxygen deficient conditions with expected dissolution of inclusions during annealing [146].Nanometer size nickel-oxide precipitates were also detected during the growth of $LaNiO_3$-$LaAlO_3$ superlattices on $SrTiO_3$ substrate, changing their electronic properties [233]. Similar phase segregation processes are also observed in other manganite systems with cationic deficiency, strongly affecting the magnetic and transport properties of the materials [234].

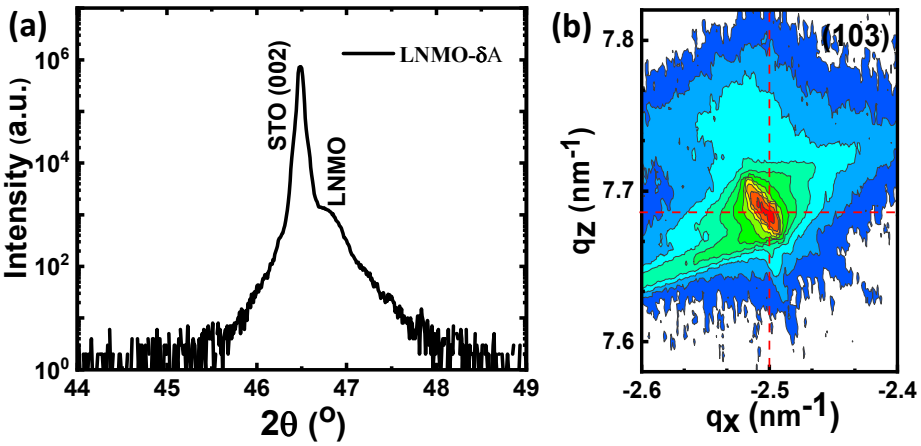


Figure 3.27 (a) High-resolution θ/2θ XRD scans of the (002) reflection and (b) RSM around (103) reflection of LNMO-δA sample. The red dotted line indicates the position of the STO peak.

A deeper insight in the films' structure was obtained by X-ray diffraction and reflectivity techniques. The high resolution θ/2θ X-ray diffraction allows identifying the LNMO peak in the proximity of the intense substrate one (see Fig. 3.27(a)) with an out-of-plane lattice parameter of $a_{\perp}$= 3.877±0.003 Å. The estimated LNMO unit cell volume (~59.12 $Å^3$) is very similar to the unit cell volume of Ni-deficient bulk counterpart ($LaNi_{0.25}Mn_{0.75}O_{3+\delta}$) [99]. The in-plane lattice parameter of the film determined from the reciprocal space maps, around $(103)_{STO}$ reflection, perfectly matches with that of the STO substrate, indicates strained film (see Fig. 3.27(b)).

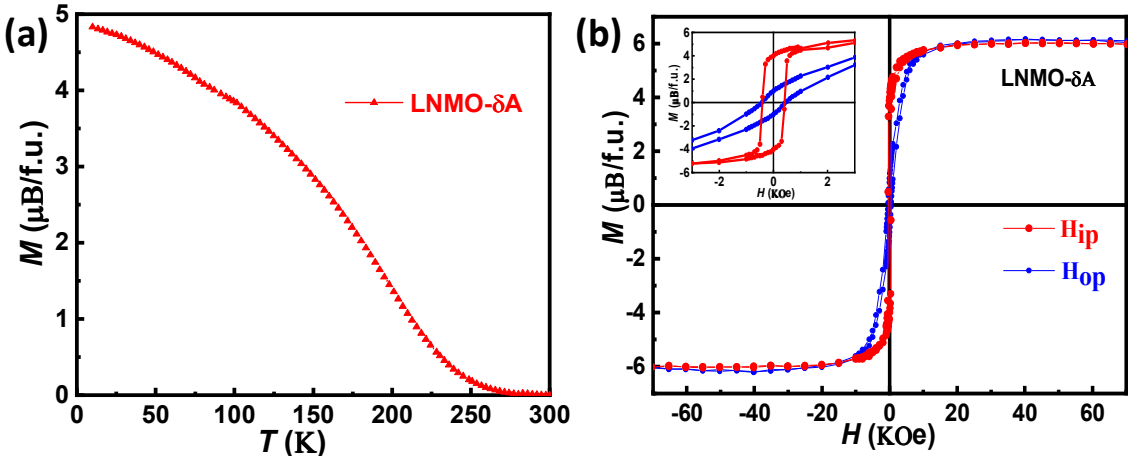


Figure 3.28 (a) In-plane magnetization as a function of temperature under an applied field of 5 KOe ($\mu_0$H =0.5 T) of LNMO-δA sample (thickness, t=42 nm), (b) M(H) hysteresis loops at 10 K for H applied in-plane and out-of-plane. Inset shows the low field region in detail.

In-plane magnetization as a function of temperature in applied magnetic field of 5 KOe of LNMO-δA sample is shown Fig. 3.28 (a) The Tc value found is slightly lower compared to the bulk value, as expected for nickel deficient samples [39] [99]. M(H) hysteresis loops for the field applied in-plane (IP) and out-of-plane (OP) configurations, measured at 10 K (Figure 3.28 (b)), exhibit the expected hysteretic behavior with similar coercive field, Hc~400 Oe respectively. The magnetic remanence, which can be appreciated in the inset, for the in-plane configuration ($M_r \approx 4$ $\mu_B$/f.u) is larger than that found for the out-of-plane ($M_r \approx 1.0 \mu_B$/f.u), besides a saturation magnetization of $M_s \approx 5.8$ $\mu_B$/f.u is found to be somewhat larger than the expected theoretical value (~5 $\mu_B$/f.u.) for fully ordered stoichiometric LNMO, as discussed previously (see section 3.2.2).

Finally, it should be noted that this sample has higher Ms and lower Hc compared to the LNMO sample studied in section 3.2.2 (see Fig 3.17 (b)). This fact is due to the greater Ni deficiency present in this sample, thus the content of $Mn^{3+}$ increases, favoring an increase in Ms. In addition, the anisotropy of this sample is lower since it is favored by Ni, as previously studied (see section 3.2.2).

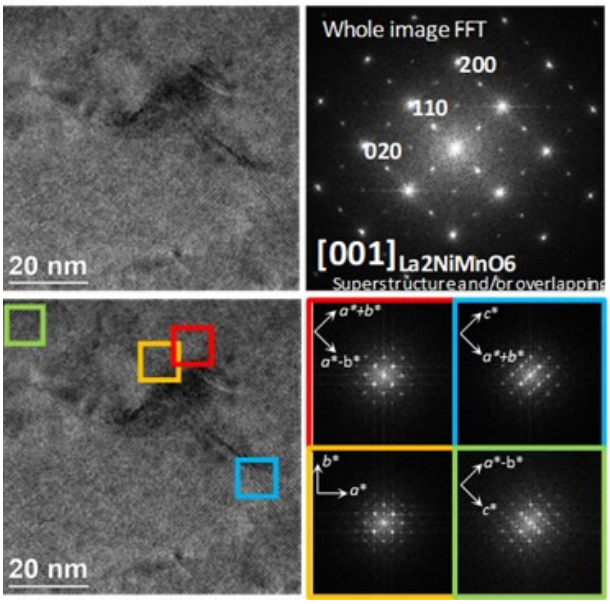


Figure. 3.29**.** A plan-view HRTEM image of LNMO-δA sample. Fourier transform (FT) shows the coexistence of nanodomains with different orientations.

In Fig. 3.29 shows a plan-view in high resolution TEM (HRTEM) images, acquired in order to obtain information about the microstructure and crystallographic features of LNMO-δA sample. Also, another interest was to determine the composition of the nanocuboids, but the preparation process that this measurement requires has eliminated the particles in the

determined region. The sample was cut parallel to the sample surface (perpendicular to the (00l) planes). HRTEM images show a non-homogeneous structure with the coexistence of domains with different orientations. The Fourier transform (FT) of selected areas of the image were computed in order to assess the periodicity of the crystal lattice. The FT of a large area was marked by squares, which shows different spots corresponding to the enlargement of the LNMO lattice with respect to STO (LNMO cell parameters are of the type $a \approx b \approx \sqrt{2}a_p$, $c \approx 2a_p$ where $a_p$ is the primitive perovskite cell parameter) [44] [194]. These spots can be indexed as (0 k/2 l/2) (k and l odd), (0 k/2 l/) (k odd), and (0 k l/2) (l odd) and indicate different orientations of the LNMO cell in the film, as previously mentioned (see section 3.2.1).

## 3.3.2.2 Ex-situ annealed thin film

To gain a deeper insight into the formation of NiOx nanocuboids, successive annealing processes at different temperatures are applied ex-situ to a non-annealed as-grown film. The evolution of the physical and structural properties was followed on the same LNMO thin film after each annealing process and the changes on the morphology are presented in Fig. 3.30(a)-(c).

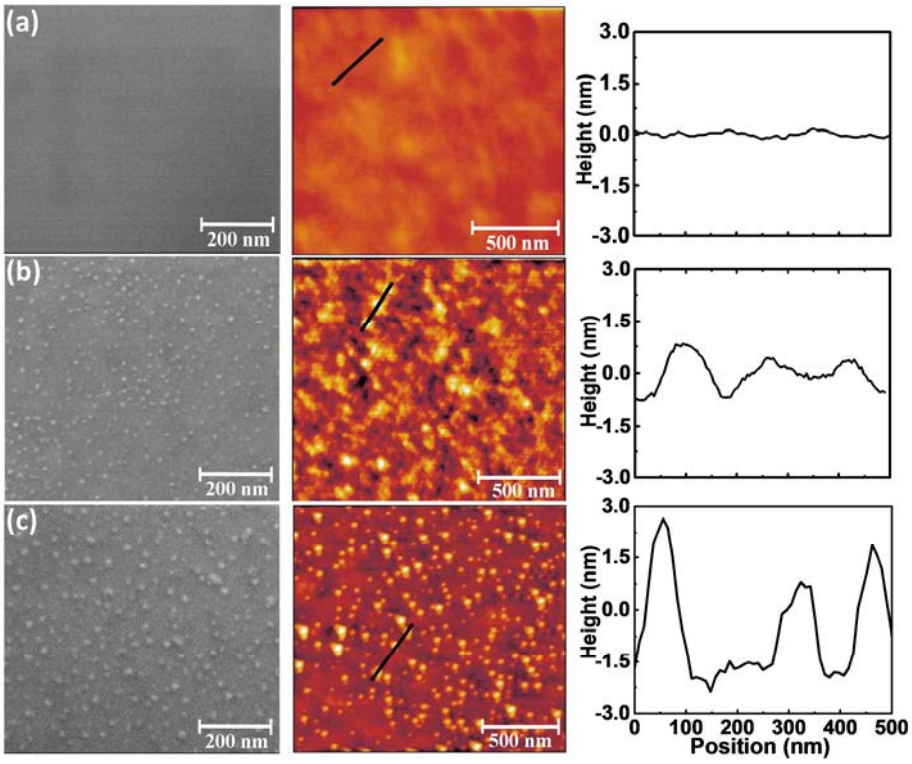


Figure 3.30 SEM micrographs (left-hand image) and AFM images (right-hand image) with the typical line profile of the same LNMO thin film (thickness, t=48 nm) after different annealing processes: (a) as-grown film (no-annealing process), (b) annealing at 800°C and (c) annealing at 900°C.

SEM (left-hand image) and AFM (right-hand image) micrographs in Fig. 3.30(a) of the as-grown LNMO film without annealing process show a flat surface with an average roughness of rms~0.3 nm. In this case, no signals of segregation were detected, indicating that in as-grown LNMO films segregation does not occur, which happens after the films are subjected to high annealing temperatures (800°C-900°C). In this regard, after an ex-situ annealing at 800°C, segregated nanostructures appears distributed through the whole surface as shown in Fig. 3.30(b). SEM micrographs revealed the presence of uniformly distributed small nanoparticles. The corresponding AFM confirms the presence of these nanoparticles, reflected in a higher value of global surface roughness (rms~0.45 nm). Log-normal distribution indicates the most probable nanoparticle size of around $S_0$~13.5 nm with the distribution width of σ~0.13 (see Fig. 3.31 (a)). However, the mean-size of nanostructures remains rather small and with a height of few nanometers ~2 nm (see the line profile in Fig. 3.30(b)). Performing further ex-situ annealing process at higher temperatures (900°C) on the very same LNMO film resulted in an enhancement of the growth of the nanoparticles. Nanoparticles became larger in-size as shown in Fig.3.30(c). Log-normal distribution reveals the most probable nanoparticle size of $S_0$~18.5 nm with the distribution width of σ~0.17 (see Fig. 3.31(b)). The average nanoparticle height increases to around ~5 nm which is also reflected in an increase of the roughness (rms~0.7 nm).

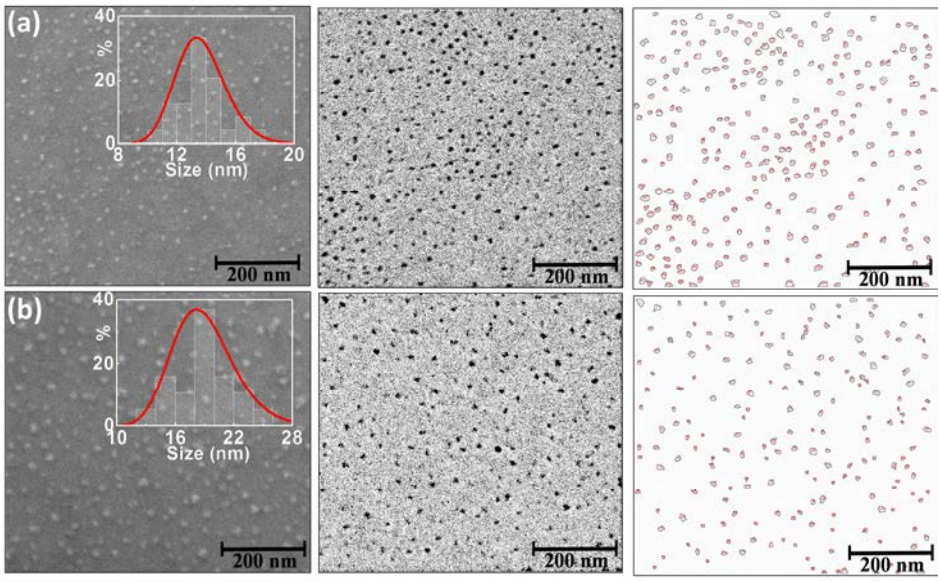


Figure. 3.31. SEM micrographs with a magnification of 200 000x of the same LNMO thin film (thickness, t=48 nm) after different ex-situ annealing temperatures: a) Annealing at 800°C and b) Annealing at 900 °C. Filtered image of its corresponding SEM image (medium) and automated grains counting with ImageJ software (right).

Table 3.5. Surface density, average nanoparticle volume, total volume of the nanoparticles ($NiO_X$) per unit surface ($1\mu m^2$) and nanoparticle fraction volume of the same LNMO thin film after different ex-situ annealing temperatures, determined from Fig. 3.31

| Annealing T (ex-situ) | Density (NP/μm²) | NP volume (nm³) | NPs volume (nm³)/μm² | NP fraction volume |
|---|---|---|---|---|
| 800°C | ~5.34*10² | ~ 3.7 10² | ~2.0 10⁵ | ~0.004 |
| 900°C | ~3.70*10² | ~ 1.8 10³ | ~6.5 10⁵ | ~0.014 |

Although the density of nanoparticles appears to decrease by increasing the annealing temperature (from $5.34*10^{-4}$ nanoparticles/$nm^2$ for Annealed-800°C, to $3.70*10^{-4}$ nanoparticles/$nm^2$ for Annealed-900 °C) the average volume of $NiO_x$ at the surface has been estimated to increase around three times (see table 3.5), thus confirming that annealing process enhances the segregation.

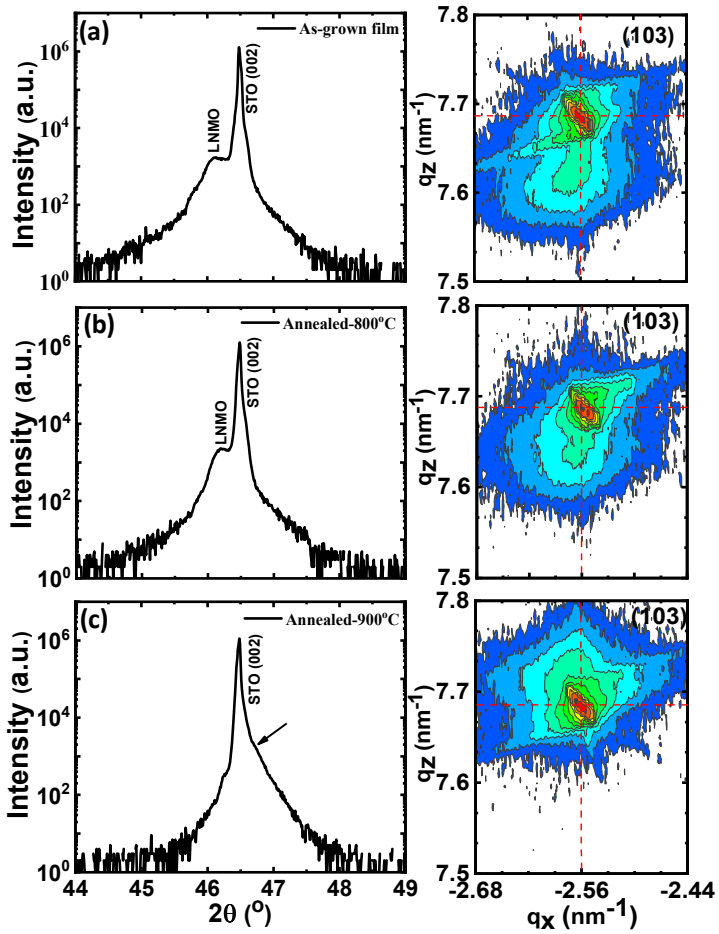


Figure 3.32. High-resolution θ/2θ XRD scans of the (002) reflections (left ) and RSM around $(103)_{STO}$ reflection (right) of the same LNMO thin film (thickness, t=48 nm) after different annealing temperature: a) as-grown film b) annealing at 800°C and c) annealing at 900°C. The arrow indicates position of LNMO peak and the red dotted line indicates the position of the STO peak.

In Fig 3.32 (a)-(c), the effect of different annealing processes on the structural properties of the same LNMO thin film has been followed by high resolution XRD scan of the (002) reflection and the asymmetric Reciprocal Space Map (RSM) around $(103)_{STO}$ reflection. In Fig. 3.32 (a), a shoulder could be distinguish in proximity of the prominent substrate (0 0 2) peak, which can be associated to the LNMO peak with an out-of-plane parameter of $a_{\perp}$=3.939±0.002 Å. At the same time, RSM around $(103)_{STO}$ reflection of the same film, indicates the position of the LNMO film just below the substrate peak (right-hand image in Fig.3.32 (a)), indicated that as-grown film is fully strained with the in-plane parameter that mimics the lattice parameter of underlying substrate ($a_{STO}$=3.905 Å). The first annealing process at 800°C (Fig.3.32 (b)), does not change significantly the structural parameters. From θ/2θ XRD scans (left-hand image in Fig 3.32 (b)), the out-of-plane lattice parameter is found to decrease to $a_{\perp}$=3.929±0.002 Å, remaining elongated than the corresponding pseudocubic perovskite lattice parameter of bulk LNMO, LNMO ($a_{bulk}$=3.876 Å) [41]. However, under annealing process at 900°C in Fig 3.32 (c), the shoulder in θ/2θ XRD scan disappears completely and only the substrate peak can be clearly observed. Nevertheless, the RSM around $(103)_{STO}$ reflection indicates that the LNMO film peak is just above the substrate peak corresponding to a slight anomaly detected in θ/2θ XRD scan (see arrow in left-hand Fig.3.32 (c)). While the in-plane lattice parameter still remains constant ($a_{\parallel}$=3.905±0.005 Å), the out-of-plane lattice parameter further decreases to $a_{\perp}$=3.883±0.001 Å.

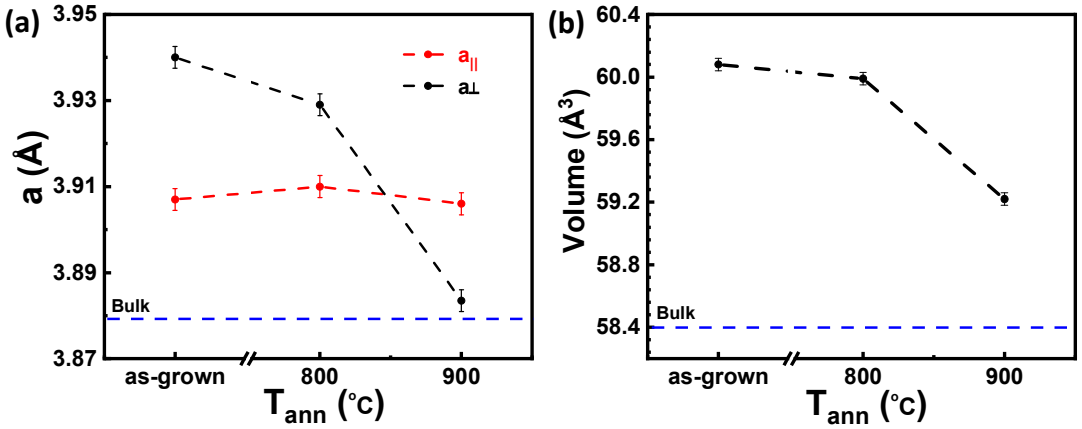


Figure 3.33 (a) Variation of in-plane (red dashed line) and out-of-plane (black dashed line) lattice parameters of LNMO film after different ex-situ annealing processes. (b) Shows the variation of the volume of the LNMO film after different ex-situ annealing processes in pseudocubic unit cell ($A^3$). The blue dashed line represents the bulk counterpart value [41].

The variation of the in-plane and the out-of-plane cell parameters in pseudo-cubic notation after different annealing processes are depicted in Fig. 3.33(a). The in-plane lattice parameters (red dashed line in Fig. 3.33 (a)) match the $SrTiO_3$ lattice parameter indicating that the films remains strained even after annealing processes. On the other hand, the out-of-plane lattice

parameter (black dotted line in Fig. 3.33 (a)) decreases progressively towards the LNMO bulk value (blue dashed line).

It is worth to note that non-annealed as-grown film has a larger out-of-plane lattice parameter than expected and consequentially larger unit cell volume (~60.06 $Å^3$). This larger unit cell usually denotes some oxygen deficiency and the presence of $Mn^{3+}$ [235]**.** In fact, as can deduced from Fig. 3.33 (a), the shrinkage of the out-of-plane lattice parameter while in-plane parameters remain unchanged results in a reduction of the unit cell volume after successive annealing (see Fig. 3.33(b)), which is consistent with oxygen incorporation during the annealing processes and the formation of $Mn^{4+}$, as previously observed in similar manganite systems [235] [153] [236]. On the othe hand, it should be note that we cannot exclude the presence of NiOx segregations inside the film matrix and that the presence of NiO secondary phase may also contribute to the increment of the out-of-plane lattice parameter in as-grown samples besides oxygen deficiency.

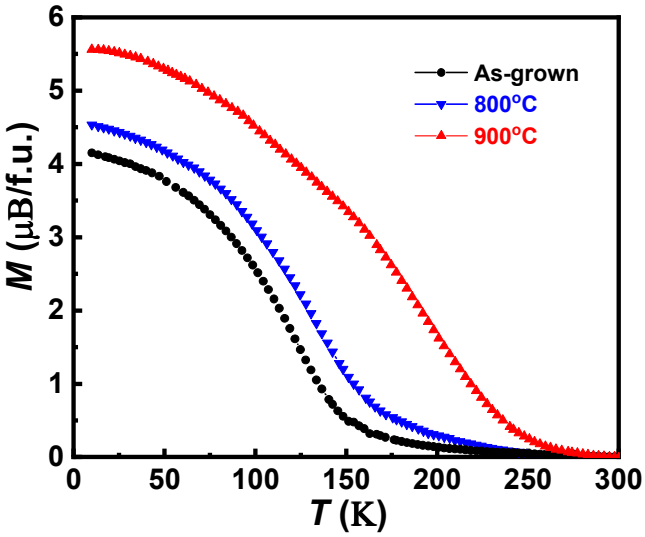


Figure 3.34 In-plane magnetization as a function of temperature under an applied field of 5 KOe ($\mu_0 H$ =0.5 T) of the same LNMO thin film (thickness, t=48 nm) after different annealing (ex-situ) temperature: as-grown film (black curve), annealing at 800°C (blue curve) and annealing at 900°C (red curve).

As mentioned before, high annealing temperatures (800 and 900°C) significantly improve the magnetic properties of the films, which is due to the incorporation of oxygen inside the structure. In fact, it can be appreciated (Fig. 3.34) that the magnetic properties are not affected by the formation of NiOx segregates on the surface of the films. Fig 3.34 shows in-plane magnetization as a function of temperature in the applied magnetic field of 5 KOe for different annealing (ex-situ) temperatures of the same LNMO film. It is found that as-grown non-annealed films exhibit clearly depressed values of Curie temperature (see black curve), while $T_C$ is substantially improved after annealing treatment (blue and red curves in Fig.3.34).

These results agree with previous studies showing that annealing processes in oxygen rich atmosphere promote an increase of the Curie temperature in $La_2NiMnO_6$ films and other double perovskites [90] [237]. Furthermore, it has been shown that post-growth annealing treatments are also effective to reduce the number of antisite defects [106] and to dissolve NiO segregations, thus contributing to increase the saturation magnetization [146]. Nevertheless, in our case, in spite of a clear improvement of the ferromagnetic properties after post-growth annealing (ex-situ or in-situ), nanometric nickel-oxide segregations are still present at the LNMO surface. It is worth mentioning that Curie temperatures found in our samples although significantly improved, are still lower than that found in the bulk counterpart even after oxygen annealing at the highest temperature (900°C). This could be attributed to the non-homogeneity of the sample detected by HRTEM (see Fig. 3.29), that causes the formation of NiO secondary phases (as detected from EDX measurements) and cationic vacancies, giving rise to octahedral distortions in the film, and thus affecting their ferromagnetic properties [238] [194]. Moreover, as Ni agglomeration at the surface is larger after annealing process it is sound to assume that the Ni deficiency inside the film increases that, as a consequence, could further affect the ferromagnetic transition, as $T_C$ is known to decrease when reducing the Ni content [39] [99]. In conclusion, the strong structural strain exerted by the substrate on thin layers clamped to it allows only the contraction of the out-of-plane cell parameter. Thus, high-temperature annealing in oxygen atmosphere promotes a vertical cationic migration (the entry of oxygen ions as well as nickel migration towards surface), allowing the formation of nickel-oxide nanoparticles at film surface.

### 3.3.2.3 Surface electrical properties

Additionally, the presence of nickel-oxide nanoparticles at the surface of LNMO films may strongly influence local electrical properties. To analyze the electronic properties of the different phases present at the LNMO film surface, conductive atomic force microscopy measurements were performed in films prepared after an in-situ annealing at 900°C.

The Fig.3.35 (a) shows topography image in a 2x2 $\mu m^2$ area of a LNMO film with NiOx nanoparticles formed on its LNMO film, while Fig. 3.35 (b) depict its simultaneous acquired current map (applying 1.5V). In the topography image NiOx particles can be identified as the parts of the surface with higher height (bright circles) while in the current map a conductive matrix (white background) is disrupted by less conductive circles (black). Comparing both images allows identifying NiOx nanoparticles as the less conductive parts of the current map, i.e. NiOx particles are more resistive than the LNMO film. This correlation can be better appreciated in figure 3.35 (c), where the profiles of the topography (black) and the current (red) of the lines (see Fig. 3.35 (a) and (b)) are depicted. In Fig 3.35 (c), it can be clearly

observed that in the higher height (z) region, which corresponds to a NiOx particle, the current drops to ≈1nA, while in the flat surrounding regions, where the LNMO film is directly measured, the current is almost two orders of magnitude higher (≈100nA).

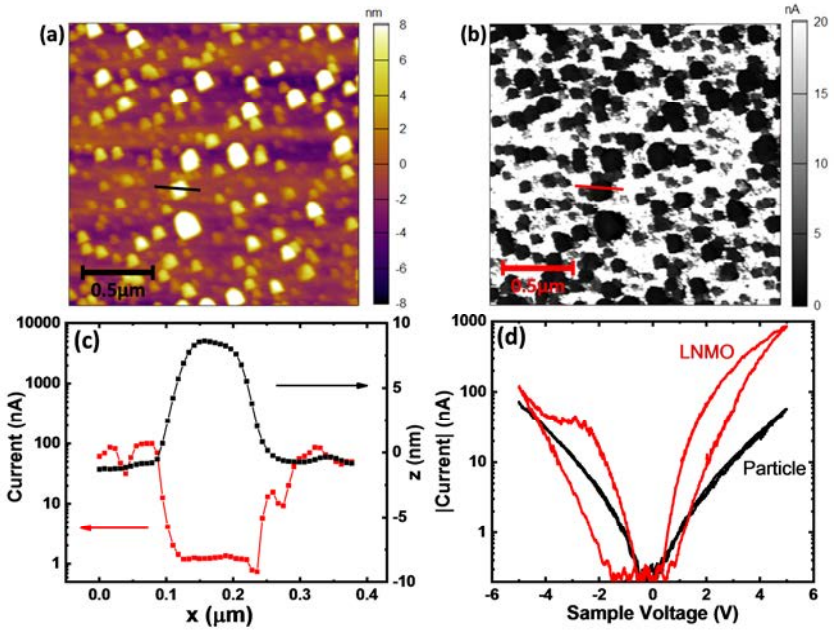


Figure 3.35 Local electric properties of the LNMO films with NiOx particles measured by C-AFM. (a) Topography image of a 2x2 $\mu m^2$ area of the film. (b) Simultaneous current map of the same area taken (applying 1.5 V), where the less conductive parts can be related with the particles observed in the topography. (c) Current (red) and height (black) profiles of a NiOx particle and the surrounding LNMO film marked in (a) and (b). In (d) I-V curves on the LNMO film (red) and on a particle (black), respectively.

Furthermore, the response of the LNMO film and the $NiO_x$ particles to voltage cycling is clearly different, as evidenced in Figure 3.35 (d). Voltage cycles taken directly on the LNMO surface (red curve) show a hysteretic behavior pinned at 0 V characteristic of a resistive switching behavior [239]. At the same time, it is also observed that the application of a negative voltage (-5V) increases locally the resistance of the film, switching the affected area to the so-called high resistance state (HRS). This HRS can be reverted back by the application of a positive voltage (+5V) which returns the affected area of the film back into a more conductive state, i.e., the low resistance state (LRS).

It is important to mention that both HRS and LRS are of a non-volatile nature and can be switched between them multiple times, stating the base for a bipolar resistive switching behavior suitable for the implementation of memory devices. A totally different behavior is observed sweeping the voltage on the top of a particle (black line). In this case, a non-hysteretic symmetrical curve is obtained, where the application of positive or negative voltage does not have any influence in the resistivity properties of the particles. The absence

of Resistive Switching in the particles can be also visualized in the Fig. 3.36. After switching an area to the HRS, the LNMO current is heavily reduced while the particles included in the area maintain their initial current, thus, showing more conductivity than the high resistive state. Thus, our results show that nanostructured LNMO films may be switched from a system of poor conductive particles onto a conductive matrix to the opposite case, conductive particles onto an insulating matrix, thus behaving as a model toy to study interfacial local transport.

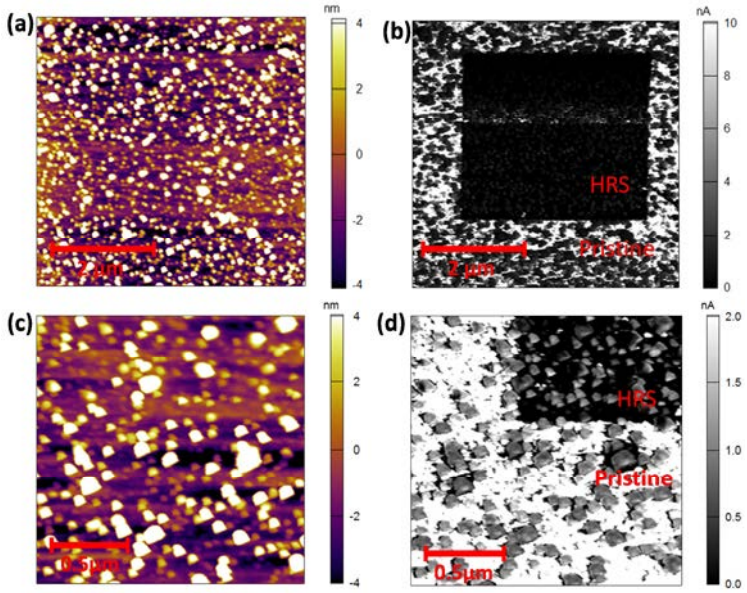


Figure 3.36 Switching of a 3x3μm$^2$ area of the LNMO film into the HRS. (a) Topography and (b) current map images of a 5x5μm$^2$ area, where the central 3x3 μm$^2$ has been previously scanned at -4V of sample Voltage. The current map shows a switching to the HRS of the LNMO film in the scanned area, which does not induce any changes in the topography. (c) Topography and (d) Current map images of a detailed area (2x2 μm$^2$) showing the lack of switching of NiOx particles that are more resistive than the film in the pristine state but more conductive than the film in the HRS.

The Resistive switching characteristics (or their absence), depicted in Fig. 3.35 (d) of the main text, has also been probed on large surface areas to assess its reproducibility. Fig. 3.36 (a) and (b) depict the topography and current images of a 5x5 μm$^2$ area. In the center of this area a 3x3μm$^2$ square has been previously scanned at -4V. As a consequence of this initial scan, the area has been switched into the HRS without harming the surface, as can be noticed in the topography image. Figure 3.36 (c) and (d) show a detail picture (2x2 μm$^2$) of the previous image. Adjusting the scale of the current map it can be observed that, inside the switched area, the particles are more conductive than the LNMO film in the HRS while in the pristine state the particles are more resistive. The lack of resistance change after the biased scan supports the I-V curves presented in the main text and confirms the absence of RS behavior in the NiOx particles.

In conclusion, the formation of NiOx nanoparticles at the LNMO films surface, significantly changes the local surface transport properties, allowing one to obtain a composite surface in which areas exhibiting a resistive switching behavior alternate with other insulating behaviors.

# Summary

We have shown that high quality epitaxial thin films of the LNMO double perovskite, with Curie temperatures Tc ≈ 240 K and saturation magnetization Ms = 5.3 $\mu_B$/f.u., can be prepared by RF sputtering technique. However, magnetic properties turn out to be strongly dependent on the preparation conditions, particularly on the oxygen partial pressure $PO_2$ used during the growth process. Samples prepared at low $PO_2$ (≤ 140 mTorr) are Ni-deficient with a Ni/Mn ratio of about 0.43, while those prepared at high $PO_2$ (≥ 300 mTorr) show the expected Ni/Mn ≈ 1 ratio. In contrast, nonstoichiometric samples exhibit good ferromagnetic properties (i.e., high $T_C$ ≈ 240 K and high saturation magnetization Ms ≈ 5.3 $\mu_B$/f.u), while stoichiometric samples show poor ferromagnetic properties (i.e., low $T_C$ and low Ms). Therefore, to explain the excellent magnetic properties found in Ni-deficient samples, XAS measurements allow concluding that some kind of cationic ordering between $Ni^{2+}$, $Mn^{3+}$, and $Mn^{4+}$ at the B sublattice has to be assumed, and thus, the question of whether a Ni deficiency can favor Ni/Mn ordering arises. At the same time, XMCD measurements show that the contribution of the orbital moment to the magnetic moment of Mn ions is negligible, but for Ni ions it is quite important, with $\mu_L^{Ni}/\mu_S^{Ni} = 0.32$, thus allowing us to conclude that magnetic anisotropy observed in the magnetic measurements ($M(H)$ loops) is of magnetocrystalline origin induced by Ni. On the other hand, irrespectively of the growth conditions, the formation of organic nanostructures with fractal-like geometry has been observed over the surface of LNMO films, when using a target prepared by sol-gel method. XAS experiments have allowed to detect that the presence of OP islands changes the manganese valence from mixed valence state towards $Mn^{2+}$ states, which is not desired on the film surface. Consequently, we have concluded that using PVA during the target fabrication can greatly affect the surface of the films, by being responsible of the formation of $Mn^{2+}$.

Additionally, we have observed that annealing treatments in oxygen atmosphere at high temperatures (800-900$^o$C) improve the magnetic properties of LNMO thin films (as commonly reported). Nevertheless, under these growth conditions, the oxygen annealing process promotes Ni segregation towards the film surface, giving place to the formation of a nanostructured surface where $NiO_x$ nanoparticles are detected. Oxygen deficiency and cationic vacancies in LNMO films could favor the formation of $NiO_x$ phase segregation, thus affecting the ferromagnetic and surface transport properties.

# Chapter 4

# Growth and physical properties of $Pr_{2-\delta}Ni_{1-x}Mn_{1+x}O_6$ thin films

As mentioned before, double perovskites $R_2NiMnO_6$ (R = rare earth element) have received considerable interest because they are ferromagnetic insulators (FM-Is). The combination of ferromagnetic and insulator characteristic in a single system, can achieve potential applications in the fields of spintronics and multiferroic devices [32] [28] [240]. $La_2NiMnO_6$ has been of prime interest in the study of this thesis due to ferromagnetic transition near room temperature ($T_C \approx 280$ K) [28] and multifunctional properties (chapter 3), followed by $Pr_2NiMnO_6$ ($T_C \approx 228$ K) [120].

In this chapter, we report the growth optimization and characterization of $Pr_2NiMnO_6$ (PNMO) double perovskite thin films deposited on (001)-oriented $SrTiO_3$ substrates by RF magnetron sputtering technique. The influence of the growth parameters, such as growth temperature, oxygen partial pressure and annealing, have been studied in order to obtain PNMO thin films with high B-site cationic ordering. After determining the optimal growth conditions, PNMO thin films of different thicknesses were grown on two different $SrTiO_3$ (STO) and $LaAlO_3$ (LAO) substrates in order to explore the role of the structural mismatch between film and substrate, expected to have an impact on the structural and magnetic properties. Finally, the valence states of PNMO films have been investigated by X-ray absorption spectroscopy (XAS) and X-ray magnetic circular dichroism (XMCD) measurements, carried out at Pr $M_{4,5}$, Ni $L_{2,3,}$ Mn $L_{2,3}$ and O $K$ edges and thoroughly analyzed by theoretical simulations.

# 4.1 Optimization of growth conditions

Deposition of high quality PNMO thin films is of great interest for multifunctional applications, such as spintronic devices. So far, there are few reports on the synthesis conditions and ferromagnetic properties of PNMO thin films [241] [30] [29]. As previously mentioned in the introduction, physical methods such as pulsed laser deposition (PLD) have been amongst the few techniques used to grow these films. There, high oxygen pressures (400-950 mTorr) and high growth temperatures (750°C-850°C) are used in order to obtain a high degree of B-site cation ordering [29]. It is worth noticing that no report is available on PNMO thin films grown by RF magnetron sputtering. In this section, the optimization of growth conditions of PNMO thin films on $SrTiO_3$ (001) substrates by RF magnetron sputtering technique is presented. For the growth of the films, we have used a stoichiometric $Pr_2NiMnO_6$ target prepared by solid state reaction method, starting from the optimization process exposed in chapter 2 (see chapter 2, sections 2.2). The structural, magnetic and transport properties of the films are studied as a function of the growth parameters (i.e. chamber oxygen pressure, growth temperature and annealing). At the same time, the stoichiometric composition of our films has been studied by electron probe microanalysis (EPMA) measurements.

## 4.1.1 Structural properties

The physical properties of PNMO thin films can be tailored by controlling the growth conditions. As discussed previously in case of LNMO thin films, we will present the variation of the structural properties as a function of two main growth parameters: the oxygen pressure and the growth temperature.

### 4.1.1.1 Structural properties under different oxygen pressures

Oxygen pressure during thin film growth plays an important role on tailoring the crystal structure. In order to evaluate the effect of oxygen pressure on the structural properties of the films, a series of PNMO thin films on (001)-oriented $SrTiO_3$ (STO) substrates were grown under different oxygen pressures (ranging from 100 to 750 mTorr), by keeping fixed the growth temperature (T = 850°C for 1h). After film deposition, as-grown samples were

annealed (in-situ) at the same growth temperature (1h under 420 Torr $O_2$). After annealing process, the cooling rate was 10°C/min. Similarly as in LNMO systems, we have started the optimization of PNMO films using high growth temperatures (850°C), following previous studies [29].

Fig. 4.1(a) shows the XRR measurements that were carried out to determine the thickness of the samples. Thickness is obtained from the positions of the minimum in XRR curve (see appendix A.4.5). In Fig 4.1(b), one can observe the strong influence of oxygen pressure on the film thickness. By increasing the oxygen pressure from 100 to 750 mTorr the thickness decreases monotonously from 95 nm to 28.5 nm. Accordingly, the growth rate decreases from 1.6 to 0.5 nm/min.

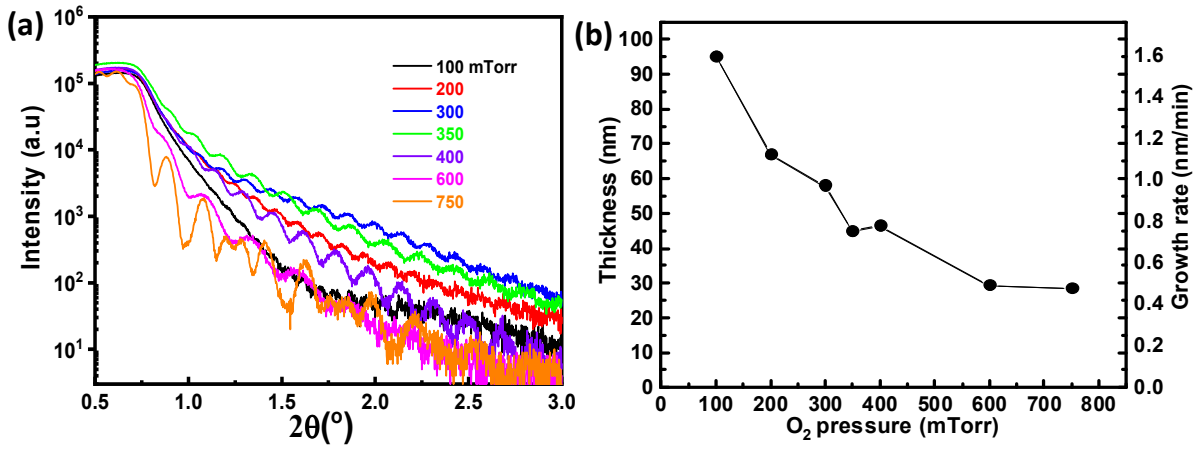


Figure 4.1. (a) XRR data of PNMO thin films on STO substrates grown at 850°C under different oxygen pressures ranging from 100 to 750 mTorr. (b) Thickness and growth rate as a function of oxygen pressure of the same samples.

This decrease in thickness with oxygen pressure could be due to two possibilities. The first possibility could be related to the fact that, by increasing pressure, the mean free path of adatoms decreases, thus decreasing the quantity of arriving adatoms and growth rate. The second, this effect could be associated to the phenomenon of resputtering, which would be due to negative-ion bombardment of the growing thin film [193]. It is considered that oxygen may induce resputtering by forming positive molecular oxygen ions, which interact with the target to produce high-energy negative oxygen ions at the target surface. Thus, negative oxygen ions from the target itself may be responsible for a resputtering effect [193].

This phenomenon of resputtering can be placed into two categories: first, there is negative ion resputtering that may form near the target. In that case the positive molecular oxygen ions may interact with the target to produce negative oxygen ions at the target surface and subsequently accelerate toward the substrate [242]. The process might be a collision (involving the incident positive oxygen ion, a target's atom, and secondary electrons) resulting in negative oxygen ion production at the target surface. Resputtered species gain

their energy from acceleration in the electric field near the target. Second, there is resputtering formed by neutralization collisions between the sputtering ions and target atoms. The consequent bonded oxygen atoms are eventually sputtered from the target as negative ions. In this case, the energy is gained kinetically from collisions with the target [242] [193].

On the other hand, this effect of resputerring with oxygen pressure was not remarkable in LNMO films grown/annealed at 850°C, as the growth rate remained almost constant with increasing oxygen pressure (see chapter 2, section 2.2.1.1). Nevertheless, in LNMO films grown/annealed at 900°C, a similar thickness variation, also attributed to resputtering was observed in samples deposited from 600 mTorr $O_2$ (see chapter 3, section 3.1.1.2).

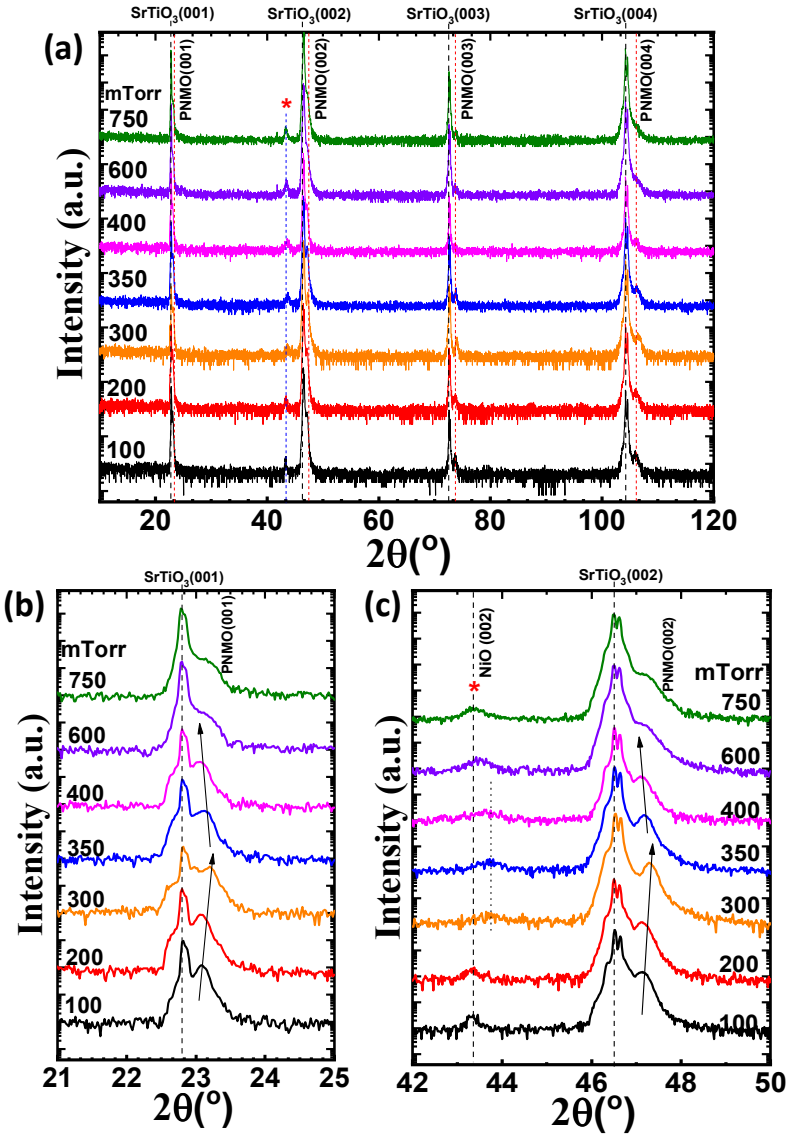


Figure 4.2. (a) XRD θ/2θ scans of PNMO thin films grown at 850°C under different oxygen pressures (ranging from 100 to 750 mTorr), and with in-situ annealing at the same growth temperature (1h under 420 Torr $O_2$). The parasitic phase NiO is denoted by (*). (b) Zoom of the (001) reflection of both STO and PNMO (c) Zoom of the (002) reflection of both STO and PNMO.

The structural properties of the films have been evaluated by X-ray diffraction. θ/2θ scans of PNMO thin films grown at 850°C under various oxygen pressures are shown in Fig. 4.2 (a). As mentioned in chapter 1 (see section 2.2), for the sake of simplicity and also of comparison between film and substrate, the indexing of cell parameters will be referred to the pseudocubic notation. The epitaxial PNMO film ($a_{p\ \mathrm{PNMO\ bulk}} \approx 3.848$ Å [30] where $a_p$ is the perovskite subcell parameter) deposited on STO substrate ($a_{p\ \mathrm{STO}} \approx 3.905$ Å) is submitted to a tensile in-plane strain (see chapter 2, section 2.2).

In Fig. 4.2 (a), the highest intensity peak (identified by dashed vertical black line) in each diffractogram corresponds to the STO (001) substrate reflection. On all XRD patterns the (00*l*) reflections of the PNMO phase (indexed in the pseudocubic notation) can be clearly observed (see red vertical line), thus indicating a good crystalline quality. Moreover, the (00*l*) reflections of the PNMO peaks occur at 2θ values slightly higher than the ones of $SrTiO_3$ (see Fig 4.2 (b) and (c)). This was expected as the lattice parameter of pseudo-cubic PNMO is smaller than the STO one. Nevertheless, the values of out-of-plane cell parameter *c* are larger than the bulk value (see Fig. 4.3), which is in contradiction with the lattice mismatch, which imposes a tensile in-plane strain, thus the shrinking of the out-of-plane parameter is expected. The later observation could be related to the presence of oxygen vacancies in the PNMO lattice, which is known to expand out-of-plane the unit cell (as discussed previously in LNMO films; see chapter 3, section 3.3.2).

For closer inspection, Fig. 4.2 (b) and (c) show the (001) and (002) reflections of both STO substrate and PNMO film. At 100 mTorr $O_2$, PNMO's (001) and (002) reflections are located at $2\theta \approx 23.08^o$ and $2\theta \approx 47.17^o$, respectively, giving rise to an out-of-plane cell parameter of 3.864 Å. By increasing oxygen pressure from 100 to 300 mTorr, the PNMO peaks show a shift towards slightly higher 2θ angles (see arrow). This displacement, according to Bragg's Law ($n\lambda = 2d\sin\theta$), is associated with a decreasing of the out-of-plane cell parameter *c*, approaching the bulk value of 3.848 Å [30] (see Fig. 4.3). At intermediate oxygen pressures (350 and 400 mTorr), a shift of the PNMO peak towards lower angles can be seen (see arrow), indicating an expansion of the *c* parameter. With further increasing of oxygen pressure (above 400 mTorr), it can be appreciated that the out-of-plane parameter *c* decreases again, towards the bulk value. The latter could be associated with a variation in the concentration of defects and oxygen vacancies into the structure under different oxygen pressure.

Finally, in addition to the $Pr_2NiMnO_6$ reflections, XRD patterns show additional reflections corresponding to parasitic phases. In all the XRD patterns of samples grown at very high and low oxygen pressures, the (002) reflection of the NiO phase can be clearly observed at $2\theta \approx 43.4^o$ (see asterisk and dashed line in Fig.4.2(c)). At intermediate oxygen pressure (from 300 to 400 mTorr), a slight shift of this peak towards greater angles can be observed around $2\theta \approx 43.7^o$. The reason of the presence of NiO phase in PNMO samples (grown/annealed at 850°C) is not well understood, although this phase segregation may be of the same origin as seen in LNMO thin films (see chapter 3). Also, it could be a consequence of a certain degree

of Pr deficiency, as revealed by electron probe microanalysis (EPMA) measurements (see below section 4.1.5). This Pr deficiency may indeed induce the formation of secondary phases in $R_2NiMnO_6$ double perovskite, as reported by Dass et al. [28]. Similarly, a secondary phase located at 43.24° identified as NiO was also observed in XRD pattern of $Nd_2NiMnO_6$ samples [243].

As a conclusion, according to XRD data, PNMO films grown at 850°C under different oxygen pressures have good crystalline quality. In addition, although secondary phases are formed (NiO) together with PNMO phase, films grow epitaxial on (001) STO substrates.

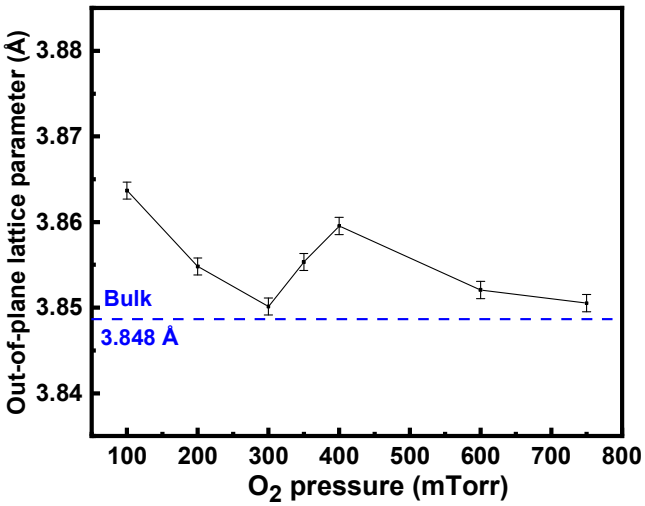


Figure 4.3. Out-of-plane lattice parameter of PNMO thin films on STO (001) substrates grown at 850°C as a function of oxygen pressure. The dashed line represents the PNMO bulk-value in pseudocubic notation [30].

## 4.1.1.2 Structural properties at different growth temperatures

In order to further optimize the deposition conditions, PNMO thin films were grown at different substrate temperatures. According to the results on PNMO films grown at different oxygen pressures (see section 4.1.3.1), good ferromagnetic properties were obtained for samples deposited at intermediate oxygen pressures ranging from 350 to 400 mTorr $O_2$, i.e., a significantly higher pressure than for LNMO (see chapter 3). Therefore, in this section, PNMO thin films on STO (001) substrates were grown at different substrate temperatures (ranging from 200ºC to 900ºC) by keeping a fixed oxygen pressure of 350 mTorr for 1h. After film deposition, as-grown samples were annealed (in-situ) at the same growth temperature under 420 Torr $O_2$ for 1h. As previously, after annealing process, the cooling rate was 10°C/min.

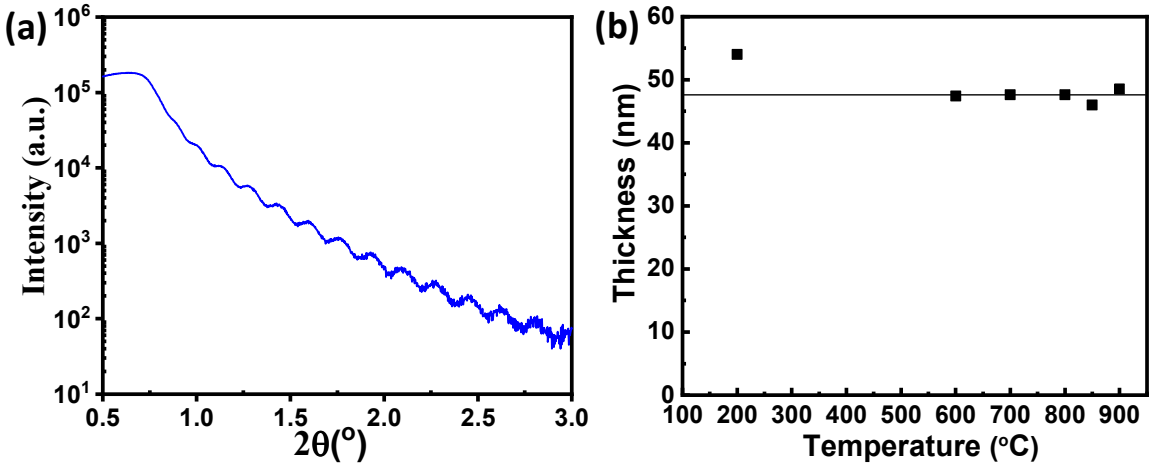


Figure 4.4. (a)XRR data of a PNMO film deposited at a temperature of 700°C under 350 mTorr $O_2$. (b) Thickness as a function of growth temperature. The thickness is obtained from position of minima in the XRR curve.

Fig. 4.4 (a) shows a typical XRR curve of a PNMO film deposited at high temperature (T = 700°C). The thickness dependence as a function of the growth temperature (ranging from 200ºC to 900ºC) is shown in Fig 4.4 (b). It can be observed that the film thickness remains almost constant above 600°C. Thickness values found via XRR analysis for all PNMO samples grown at different temperatures were very similar (~ 48 nm) with a growth rate of about 0.8 nm/min. In a particular case, the sample deposited at a substrate temperature of 200°C was thicker (~ 54 nm). This slight thickness variation with temperature can be attributed to the phenomenon of resputtering [187]. A similar behaviour was also observed in the growth of LNMO thin films, where films deposited at low temperatures were thicker. In fact, this phenomenon of resputtering with the change of temperature was more pronounced in LNMO films, whereas for PNMO films this effect is almost negligible (see chapter 2, section 2.2.1.1 for more details).

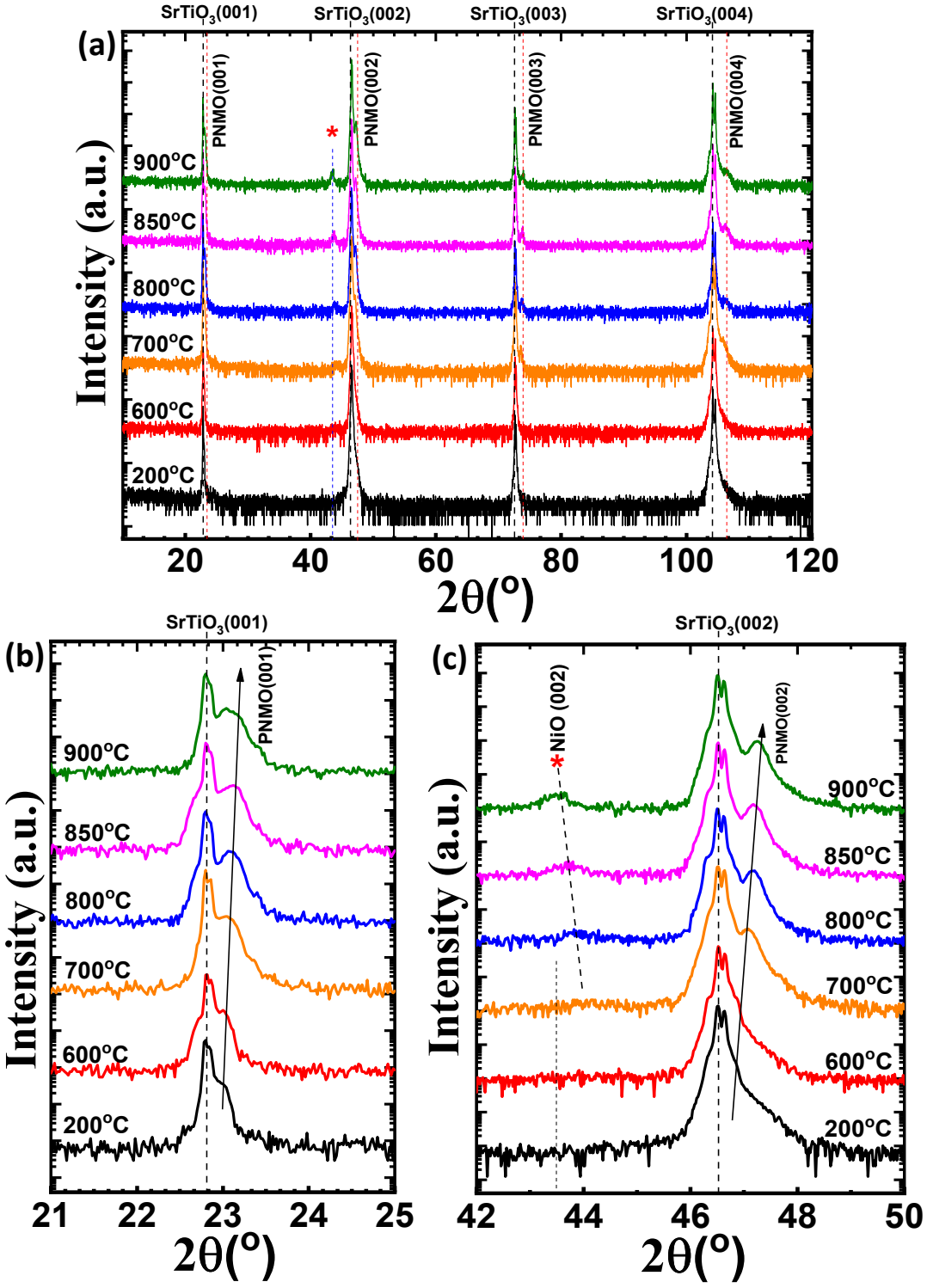


Figure 4.5. (a) XRD θ/2θ scans of PNMO thin films grown at different substrate temperatures (ranging from 200°C to 900°C) under 350 mTorr $O_2$. After film growth, as-grown samples were annealed (in-situ) at the same growth temperature under 420 Torr $O_2$ for 1h. Parasitic phases are denoted by (*). (b) Zoom of the (001) reflection of both STO and PNMO. (c) Zoom of the (002) reflection of both STO and PNMO.

Structural properties of PNMO films deposited at different growth temperatures were studied by X-ray diffraction (XRD). Fig. 4.5 (a) shows θ/2θ scans of ~48-nm-thick PNMO films grown under 350 mTorr at different temperatures. The highest intensity peak in each diffractogram corresponds to the STO (00*l*) substrate reflections which are identified by dashed vertical black lines. In addition, in all XRD patterns, only (00*l*) diffraction peaks of PNMO phase were clearly observed in samples grown at temperatures above 600°C (see dashed vertical red line), indicating that PNMO films have good crystalline quality. As previously discussed, the (00*l*) reflections of the PNMO peaks take place at 2θ values slightly higher than the ones of $SrTiO_3$ (see Fig 4.5 (c), as expected since the lattice parameter of PNMO is smaller than $SrTiO_3$ one. However, the values of out-of-plane parameter *c* are larger than the bulk value (see Fig. 4.6), which is in contradiction with the lattice mismatch imposing a tensile in-plane strain, where the shrinking of the out-of-plane parameter is expected as mentioned before.

For more details, Fig. 4.5 (b) and (c) show the (001) and (002) reflections, respectively, of both STO substrate and PNMO film. In Fig. 4.5 (b), the (001) diffraction peaks of PNMO are not well defined for films deposited at 200°C and 600°C. The PNMO peak of the film grown at 200°C is located at $2\theta \approx 23.04^{o}$, corresponding to an out-of-plane cell parameter $c = 3.863$ Å. As the growth temperature increases, it can be observed that this peak increases in intensity and shifts towards greater angles (see arrow in Fig. 4.5(b)). At higher temperatures (T ≥ 700°C), the PNMO (002) peaks become sharper and more intense, indicating that the high growth temperatures favor good crystallinity of the film. In addition, the position of the (002) reflection shows a shift towards larger angles from $2\theta = 46.8^{o}$ to $2\theta = 47.3^{o}$ (see arrow in Fig 4.5 (c)). Therefore, from Bragg's law ($n\lambda = 2d\sin\theta$), a progressive shrinking of the out-of-plane parameter *c* of PNMO films takes place by increasing growth temperature, approaching PNMO bulk value of $a_{bulk} = 3.848$ Å [30] (see Fig. 4.6).

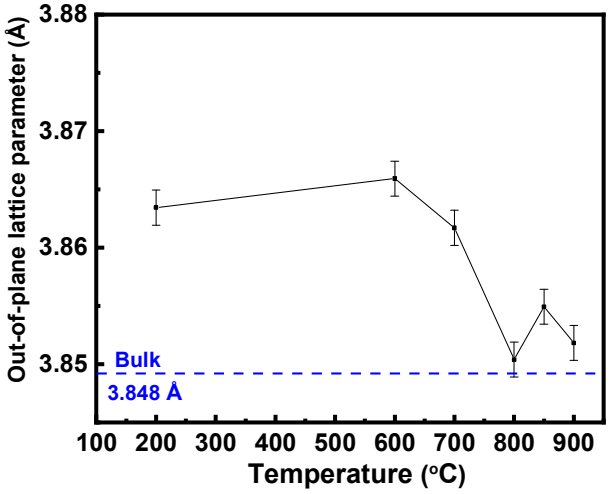


Figure 4.6. Out-of-plane lattice parameter of PNMO thin films on STO substrates as a function of growth temperature. The dashed blue line represents the cell parameter of pseudocubic bulk PNMO [30].

In addition to the PNMO reflections, all XRD patterns show the existence of secondary NiO phase (see asterisk and dashed line in Fig.4.5 (a) and (c)), as previously detected in samples deposited at different pressures (Fig 4.2). It can be seen that the secondary NiO phase is formed, independently of the growth temperature. Nevertheless, for the films grown/annealed in the 200°C-700°C range, the (002) NiO reflection has very low intensity. As the growth temperature increases, it can be observed that the NiO peak is slightly more intense and presents a slight shift towards lower angles ($2\theta \approx 43.8^o$ and $43.6^o$ for 800 and 900°C, respectively). As discussed before, the presence of the secondary NiO phase in the PNMO system is not well understood, although this phase segregation may be of the same origin as seen in LNMO thin films (see chapter 3 and section 3.3.2).

In conclusion, according to XRD patterns, PNMO films deposited under 350 mTorr $O_2$ at different growth temperatures grow epitaxially on STO substrates, and with a good crystalline quality. However, secondary phases (NiO) are present in all films.

## 4.1.2 Surface morphology

The surface morphology of the films plays an essential role in multilayer structures for applications such as tunnel junctions, spin valves, etc. To grow high-quality ultrathin films, a layer-by-layer growth mode i.e. “Frank–van der Merwe” with step-terraces morphology is desired to ensure the continuity of the layers. Therefore, to better evaluate the optimum growth conditions, the surface morphology of PNMO films is examined below.

### 4.1.2.1 Morphology under different oxygen pressures

As in the case of LNMO thin films, atomic force microscopy (AFM) and scanning electron microscopy (SEM) measurements were carried out to evaluate the surface morphology. AFM images in tapping mode of PNMO thin films as a function of oxygen pressure are summarized in Fig. 4.7.

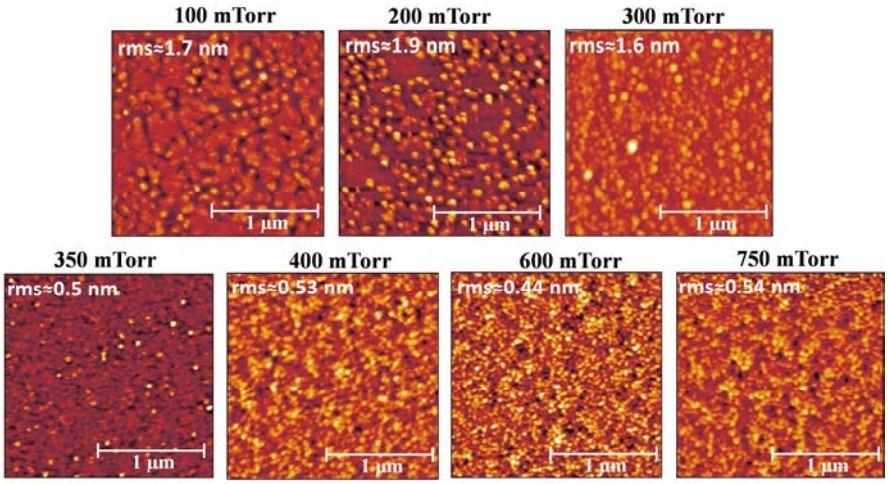


Figure. 4.7 AFM topography (2x2 µm$^2$ area) of PNMO thin films grown under different oxygen pressures (ranging from 100 to 750 mTorr) at 850$^o$C, with in-situ annealing at the same growth temperature (1h under 420 Torr $O_2$).

All images in Fig. 4.7 show granular morphology (no step-terrace morphology detected). It can be appreciated that PNMO films deposited under low oxygen pressures (ranging from 100 to 300 mTorr) have high root mean square (rms) roughness values (rms > 1.5 nm) (see Fig 4.8). By increasing the oxygen pressure from 350 to 750 mTorr, films morphology becomes more flat and smooth with low roughness values (rms ≈ 0.5 nm). At the same time, the presence of very fine grains distributed all over the film surface can be observed. The lower roughness can be related to the fact that the films grown under high oxygen pressure are thinner. However, the decrease of film thickness with oxygen pressure is monotonous, while the roughness decreases abruptly above 350 mTorr, indicating that the growth process at higher pressure favors a flatter surface.

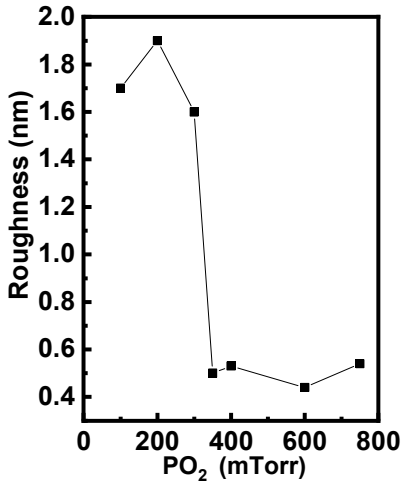


Figure 4.8. Roughness as a function of oxygen pressure of PNMO thin films grown at 850$^o$C under different oxygen pressures (ranging from 100 to 750 mTorr)

Additionally, the effect of oxygen pressure on film morphology was also explored by SEM measurements. Fig. 4.9 shows the SEM images of corresponding AFM images, given in Fig. 4.7. Films deposited at low oxygen pressures ($PO_2$ < 350 mTorr) show a rather flat morphology covered with small grains distributed homogeneously over the film surface. The latter corroborates the morphology observed by AFM and consequently increases the roughness of the films. On the other hand, at high oxygen pressures ($PO_2 \geq 350$ mTorr), SEM images reveal a flat and smooth morphology. Additionally, some small grains randomly distributed over the film surface can be observed. As mentioned before, high pressures favor a smoother surface.

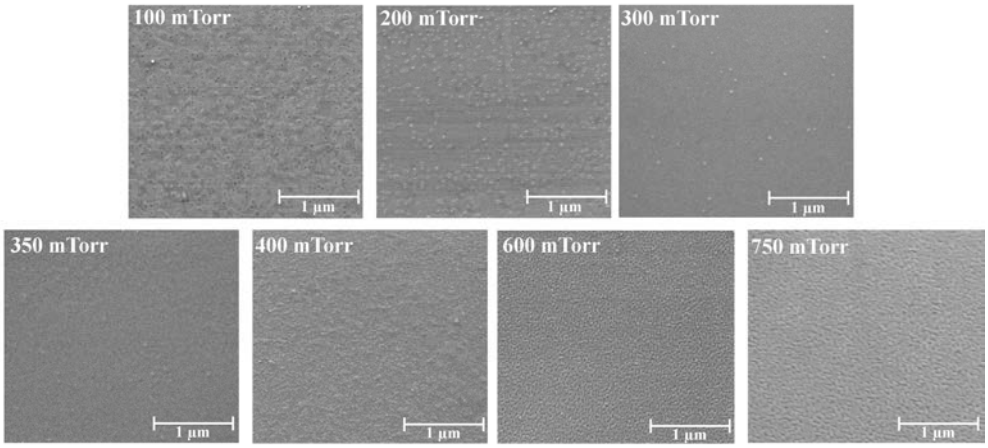


Figure 4.9 SEM micrographs of corresponding AFM images (see Fig.4.7) of PNMO thin films grown at 850°C under different oxygen pressures (ranging from 100 to 750 mTorr).

The presence of these small grains at the film surface may be due to the presence of NiO secondary phase, as previously detected by XRD patterns (see Fig 4.2). On the other hand, the existence of a nanostructured surface was also detected in LNMO systems, and it was attributed to the formation of $NiO_x$ segregates after high annealing temperatures (800°C-900°C). A detailed study on $NiO_x$ segregates was carried out in chapter 3 (see section 3.3.2).

## 4.1.2.2 Morphology at different growth temperatures

In order to evaluate the surface quality of PNMO films as a function of the growth temperature, the morphology of the films has been studied by AFM and SEM measurements. Fig. 4.10 depicts AFM images in tapping mode of films grown under a fixed oxygen pressure of 350 mTorr at different growth temperatures (ranging from 200 to 900°C).

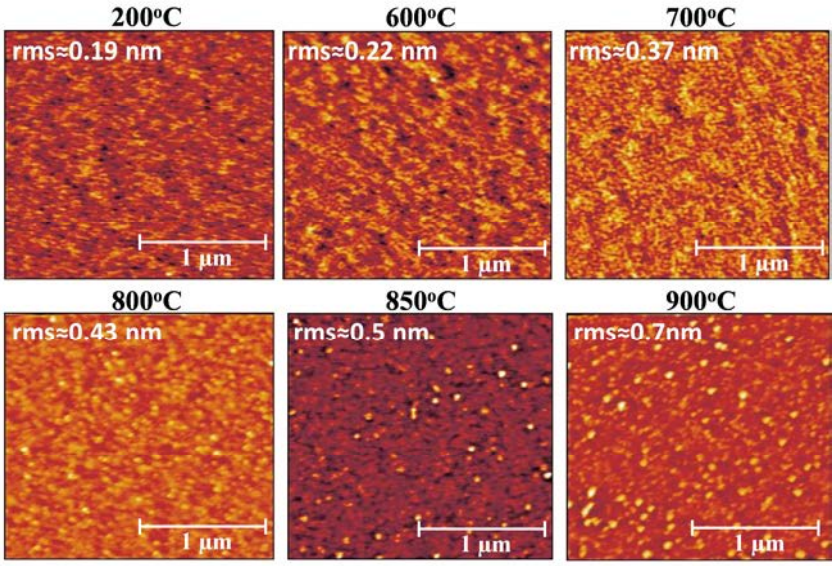


Figure 4.10. AFM topography ($2x2\mu m^2$ area) of PNMO thin films grown under 350 mTorr $O_2$ at different growth temperatures (ranging from 200°C to 900°C) with in-situ annealing at the same growth temperature (1h under 420 Torr $O_2$).

Fig. 4.10 depicts AFM images of PNMO films for different growth temperatures. It can be observed that for PNMO films grown at low temperatures, from 200°C to 700°C, AFM images show a flat surface without the presence of grains. Moreover, rms roughness values of the films obtained from the AFM data are below 0.4 nm, indicating that the surface roughness is similar than that of the steps-terraces morphology of the underlying substrates (see chapter 2 section 2.2.1.2). At higher growth temperatures ($T \geq 800^oC$), films show a granular morphology over the entire surface. The presence of grains is probably due to NiO segregations (detected by XRD), as observed previously in LNMO films (chapter 3, section 3.3.2). In this regard, this variation in morphology can be also appreciated in the roughness of the samples, whose value increases up to rms ≈ 0.7 nm for 900°C (see Fig. 4.11). Nevertheless, a low roughness values (rms < 1 nm) can be appreciated in all PNMO films, grown at 350 mTorr $O_2$.

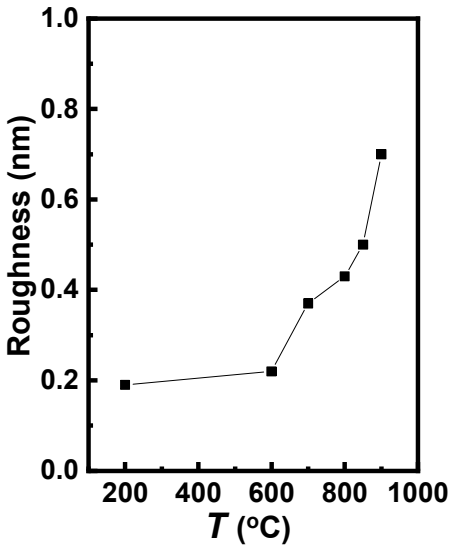


Figure 4.11. Roughness as a function of temperature of PNMO thin films grown under 350 mTorr $O_2$ at different growth temperatures ranging from 200°C to 900°C.

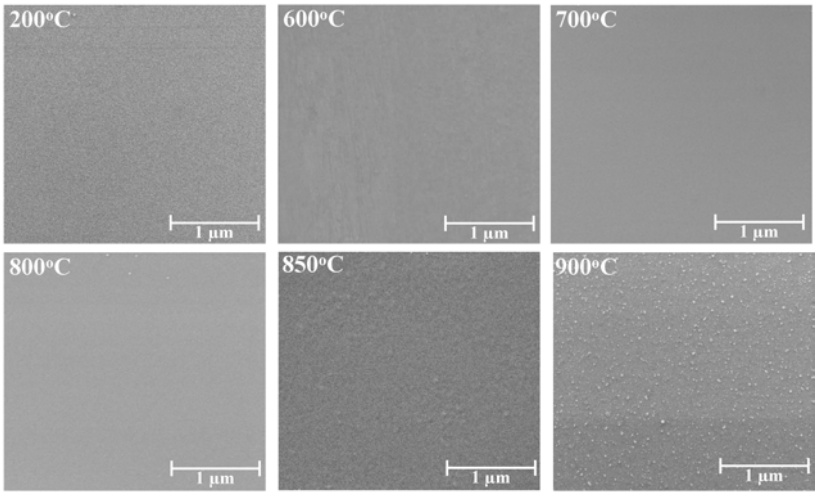


Figure 4.12. Corresponding SEM micrographs of PNMO thin films grown under 350 mTorr $O_2$ at different growth temperatures (from 200°C to 900°C) with in-situ annealing at the same growth temperature (1h under 420 Torr $O_2$).

Additionally, the surface of PNMO films deposited at different substrate temperature was also examined by SEM (Fig. 4.12). SEM images reveal a flat and homogeneous surface for all PNMO films, which corroborates the morphology observed by AFM (see Fig 4.10). Nevertheless, some small grains, distributed randomly at the surface, can also be observed, especially in samples grown/annealed at high temperatures (800°C-900°C). In particular, the sample grown at 900°C has a surface morphology with higher grain density, which is also

reflected in an increase of the roughness (rms ≈ 0.7 nm). In addition, XRD patterns showed the existence of a secondary NiO phase (see Fig 4.5). The NiO peak becomes more intense at high growth temperatures (800°C-900°C), which could be related to the formation of $NiO_x$ segregates at the film surface. For the films grown/annealed in the 200°C-700°C range, the secondary NiO phase was not clearly detected by XRD, as corroborated by AFM and SEM images. As previously mentioned, the existence of a nanostructured surface was also detected in LNMO systems and was attributed to the formation of $NiO_x$ segregates after annealing at high temperatures (800°C-900°C). In fact, in the series of PNMO samples (grown/annealed in the 800°C-900°C range) presented in this section, the formation of $NiO_x$ segregates was more pronounced, which corroborates what was discussed in LNMO films (see chapter 3, section 3.3.2).

## 4.1.3 Magnetic properties

Synthesis conditions greatly influence the magnetic properties and ferromagnetic (FM) transition temperature $T_C$ of PNMO systems. As previously discussed, in case of RNMO systems (see chapter 1), the ferromagnetism arises by superexchange interaction of B-site cations i.e., $Ni^{2+}$ and $Mn^{4+}$, while disorder arises due to the $Ni^{3+}$–O–$Ni^{3+}$ antiferromagnetic (AF) superexchange interactions. Defects and cationic vacancies (affected by growth conditions) can also affect the B-site cationic ordering and suppress ferromagnetism [37]. On the other hand, a gradual structural change occurs into RNMO structure when R (≠ La) is replaced by a rare-earth element with smaller ionic radius, thus affecting magnetic properties. Consequently, the FM transition temperature $T_C$ monotonically decreases with decreasing the $R^{3+}$ ionic radius [244]. Therefore, compared to LNMO systems, a lower $T_C$ is expected for PNMO thin films. In this section, the dependence of magnetic properties on growth conditions (namely growth temperature and oxygen pressure) has been studied in order to obtain qualitative information about the Ni/Mn cation ordering at the B sites in our PNMO films.

### 4.1.3.1 Magnetic properties as a function of oxygen pressure

To study the dependence of oxygen pressure on the magnetic properties of films, the temperature-dependent in-plane magnetization under an applied field of 5 kOe of PNMO thin films (deposited at 850°C under different oxygen pressures) are shown in Fig. 4.13 (a). For more details, Fig. 4.13 (b) shows the $T_C$ (estimated from inflection point) as a function of oxygen pressure.

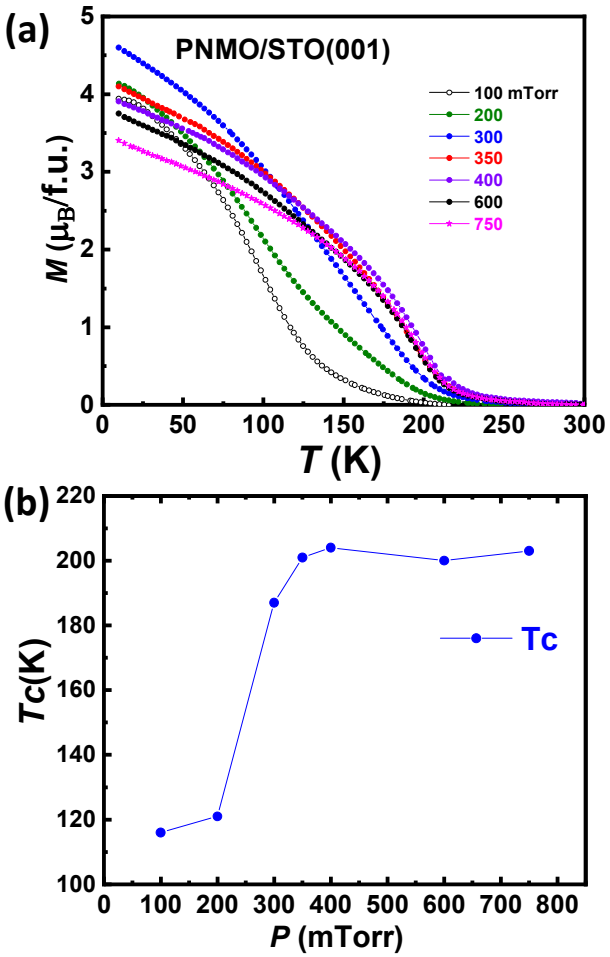


Figure 4.13 (a) Temperature dependence of in-plane magnetization under an applied field of 5 kOe ($\mu_0$H =0.5 T) of PNMO thin films grown at 850°C under different oxygen pressures (ranging from 100 to 750 mTorr). (b) Curie temperature $T_C$ as a function of oxygen pressure for the same films.

In Fig 4.13, it can be appreciated that, by increasing the oxygen pressure, the Curie temperature $T_C$ of the PNMO films improves (increases), as typically expected for a FM ordering. Samples grown under oxygen pressures ranging from 100 to 300 mTorr show a sharp increase of $T_C$ from ~116 K to ~187 K. Above 350 mTorr, the $T_C$ remains mainly constant around 200 K. In addition, no secondary magnetic transition was observed at low temperature. These results clearly demonstrate that the ordering of $Ni^{2+}$ and $Mn^{4+}$ ions is strongly affected by the oxygen pressure during deposition. The value of FM-$T_C$ in RNMO structure is determined by the magnitude of the spin-transfer integral within the superexchange framework [244] [245]. The low-$T_C$ phase of RNMO has been attributed to trivalent oxidation states, $Ni^{3+}$ and $Mn^{3+}$, while the high-$T_C$ phase has been shown to be characteristic of atomically ordered $Ni^{2+}$ and $Mn^{4+}$ [96].

Nevertheless, lowering the oxygen growth pressure ($PO_2 \leq 300$ mTorr) can result in variation in the defect concentration (such as oxygen vacancies or cation related defects), which can

induce structural distortions thus affecting the perovskite structure and the B-site cation order [91]. Oxygen vacancies concentration increases when films are deposited at low oxygen pressure, which breaks the $Ni^{2+}$–O–$Mn^{4+}$ superexchange ferromagnetic interaction and leads to higher spin disorder, hence decreasing $T_C$.

In this series of samples, good FM-$T_C$ properties have been obtained in two samples grown under oxygen pressure of 350 and 400 mTorr $O_2$ with $T_C$ values about ~200K (see Fig. 4.13(b)). M(H) hysteresis loops measured at 10K with *H* applied in-plane corresponding to these two samples are shown in Fig. 4.14. The shape of the M(H) loop is practically identical for both samples. Consequently, similar coercive field (Hc ≈ 500 Oe) and same saturation magnetization *(M*s ≈ 5 $\mu_B$/f.u) were extracted for both samples. Magnetization remanence $M_r$ slightly decreases by increasing oxygen pressure from $M_r \approx 2.7$ $\mu_B$/f.u to 2.6 $\mu_B$/f.u, for 350 and 400 mTorr $O_2$, respectively. The estimated values of saturation magnetization equal to the theoretical spin-only value of 5 $\mu_B$/f.u [1] [145] [28], encountered in fully ordered $Pr_2Ni^{2+}Mn^{4+}O_6$ systems.

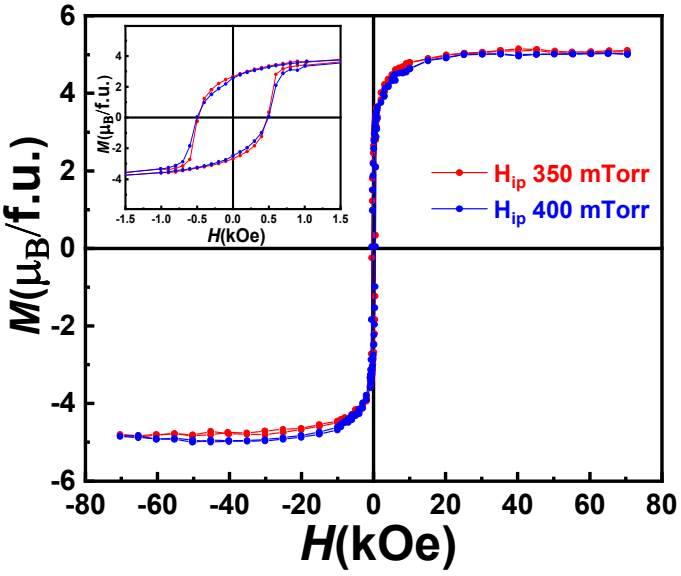


Figure 4.14. M(H) hysteresis loops of two samples grown/annealed at 850°C under an oxygen pressure of 350 mTorr and 400mTorr, measured at 10K for H applied in-plane. The inset shows in detail the low field region.

On the other hand, previous reports by M. P. Singh et al., [29] signaled that good FM properties (i.e., $T_C \approx 214$ K and Ms ≈ 4.35 $\mu_B$/f.u at 10K) have been found in PNMO thin films grown by PLD under 900 mTorr $O_2$ at 800°C. Nevertheless, they found the presence of an additional magnetic transition $T_{C2} \approx 126$ K, which was assigned to cation disordering and the coexistence of multiple oxidation states of Ni and Mn [29].

In summary, the oxygen pressure used during deposition of PNMO thin films plays an important role to stabilize the distinct valence states of Ni and Mn cations in the films, which subsequently affects the magnetic properties. Therefore, in our films grown/annealed at 850°C under different oxygen pressures, the optimal $T_C$ and Ms (very close to the optimal values [120] [30] [29]) have been obtained only at high oxygen pressure (350-400 mTorr $O_2$).

### 4.1.3.2 Magnetic properties as a function of substrate temperature

In the following, the ferromagnetic transition temperature $T_C$ of PNMO thin films grown under 350 mTorr $O_2$ at different growth temperatures (200°C ≤ Tg ≤ 900°C) was explored. Fig. 4.15 (a) shows in-plane magnetization measurements as a function of temperature, under an applied field of 5 kOe, while Fig. 4.15 (b) depicts the evolution of $T_C$ as a function of deposition temperature.

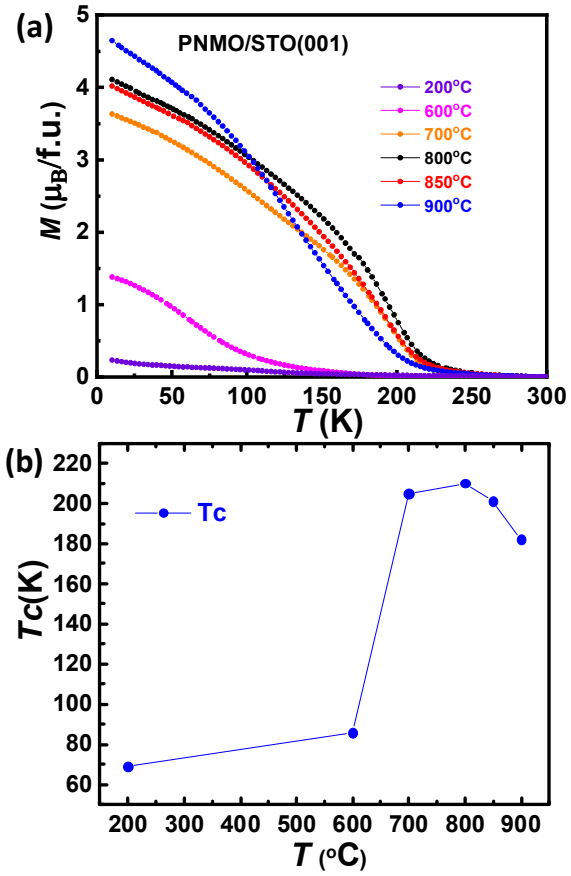


Figure 4.15 (a) Temperature dependence of in-plane magnetization under an applied field of 5 kOe ($\mu_0 H$ = 0.5 T) of PNMO thin films grown under 350 mTorr $O_2$ and deposited at different growth temperatures (ranging from 200°C to 900°C). (b) Curie temperature $T_C$ as a function of the growth temperature for the same films.

In all films, M(T) curves are characterized by a single magnetic transition. Samples grown/annealed at temperatures below or equal to 600°C show very deficient magnetic properties with $T_C \leq 86$ K. When the growth temperature increases to 800°C, $T_C$ rises up to ~210 K; while from 850 °C on, the ferromagnetic transition slightly decreases again. The evolution of $T_C$ as a function of the growth temperature is shown in Fig. 4.15 (b).

According to these results, the reduced $T_C$ in samples grown/annealed underneath 700°C could be attributed to the fact that the growth temperature may not be sufficient to promote ordering of Ni and Mn cations. Ordering processes take place by a thermally activated diffusion of cations. Therefore, higher temperatures control growth kinetics and tend to increase ordering [246] [247]. Besides, as mentioned before (see chapter 3), high growth and annealing temperatures maximize the B-site cation ordering. In conclusion, the improvement of $T_C$ in PNMO films grown/annealed at high temperatures ($T \geq 700$°C) promotes Ni/Mn cation ordering and consequently an increase in the $T_C$ to values very close to the bulk value of 228 K [120]. At the same time, the absence of a secondary transition at low temperatures in our films indicates a very low concentration of anti-site disorders.

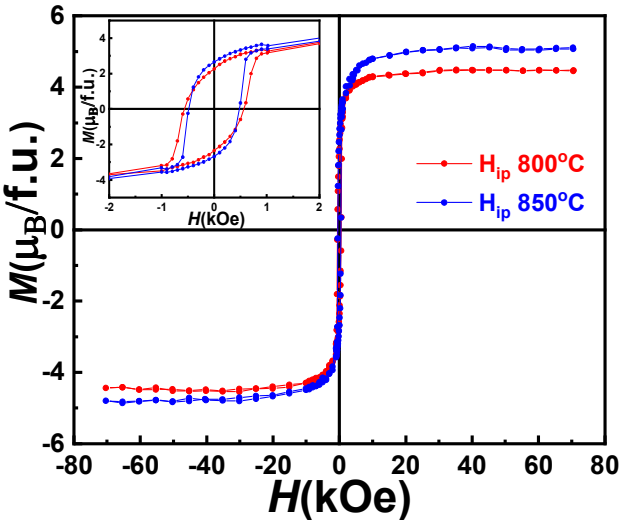


Figure 4.16. M(H) hysteresis loops of two samples grown/annealed at 800°C and 850°C under an oxygen pressure of 350 mTorr, measured at 10K for H applied in-plane. The inset shows in detail the low field region.

M(H) hysteresis loops corresponding to two PNMO samples with good FM-$T_C$ properties, grown/annealed at 800°C ($T_C$ ~ 210 K) and 850°C ($T_C$ ~ 201 K) (see Fig 4.15 (b)), measured at 10K with a magnetic field applied in-plane, are shown in Fig. 4.16. For both samples, the hysteretic M(H) behavior can be clearly observed, confirming the ferromagnetic character of PNMO thin films. The inset in Fig. 4.16 shows the low field region in detail. The coercive field *H*c was found to be Hc = 565 Oe and 482 Oe for samples deposited at 800°C and 850°C, respectively. On the other hand, the magnetization remanence *M*r increases from

*M*r ≈ 2.3 $\mu_B$/f.u to 2.7 $\mu_B$/f.u and the saturation magnetization increases from Ms ≈ 4.5 $\mu_B$/f.u. to 5 $\mu_B$/f.u, while increasing the growth temperature, from 800°C to 850°C. These Ms values are close to the expected spin-only value of 5.0 $\mu_B$/f.u, for ferromagnetic ordering of $Ni^{2+}$ (S=1) and $Mn^{4+}$ (S=3/2) ions [1].

The $T_C$ and Ms values of our samples are in good agreement with previous reports, where bulk PNMO samples showed a single ferromagnetic-to-paramagnetic transition at 228 K and a Ms ≈ 4.95 $\mu_B$/f.u at 50 kOe field with a Hc ≈ 450 Oe [120]. Additionally, in PNMO samples synthesized by conventional solid-state reaction route, the FM-$T_C$ occurred at 210 K and a Ms was found be around 4.8 $\mu_B$/f.u (15K, 5T) [248]. On the other hand, in our results, although the $T_C$ is slightly higher in the sample grown at 800°C, this film showed a lower *Ms* value than that of the film grown at 850 °C. This reduction of magnetization could be caused by the formation of oxygen vacancies, antiphase boundaries and alternatively some antisite defects (i.e., Ni–O–Ni or Mn–O–Mn), all common defects in double perovskites structures [41] [104]. In conclusion, films with a $T_C$ and Ms very close to the optimal values [120] [30] [29] have been obtained only at growth temperatures in the 800-850°C range.

## 4.1.4 Transport properties

As mentioned before (see chapter 3), RNMO (R = La, Pr) compounds have potential applications in spintronic devices such as magnetodielectric capacitors and spin filtering tunnel junctions [1] [19] [144] [192], where films have to be insulating. Therefore, we have studied the temperature dependence of the resistivity of a 47.6 nm-thick PNMO film (grown/annealed at 800°C under 350 mTorr $O_2$) displaying good ferromagnetic properties (i.e., $T_C$ ≈ 210 K and Ms ≈ 4.5 $\mu_B$/f.u. at 10K).

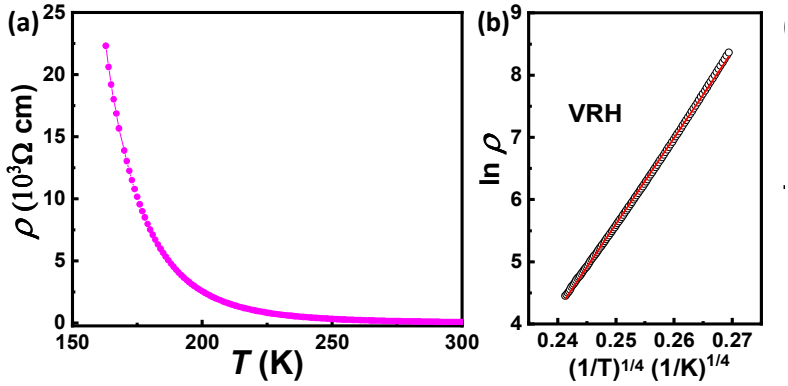


Figure 4.17. (a) Temperature-dependent resistivity of a 47.6-nm-thick PNMO film (grown/annealed at 800°C under 350 mTorr $O_2$) under zero magnetic field. (b) Plot of ln $\rho$ *vs* $(1/T)^{1/4}$ for the same sample. The red line represents the fitting of the experimental data.

The temperature dependence of the resistivity $\rho$(T) measured in the range 150K ≤ T ≤ 300K (at zero magnetic field) of the PNMO film is shown in Fig. 4.17 (a). The measurement shows that the resistivity increases with decreasing the temperature, thus exhibiting an insulating behaviour in the whole measured temperature range. At lower temperatures (T < 150 K), $\rho$(T) was not measurable due to the high sample resistance. A three-dimensional (3D) variable-range hopping (VRH) as described in the equation (3.1) (chapter 3, section 3.1.4) describes well the experimental results. Indeed, Fig. 4.17 (b) shows the 3D VRH fitting of the ln $\rho$ versus $(1/T)^{1/4}$ plot, where the slope of the curve corresponds to $T_0^{1/4}$. From the fit, the extracted $T_0$ value is of ~ $4.1 \times 10^8$ K, which is in good agreement with previous reports on RNMO compounds [73] [36].
Finally, it should be noticed that the temperature dependence of the resistivity at high temperature range does not allow to rule out the thermal activation mechanisms. This latter is described by an Arrhenius law [198] [199]. The extracted value of the activation energy $E_0$ for our PNMO film was found to be $E_0 \approx 0.18 \pm 0.1$ eV, which is comparable to that of charge-ordered RNMO compounds [73] [200] and $La_2MRuO_6$ (M=Mg; Co; Ni and Zn (~0.07-0.17 eV) [201].

## 4.1.5 Chemical composition

The physical properties of the films can be affected by their stoichiometry; therefore the study of their composition can provide useful information on the material. In this section, we will explore the influence of the oxygen pressure and growth temperature on the chemical composition and stoichiometry ratio of PNMO thin films, whose structural, morphological and magnetic properties were presented in the previous sections.

The chemical composition and the stoichiometry ratio of PNMO thin films grown on STO substrates under different oxygen pressures (ranging from 100 to 750 mTorr) and temperatures ($200^oC \leq T \leq 900^oC$) have been analyzed by electron probe microanalysis (EPMA). Fig. 4.18 (a) and (c) show the stoichiometry ratio and Fig. 4.18 (b) and (d) show the atomic percentage of each element for the same samples deposited under different oxygen pressures and temperatures. The quantitative data, accessed by EPMA, are shown in Table 4.1 and 4.2. Tables show for each oxygen pressure/growth temperature (1st column), the atomic percentage of each element (2nd-5th columns) which is normalized by their atomic weight, the proportion of Pr per unit formula f.u. (6th column), the Ni:Mn ratio (7th column), and the value of x (8th column). Due to the presence of oxygen in both film and substrate, oxygen concentration is not computed due to the presence of the relatively large O background signal from the substrate, which is difficult to separate from the one coming from the film. Therefore, a nominal stoichiometry is imposed for oxygen, in the composition of the samples expressed as $Pr_{2-\delta}Ni_{1-x}Mn_{1+x}O_6$.

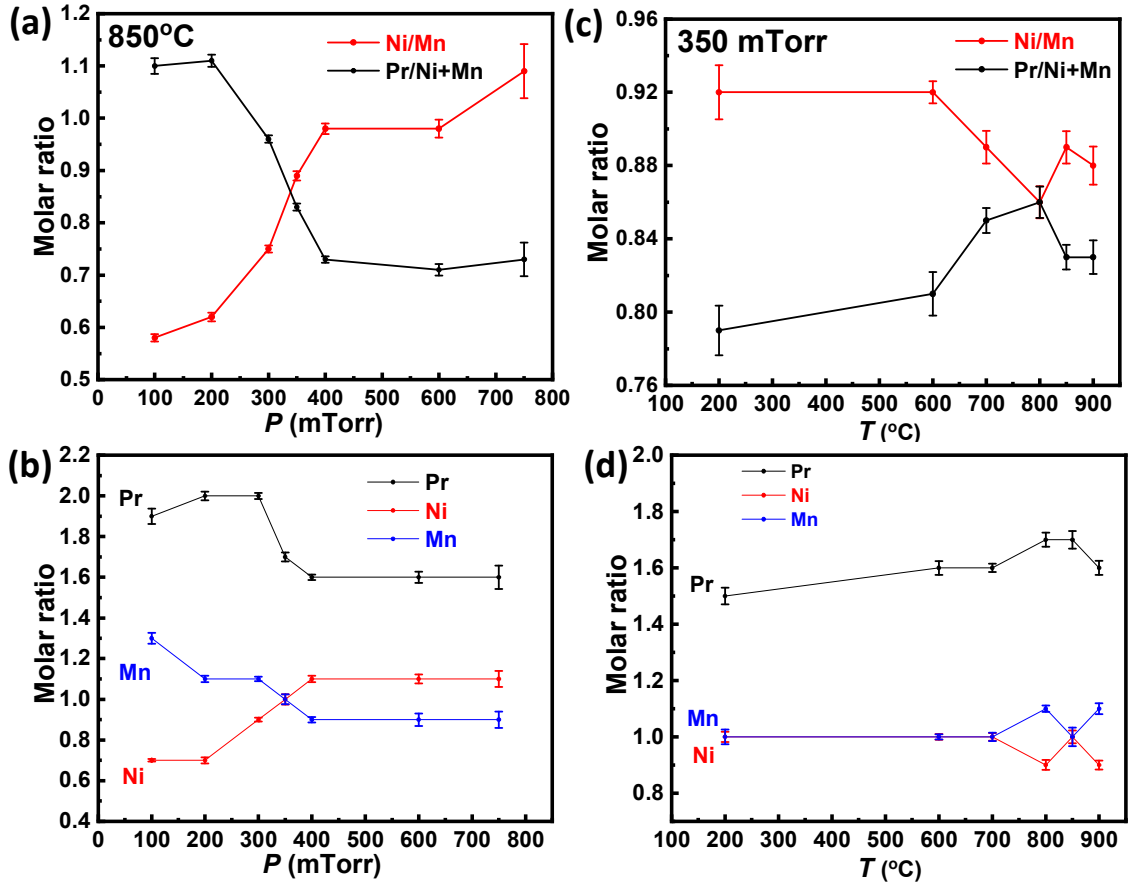


Figure. 4.18 (a) Stoichiometry ratio of PNMO thin films grown on STO (001) substrates under different oxygen pressures (ranging from 100 to 750 mTorr) at 850°C for 1h and (c) under different temperatures (200°C ≤ T ≤ 900 °C) at 350 mTorr $O_2$ for 1h. (b) and (d) atomic percentage of the chemical elements for the same samples (obtained by EPMA). Error bars have been estimated from the dispersion of the EPMA results at different point of the samples.

**Table 4.1:** Chemical composition and stoichiometry ratio of $Pr_{2-\delta}Ni_{1-x}Mn_{1+x}O_6$ thin films grown under different oxygen pressures (ranging from 100 to 750 mTorr) at 850°C.

| $PO_2$ (mTorr) | Pr (atom %) | Ni (atom %) | Mn (atom %) | O (atom %) | Pr (per f.u.) | Ni:Mn | x |
|---|---|---|---|---|---|---|---|
| 100 | 19.1 (1) | 7.1 (2) | 13.0 (8) | 65.3 (3) | 1.91 (2) | 0.55 (1) | 0.29 (2) |
| 200 | 20.0 (7) | 7.2(4) | 11.3 (5) | 66.6 (1.3) | 2.17 (1) | 0.64 (1) | 0.22 (2) |
| 300 | 20.0 (4) | 9.0 (3) | 11.0 (3) | 68.0 (9) | 2.00 (3) | 0.82 (2) | 0.10 (3) |
| 350 | 17.2 (3) | 10.0 (1) | 10.0 (1) | 69.7 (6) | 1.72 (3) | 1.00 (2) | 0.00 |
| 400 | 16.4 (4) | 11.2(5) | 9.1 (4) | 68.1 (8) | 1.62 (2) | 1.23(1) | -0.10 (2) |
| 600 | 16.3 (1) | 11.0 (1) | 9.2 (1) | 66.1(3) | 1.62 (1) | 1.20 (2) | -0.09 (2) |
| 750 | 16.0 (3) | 11.1 (2) | 9.2 (2) | 65.8 (7) | 1.58 (3) | 1.21 (2) | -0.10 (2) |

**Table 4.2:** Chemical composition and stoichiometry ratio of $Pr_{2-\delta}Ni_{1-x}Mn_{1+x}O_6$ thin films deposited at different growth temperatures (ranging from 200°C to 900°C) under 350 mTorr $O_2$.

| T(°C) | Pr (atom %) | Ni (atom %) | Mn (atom %) | O (atom %) | Pr (per f.u.) | Ni:Mn | x |
|---|---|---|---|---|---|---|---|
| 200 | 15.2 (4) | 10.1 (2) | 10.1 (2) | 67.5 (7) | 1.50 (2) | 1.00 (1) | 0.00 |
| 600 | 16.3 (5) | 10.0 (1) | 10.0 (1) | 64.5 (6) | 1.63 (2) | 1.00 (1) | 0.00 |
| 700 | 16.0 (3) | 10.1 (1) | 10.0 (1) | 64.0 (3) | 1.58 (3) | 1.00 (2) | 0.00 |
| 800 | 17.2 (2) | 9.1 (2) | 11.2 (2) | 63.7 (4) | 1.69 (2) | 0.81 (2) | 0.10 (1) |
| 850 | 17.2 (3) | 10.0 (1) | 10.0 (1) | 69.7 (6) | 1.72 (3) | 1.00 (2) | 0.00 |
| 900 | 16.1 (3) | 9.3 (2) | 11.4 (2) | 63.5 (5) | 1.56 (2) | 0.82 (2) | 0.10 (1) |

In Fig 4.18 (a), one can observe that the stoichiometry ratio of PNMO films (grown at 850°C) show a strong dependence on oxygen pressure $PO_2$. Samples grown at low oxygen pressures (ranging from 100 to 300 mTorr) present a Pr:(Ni+Mn) atomic ratio near 1 (see black line), while the Ni/Mn ratio is below 1 (see red line).One can conclude that these samples become slightly Ni-deficient with a slight Mn excess. Contrarily, in samples grown at high oxygen pressures ($Po_2 \geq 350$ mTorr), the Pr:(Ni+Mn) ratio is clearly below 1, while the Ni/Mn ratio is close to 1, indicating that films have a certain degree of Pr deficiency (see table 4.1).

In this regard, samples grown at 100 mTorr and 200 mTorr $O_2$ show a Ni/Mn ratio of about 0.55 ($x \approx 0.29$, $Pr_{1.9}Ni_{0.7}Mn_{1.3}O_{6.0}$) and 0.64 ($x \approx 0.22$, $Pr_{2.0}Ni_{0.7}Mn_{1.1}O_{6.0}$), respectively, i.e. with Ni deficiency which thusaffects the ferromagnetic properties ($T_C < 120$ K) (see Fig. 4.13). At high oxygen pressures ($PO_2 \geq 350$ mTorr), the Pr:(Ni+Mn) ratio is below 1 and, in spite of this slight Pr deficiency, samples exhibit good FM properties. In particular, films grown at 350 mTorr and 400 mTorr $O_2$, with Pr:(Ni+Mn) ratio of ~ 0.86 ($Pr_{1.7}Ni_{1.0}Mn_{1.0}O_{6.0}$) and ~ 0.82 ($Pr_{1.6}Ni_{1.1}Mn_{0.9}O_{6.0}$), respectively, have good saturation magnetization $Ms \approx 5\ \mu_B$/f.u., and $T_C \approx 201$ K and $\approx 204$ K , (see Fig 4.14).

Finally, Fig 4.18 (c) shows the atomic ratio of PNMO films deposited at different growth temperatures for $P_{O2}$ = 350 mTorr. It is found that all samples present a Pr:(Ni+Mn) atomic ratio clearly below 1, while Ni/Mn is near 1, indicating that the films show Pr deficiency (see table 4.2). Similar results were also observed in samples deposited at different oxygen pressures (see Fig 4.18 (a)). At the same time, it can be also observed that by increasing the growth temperature ($T \geq 700$°C) the amount of Pr slightly increases, but is still below the expected stoichiometry.

In conclusion, in films grown/annealed at high temperatures ($700°C \leq T \leq 850°C$), under 350 mTorr $O_2$, the stoichiometry revealed by EPMA showed a Ni/Mn ratio very close to 1 and a Pr:(Ni+Mn) ratio with certain degree of Pr deficiency. In spite of this Pr deficiency, the stoichiometry of the samples has little impact on the ferromagnetic properties. For instance, the film grown at 800°C shows good FM transition (i.e., $T_C \approx 210$ K) and high saturation magnetization ($Ms \approx 4.5\mu_B$/f.u.), while Ni/Mn ≈ 0.81 ($x \approx 0.10$, $Pr_{1.7}Ni_{0.9}Mn_{1.1}O_6$).

In summary, growth conditions such as oxygen partial pressure, growth temperature and annealing have been previously optimized, with the aim of obtaining PNMO thin films with $T_C$ and *M*s very close to the optimum values. The optimized samples with good ferromagnetic properties have been deposited under an oxygen pressure of 350 mTorr and high growth temperatures (800°C and 850°C). In this regard, the first sample, grown/annealed at 800°C, showed good FM properties (i.e., $T_C \approx 210$ K and Ms ≈ 4.5 $\mu_B$/f.u. at 10K) and a Ni/Mn ratio of about 0.81 (x ≈ 0.10, $Pr_{1.7}Ni_{0.9}Mn_{1.1}O_6$). The second sample, grown/annealed at 850°C, showed good FM properties (i.e., $T_C \approx 201$ K and Ms ≈ 5$\mu_B$/f.u. at 10K) and a Ni/Mn ratio of 1.0 (x ≈ 0, $Pr_{1.7}Ni_{1.0}Mn_{1.0}O_6$). In spite of this slight Pr deficiency, films show $T_C$ and Ms in close agreement with the reported values [120] [29]. For further studying the influence of film thickness, we have chosen PNMO thin films grown/annealed at 800°C under 350 mTorr $O_2$ as the best growth conditions. Using these conditions, we have obtained samples with good ferromagnetic properties (i.e., high $T_C$ and Ms).

# 4.2 Influence of film thickness on structural and magnetic properties

In the present section, the role of thickness is explored in PNMO thin films deposited on $SrTiO_3$ (STO) and $LaAlO_3$ (LAO) substrates. Taking into account the optimization carried out in the previous section, PNMO thin films with the best FM properties (i.e., $T_C \approx 210$ K and Ms ≈ 4.5$\mu_B$/f.u.) were obtained at – high oxygen pressures and high growth temperatures (i.e., 350 mTorr and 800°C). Here, films were deposited under these conditions and thickness was modulated by varying the deposition time (i.e., 60, 30, 15, 7, 5 and 3 min). After film deposition, all as-grown samples were in-situ annealed at 800°C (1h under 420 Torr $O_2$).

The purpose of selecting two different substrates is to study the effect of strain state (induced by lattice mismatch with the underlying substrate) on the crystal structure of the films and its impact on the magnetic properties. The strain state in the film grown on a perovskite substrate is expected to strongly depend on the film thickness. On the other hand, in order to determine spin, orbital, valence state of ions and ferromagnetic character in PNMO thin films, X-ray absorption spectroscopy (XAS) and X-ray magnetic circular dichroism (XMCD) measurements were carried out at Pr $M_{4,5}$, Ni $L_{2,3,}$ Mn $L_{2,3}$ and O *K* edges. In this section, we have carried out a comparative study on some characteristic samples (thinner and thicker films). At the same time, these experiments were also supported by theoretical simulation.

## 4.2.1 Structural properties

XRR data of PNMO thin films on STO and LAO substrates of different thicknesses are depicted in Fig.4.19 (a) and (b). Film thickness was obtained from the positions of XRR curve minima (see appendix A.4.5).

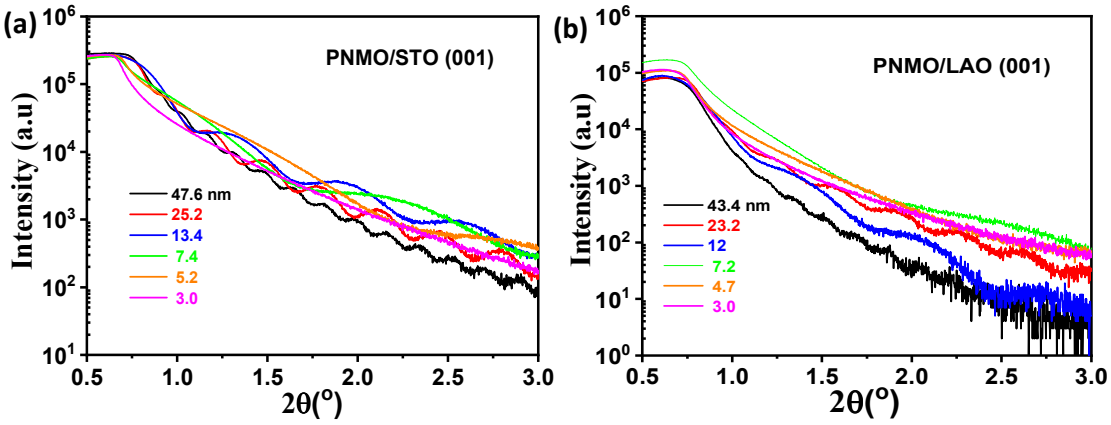


Figure 4.19. XRR data of PNMO thin films grown at 800°C under 350 mTorr $O_2$ on: a) (001) STO, and b) (001) LAO substrates, varying the deposition time (i.e., 60, 30, 15, 7, 5 and 3 min).

XRD diffraction patterns of PNMO films of different thicknesses deposited on STO (001) and LAO (001) substrates are depicted in Fig 4.20 (a) and (c). As previously, the highest intensity peak in each diffractogram corresponds to the STO and LAO substrate reflections (see dashed vertical black lines). As mentioned in chapter 2 (see section 2.2), the PNMO films ($a_{p\ \mathrm{PNMO\ bulk}} \approx 3.848$ Å [30] where $a_p$ is the bulk pseudocubic cell parameter) grown on STO substrate ($a_{p\ \mathrm{STO}} \approx 3.905$ Å) and LAO substrate ($a_{p\ \mathrm{LAO}} \approx 3.789$ Å) are under tensile strain and compressive strain, respectively. In addition, XRD patterns indicate clear thickness dependence of structural properties in PNMO films.

Figs. 4.20 (b) and (d) show the (002) reflection of both STO and LAO substrate and PNMO phase. In Fig 4.20 (b) the (002) reflections of the PNMO peaks take place at 2θ values slightly higher than the ones ones of STO. This indicates that the out-of-plane lattice parameter ($a_\perp$) of the unit cell is elongated with respect to the corresponding pseudocubic lattice parameter of bulk PNMO ($a_{bulk}$=3.848 Å) [30] (see Fig 4.22 (a)). The latter is in contradiction with the lattice mismatch imposing a tensile in-plane strain, where the shrinking of the out-of-plane parameter is expected. As mentioned before, this can be related to the presence of oxygen vacancies into structure (see section 4.1.1.1). On the contrary, in Fig. 4.20 (d), for PNMO on LAO substrates, the (002) reflection of the film occurs at lower 2θ angles than the ones of LAO (see dashed vertical black lines), indicating an out-of-plane expansion with respect to the lattice parameter of bulk PNMO. This is in agreement with the lattice mismatch imposing a compressive in-plane strain.

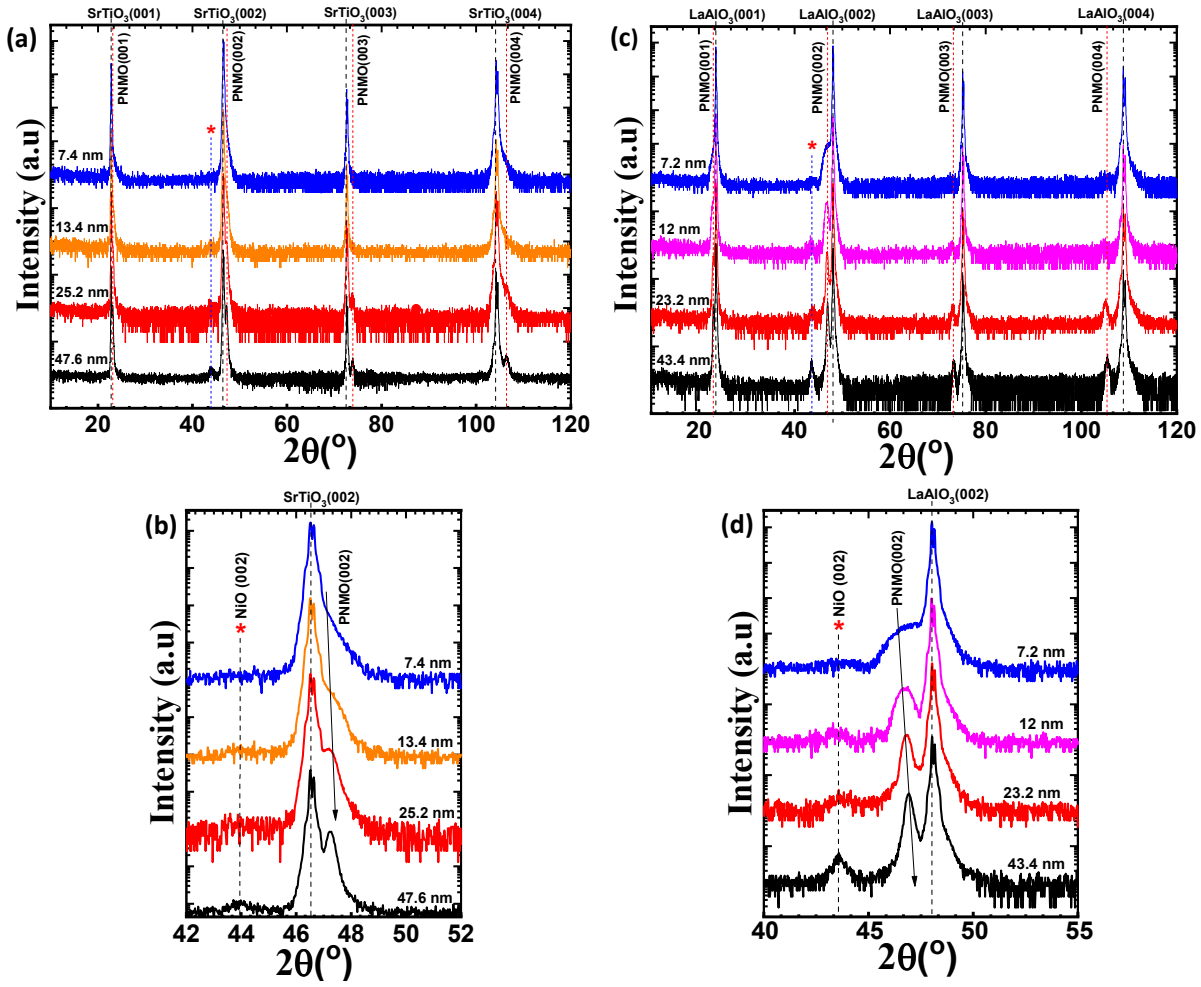


Figure 4.20 XRD θ/2θ scans of PNMO thin films grown at 800°C under 350 mTorr $O_2$ on (a) (001) STO and (c) (001) LAO substrates. (b) Zoom of the (002) reflection of both STO and PNMO. (d) Zoom of the (002) reflection of both LAO and PNMO. Parasitic phases are denoted by (*).

At the same time, in Fig 4.20 (b), the (002) reflections of the PNMO phase can be clearly observed only for the thickest films (47.6, 25.2 and 13.4 nm). Conversely, in the thinner film (7.4 nm) only STO peak can be observed. Moreover, it can also be appreciated that the position of the (002) peak shows a slight shift towards values higher 2θ when increasing the film thickness (see arrow). This observation indicates that as the film thickness increases, the out-of-plane lattice parameter ($a_\perp$) of the film decreases towards the PNMO bulk value (see Fig. 4.22 (a)). For instance, the lattice parameter ($a_\perp$) for the thicker film (47.6 nm) was found to be $a_\perp \approx 3.850$ Å.

In Fig 4.20 (d), in all XRD patterns of PNMO films on LAO , one can observe the (002) reflection of the PNMO phase. Similarly, as in PNMO films deposited on STO, by increasing the film thickness the position (002) PNMO peak shows a slight shift towards higher 2θ angles (see arrow). This indicates a decrease of the out-of-plane lattice parameter ($a_\perp$), approaching the bulk value as the film thickness increases (see Fig. 4.22 (b)). For instance,

the $a_{\perp}$ parameter of the thicker film (43.4 nm) was found to be $a_{\perp} \approx 3.874$ Å. On the other hand, it can also be appreciated (for both substrates) that when the film thickness decreases, the film peaks experience an broadening and decrease in intensity, maybe caused by interface diffusion effects and a loss of crystallinity in the films.

Finally, additional reflections denoted by (*), located at $2\theta \approx 43.9^{o}$ (PNMO/STO films) and $2\theta \approx 43.5^{o}$ (PNMO/LAO films), correspond to the parasitic NiO phase, as similarly found in samples deposited at different pressures and temperatures (see section 4.1.1). As the film thickness increases, the NiO peak increases in intensity. As discussed before, the presence of the secondary NiO phase in the PNMO compound is not well understood. This fact points out to the possibility of an increasing Pr-deficiency upon thickness as revealed by EPMA for thick samples (see section 4.1.4).

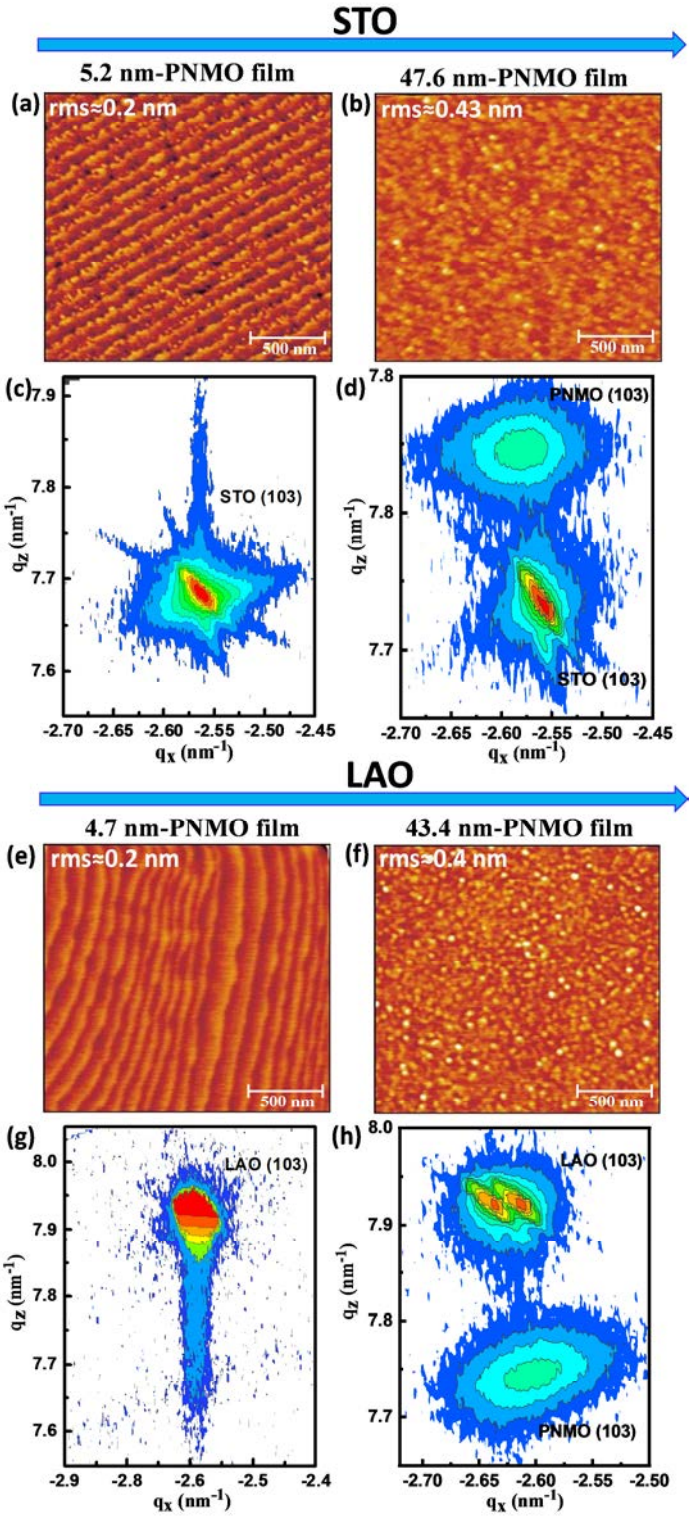


Figure 4.21. AFM topography images (2x2 μm$^2$) of PNMO thin films of different thicknesses deposited onto STO (001) [(a) and (b)] and LAO (001) [(e) and (f)] substrates. (c,d,g,h) Reciprocal Space Maps (RSMs) around (103) reflections of the same PNMO thin films (for both substrates).

In order to determine the values of in-plane ($a_{||}$) lattice parameters, reciprocal space maps (RSMs) were performed on PNMO/STO and PNMO/LAO samples. In the RSMs shown in Fig. 4.21, the *x* axis corresponds to the in-plane $q_x$ [100] direction and the *y* axis corresponds to out-of-plane $q_z$ [001] direction. In Fig. 4.21 (c,d), RSMs around the (103) STO and (103) PNMO reflections of the thinner (5.2 nm) and thicker (47.6 nm) PNMO/STO samples, are shown. In Fig. 4.21 (g,h), analogue RSMs around the (103) LAO and (103) PNMO reflections of the thinner (4.7 nm) and thicker (43.4 nm) PNMO/LAO samples are shown.

For comparison, AFM topography images of PNMO/STO and PNMO/LAO samples are also depicted in Fig 4.21. Topography images (Fig 4.21 (a) and (e)) for thinner samples deposited on STO (5.2-nmthick PNMO film) and LAO (4.7-nm-thick PNMO film) substrates reveal very high-quality surfaces with monoatomic steps suggesting layer-by-layer growth mode. Thus, the final film surface reproduces the starting substrate surface morphology with a very low roughness of ~0.2 nm (the same order as the roughness of the substrate after the thermal treatment). For thicker PNMO films (Fig 4.21 (b) and (f)) deposited on STO (47.6-nm-thick PNMO film) and LAO (43.4-nm-thick PNMO film) substrates, AFM images show a granular morphology over the entire film surface. Nevertheless, films present low rms roughness values around ~0.4 nm.

The RSM of the thinner (5.2 nm) PNMO/STO film (Fig. 4.21(c)) reveals both film and substrate (103) diffraction spots, and that the position in $q_x$ (q parallel) of (103) PNMO reflection coincides with that of the STO one. Accordingly, the in-plane pseudocubic cell parameter of this film is equal to that of the STO substrate ($a_{STO}$ = 3.905Å), showing that it grows fully strained. Concerning the thicker film (47.6 nm), in Fig. 4.21 (d), the RMS shows that the peak position of the PNMO film is slightly shifted towards a larger (absolute) value of $q_x$. The latter is idicating that the in-plane cell parameter of PNMO ($a_{||}$ = 3.877Å) is slightly smaller than the STO one ($a_{STO}$ = 3.905Å), and closer to bulk PNMO ($a_{bulk}$ = 3.848Å) [30]. On another hand, the $q_z$ value of the (103) PNMO reflection is larger than that of (103) STO (for both thin and thick films). Therefore, the out-of-plane lattice parameter ($a_{\perp}$) for 5.2-nm-thick PNMO film ($a_{\perp}$= 3.861Å) and 47-nm-thick PNMO film ($a_{\perp}$= 3.848Å) determined from $q_z$, is smaller than that of STO, in agreement with θ/2θ scans shown in Fig. 4.20 (a) and (b), respectively.

From the pseudocubic cell parameters extracted above, one can now calculate the PNMO cell parameters considering the monoclinic ($P2_1/n$) structure of the double perovskite. Therefore, these are given by the following: a = b = 5.483Å, c = 7.696Å for the 47.6-nm-thick PNMO film, and a = b = 5.519Å, c = 7.722Å for the 5.2 nm-thick PNMO film. These values are found to be similar to those of $La_2NiMnO_6$ [28] [249] and $R_2NiMnO_6$ systems [30] [248].

We turn now to PNMO films deposited on LAO substrates, RMSs in Fig. 4.21 (g) shows for thinner film (4.7 nm) that the position in $q_x$ (q parallel) of $(103)_{PNMO}$ reflection film coincides with the position of $(103)_{LAO}$ reflection. This indicates that the in-plane pseudocubic cell parameter of this film adopts the same value of the LAO substrate lattice parameter

($a_{LAO}$ = 3.789 Å and therefore that the film grows fully strained. Nevertheless, for the thicker film (43.4 nm), shown in Fig. 4.21 (h), it can be appreciated that the position of the peak from the PNMO film is slightly shifted towards a smaller (absolute) value of $q_x$, indicating that the in-plane cell parameter of PNMO ($a_{||}$ = 3.842Å) is slightly larger than that of LAO, and close to bulk one (3.848Å [30]). On the other hand, the value of $q_z$ $(103)_{PNMO}$ reflection is smaller than that of $(103)_{LAO}$ (for both thicknesses). This indicates that the out-of-plane lattice parameter for 4.7-nm-thick PNMO film ($a_{\perp}$= 3.891Å) and 43.4-nm-thick PNMO film ($a_{\perp}$= 3.874Å), determined from the $q_z$ value of $(103)_{PNMO}$ reflection, is larger than that of LAO, in agreement with θ/2θ scans in Fig. 4.20 (c) and (d).

Similarly to the calculations for PNMO/STO samples shown above, the monoclinic cell parameters of the PNMO/LAO films were calculated as: a=b=5.434Å, c=7.747Å for the 43.4-nm-thick PNMO film; and a=b=5.358Å, c=7.782Å for the 4.7-nm-thick PNMO film.

In summary, the variation of the in-plane and the out-of-plane cell parameters (in pseudo-cubic notation) for PNMO/STO and PNMO/LAO films are depicted in Fig 4.22 (a) and (b), respectively. For the thinner films, one can observe that the in-plane lattice parameters (red dashed line) match the STO and LAO lattice parameters ($a_{STO}$ = 3.905Å and $a_{LAO}$ = 3.789 Å, resp.), indicating that the film remains fully strained. When the film thickness increases, the in-plane lattice parameter decreases (resp. increases) for STO (resp. LAO) towards the bulk value (blue dashed line). In addition, the out-of-plane lattice parameter (for both substrates) decreases progressively towards the bulk value (blue dashed line) with increasing thickness. However, the values of out-of-plane parameter for PNMO/STO films are larger than the bulk value which is in contradiction with the lattice mismatch imposing a tensile in-plane strain, and thus a shrinking of the out-of-plane parameter is expected (as mentioned before). From these observations, we can conclude that a (partial) relaxation of the PNMO/STO and PNMO/LAO films takes place when thickness increases.

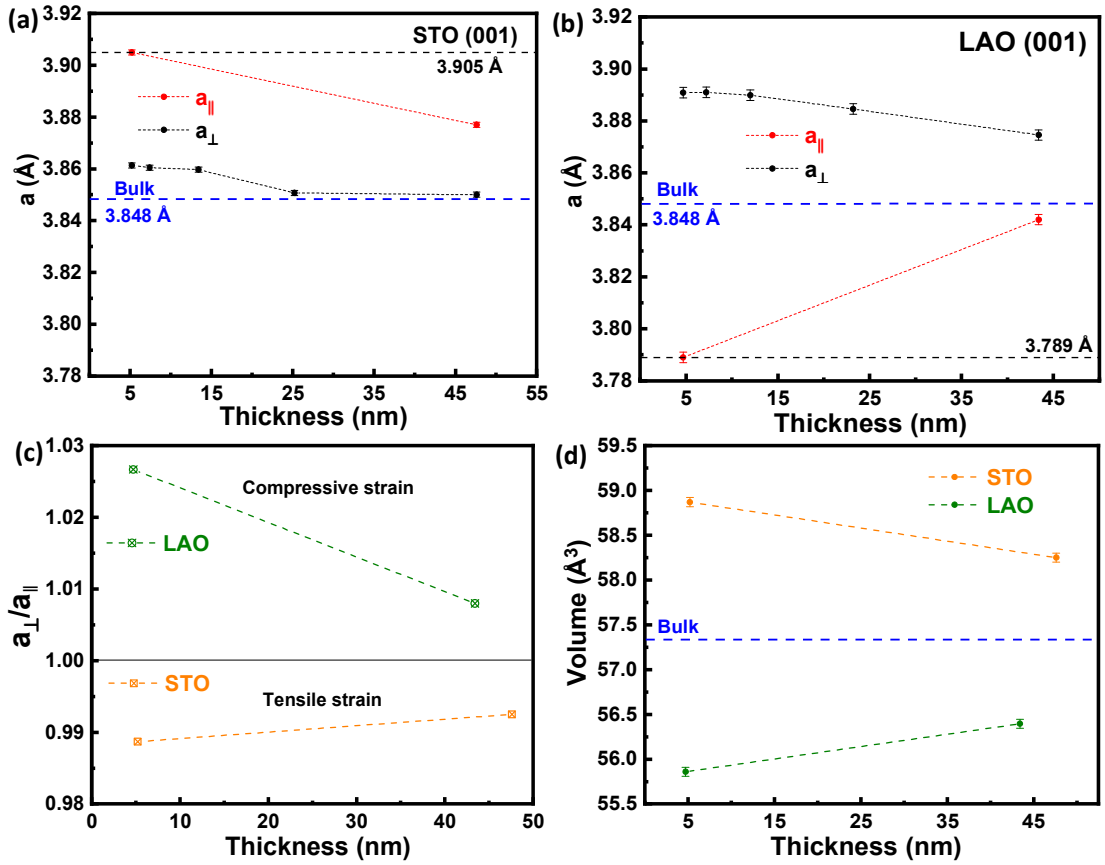


Figure 4.22 (a,b) variation of in-plane (red dashed line) and out-of-plane (black dashed line) lattice parameters of PNMO films as a function of thickness deposited on STO (001) and LAO (001) substrates. The blue and black dashed line represents the bulk counterpart value and the substrate lattice parameter [30]. (c) Corresponding $a_{\perp}/a_{\parallel}$ ratio as a function of thickness and (d) volume ($Å^3$) of the same PNMO films (for both substrates)

The variation of $a_{\perp}/a_{\parallel}$ as a function of thickness for both substrates is depicted in Fig. 4.22 (c). The strain state according to the PNMO unit cell can be analyzed from the $a_{\perp}/a_{\parallel}$ ratio [28] [250]. Thus, $a_{\perp}/a_{\parallel}=1$ is expected for a perfect cubic unit cell (in PNMO bulk value is close to 0.997). In graph 4.22 (c), it can be appreciated for tensile strain films (STO), the $a_{\perp}/a_{\parallel}$ ratio is lower than 1; in this case the pseudocubic unit cell of PNMO is elongated in the interface i.e., along the in-plane parameter ($a_{\parallel}$) with respect to the bulk value ($a_{bulk}$=3.848 Å). For compressive strain films (LAO), the $a_{\perp}/a_{\parallel}$ ratio is higher than 1; thus indicating, the unit cell is elongated along the out-of-plane parameter ($a_{\perp}$). We note that by varying the film thickness, the $a_{\perp}/a_{\parallel}$ ratio change from 0.988 (thinnest film) to 0.992 (thickest film) for PNMO/STO films, and from 1.026 (thinnest film) to 1.008 (thickest film) for PNMO/LAO films. Indeed, for thicker PNMO films on STO and LAO, the $a_{\perp}/a_{\parallel}$ value is close to the bulk one ($a_{\perp}/a_{\parallel} \approx 0.997$), and the deviation is in accordance with the mismatch ($\delta_{STO} \approx -0.72\%$ and $\delta_{LAO} \approx +1.39\%$), thus for both cases a (partial) relaxation of the PNMO films is observed in

thicker films. Therefore, the epitaxial strain significantly varies with the thickness of the PNMO films following the mismatch imposed by the substrate.

Finally, Fig 4.22 (d) presents the evolution of the unit cell volume for the thinnest (5.2 nm) and thickest (47.6 nm) PNMO films deposited on STO substrates (orange dashed line); and equally for the thinnest (4.7 nm) and thickest (43.4 nm) film deposited on LAO substrates (green dashed line). For PNMO films on STO substrates, it can be observed that the thinnest film has a large unit cell volume (~ 58.87 $Å^3$), while the one of the thickest film is smaller (~ 58.25 $Å^3$). Indeed, the decrease and partial relaxation of the in-plane lattice parameters from the thinnest film to the thickest one (i.e., $a_{||}$ = 3.905Å to 3.877Å), while the out-of-plane lattice parameter also decreases, closer to bulk ($a_{bulk}$ = 3.848Å), result in a reduction of the unit cell volume for thick films. The variation of out-of-plane lattice parameter is related with the presence of oxygen vacancies. A larger unit cell volume denotes oxygen deficiency into the structure and cation disorder, due to the electrostatic repulsion between the highly charged B' cations [247] (more important in the case of thinner films). The smaller unit cell, observed in thicker case, is consistent with oxygen incorporation into the structure and the formation of $Mn^{+4}$, as previously reported [235] [153] [236].

Contrary, in PNMO films on LAO substrates, the different film-substrate lattice mismatch (now compressive, whereas STO applies a tensile strain) results in a small unit cell volume for the thinnest film (~ 55.86 $Å^3$), increasing for the thickest film (~ 56.39 $Å^3$). The increasing of in-plane lattice parameter (i.e., $a_{||}$ = 3.789 Å to 3.842 Å), approaching the bulk value, is consistent with almost fully relaxed structure in the thickest film. The relaxation process with increasing thickness can explain the qualitative variation of both the in-plane and out-of-plane lattice parameters. However, the out-of-plane lattice parameter remains larger than the corresponding bulk, resulting in an increase of the unit cell volume for thicker film. The later indicates that the presence of oxygen vacancies is also important in PNMO films grown on top of LAO substrates.

In summary, it has been clearly seen that, for both substrates (STO and LAO), strain effects modify both in-plane and out-of-plane parameters by varying the film thickness. Both the tensile and compressive strain has dominant effect in PNMO films with low thickness, affecting lattice parameters strongly. Thus, the in-plane lattice parameters of the film tend to acquire the same value as that of the substrate. By increasing film thickness, a (partial) relaxation of the in-plane tensile strain and compressive strain takes place, and consequently the lattice parameters tend to acquire the bulk value [251] [125].

## 4.2.2 Magnetic properties

In order to explore the thickness dependence of the magnetic properties, PNMO films (grown/annealed at 800°C under 350 mTorr $O_2$) of different thicknesses (t) deposited on STO (001) and LAO (001) substrates, and whose structural characterization was studied in the previous section, have been used for the magnetic characterization. In-plane magnetization of PNMO/STO and PNMO/LAO samples as a function of temperature under an applied magnetic field of 5 kOe are shown in Fig 4.23.

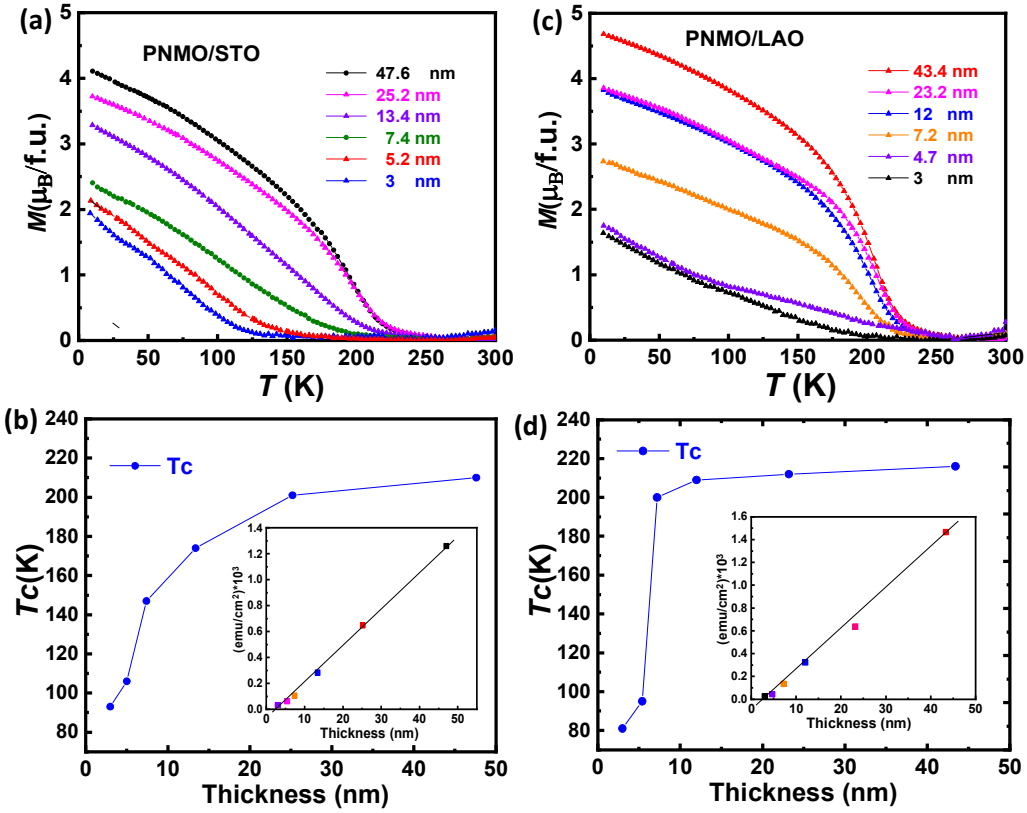


Figure 4.23 In-plane magnetization of (a) PNMO/STO and (b) PNMO/LAO thin films of different thicknesses as a function of temperature and under a magnetic field of $\mu_0 H = 0.5$ T. Curie temperature $T_C$ of (b) PNMO/STO and (d) PNMO/LAO thin films as a function of thickness. Insets show the magnetization (emu/cm$^2$)*10$^3$ at 60K as a function of thickness of the same samples.

Temperature-dependent magnetization $M(T)$ of PNMO films grown on STO and LAO substrates with different thickness (t) are depicted in Fig 4.23 (a) and (c), respectively. The $T_C$ was extracted and plotted in Fig 4.23 (b) and (d). In the results, it can be appreciated that the

magnetization and the Curie temperature $T_C$ (onset of the ferromagnetic behavior) reach lower values as the film thickness decreases. In this regard, a notable degradation of the magnetic properties takes place as the samples become thinner. It should also be noticed that the M(T) curve, for thickest (47.6 nm) PNMO/STO, displays a FM transition at $T_C \approx 210$ K and saturation magnetization of Ms ≈ 4.5 $\mu_B$/f.u. at 10K (see Fig 4.24 (a)), very similar to that reported in the literature [29]. The thickest (43.4 nm) PNMO/LAO film displays $T_C \approx 216$ K and $M_s \approx 4.85$ $\mu_B$/f.u. at 10K (see Fig 4.24 (b)), very close to the bulk value $M_s = 5$ $\mu_B$/f.u., [28].

As mentioned in chapter 3 (see section 3.1.5), in the case of ultrathin films (t < 4 nm), it has been shown that they do not have ferromagnetic character, and it has been attributed to the existence of an interface dead layer that affects the magnetic properties. The insets in Fig. 4.23 (b) and (d) depict the magnetization (emu/cm$^2$)*10$^3$ at 60K as a function of thickness. Therefore, by extrapolation to zero, the thickness of the dead layer for PNMO films was estimated to be of ~2.6 nm (STO) and ~2.5 nm (LAO). The existence of a dead layer in highly strained thin films has been attributed to a phase separation phenomenon at the interface, [209] [210] caused by structural changes and a non-uniform distribution of the strain state at the interface between film and substrate [206] [207].

On the other hand, the decrease of $T_C$ and Ms for the thinner PNMO films (on both substrates) (see Figs., 4.23 and 4.24) could be explained by considering the lattice mismatch (film-substrate) and strong structural in-plane tensile strain and compressive strain to which the films are subjected due to the decoupling of the lattice parameters. This strain effect can generate distortions into the perovskite structure, which in turn impose different Ni–O–Mn bond length and bond angle, thus reducing $T_C$. At the same time, the presence of anti-site disorder (ASD) (i.e., a point defect with a Mn ion occupying a Ni site or viceversa) has been suggested to give rise to $Ni^{2+}$–$O^{2-}$–$Ni^{2+}$ and $Mn^{4+}$–$O^{2-}$–$Mn^{4+}$ antiferromagnetic (AF) interactions reducing the Ms value [104]. In addition, by varying the film thickness the degree of distortion $a_\perp/a_{||}$ is not the same and the strain state becomes different. Thus, when the film thickness increases the strain state decreases and, as the elastic energy accumulated in the structure is very large, this latter dissipates through structural defects, lattice volume change etc., [202] [212] [205] [252] [41] [253].

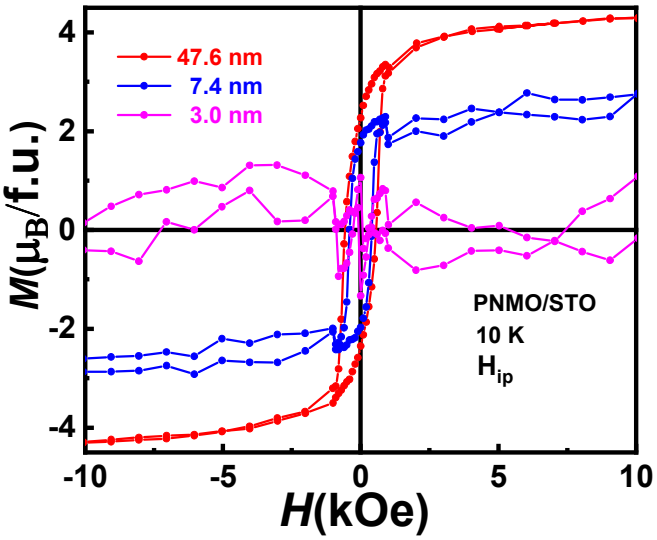


Figure 4.24. M(H) hysteresis loops, with in-plane applied field and measured at 10K, of PNMO films of different thicknesses deposited on STO substrates.

Fig. 4.24 shows M(H) hysteresis loops (with in-plane magnetic field; at 10K) of three PNMO samples of different thicknesses deposited on STO substrates. These M(H) curves reveal that the thinnest sample (~ 3 nm) does not show any hysteretic loop, indicating that the PNMO samples deposited under this critical thickness do not present ferromagnetism. On the other hand, the 7.4-nm-thick sample shows half the saturation magnetization of the thickest sample ($t \approx 47.6$ nm).

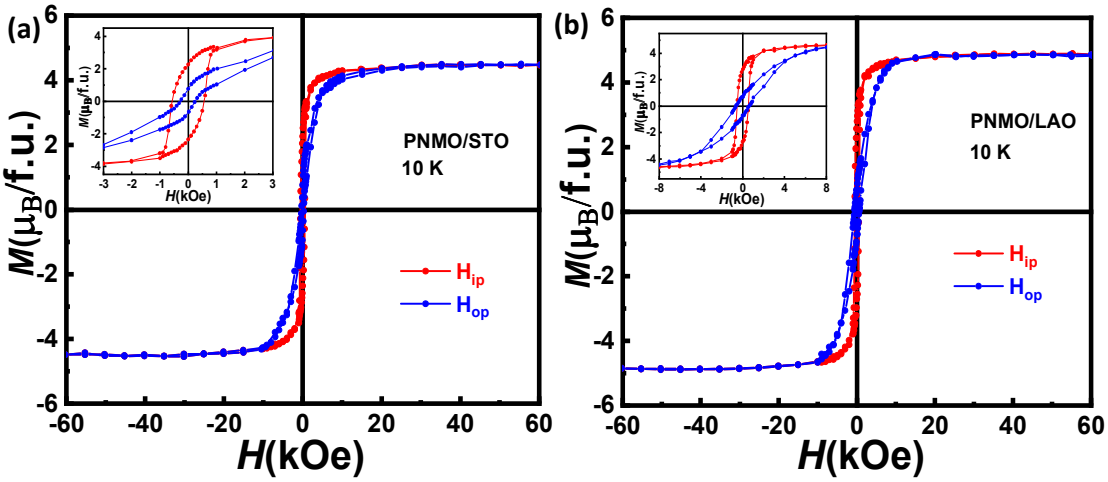


Figure 4.25. M(H) hysteresis loops (measured at 10 K) with in-plane (red curve) and out-of-plane (blue curve) applied magnetic field of: (a) 47.6-nm-thick PNMO film deposited on a STO substrate. (b) 43.4-nm-thick PNMO film deposited on a LAO substrate. The insets show in detail the low field region.

M(H) hysteresis loops (measured at 10 K) with in-plane and out-of-plane applied field were measured on two thick samples (for both substrates) with good ferromagnetic properties. Fig 4.25 (a) shows the M(H) loops corresponding to a 47.6-nm-thick PNMO film deposited on a STO substrate with good FM-$T_C \approx 210$ K. Additionally, Fig 4.25 (b) represents M(H) loops corresponding to a 43.4-nm-thick PNMO film deposited on a LAO substrate with good FM-$T_C \approx 216$ K. From Fig. 4.25, it can be appreciated that the M(H) hysteresis loops exhibit the expected hysteretic behavior (Curie temperature ($T_C$), saturation magnetization (Ms), coercive field (Hc) and remanence magnetization (Mr) data are listed in table 4.3). In fact, the M(H) curves reveal that the easy magnetization axis prevails in the IP orientation for both films. The Hc and Mr reinforce that the easy axis lies in the IP orientation. On the other hand, a coercive field Hc of about 565 Oe (IP field) and 264 Oe (OP field) is found for the 47.6-nm-thick PNMO/STO film, while a coercive field Hc of about 538 Oe (IP field) and 631 Oe (OP field) is found for the 43.4-nm-field PNMO film. This could indicate that the IP anisotropy is higher in the PNMO/LAO film, in agreement with the larger coercive field (OP), than in the PNMO/STO film.

Table 4.3. Magnetic properties of 47.6-nm-thick PNMO/STO film and 43.4-nm-thick PNMO/LAO film, grown/annealed at 800°C under 350 Torr $O_2$.

| **M(H) loops** | **$T_C$ (K)** | **Ms ($\mu_B$/f.u)** | **Hc (Oe)** | **Mr ($\mu_B$/f.u)** |
|---|---|---|---|---|
| **47.6 nm-PNMO/STO film at 10 K** | | | | |
| ip | 210 | 4.5 | 565 | 2.3 |
| op | | | 264 | 0.8 |
| **43.4 nm-PNMO/LAO film at 10K** | | | | |
| ip | 216 | 4.85 | 538 | 2.81 |
| op | | | 631 | 0.7 |

In addition, according to previous reports on manganites thin films [254] [255] [250], the magnetic properties depend strongly on the epitaxial strain state imposed by the substrate. From X-ray diffraction measurements (RSMs), $a_\perp/a_{||}$ ratios of 0.992 and 1.008 were found in 47.6-nm-thick PNMO/STO film and 43.4-nm-thick PNMO/LAO film, respectively. When $a_\perp/a_{||} < 1$, as in the case of PNMO/STO (tensile strain), both Curie temperature $T_C$ and saturation magnetization *M*s are lower. Inversely, when $a_\perp/a_{||} > 1$, as in the case of PNMO/LAO (compressive strain), $T_C$ and Ms increase. In this case, the compressive strain (PNMO/LAO film) favors an improvement of the $T_C$ and *M*s values (with $T_C \approx 216$ K and $M_s \approx 4.85$ $\mu_B$/f.u. at 10K ), approaching the reported PNMO bulk value ($T_C \approx 228$ K and $M_s \approx 5$ $\mu_B$/f.u.) for perfectly ordered stoichiometric $Pr_2Ni^{2+}Mn^{4+}O_6$ [120] [30]. In the case of the PNMO/STO film, the lattice distortion and inhomogeneities induce a decrease in magnetic properties [144].

# 4.3 X-ray absorption spectroscopy (XAS)

In this section, to evaluate the spin, orbital moment, valence state of ions and the nature of the ferromagnetic (FM) interaction in the PNMO compounds, X-ray absorption spectroscopy (XAS) and X-ray magnetic circular dichroism (XMCD) measurements were carried out at Pr $M_{4,5}$, Ni $L_{2,3,}$ Mn $L_{2,3}$ and O $K$ edges by the total electron yield (TEY) mode at 100 K. At the same time, in order to qualitatively analyze the ferromagnetic character in PNMO system, we have carried out simulations of XAS and XMCD spectra by utilizing the CTM4XAS program. For this study, we have chosen three PNMO samples of different thicknesses grown/annealed at 800$^{o}$C under 350 mTorr $O_2$ deposited on STO and LAO substrates. The first one is a 47.6-nm thick PNMO/STO sample, with good FM properties (i.e., Tc≈210 K and Ms≈4.5$\mu_B$/f.u at 10K), and a Ni/Mn ratio of about 0.81 (x≈0.10, $Pr_{1.7}Ni_{0.9}Mn_{1.1}O_{6.0}$) (see sections 4.1.3. and 4.1.5), the second one is a 43.4-nm thick PNMO/LAO sample with good FM properties (i.e., $T_C$≈216 K and Ms≈4.7$\mu_B$/f.u at 10K) and the third is a 4.7-nm thick PNMO/LAO sample with bad FM properties (i.e., $T_C$≈95 K at 10K), (see section 4.2.2). In the following, the PNMO sample grown on a STO substrate with high-$T_C$ was labeled as PNMO-δA, and the thicker (high-$T_C$) and the thinner (low-$T_C$) samples grown on LAO substrates were labeled as PNMO-δB and PNMO-δC, respectively.

## 4.3.1 XAS and XMCD at Ni- and Mn- $L_{2,3}$ edges

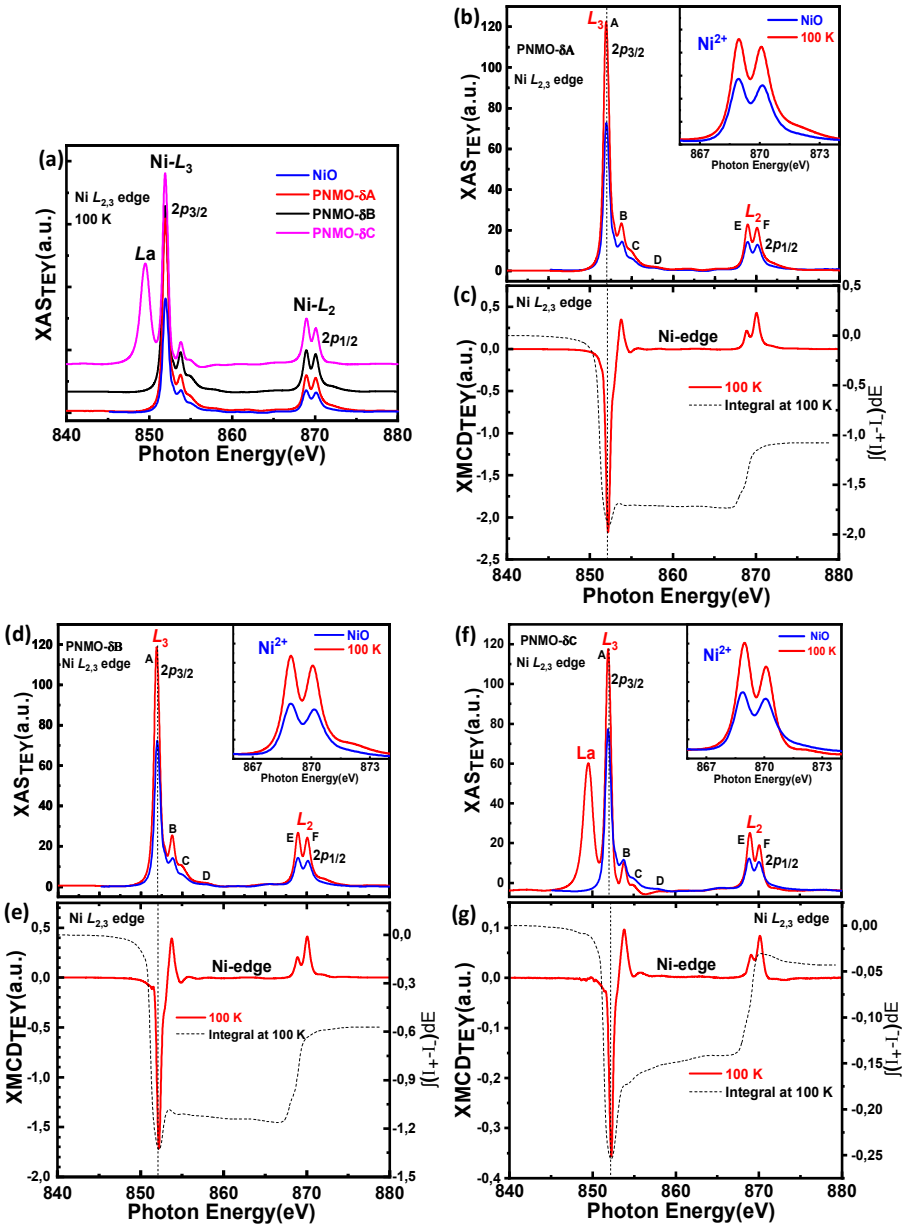


Figure.4.26. X-ray absorption spectroscopy (XAS) spectra of Ni $L_{2,3}$ edge collected in the total electron yield (TEY) mode at 100 K for three PNMO thin films deposited on STO and LAO substrates of different thicknesses with high-$T_C$ and low-$T$c. (a) XAS spectra at Ni-$L_{2,3}$ edge for the three samples, for the sake of comparison absorption spectrum of NiO was also plotted. XAS spectra at Ni-$L_{2,3}$ edge for each sample are displayed at: (b) PNMO-δA, (d) PNMO-δB and (f) PNMO-δC, for comparison the XAS spectrum of NiO is also plotted (blue curve). The insets show an enlargement of Ni-$L_2$ absorption peak. X-ray magnetic circular dichroism (XMCD) data collected over Ni $L_{2,3}$ edge at 100 K with an applied field of $\mu_o$H=2T are plotted at (c), (e) and (g). The dashed black line shows the corresponding integral at 100 K.

Taking into account that the ferromagnetic character of $Pr_2NiMnO_6$ is understood in terms of the superexchange interactions between $Ni^{2+}$ and $Mn^{4+}$ according to the Goodenough-Kanamori rules, it is of major interest to characterize the valence states and orbital occupancies of these two ions. With this purpose, the Ni $L_{2,3}$ edge ($2p \rightarrow 3d$ transitions) XAS spectra for the three samples are shown in Fig. 4.26 [(a), (b), (d) and (f)].

Therefore, Fig. 4.26 (a) displays the normalized XAS spectra at Ni-$L_{2,3}$ edge for the three samples. By comparing, one can observe that the strong Ni $L_3$ edge peak and the Ni $L_2$ edge double-peak structure of (b) PNMO-δA, (d) PNMO-δB and (f) PNMO-δC samples are very similar to those measured and published in recent reports on $La_2NiMnO_6$ [83] [98] [104], $Pr_2NiMnO_6$ [248] and $Nd_2NiMnO_6$ [256] double perovskites. For the thinner PNMO-δC sample (low-$T_C$) grown on a LAO substrate, one can observe a sharp peak located at 849.5 eV corresponding to the La $M_4$ ($3d_{3/2} \rightarrow 4f$) peak from the substrate. On the other hand, for comparison, in the spectra two main groups of peaks due to the $2p_{3/2}$ and $2p_{1/2}$ edges are labeled with letters from A to F. It can be observed, that the line shape in all XAS spectra of Ni $L_3$ edge ($\hbar\upsilon \approx$ 850-855 eV) and $L_2$ edge ($\hbar\upsilon \approx$ 865−875 eV) absorption peaks (shown in the inset) is quite similar and can be easily compared with the Ni $2p$ edges of divalent $Ni^{2+}$ compounds, as isoelectronic NiO (also shown in the inset) or Ni dihalides [257].

According to the electric dipole selection rules (Fermi's Golden rule), Ni $2p$ electrons may be excited into empty states either with $3d$ or $4s$ symmetry. The $2p \rightarrow 3d$ transitions are about 30 times stronger in intensity than $2p \rightarrow 4s$ ones due to the large overlap of the $3d$ wave functions with the $2p$ ones [218]. The presence of this double peak or small satellites (labeled as E and F and shown in the inset) in Ni $L_2$ edge is well understood in terms of a covalent ground state of mainly $Ni^{2+}$ ($3d^8$ character, which in $O_h$ symmetry can be written as $^3A_{2g}$ ($t_{2g}^6\ e_g^2$) plus an anion dependent fraction of the $3d^9\underline{L}$ and $3d^{10}\underline{L}$ configurations, where $\underline{L}$ corresponds to a ligand hole in the O $2p$ state [257]. This small satellite of Ni $L_2$ edge was also observed in a nonstoichiometric sample of $La_2Ni_{1-x}Mn_{1+x}O_6$ with Ni deficiency [229] (see chapter 3, section 3.2.4). In a similar way, this double peak was also displayed by $L_2$ edge in stoichiometric samples of $R_2NiMnO_6$ ($R$ = La, Pr and Nd) with almost full cationic ordering but yet very different from the $L_2$ peak of $PrNiO_3$ and $NdNiO_3$ corresponding to ($Ni^{3+}$) [83] [248] [256]. Therefore, we can conclude from the Ni $L_{2,3}$ XAS results that the oxidation state of Ni ions in in our three samples is 2+. We further examined this by means of simulations of XAS and XMCD spectra of Ni $L_{2,3}$ edges (see section 4.3.1.1).

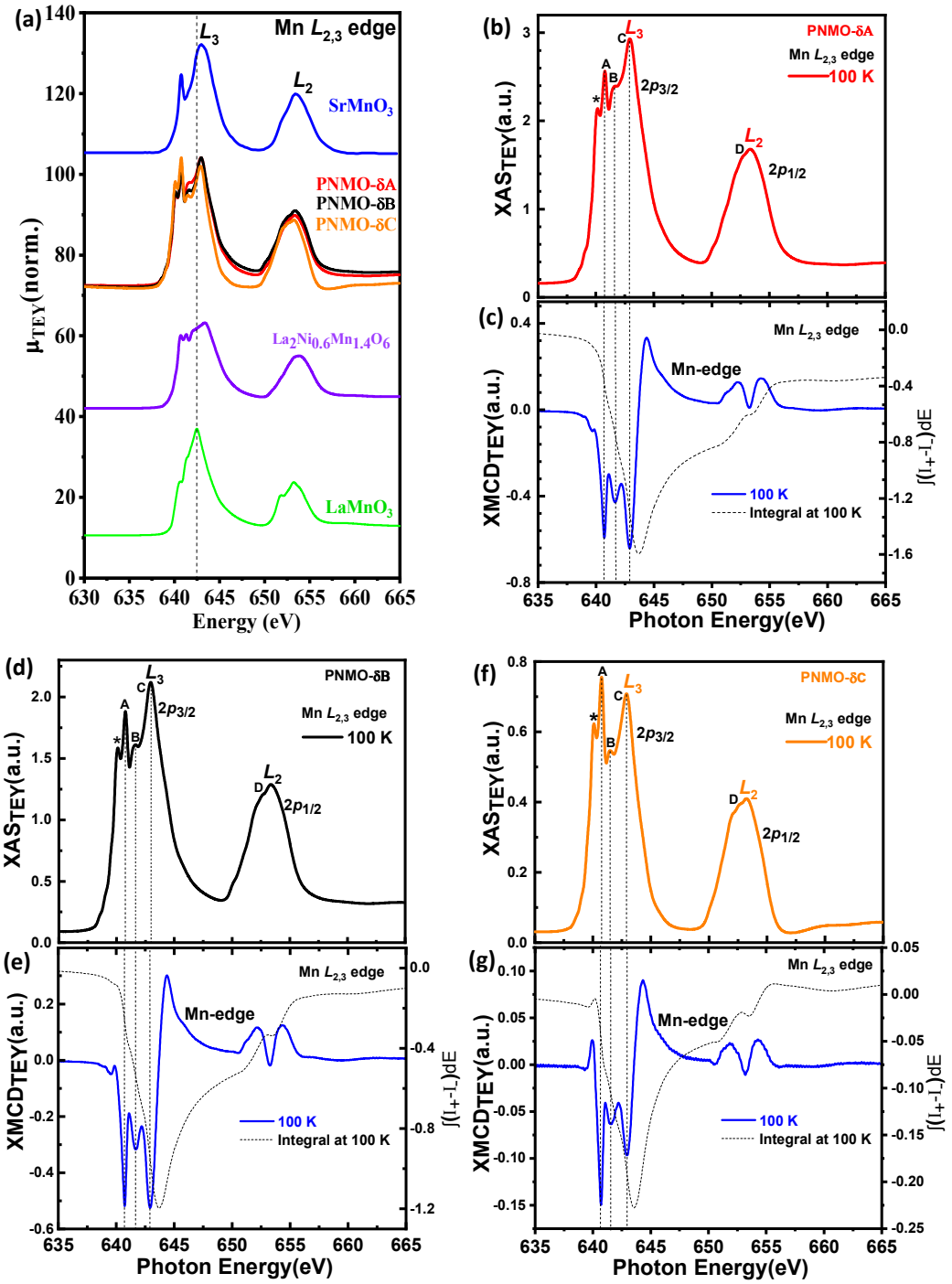


Figure 4.27. X-ray absorption spectroscopy (XAS) spectra of Mn $L_{2,3}$ edge collected in the total electron yield (TEY) mode at 100 K for the same three PNMO thin films deposited on STO and LAO substrates. Mn- $L_{2,3}$ XAS spectra are displayed for (b) PNMO-δA, (d) PNMO-δB and (f) PNMO-δC. For comparison the Mn $L_{2,3}$ XAS edge of PNMO-δA, PNMO-δB and PNMO-δC samples are plotted in (a) and compared with reference spectra such as: $LaMnO_3$ ($Mn^{3+}$), $La_2Ni_{0.6}Mn_{1.4}O_6$ (mixed-valence, $Mn^{3.6+}$) and $SrMnO_3$ ($Mn^{4+}$). These spectra were collected in the TEY mode at 300 K. X-ray magnetic circular dichroism (XMCD) data collected over the Mn $L_{2,3}$ edge at 100 K with an applied field of $\mu_oH$=2T of the same three samples are plotted at (c),(e) and (g). The dashed black line shows the corresponding integral at 100 K.

The Mn-$L_{2,3}$ edge XAS spectra for the three PNMO samples are shown in Fig. 4.27 [(b), (d) and (f)]. From Fig. 4.27, one can notice that the Mn-$L_{2,3}$ edge for the three samples are very similar to those measured and published in recent reports on $La_2NiMnO_6$ [83] [98] [104] $Pr_2NiMnO_6$ [248] and $Nd_2NiMnO_6$ [256] double perovskites. On the other hand, in order to qualitatively evaluate the valence state of Mn of our three PNMO samples, we have also measured the Mn $L_{2,3}$ edge of some reference samples: $LaMnO_3$ ($Mn^{3+}$), $La_2Ni_{0.6}Mn_{1.4}O_6$ (mixed-valence, $Mn^{3.6+}$) and $SrMnO_3$ ($Mn^{4+}$). Spectra measured by TEY method at room temperature are compared in Fig. 4.27 (a). All spectra are very similar to each other and also resemble the one of $La_2Ni_{0.6}Mn_{1.4}O_6$ (mixed-valence manganite), as expected for compounds with a similar perovskite structure [258] [259]. In Fig 4.27 (a), by comparing $L_3$ absorption peaks of $LaMnO_3$ at 642.5 eV ($Mn^{3+}$) and $SrMnO_3$ located at 643.1 eV ($Mn^{4+}$) with our three PNMO samples (located between both compounds), one can observe a shift of the Mn $L_3$ peak toward higher energies for all XAS spectra in the set of samples (see dashed black line). On the other hand, the Mn-$L_{2,3}$ XAS spectra measured of our $Pr_{2-\delta}Ni_{1-x}Mn_{1+x}O_6$ (PNMO) samples is quite similar to that of $SrMnO_3$ (SMO) and to other $Mn^{4+}$ references on $O_h$ crystal field symmetry, like $LaMn_{0.5}Ni_{0.5}O_3$ [85], $LaMn_{0.5}Co_{0.5}O_3$ [260] and $Ca_3CoMnO_6$ [261], but different from that of $LaMnO_3$ (LMO). Nevertheless, a small peak labeled with (*), which has been identified as $Mn^{2+}$, is present in our spectra. In spite of the presence of this small peak, the Mn-$L_{2,3}$ XAS spectra of PNMO and SrMO are quite similar, which indicates that the oxidization state of Mn in our PNMO samples might be in a valence state of $Mn^{4+}$. For further confirmation of this statement, simulated XAS and XMCD spectra of Mn-$L_{2,3}$ edges for PNMO were carried out next.

In Fig. 4.27 [(b), (d) and (f)], for comparison, the $L_3$-edge peaks have been labeled as A, B and C, and the one labeled as D belongs to the $L_2$-edge. Moreover, a small peak corresponding to the presence of $Mn^{2+}$ was labeled with (*). In the Mn-$L_{2,3}$ XAS spectra, it can be observed that the peak's width and shape of the $L_2$-edge (peak D) of the three PNMO samples are very similar. Nevertheless, by comparing the intensity of peak D of these three samples (see 4.27 figure (a)), it can be observed, that peak D of the sample PNMO-δC has a higher intensity and is slightly sharper than the two other samples. At the same time, in the $L_3$-edge region, the width and shape of the peaks labeled as A, B, and C are very similar for the three samples, but a slight difference in the intensity for the sample PNMO-δC can be observed. In this case, the branching ratio that is defined as I($L_2$)/I($L_3$), where I($L_3$) and I($L_2$) are the intensities of $L_3$ and $L_2$ peaks respectively, is larger for the PNMO-δC sample. This difference in the intensity of the peaks could be associated with an electron-yield saturation effect in $L$-edge due to the thickness of the samples [262] [263]. PNMO-δC is the thinnest sample (4.7 nm) and a saturation effect could increase the structures at low energy, compared to the structures at higher energy.

Typically, saturation effects, which are also called thickness effects [264] [265] are discussed in conjunction with fluorescence or electron yield detection in x-ray absorption spectroscopy [262] [263]. Saturation effects result in a recorded signal which is not proportional to the

photoabsorption cross-section as the photon energy is varied. In particular, the intensities of prominent absorption peaks are reduced or ‘‘saturated.’’[266] [267] Though saturation effects are stronger at more grazing photon incidence, in sufficiently thin films a small saturation can affect spectra even at normal incidence [268] (3% effect in a 3 nm film is reported in Ref. [266]). The degree to which saturation of the signal occurs in the electron yield signal depends on the relative photon penetration depth and electron escape depth. The saturation mechanism in electron yield can be illustrated by the example of the extreme case where the x-ray penetration depth is much shorter than the electron escape depth. All incident photons will be converted into photoelectrons and therefore the electron signal will be proportional only to the incident photon intensity $I_0$ and not to the absorption coefficient $\mu$. Hence, we say that the electron yield signal has completely saturated in the limit $\lambda_e > \lambda_x \cos\theta$ [266]. Previous reports by A. Ruosi et al. [268] determined the sampling depth $d$ by measuring the EY in normal photon incidence for a series of LCMO films of different thicknesses $t \leq 5d$. (The experimental sampling depth quantifies the depth sensitivity $d$ of the signal measured in the TEY experiment.) Peak heights of absorption intensity $I_{TEY}$ at the Mn $L_{2,3}$ edges were studied as a function of LCMO film thickness $t$ (measured at room temperature). A linear slope that was fitted to the pre-edge background was subtracted from the spectra to determine the peak height. The exponential best fit with $d$ as a free parameter resulted in a value of the sampling depth $d = 2.6 \pm 0.3$ nm for the $L_3$ and $d = 2.7 \pm 0.3$ nm for the $L_2$ edges. The Mn signal rapidly increased for film thickness up to about 5 nm, at which a thickness of 90% of the saturation value has been reached; while above 10 nm the curve was very nearly constant [268]. On the other hand, in Fig. 4.27 [(b), (d) and (f)] the peak labeled as (*) located at 640.2 eV has been assigned to $Mn^{2+}$. The presence of $Mn^{2+}$ on the samples could be related to a surface contamination of the films by exposure to air.

In addition, X-ray magnetic circular dichroism (XMCD) has been used to investigate the specific magnetic ordering, into the nature of exchange couplings between different magnetic sites, namely Ni, Mn, Pr and O in the $Pr_{2-\delta}Ni_{1-x}Mn_{1+x}O_6$ compounds. Figs 4.26 and Figs 4.27 [(c), (e) and (g)] show the XMCD spectra of Ni and Mn $L_{2,3}$ edges ($2p \rightarrow 3d$ transitions) of PNMO-δA, PNMO-δB and PNMO-δC films. The spectra were measured by total electron yield mode (TEY) method at 100K under applied field of $\mu_o H$=2T. This temperature is chosen to be well below the high-temperature magnetic transition at 216 K. All the XMCD spectra have been normalized to the integrated area of the corresponding XAS spectra [113]. The XMCD signal is directly related to the local magnetic moment of the photoexcited atom when the core electron is promoted into final states that are responsible for ferro- and ferrimagnetic behaviors [85]. The sign of the leading edge of the XMCD signal of both Ni and Mn exhibits substantial intensity, clearly establishing the ferromagnetic nature of both Ni and Mn sublattices, which is given by the orientation of the spin moment contributed by that magnetic site. In addition, one can observe that the intensity of both Mn and Ni XMCD signals for the samples with high $T_C$ (PNMO-δA and PNMO-δB) is larger than those of low $T_C$ (PNMO-δC), which corroborates the poor magnetic properties in this last sample (see section 4.2.2).

On the other hand, the strong negative peak in the XMCD signal, observed in both Mn and Ni-$L_3$ regions, indicates the same orientation of the spin moments on Ni and Mn sites, establishing the ferromagnetic exchange coupling between Mn and Ni sublattices, leading to a ferromagnetic Ni-Mn sublattice below the phase transition temperature of 216 K, as also proposed in the case of $La_2NiMnO_6$ [86] [256].

In order to extract quantitative information about orbital magnetic moment $\mu_{orb}$ and spin magnetic moment $\mu_{spin}$ contributions to the magnetic moment of Mn 3*d* and Ni 3*d* states, we apply the so-called sum-rules in the XMCD spectra [83] [219] [220]. In this regard, the corresponding integral of the XMCD signal is also depicted in Figs 4.26 and Figs 4.27 [(c), (e) and (g)] (see dashed black line). Therefore, using the equations in appendix (see section A.7.2), for the thicker samples with high-$T_C$, we obtained from the integral of XMCD signal for PNMO-δA sample that $\mu_L^{Ni}/\mu_S^{Ni} = 0.241$. In the case of Mn ions, from the integral of XMCD signal it is found that $\mu_L^{Mn}/\mu_S^{Mn} = 0.099$ at 100K. For PNMO-δB sample, the Ni and Mn ions from the integral of XMCD signal it was found that $\mu_L^{Ni}/\mu_S^{Ni} = 0.167$ and $\mu_L^{Mn}/\mu_S^{Mn} = 0.055$, respectively. For the thinner PNMO-δC sample with low-$T_C$, it was obtained from the integral of XMCD signal that $\mu_L^{Ni}/\mu_S^{Ni} = 0.077$ for the Ni $L_{2,3}$ XMCD spectra and $\mu_L^{Mn}/\mu_S^{Mn} = -0.018$ for the Mn $L_{2,3}$ XMCD spectra at 100K (see Figs 4.26 and Figs 4.27 [(c), (e) and (g)]). These calculated values are similar to previous reports [83] [85]. Indeed, for Mn $L_{2,3}$ XMCD in the determination of $m_S$ an error as large as 200% could be found [269], which is due to the fact that to apply the spin-sum rule the Mn $2p_{3/2}$ and $2p_{1/2}$ regions should be well separated in the spectra. On the other hand, in Figs 4.27 [(c), (e) and (g)], it can be appreciated a non-zero positive XMCD signal between the Mn $2p_{3/2}$ and $2p_{1/2}$ regions which indicates that the spin-orbit splitting of the Mn core hole is not large enough to prevent the mixing of *J* contributions of both $L_3$ and $L_2$ edges, which means that the orbital moment for the $Mn^{4+}$ ions is nearly quenched [83] [85]. In fact, for the $3d^3$ configuration in $Mn^{4+}$ compounds, the majority $t_{2g}$ shell is fully occupied without orbital degree of freedom and thus a practically quenched orbital moment is to be expected.

#### 4.3.1.1 Simulated XAS and XMCD spectra of $Ni^{2+}$ and $Mn^{4+}$ edges

In order to obtain more detailed information on the local electronic structure of Ni and Mn edges, theoretical simulations of the XAS and XMCD spectra have been performed to fit the experimental data. $Ni^{2+}$ and $Mn^{4+}$ 2*p* XAS and XMCD spectra were simulated using the Charge Transfer Multiplet program CTM4XAS [270]. This program is based on a semi-empirical approach that includes explicitly the important interactions to simulate the *L* edges of transition metal systems. The multiplet model was implemented by Thole [271], based on the atomic theory developed by Cowan [272], the crystal field interactions described by Butler [273**],** and further developed by de Groot [274] [275]. This approach includes both electron−electron interactions and spin−orbit coupling for each open subshell [276]. Atomic Slater−Condon parameters ($F_{dd}$, $F_{pd}$, and $G_{pd}$) are scaled to 80% of the Hartree−Fock calculated values [272].

A brief introduction of the input parameters for the multiplet calculation with the CTM4XAS program is as follows [270] [277]:

1) The configuration of the initial and the final state ($2p^6 3d^n \rightarrow 2p^5 3d^{n+1}$)

2) Slater integral reduction (%). In the CTM4XAS program, all Slater integral numbers ($F_{dd}$, $F_{pd}$, and $G_{pd}$), which measures the exchange interaction between two pair of electrons are set as default; nevertheless, these default values of 80% may be changed in a particular case, i.e., if screening effects are particularly strong.

3) Crystal-field energy is described with empirical parameters 10 Dq, Ds, Dt and M, the choice of the point group symmetry must be taken into account. The symmetries are limited to octahedral ($O_h$), tetragonal ($D_{4h}$), four-fold symmetry ($C_4$) and tetrahedral ($T_d$). This latter can also be calculated for 2*p* and 3*p* XAS as this calculation is equivalent to an $O_h$ calculation with negative crystal field values. In $O_h$ symmetry, only the value of the cubic crystal field splitting 10Dq can be provided, as the other parameters are zero. According to ligand field theory, the 3*d* level in an octahedral crystal field splits into a low-lying $t_{2g}$ triplet and a high-lying $e_g$ doublet, separated by the crystal-field splitting 10Dq. The ionic ground-state configurations for the TM cations range from $d^3$ for $Mn^{4+}$ to $d^8$ for $Ni^{2+}$ [278]. On the other hand, the $C_4$ symmetry option is used to describe the exchange field in ferromagnetic systems and, as such, it separates the magnetic substrates. The direct consequence of the exchange field is the occurrence of a XMCD signal and for the simulation an extra parameter is needed: the Zeeman Splitting (M) with value 10 meV [270] [277].

4) Charge transfer parameters given by: the charge-transfer energy (Δ), the Coulomb repulsion energy ($U_{dd}$ and $U_{pd}$), and the 3d→L transfer integral. The $U_{3d3d}$ parameter defines the Hubbard U value and the $U_{2p3d}$ parameter the core hole potential. In case of a two-configuration charge transfer multiplet calculation for XAS, $U_{dd}$ has no direct influence and only the energy difference $U_{pd} - U_{dd}$ is important [270]. The so-called "charge-transfer energy (Δ)" is the transition of a $3d^N$ configuration to a $3d^{N+1}\underline{L}$ configuration, where a ligand electron is transferred to the metal site and a ligand hole $\underline{L}$ is created, which is defined as [277]:

$$\Delta_d^{\,n} = E(d^{n+1}\underline{L}) - E(d^n) \cong \Delta_d^{\,n+1} - U$$

where $\underline{L}$ denotes a ligand hole residing at the oxygen site, and Δ corresponds to a large charge transfer from/to a ligand hole when a small or negative value is assigned (whereas a large value for Δ forbid any charge transfer). By increasing the valence of the metal element, Δ systematically decreases and it is found that Δ may become very small or negative for compounds with unusually high valences, such as $Fe^{4+}$, $Ni^{3+}$ and $Cu^{3+}$. Therefore, for a high covalency, the charge-transfer energy may be in the negative regime due to the strong hybridization with the oxygen band [279]. On the other hand, U represents the Coulomb repulsion energy and is defined as $U=E(d^{n+1})+E(d^{n-1})-2E(d^n)$. In the special case, i.e. when charge-transfer energy is small or negative, the energy gap is strongly dependent on the parameters U, Δ and the 3*d*-2*p* hybridization strength *T*. The hybridization between the metal 3*d* and O 2*p* are defined by the off-diagonal matrix elements, $T = \langle d^n|H|d^{n+1}\underline{L}\rangle = \langle d^n\underline{L}|H|d^{n+2}\underline{L}^2\rangle$ and, in turn, the strength of the 3d-3d and 2p-3d hybridizations is related to Slater–Koster transfer integrals. Thus, due to the fact that the *d* electron hopping is mediated by the ligand *p* orbital, the 3d-2p hybridization is very sensitive to the bond length and bond angle [280].

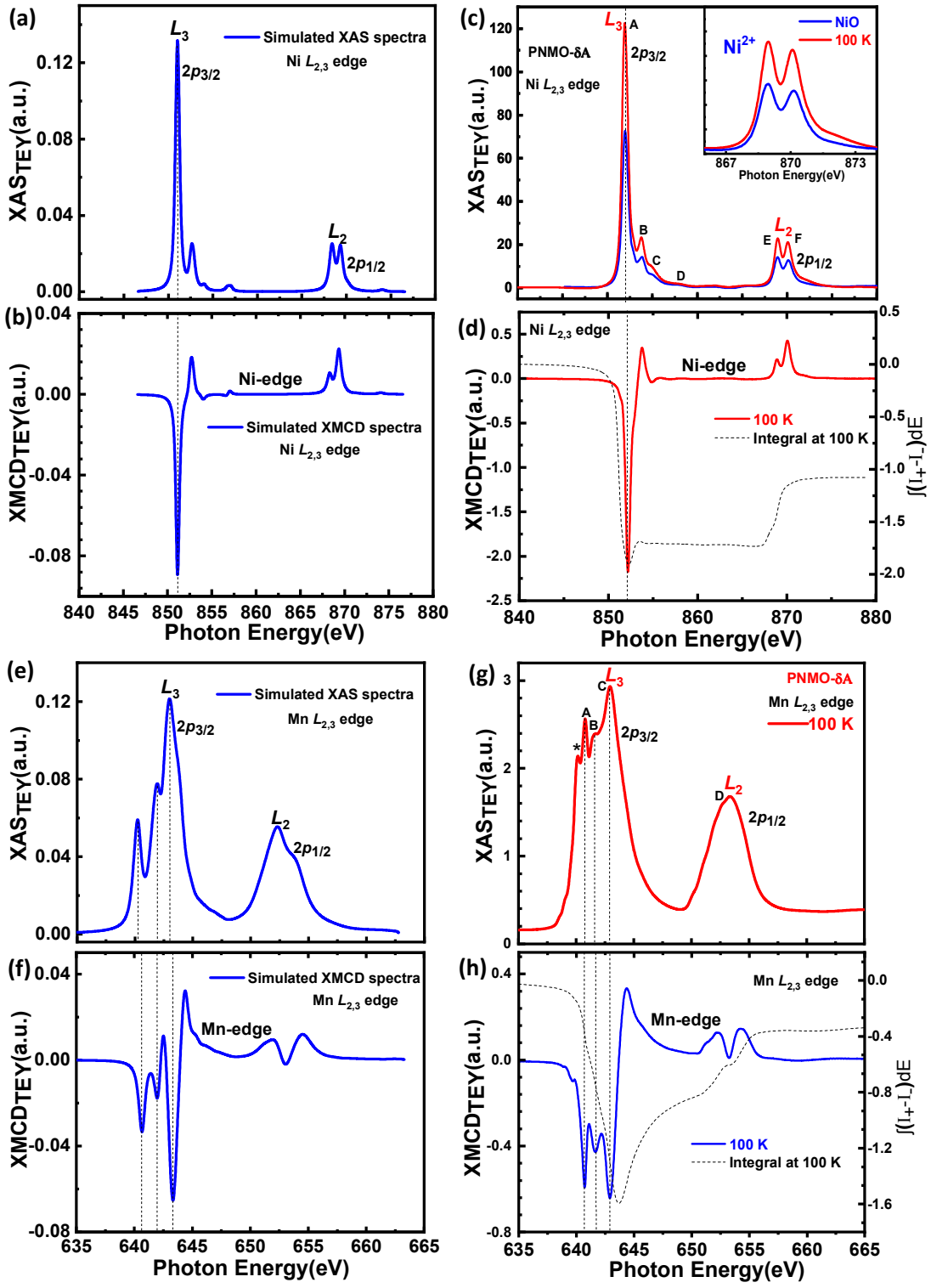


Figure 4.28 Comparison of calculated spectra together with experimental spectra. Ni and Mn $L_{2,3}$ edges of calculated XAS [(a) and (e)] and XMCD [(b) and (f)] spectra for $Ni^{2+}$ and $Mn^{4+}$ in $O_h$ symmetry. Experimental XAS [(c) and (g)] and XMCD [(d) and (h)] spectra of Ni and Mn $L_{2,3}$ edges collected in the total electron yield (TEY) mode at 100 K for PNMO-δA sample.

To obtain multiplet simulation parameters and compositions most consistent to experimental data of our PNMO compounds, theoretical simulation of the 2*p* XAS and XMCD spectra for individual $Ni^{2+}$ and $Mn^{4+}$ ions were done using charge transfer multiplet program CTM4XAS. Fig. 4.28 [(a),(e) and (b),(f)] displays the simulated XAS and XMCD spectra for $Ni^{2+}$ and $Mn^{4+}$ ions. The parameters for the XMCD calculations are the same than those used for calculating the XAS spectra. For comparison, Fig 4.28 [(c),(d) and (g),(h)] shows the XAS experimental spectra at the Ni-$L_{2,3}$ and Mn-$L_{2,3}$ edges together with XMCD spectra for the PNMO-δA sample studied in the previous section. All experimental Ni-$L_{2,3}$ and M-$L_{2,3}$ XAS spectra studied in this section are compared with simulated spectra of $Ni^{2+}$ and $Mn^{4+}$. The Ni and Mn-$L_{2,3}$ edges spectra are calculated from the sum of all possible transitions for an electron excited from the 2*p* core level to an unoccupied 3*d* level. The ground state is approximated by the electronic configuration $3d^n$. In the ground state, both the 3*d* spin−orbit coupling and the crystal field affect the $3d^n$ configuration. The $3d^n$ ground state and the $2p^5 3d^{n+1}$ final state are affected by the 3*d*3*d* multiplet coupling. In the final state, the 2*p*3*d* multiplet coupling, the 2*p* and 3*d* spin−orbit couplings, and the crystal field potential in appropriate symmetry, are also included [276]. The $Ni^{2+}$ ion in $Pr_2MnNiO_6$ compound is surrounded by oxygen octahedral ($d^8$ configuration), similar to that of NiO, which in $O_h$ symmetry can be written as ${}^3A_{2g}(t_{2g}^6 e_g^2)$. The $Mn^{4+}$ ion has a $d^3$ configuration in ground state, which can be written as ${}^4A_{2g}(t_{2g}^3)$ in $O_h$ symmetry [248].

For simulated $Ni^{2+}$ spectra, the charge transfer configurations $d^8L$ and $d^9L^2$ were considered, where *L* corresponds to a ligand hole in the O 2*p* state. In this regard, spectra were broadened by convoluting the line spectra with a Lorentzian broadening from 0.3 eV (resp. 0.2 eV) at the $L_2$ edge (res. the $L_3$ edge) and a Gaussian broadening of 0.1 eV. The calculation of $Mn^{4+}$ spectra generally involves two charge transfer configurations, therefore $d^3$ and $d^4L$ configurations in the ground state have been considered. Nevertheless, $Mn^{4+}$ in the ground state can be composed of more than two terms, which is difficult to work on this program. The $d^5L^2$ configuration was not so prominent in the calculation of $Mn^{4+}$ spectra. On the other hand, the simulated $Mn^{4+}$ spectra were broadened with a Lorentzian broadening from 0.8 eV (resp. 0.3 eV) at the $L_2$ edge (res. the $L_3$ edge) and a Gaussian broadening of 0.1 eV. As mentioned before, by comparing the simulated $Ni^{2+}$ XAS spectra in Fig 4.28 (a) with the experimental Ni-$L_{2,3}$ edge XAS in Fig 4.28 (c), it can be seen that both spectra (experimental and simulated) display characteristic features of a $Ni^{2+}$ system [281] [257].

For more details, XAS spectra (both experimental and simulated) contain characteristic peaks marked with letters from A to F. In the simulated spectrum, the double peak feature at both the $L_3$ and $L_2$ edges is strongly affected by the charge transfer energy (Δ). Indeed, for small Δ values (Δ<3eV) or even negative Δ values, the simulated spectra cannot fit well the experimental data at the $L_2$ edge, which leads to the formation of weak satellites and to changes of the multiplet structure in the (Ni-$L_{2,3}$) XAS spectrum. For a $Ni^{2+}$ system (similar to NiO), Ni ions are in $O_h$ symmetry with $Ni^{2+}$ ($d^8$ configuration). We have thus obtained a good

fit with a positive Δ value (Δ= 3.0 eV) and a crystal-field energy 10Dq = 1.2 eV (see more details in table 4.4). The features of double peak and/or satellite visible in our spectrum experimental, both at the $L_3$ and $L_2$ edges, have been very well reproduced (see Fig. 4.28 (a) and (c)). At the same time, $Ni^{2+}$ XAS spectra (simulated and experimental) show very similar peaks (B and C) compared to that observed in Ni dihalides [257].

Table 4.4 Best-fit parameters used for the multiplet calculations-based simulations of the experimental Ni and Mn $L_{2,3}$- edge XAS and XMCD spectra of PNMO systems

| **Parameter** | **$Ni^{2+}$** | **$Mn^{4+}$** |
|---|---|---|
| $d^n$ | $d^8$ | $d^3$ |
| Site symmetry | $O_h$ | $O_h$ |
| Crystal Field (*10Dq*) (eV) | 1.2 | 2.5 |
| Charge transfer energy (Δ) (eV) | 3.0 | 2.5 |
| $U_{dd}$(eV) | 7.5 | 6.5 |
| $U_{pd}$(eV) | 7.3 | 8.5 |
| Slater's integrals reduction (%) ($F_{dd}$, $F_{pd}$, $G_{pd}$) | 0.8 | 0.7 |
| Main peak | $d^8L$ | $d^3$ |
| Satellite peak | $d^9L^2$ | $d^4L$ |

Fig. 4.28(e) displays the simulated XAS spectrum for $Mn^{4+}$ ions for $Pr_{2-\delta}Ni_{1-x}Mn_{1+x}O_6$ compound. By comparing the XAS spectra (experimental and simulated) in Fig. 4.28 (e), (g), it can be observed that the multiplet structure (spectrum shape) and the peaks marked as A, B, C and D at the Mn-$L_3$ and Mn-$L_2$ edges fit well the experimental data. The Mn 2*p* XAS spectrum is highly sensitive to the crystal-field splitting 10Dq. Therefore, according to the multiplet calculation of $Mn^{4+}$ in $O_h$ symmetry, our experimental spectra were obtained with a good fit for 10Dq = 2.5 eV and Δ= 2.5 eV (see more details in table 4.4). These calculations lead to 6.69 holes in the Mn 3*d* band (i.e. 70% of $Mn^{4+}$ and 30% of $Mn^{3+}L$). Interestingly, similar 10Dq and Δ parameters were used for simulation of $Pr_2NiMnO_6$ [248] and $La_{0.1}Sr_{0.9}MnO_3$ [282] which is mainly an $Mn^{4+}$ system.

Fig. 4.28 (b) and (f) display the simulated XMCD spectra for $Ni^{2+}$ and $Mn^{4+}$ (the parameters for XMCD calculations are the same for calculating the XAS spectra, see details in table 4.4). Comparing the simulated XMCD spectrum for $Ni^{2+}$ with the experimental one (Fig 4.28 (b) and (d)), all structures (peaks A to E) are reproduced by the multiplet calculation, and the spectral shape of $Ni^{2+}$ (width and structure of peak) seems to fit the experimental data quite well. The simulated XMCD spectrum for $Mn^{4+}$ (Fig. 4.28 (f)) is quite similar to the experimental spectrum (Fig. 4.28 (h)) and all structures (peaks A to C) at the Mn-$L_3$ edge fit very well. On the other hand, as previously mentioned, the XMCD signal is largely negative at both the Mn-$L_3$ and Ni-$L_3$ edges, indicating that the Mn and Ni spins are aligned ferromagnetically.

According to these results, by comparing our theoretical simulations, based on charge transfer multiplet calculations of Ni and Mn $L_{2,3}$ XAS and XMCD data, with the experimental spectra of our PNMO compounds, it can be concluded that the experimental spectra are in a good agreement with calculated spectra of $Ni^{2+}$ and $Mn^{4+}$ in $O_h$ symmetry and HS configuration. At the same time, we conclude that irrespective of the structural strain (tensile or compressive), thickness and magnetic properties of the films (see Figs., 4.22 and 4.23), the oxidization states of Ni and Mn ions in our $Pr_{2-\delta}Ni_{1-x}Mn_{1+x}O_6$ systems are typical of $Ni^{2+}$ and $Mn^{4+}$. Similar results were observed on LNMO compounds [104] [149].

## 4.3.2 XAS and XMCD at Pr $M_{4,5}$ edge

The Pr $3d_{5/2\text{-}3/2}$ absorption edge XAS spectra for the three samples with high-$T_C$ and low-$T_C$, which probe the unoccupied density of 4*f* states, are shown in Fig. 4.29 (a). The spectrum of $PrCoO_3$ ($Pr^{3+}$) at 300 K is shown as reference [283] in the same plot. The spectral features are divided in two groups whose separation corresponds roughly to the $3d_{3/2}$-$3d_{5/2}$ spin-orbit splitting. The individual groups show considerable structure which is due to coupling of the spin and orbit moments of the 3*d* and 4*f* electrons. The spectra must be described in intermediate coupling and hence the designations $3d_{3/2}$ ($M_4$) and $3d_{5/2}$ ($M_5$) are only approximate [271]. At the same time, the features present in the spectra are related to the transitions into 4*f* states and are mainly due to the multiplet splitting of the quasi-atomic initial and final states [284] [285]. By comparing the Pr $M_{4,5}$ edge with previous XAS measurements of well-characterized materials, one should be able to provide information on the valence of the rare earth in our three samples with high-$T_C$ and low-$T_C$. In previous XAS reports of 3d rare-earth dioxides (namely $CeO_2$, $PrO_2$, and $LaO_2$), a main peak with some multiplet structures and a satellite were typically observed in their $3d_{5/2}$ and $3d_{3/2}$ components [286] [287]. The electronic structure of these materials is characterized by a strong Coulomb interaction between 4*f* electrons, as well as by a covalency mixing between rare-earth 4*f* and oxygen 2*p* states. As analyzed by Thole et al.,[271] XAS studies of rare-earth metals from

$Ce^{3+}$, $La^{3+}$, $Pr^{3+}$, $Nd^{3+}$,$Sm^{3+}$ etc report very complex multiplet structure. However, XAS plays a role of "fingerprint" in examining the valence number of rare-earth ions but, due to the complexity of full multiplet calculations, the interpretation of the XAS multiplet structure in rare-earth dioxides produced quite a large amount of confusion. Nevertheless, previous reports on $RNiO_3$ compounds, by M. Medarde et al., [285] show that all XAS spectra of the rare-earths (3d) La, Pr and Nd in $LaNiO_3$, $PrNiO_3$ and $NdNiO_3$ recorded in TEY mode are characterized by a strong main peak rare-earth attributed to $3d_{5/2} \rightarrow 4f$ transitions. In these studies, they concluded that all rare-earths are in a trivalent state. For the case of Pr $3d_{5/2}$ in $PrNiO_3$, absorption edge occurs at 930eV and the characteristic shape of the spectrum is very similar to that obtained in the XAS spectra of our three PNMO samples. In this regard, the main peak in our samples was found to be at 928.2eV, correlated to an edge shift of 0.2 eV towards low energy.

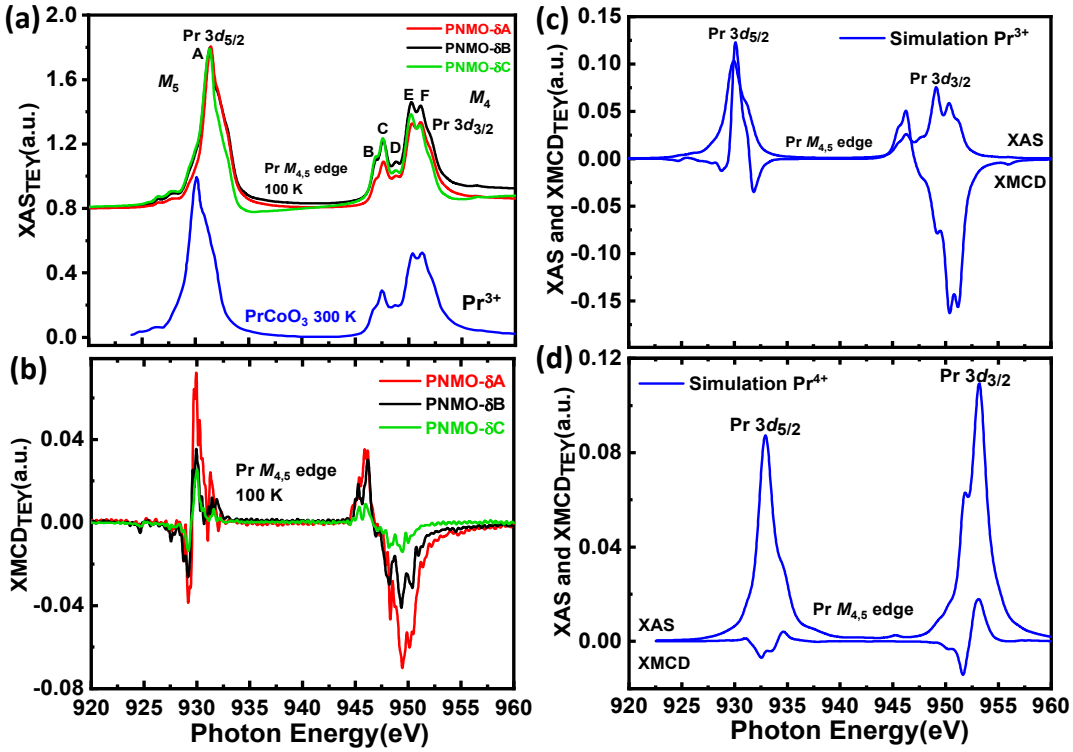


Figure. 4.29. (a) Pr $M_{4,5}$ edge XAS spectra measured in TEY mode for the same three PNMO samples, namely, PNMO-δA, PNMO-δB and PNMO-δC, collected at 100K. For comparison, the spectrum of $PrCoO_3$ ($Pr^{3+}$) at 300 K is shown [283]. (b) XMCD data of the same samples collected over Pr $M_{4,5}$ edge at 100K with an applied field of $\mu_o H$=2T. (c-d) Pr $M_{4,5}$ edge of calculated XAS and XMCD spectra for $Pr^{3+}$ and $Pr^{4+}$, respectively.

Therefore, in Fig 4.29 (a) by comparing the XAS edges of the rare earth and the shape of the observed spectra of our three PNMO samples with that of $PrCoO_3$ ($Pr^{3+}$) [283] XAS spectrum taken as reference and those found in the literature for $La^{3+}$, $Pr^{3+}$ and $Nd^{3+}$ [218] [256] we can

reasonably conclude that Pr ions in our three samples might be in a trivalent state. Therefore, in order to confirm this statement and determine the Pr content in our $Pr_{2-\delta}Ni_{1-x}Mn_{1+x}O_6$ systems, we explicitly calculated the XAS and XMDC spectra at Pr $M_{4,5}$ edge using the crispy interface. Crispy is a graphical user interface for the simulation of core-level spectra using the semi-empirical multiplet approaches implemented in quanty [288]. More information about crispy, can be found at [289].

In order to simulate the Pr $M_{4,5}$ XAS and XMCD spectra, we considered the $Pr^{3+}$ ion for initial $3d^{10}$ $4f^2$ state and $Pr^{4+}$ ion for initial $3d^{10}4f^1$ state in $O_h$ symmetry. For comparison with experimental data, the simulated spectrum of $Pr^{3+}$ and $Pr^{4+}$ are plotted in Figs 4.29 (c) and (d). According to the simulated spectra, all structures (width and shape of peak) corresponding to $Pr^{3+}$ (Fig. 4.29 (c)) reproduce quite well the main features of our experimental data and it is in a good agreement for all spectra in Fig 4.29 (a). Therefore, the valence state of Pr in our PNMO systems is indeed $Pr^{3+}$. Moreover, we can also conclude that the A-site deficiency in our $Pr_{2-\delta}Ni_{1-x}Mn_{1+x}O_6$ compound as analyzed by EPMA (see section 4.1.5) has no evident impact on the oxidation state of Pr.

XMCD results obtained at Pr $M_{4,5}$ edge (at 100K with $\mu_oH$= 2T) in our three samples (see Fig. 4.29 (b)) showed a dichroic signal with similar characteristics to the one measured in Nd $M_{4,5}$ edge (at 15, 25 and 75K with $\mu_oH$=5T) on $Nd_2NiMn0_6$ double perovskite [256]. In the XMCD signal from Nd, the authors observed that the leading edge of the XMCD spectrum showed the opposite sign compared to those at the Ni and Mn edges. This same behavior was also observed in the XMCD signal of the Pr edge of our three samples, indicating that the spin orientation of Pr moment is antiparallel to Ni-Mn spin moments. By applying an external magnetic field, it would be expected that the spin moments of the Ni-Mn ferromagnetic sublattice and that of the Pr sites would both be aligned with the applied field, leading to a parallel arrangement of spins between Pr and Ni-Mn, which is at odds with our experimental results. This contradiction observed in the XMCD signal at the Nd edge on $Nd_2NiMnO_6$ double perovskite [256] and in the one of Pr in our three samples (Fig 4.29 (b)) can be understood by noticing that the moment at the Pr and Nd site is not given only by the spin moment, but by the spin-orbit coupled total moment. In this regard, the antiparallel orientation of the Pr spin moment with respect to the spin moment of Ni-Mn sublattice ensures a parallel orientation of the total moment, since dominant orbital moment of Pr is oriented in a direction opposite to the one of its spin moment.

Fig. 4.29 (c) and (d) display the simulated XMCD spectra of $Pr^{3+}$ and $Pr^{+4}$, respectively. The parameters for the XMCD calculations are the same for calculating the XAS spectra. In these results, it can be observed that the dichroic signal corresponding to the calculated XMCD spectrum of $Pr^{3+}$ fits pretty well to the experimental data, which further corroborates that the valence state of Pr in our samples is 3+.

## 4.3.3 XAS and XMCD spectra at O *K*-edge

Fig. 4.30 (a) Shows the O *K* XAS edge spectra of the same three samples with high-*T*c and low-*T*c measured at 100K in the total electron yield mode (TEY). These states reflect, through the oxygen-metal hybridization of the O 2*p* states with the unoccupied Ni/Mn 3*d* and Pr 5d states, bands of mostly metallic character [290]. The first peak, so-called "pre-edge" peak and located around 529.8 eV (in the three samples), corresponds to transitions from the O 1*s* core level to the O 2*p* orbitals hybridized with 3d orbitals of Ni and Mn band region. The broad structure around 535 eV corresponds to the mixed states of O-2*p* and Pr 5*d* band region, and the bumps around 540–545 eV correspond to the hybridization of O 2*p* and Ni, Mn 4*sp* band region, which are consistent with previous analysis of the $LaMnO_3$, $LaFeO_3$ and $LaCoO_3$ spectra [291] [292] [293]. In the same way, O 1s XAS spectra at room temperature of $RNiO_3$ (R= La, Pr and Nd) indicate that, at high energies between 532 and 538.5 eV, the oscillations in the absorption cross section are due to transitions to oxygen 2*p* states hybridized with Ni (4s, 4p) and R (5d, 4f) states [294] [218]. As shown previously by de Groot and coworkers [295] and recent reports of O 1s XAS spectrum collected in the TEY mode of $Pr_2NiMnO_6$ [248] and $Nd_{2-x}Sr_xNiMnO_6$ [296] the pre-edge structure (< 532 eV) arises due to transitions from O 1*s* state to unoccupied O 2*p* states that are hybridized with 3*d* states of Mn and Ni above the Fermi energy ($E_F$). To determine $E_F$, they included the spectra of $LaNiO_3$, which is a metallic compound (at the rising edge the $E_F$ was fixed), as well as $LaMnO_3$, which is an insulator (at the rising edge above $E_F$). $Pr_2NiMnO_6$ compared along with $LaNiO_3$ and $LaMnO_3$ indicate that the first peak in O 1s spectrum of $Pr_2NiMnO_6$ occurs around 2.5 eV above $E_F$ and the peak intensity is almost twice that of $LaNiO_3$ and $LaMnO_3$ [248]. The larger intensity of the first peak indicates a greater covalent character of the system as compared to $LaMnO_3$. The intensity of this peak is roughly proportional to $\beta_0^2$, which is a measure of the covalency of the ground state. Moreover, along with lower *d* electron count in the $Mn^{4+}$ ion, the intensity is also affected by the larger covalency between the Mn–O and Ni–O bonds [218]. Thus the large enhancement of the unoccupied states above $E_F$ indicates greater overlap between the Mn 3*d* and Ni 3*d* states in $Pr_2MnNiO_6$.

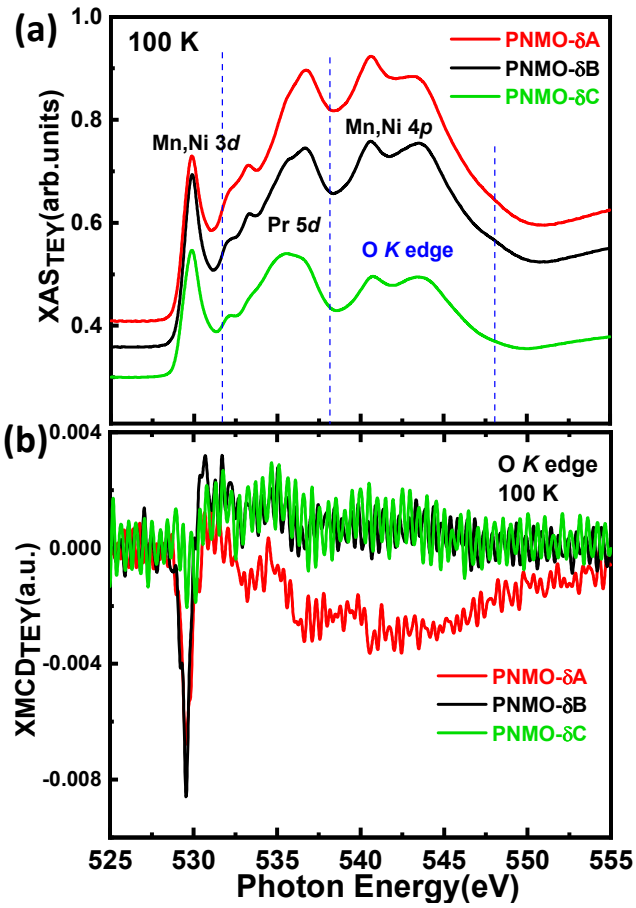


Figure. 4.30 (a) O *K*-edge XAS spectra for the same three samples collected at 100K. (b) XMCD data collected over O *K*-edge at 100K with an applied field of $\mu_o H$=2T.

On the other hand, a similar structure to this sharp prepeak is also present in the NiO O 1s edge, but its position at $E \approx 532$ eV is about 3 eV higher than that of the $RNiO_3$ pre-peak. The intensity of the prepeak in $RNiO_3$ spectra is very important, thus suggesting the existence of a highly covalent ground state. The results of magnetic neutron-diffraction experiments ($Ni^{3+}$ low spin, $\mu_{Ni}=1\mu_B$) implicitly support this finding [218]. In NiO, Ni atoms are surrounded by six equivalent O atoms ($d_{Ni-O}$ = 2.090 Å). In the $RNiO_3$ compounds ($d_{Ni-O}$ = 1.942 Å), by calculating the base state, the result suggests that the Ni 3d-O 2p hybridization is stronger in $RNiO_3$ than in NiO [285]. This feature, which has been also found in the O 1s edge of other TM monoxides [257] [297], is due to the O 2*p* weight in states of predominantly Ni 3*d* character. In this regard, this comparison is also applicable in case of O 1s edge XAS of $PrMnO_3$ [298], since in $RMnO_3$ variation in R does not affect the covalency character and the bandgap unlike the nickelates [299]. This first intense peak at 529 eV was also observed in the O K-edges of (Pr,Sr)$MnO_3$, (Pr,Ca,Sr)$MnO_3$ and (Nd,Ca)$MnO_3$ at RT, and was attributed to holes in a non-resolved set of $e_g^{\uparrow}$ and $t_{2g}^{\uparrow}$ molecular orbitals which holds for a strong Jahn–Teller distortion around the manganese site. The splitting of $e_g$ orbitals due to a strong axial

distortion of the octahedra can be as high as 1 eV due to their large σ hybridization with oxygen 2*p* orbitals [300] [298].

XMCD results obtained at the O *K* edge (at 100K with $\mu_o H = 2T$) in our three samples are shown in Fig. 4.30 (b). XMCD measurements at the O-K edge are particularly relevant here, as the magnetic interaction is mediated by O ions. In Fig. 4.30 (b) a strong negative XMCD peak can be observed in all three samples with an intensity equivalent to several percent of the total XAS intensity of the $t_{2g}$ region. This O *K*-edge XMCD signal is attributed to the 3d orbital moment on the neighboring sites of the Ni or Mn ions interacting through the p-d hybridization [301]**.** Because of the absence of spin-orbit splitting for the 1s core level, the O K-edge XMCD spectra show simply the orbital moment but are insensitive to the spin moment. Therefore, the integral area of the O *K*-edge XMCD is directly proportional to the orbital moment and, since the negative XMCD signal indicates a positive magnetic moment ($\mu_L > 0$), the orbital magnetic moment of O 2*p* is parallel to that of Ni/Mn 3*d* [302] [303].

# Summary

We have achieved the epitaxial growth of double perovskite PNMO thin films on (001) STO and (001) LAO substrates, by RF sputtering technique. Ferromagnetism is significantly influenced by oxygen pressure and growth/annealing temperature. The optimization of the growth conditions has revealed that only under a narrow window of deposition conditions, particularly at an oxygen pressure of 350 mTorr and deposition temperatures around 800-850$^o$C, PNMO films with good ferromagnetic properties can be obtained with Ms and Tc very close to the bulk value. High annealing temperatures (800-900$^o$C) promote the existence of a nanostructured surface, attributed to the formation of NiOx segregates as previously observed and discussed in LNMO systems. Additionally, XRD patterns showed the existence of a secondary NiO phase, as observed by AFM and SEM images. However although secondary phases are formed (NiO) together with the PNMO phase, films grow epitaxially on (001) STO substrates. On the other hand, the stoichiometry (measured by EPMA) showed that PNMO films grown/annealed at different growth temperatures (ranging from 200$^o$C to 900$^o$C) under a high oxygen pressure of 350 mTorr, has a Ni/Mn ratio close to 1 and a Pr: ( Ni + Mn) ratio with a certain degree of Pr deficiency. In spite of this Pr deficiency, the stoichiometry of the samples has little impact on the ferromagnetic properties. Additionally, thickness variation of PNMO thin films, grown on two different $SrTiO_3$ (STO) and $LaAlO_3$ (LAO) substrates, shows a strong influence on structural and magnetic properties. Reciprocal space maps (RSMs) around (103) reflection (for both substrates) reveal for the thinner films, that the in-plane pseudocubic cell parameters are equal to that of the substrate, indicating that it grows fully strained. However, a (partial) relaxation of the in-plane tensile strain and compressive strain takes place when thickness is increased, and the in-plane lattice parameters tend to

acquire the bulk value. Consequently, the thinnest films showed a loss of ferromagnetism at the (film-substrate) interface.

XAS measurements on two optimal ferromagnetic samples (i.e. with $T_C$ and Ms close to the bulk value) and in an other sample with poor magnetic properties (i.e., low $T_C$ and Ms), deposited on STO and LAO substrates, reveal that irrespective of the structural strain state (tensile or compressive) and the film thickness, the oxidization states of Ni and Mn ions are stabilized as $Ni^{2+}$ and $Mn^{4+}$, even in the one with poor magnetic properties. In addition, the intensity of both Mn and Ni XMCD signals for the samples with high Tc is larger than those of low Tc, which corroborates the results from magnetic measurements. At the same time, the Pr $M_{4,5}$ edge XAS spectra of the rare earth element reveal that the valence state of the Pr ions is 3+, indicating that the Pr deficiency in our $Pr_{2-\delta}Ni_{1-x}$ $Mn_{1+\ x}O_6$ compound, as analyzed by EPMA, had no evident impact on the oxidation state of Pr. Theoretical simulations based on charge transfer multiplet model of XAS and XMCD data at Ni $L_{2,3}$ and Mn $L_{2,3}$ edges, allow us to conclude that the experimental spectra are in a good agreement with calculated spectra of $Ni^{2+}$ and $Mn^{4+}$ in $O_h$ symmetry and high-spin configuration. The dichroic signal corresponding to the calculated XMCD spectrum of $Pr^{3+}$ further corroborates that the valence state of Pr in our samples is 3+.

# Chapter 5

# Conclusions

In the present thesis, two kind of ferromagnetic transition metal oxides, namely $R_2NiMnO_6$, where R = La, Pr, (i.e. $La_2NiMnO_6$ and $Pr_2NiMnO_6$), have been investigated for their potential applications in spintronics. We have shown that high-quality epitaxial thin films of the double perovskite LNMO and PNMO, with good ferromagnetic properties (i.e., Tc and Ms very close to the bulk value), can be prepared by using the magnetron sputtering deposition technique. In this process, it has been observed that the magnetic properties of the films turn out to be strongly dependent on the growth parameters, particularly on the oxygen pressure used during deposition. In particular, good B-site cationic ordering of the double perovskite RNMO has been achieved only under a narrow window of deposition conditions. Nevertheless, the optimization of the growth parameters did not imply obtaining stoichiometric samples of the expected $R_2NiMnO_6$ compound. For each RNMO system studied here, the main conclusions are presented below:

The main conclusions dedicated to the $La_2Ni_{1-x}Mn_{1+x}O_6$ compound (chapter 3) are:

- High-quality double perovskite LNMO thin films with good ferromagnetic and insulating properties (i.e., Tc ≈ 240 K and Ms ≈ 5.3 $\mu_B$/f.u. at 10K) have been achieved under low oxygen pressures ($PO_2 \leq 140$ mTorr) and using high growth/annealing temperatures (850$^o$C).

- Structural properties of LNMO films on STO substrates (thickness in the range of t ≈ 30-50 nm) have revealed that the in-plane lattice cell parameters are equal to the STO ones, indicating that LNMO films grow fully strained. On the other side, the out-of-plane lattice cell parameters remain elongated in respect to the corresponding LNMO bulk value, probably caused by the presence of oxygen vacancies and the formation of $Mn^{3+}$.

- Regarding the stoichiometry of the films, it is found that LNMO samples grown at low pressures ($PO_2 \leq 140$ mTorr) are non-stoichiometric with remarkable Ni deficiency. In spite of this Ni deficiency, samples exhibit excellent ferromagnetic properties.

In contrast, samples grown at high oxygen pressures ($PO_2 \geq 300$ mTorr) present good stoichiometry but poor ferromagnetic properties.

- XAS measurements on nonstoichiometric samples have allowed us to conclude that Ni deficiency does not affect the valence states of Ni ions that are stabilized as $Ni^{2+}$. Nonetheless, the Mn ions are in a mixed valence states $Mn^{3+/4+}$ with an effective valence of 3.6+. In this regard, some kind of cationic ordering between $Ni^{2+}$, $Mn^{3+}$, and $Mn^{4+}$ in the B sublattice has to be assumed and thus a Ni deficiency could favor Ni/Mn ordering.

The main conclusions dedicated to the $Pr_{2-\delta}Ni_{1-x}Mn_{1+x}O_6$ films (chapter 4) are:

- High-quality thin films of the double perovskite PNMO with good ferromagnetic (i.e, for PNMO/STO, $T_C \approx 210$ K and $Ms \approx 4.5\mu_B$/f.u. and, for PNMO/LAO, $T_C \approx 216$ K and $Ms \approx 4.85\ \mu_B$/f.u., at 10K) and insulating properties have been achieved under high oxygen pressures (350 mTorr) and high growth/annealing temperatures (800-850$^o$C).

- The stoichiometry of the PNMO films, determined by EPMA measurements, has revealed that films grown under high oxygen pressures ($PO_2 \geq 350$ mTorr) show a certain degree of Pr deficiency. However, in spite of this Pr deficiency, the stoichiometry of the samples has little impact on the ferromagnetic properties.

- Structural and magnetic properties of PNMO thin films grown on two kinds of substrates (STO and LAO) under the optimized growth conditions have shown a strong dependence on film thickness. Particularly, the thinnest films showed a loss of ferromagnetism at the (film-substrate) interface.

- XAS measurements and theoretical simulations, based on charge-transfer multiplet model, show that Ni and Mn ions are stabilized as $Ni^{2+}$ and $Mn^{4+}$, even in samples with low Tc. The valence state of Pr in our samples is found to be $Pr^{3+}$, indicating that a certain degree of Pr deficiency (as revealed by EPMA) has no apparent impact on the Pr oxidation state.

Finally, annealing treatments in oxygen atmosphere at high temperatures (800-900$^o$C), commonly employed to improve the magnetic properties of RNMO thin films, promote the formation of a nanostructured surface by $NiO_x$ cuboids. The formation of NiOx phase segregations could be favored by the presence of oxygen deficiency and cationic vacancies, thus affecting the ferromagnetic and surface transport properties.

# 5.1 Future work

The results discussed and exposed in this thesis can lead towards different alternatives for further research:

- An ideal tunnel barrier requires a film thickness below 4 nm, high crystalline quality and smooth surface. It is clear that, in addition to the growth parameters, the geometry of the (magnetron sputtering) deposition setup has also a significant impact on the film stoichiometry. Exploring the growth of RNMO thin films on Nb-doped STO substrates using off-axis geometry could be an alternative to obtain high-quality thin films with good ferromagnetic properties.

- The issue of nonstoichiometry in LNMO and PNMO films with good ferromagnetic properties is still under debate and deserves more attention. Preparing nonstoichiometric films using nonstoichiometric LNMO and PNMO targets could be an alternative to complement the study of their physical properties.

- The microstructure and physical properties of thin films can be influenced by various factors such as growth conditions (i.e., growth temperature, oxygen pressure and annealing), as well as the epitaxial strain induced by the film-substrate lattice mismatch. Investigations on LNMO and PNMO thin film grown on different substrates using magnetron sputtering are still scarce. Therefore, depositing RNMO (R = La, Pr) thin films on different substrates, additional to STO and LAO ones, could be interesting to further explore the role of strain on their electrical and magnetic properties.

- Oxygen annealing processes at high temperature, commonly used to improve the magnetic properties of RNMO thin films, promote the spontaneous formation of a nanostructured film surface. Controlling this outgrowths formation is of strong interest in the field of microelectronics. Therefore, achieving controlled nanostructured film surface and studying in depth the physical properties is necessary.

- Other rare earth double perovskites are still under investigation, especially in the thin film form. Therefore, the deposition of RNMO thin films by magnetron sputtering and the study of the role of the rare earth ionic radius on the structural and physical properties are of great interest.

# Appendix A

# Experimental techniques

This appendix gives a brief explanation of the most relevant experimental techniques used during this thesis. In the beginning of this appendix the growth technique used in obtaining the RNMO (R = La, Pr) thin films is briefly explained. In addition, the experimental techniques used for thin film characterization (morphological, structural, compositional *etc*.) are described.

## A.1 Thin film deposition technique

All samples prepared in this work have been grown by radio frequency (RF) magnetron sputtering at the ICMAB laboratory. This technique will be shortly explained in this section as well as the parameters to take into account during the preparation of the RNMO thin films.

### A.1.1 Magnetron sputtering

In a basic sputtering process, a target (or source) material, containing the elements to be deposited onto a substrate, is bombarded by energetic ions, usually ions of an inert sputter gas (argon) or of a reactive sputter gas (typically oxygen). The highly-energetic collisions of these ions at the target surface causes the removal (known as sputtering) of target atoms, which condense onto the substrate to form a thin film of similar stoichiometry to that of the target material. The main physical phenomenon involved in the sputtering technique is the momentum transfer between energetic atomic-sized particles (ions of noble gas) and the atoms of the surface of the target material. During this interexchange of momentum, elastic and inelastic collisions can happen. During elastic collisions, reflected particles (neutrals, ions of the target and from the gas) are mainly found; while during inelastic collisions, the secondary electrons, UV/visible photons, X-ray and implanted particles are involved [304]. On the other hand, there are various modes in magnetron sputtering technology including DC (direct current), MF (medium frequency), RF (radio frequency), or their combinations [305] [306].

In the case of conducting (target) materials, DC sputtering technique is suitable. If the target is an insulator though, positive charge accumulation can appear on its surface and impede the growth of insulating films. In this case, a RF power supply is recommended. In this thesis, as our target is insulating, the power supply that we have used is the RF magnetron. The deposition process by RF magnetron sputtering takes place in a vacuum chamber, with a residual pressure bellow $10^{-6}$ Torr, to ensure the least amount of impurities possible and prevent contamination of the films. RF magnetron sputtering is often considered the most convenient method to prepare thin, homogeneous, uniform and pure films of various materials.In RF magnetron sputtering systems, the amount of electrons involved in the ionization process is increased by employing powerful magnets. They increase the probability of electrons to hit the noble gas atoms by increasing the length of the electron path and hence the ionization efficiency. For this purpose, a ring-shaped magnet is mounted below the target to increase the ionization rate and the number of secondary electrons ejected from the surface of the target. The magnetic field thus creates traps for the electrons in cycloids, keeping them circulating over the target surface, which increases the dwell time of electrons in the gas and thus raises the ionization probability. By generating magnetic field inside the chamber an effective sputtering process at low pressure is made possible [137]. In our magnetron sputtering system, the chamber is provided with two electrodes, one of them is the target and the other one is the substrate. Ionic bombardment of the target is obtained by a flux of gas (oxygen in our case), which is ionized due to the potential difference in the ion gun. Therefore, a highly ionized plasma is created in the region between the magnetron sputtering cathode target and the anode outer crown, as the discharge process occurs between them [137]. In this regard, plasma ions bombard the target surface and, as a result of the collisions, neutral target atoms are ejected and deposited on the substrate. In the deposition chamber, the film growth is on-axis, meaning that the normal axis of the center of the target coincides with the normal axis of the substrate (see sketch in Fig A.1).

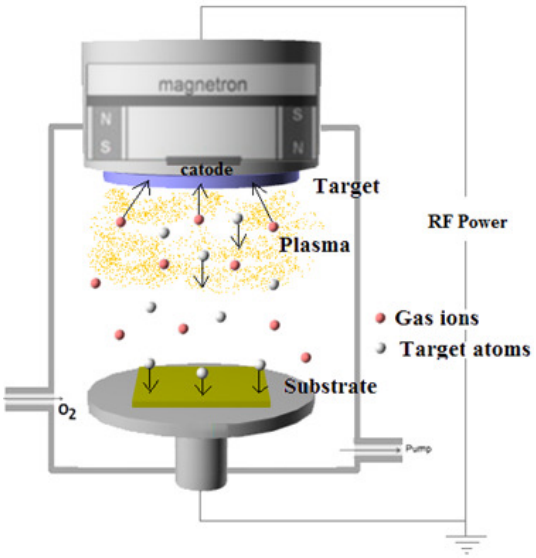


Figure A.1. Sketch of sputtering system with the main components

RF magnetron sputtering offers additional advantages, including the use of non-conductive targets, charge-up effects and reduced arching due to the use of alternating electric field (RF frequency). Another advantage of the magnetron is that fewer electrons reach the substrate (causing less heating and less substrate damage). Cold water flows inside the magnetron to prevent magnetron damage due to excessive heating. In general, this technique provides high quality thin films, presenting good adherence to the substrate and good stoichiometry. Complex oxide films can be grown under high purity gases, such as oxygen and argon, at a controllable pressure and at a wide range of oxygen pressures, from very low $5x10^{-3}$ Torr to as high as 0.5 Torr. On the other hand, as mentioned in chapter 2 (see section 2.2), the optimization of thin films grown by RF magnetron sputtering is challenging due to huge number of deposition parameters, leading to different growth modes which in turn affects the film quality and its physical properties. Besides the substrate choice, the parameters to take into account during RNMO thin film preparation are the following:

- RF power and target-to-substrate distance. These parameters influence the growth rate, and thereby affects the ion mean-free-path (energy with which the ions reach the substrate) and subsequently the crystalline quality of the deposited film. All our thin films were deposited by keeping a fixed target-to-substrate distance of 5 cm. The power used was typically of 20W or 40W.

- Sputtering gas pressure (gas mixture) and substrate temperature during deposition. These parameters influence the ion mean-free-path, the diffusion of the particles on the surface, re-sputtering process and, thus, the thin film growth mode (which affects its crystallinity, texture and roughness), as well as the film stoichiometry and growth rate. Our films were grown under different oxygen partial pressures (ranging from 70 to 750 mTorr) and different growth temperatures (ranging from 500 to 900$^{o}$C). The deposition time depends on the desired thickness, mean-thickness generally 1h in our case.

- Annealing after film growth and cooling rate. They affect the film oxygen stoichiometry, the diffusion or mobility which could cause changes of surface morphology, crystal structure and composition. Annealing after film growth is generally carried out at the same growth temperature, under high oxygen pressure (420 Torr), and with typical annealing time of 1h. After annealing treatment, films are cooled at low cooling rates down to room temperature, generally at 10°C/min. However, we have also used slower cooling rates, such as 2°C/min and 0.3°C/min, in order to improve the magnetic properties of the films (see chapter 2, section 2.2.1.2).

# A.2 Scanning Probe Microscopies

The scanning probe microscopy (SPM) is one of the powerful research techniques that allow studying the morphology and the local properties of the film surface with high spatial resolution. This includes scanning the sample surface with a very fine probe (tip), and tracking the strength of the interaction between the surface and tip. We have used Atomic Force Microscopy (AFM) and Conductive Atomic Force Microscopy (C-AFM) to characterize the film surface, which will be briefly explained in this section.

## A.2.1 Atomic Force Microscopy (AFM)

Since its appearance in the 1980s, the Atomic Force Microscope (AFM), is one of the scanning probe microscope which operates by measuring interaction forces between a tip and the sample surface. Based on the local interaction between the tip and the surface of a sample, AFM is a technique giving insight to surface properties of materials with high spatial resolution, less than 100 nm (depending on the tip used, surface roughness and/or the material hardness). It allows three-dimensional image reconstruction of surfaces (surface topography, phase, resistivity etc).

The AFM consists of a microscale cantilever with a sharp tip (commonly less than 10 nm in diameter) at its end that is used to scan the sample surface. Fig A.2 (a) shows a sketch of the process. When the tip is moved close to the surface of the sample, short-range forces (as interatomic Van der Waals) between the tip and the sample surface appear which cause the deflection of the cantilever, the cantilever is moved closer or further from the sample with a piezoelectric actuator (see Fig.A.2 (b)). Simultaneously, a detector measures this deflection by using a laser beam focused on the top of cantilever and reflected into an array of photodiodes, thus generating a surface topographic map of the sample surface by storing the deflections of the cantilever in the z direction in a computer with respect to spatial variation in the x-y plane [307].

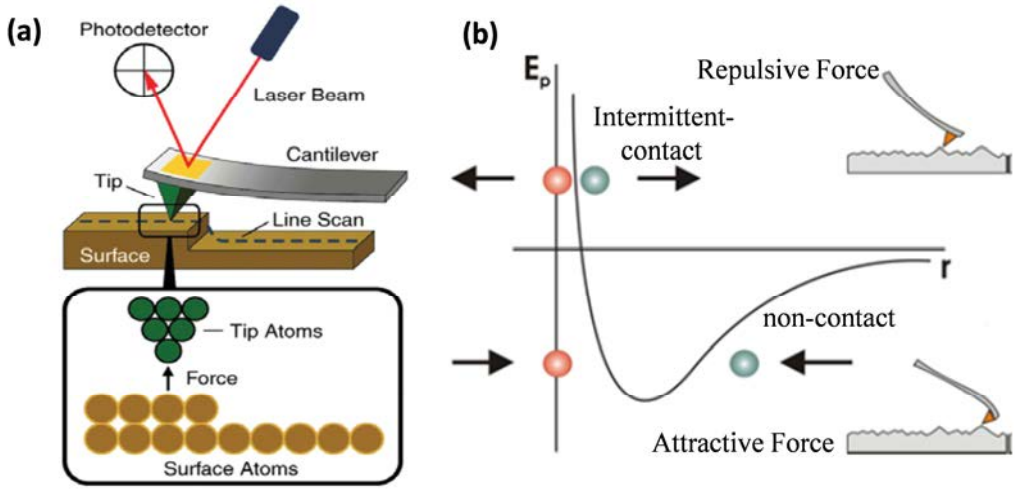


Figure A.2 (a) Sketch of working principle of Atomic Force Microscopy (AFM) (b) sketch of Van der Waals Force depending on the distance between the tip and the sample. Figs taken from ref [308].

The primary modes of imaging in AFM depending on the distance between the tip and the sample are noted as: contact mode, intermittent mode and non-contact mode; depending on the sample, different modes are recommended.

**Contact mode:** Sample and tip are very close together, so that the interactions between the tip and the surface cause repulsive forces which make the cantilever to bend in a negative direction. The magnitude of force between the tip and the sample surface depends on the spring constant and the distance between the probe and the sample. According to Hooke`s law, this force is given by: F=-k.x, where F= Force, k= spring constant and x= cantilever deflection. As contact AFM produces directly the interaction force between its tip and sample, it is the most easily used technique for rough and very rough surface samples [309].

**Non-contact mode:** the tip does not make contact with the surface of the sample and that is in the attractive force regime. The forces are small, but changes in the amplitude and resonant frequency of the cantilever can be measured. Lower resolution, interference of contaminant layer on the surface with oscillation and the need of ultra-high vacuum are the major disadvantages of this mode of scanning.

**Tapping or "intermitent contact" mode:** the cantilever is oscillated at its resonant frequency and the tip taps the sample surface and thus makes contact with the surface at the bottom of its swing during scanning. The tip oscillates (near its resonance frequency) between the attractive and the repulsive regime. Very stiff cantilevers (30- 50 N/m) are used to avoid the tip getting stuck in the water contamination layer. Its main advantage is an improved lateral resolution for soft samples because dragging forces –present in the contact mode- are completely eliminated. The disadvantage of this method of measuring is the challenges in imaging liquids and the necessity of slower scan speeds [309].

This last mode (tapping) was the mode used during this thesis work. The major advantage of using AFM technique is that it doesn't require a vacuum environment for its operation. Also high quality contrast in topography and direct measurements of surface features giving quantitative information on height are provided by AFM when compared with SEM [307]. The AFM sample doesn't need metallic coating for measurements to carry on as the process doesn't need any electrical conduction. The sample preparation is simple and inexpensive when compared with transmission electron microscopes.

In this thesis work, AFM images have been performed at the ICMAB using a MFP-3D AFM (Asylum Research) in tapping mode.

## A.2.2 Conductive Atomic Force Microscopy (C-AFM)

The method of conductive force microscopy or C-AFM is used to study conductivity at the surface and electrical properties in resistive samples [310]. In C-AFM, a conductive tip is in contact with the sample (see Fig. A3), during this contact, a bias voltage is applied between AFM tip and sample and the current flow is measured between them, as the probe raster scans across the surface, creating a conductivity or current map [310].

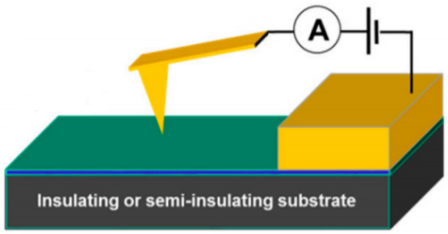


Figure A.3. Schematic illustration of conductive atomic force microscopy (C-AFM).

The electrical conductivity is measured with a low noise, high gain preamplifier. With this setup, topography and current information are collected independently in C-AFM. The conducting probe in C-AFM has a thin conducting coating. Common electrically conducting coatings are platinum, gold, tungsten, and conductive diamond. For high spatial resolution in C-AFM the tip should be as sharp as possible, highly conductive, and mechanically stable at the same time. Probes with conductive diamond coating (heavily doped diamond) are the most commonly used tips for the technique. Wear resistance and quality of conduction, thus low resistivity are the most important aspects for the choice of the tip. Apart from 2D current

images, localized single point measurements of current-voltage (I-V) curves can also be collected with C-AFM, which give greater insight of the transport properties of materials revealing several kinds of behaviours: ohmic, Schottky barriers, resistive switching behaviours, etc [310] [311]. For these electrical measurements, the user places the probe at the desired location on the sample surface and ramps the bias voltage while collecting the current [312].

At the ICMAB, the local electrical response of the films surface was explored by Conductive Atomic Force Microscopy (C-AFM), measurements were performed employing a MFP3D microscope from Asylum with an ORCA module. Diamond doped coated probes (DDESP-FM-V2 from Bruker) were used in both the current maps and the I-V curves to ensure the stability of the tip during the acquisition of the data. Moreover, these measures were carried out in a closed chamber with nitrogen atmosphere with the aim of reducing the ambient humidity and, therefore, avoid possible anodic oxidation effects.

# A.3 Electron Microscopy

Given sufficient light, the unaided human eye can distinguish two points 0.2 mm apart. If the points are closer together, they will appear as a single point. This distance is called the resolving power or resolution of the eye. Similarly, light microscopes use visible light (400-700nm) and transparent lenses to see objects as small as about one micrometer, such as a red blood cell (7 μm) or a human hair (100 μm). Light microscope has a magnification of about 1000x and enables the eye to resolve objects separated by 200 nm. Nevertheless, optical microscopes are limited by the physics of light; due to these limitations the electron microscopes were developed. Electron microscopes are capable to reach much higher magnifications and have a greater resolving power than a light microscope, thus allowing to see much smaller objects at sub cellular, molecular and atomic level [313]. In this regard, additional to topographical analysis by AFM, there are three different electron microscopes such as the Scanning Electron Microscope (SEM), Transmission Electron Microscope (TEM) and Electron Probe Microanalysis (EPMA), which allows to obtain information about the topography, the crystalline structure, microstructure and composition of the samples. A brief description of these techniques will be carried out in this section.

## A.3.1 Scanning Electron Microscopy (SEM)

The scanning electron microscope (SEM) is one of the most versatile instruments available for the examination and analysis of the microstructure morphology and chemical composition characterizations. It can be regarded as an effective method in analysis of organic and

inorganic materials on a nanometer to micrometer (μm) scale. SEM is an instrument that allows analyzing all kind of surfaces by using electrons. A beam of electrons is formed by an electron source and accelerated toward the sample using a positive electrical potential. Highly energetic electrons in the beam (20-30 keV) interact with the atoms of the sample. Different detectors inserted in the SEM chamber probe different types of interactions [314], their signal provides information about its surface topography, composition and other electrical properties that can be independently detected according to its origin (a schematic representation of the probing depth of each signal is shown in Fig.A.4). SEM can work at a high magnification reaching to 1000000x (the ratio of image distance versus object distance) and producing very precise images of wide range of materials [315].

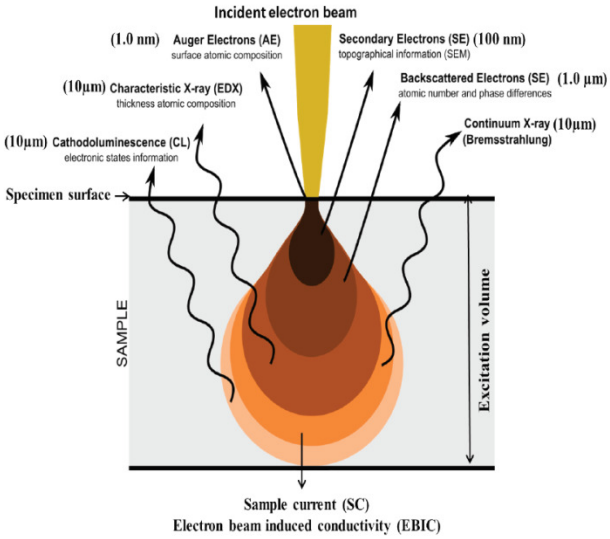


Figure A.4. Different penetration level of electron through the sample. Image taken from ref [313].

When the incident beam touches the surface of the sample produces signals such as:

**Secondary Electrons:** These low energetic electrons (<50 eV) are used primarily to reveal topographical feature of a sample. The electrons from the direct beam scatter inelastically with electrons from the sample surface (the resolving power below 10 nm).

**Back scattered electrons (BSE):**

Those highly energetic electrons are reflected from the sample by elastic scattering. Deflected, back in the direction of the beam, these electrons are used to discriminate areas of different atomic numbered elements. Higher atomic numbered elements give more backscattered electrons and appear brighter than lower numbered elements (the resolution reach the level of 1000 nm).

**Characteristic X-rays:** The highly energetic electrons interact with the shell electrons of the sample atoms. As a consequence, an inner shell electron is ejected, which temporarily ionizes the atom until an outer shell electron drops into the vacancy to stabilize the atom. Since this electron comes from a higher energy level, the energy is released as an x-ray, which equals the difference in energy between the two shells. Therefore, from the emitted X-rays, information on the chemical composition of the sample in the selected area from the SEM image can be obtained [313]. Energy dispersive x-ray (EDX) detector and Wavelength Dispersive X-ray (WDX) detector are employed for x-rays detection.

**Auger Electrons:** These are special types of low energy electrons that carry the information about the chemical nature (atomic composition) of the sample. It is a powerful tool for studying the distribution of the lighter numbered atomic elements on the surface of the sample. It has limited application in biological sciences.

**Cathodoluminescent:** This effect results when the energy of the impinging electrons is converted into visible light. Certain types of compounds are capable of cathode luminescence and detected by special types of detector. The resolution is the similar to the light microscope

**Bremsstrahlung:** Two important types of x-ray may be generated when the beam electron encounters the atoms of the sample, continuous or bremsstrahlung x-ray and characteristic x-ray are generated when incoming, beam passing close to the atomic nucleus is slowed by the coulomb field of the nucleus with the release of x- ray energy. The intensity of x-ray energy released depends on how close the electron comes to the nucleus closer. The closer passes decelerate the electron more and yield higher energy x-rays. These are used to measure sample mass thickness when quantitative analysis performed on thin sections. These are continuous x-rays also known as background or white radiation [313].

The surface morphology of the RNMO (R= La, Pr) thin films were obtained in a Scanning Electron Microscopy (QUANTA FEI 200 FEG-ESEM (Tungsten filment)) located at the ICMAB. Energy Dispersive X-Ray (EDX) analysis has been performed on a FEI Magellan 400L XHR SEM using an X-Max Ultim Extreme EDX detector (Oxford Instruments) located at the *ICN2*.

# A.3.2 Transmisson Electron Microscopy (TEM)

Transmission electron microscopy (TEM) is an imaging technique where a beam of electrons accelerated typically to 200 kV is focused onto a specimen, thus the beam of electrons passes through the specimen and analyzes the internal structure of the specimen in the form of images causing an enlarged version to appear on a fluorescent screen or layer of photographic film. TEM provide topographical, morphological, compositional and crystalline information, the images allow to view samples on a molecular level, making it possible to analyze structure and texture [316]. The amount and scale of the information which can be extracted by TEM depends critically on four parameters: the resolving power of the microscope (usually smaller than 0.3 nm), the energy spread of the electron beam (often several eV), the thickness of the specimen (almost always significantly less than 1 μm) and the composition and stability of the specimen [317]. Using different operating modes TEM allows not only image formation (image mode) but also registering diffraction patterns of selected areas of the sample (diffraction mode). However, samples need prior preparation for TEM analysis and the main limitation is the complexity of the sample preparation procedure i.e. they need to be thinned down to lower that 100 nm (below 20 nm for high resolution imaging), in order to enable electrons to pass through. If we need to probe a very small, specific region of the sample, a focused ion beam (FIB) is used to cut the very small cross-section slice of sample directly, without destroying the rest of the sample. The advantage is that it is equipped with an electron gun (like in a SEM), so that we can image in-situ the part we are cutting with the ion beam. Generally, there are two types of specimen configurations for imaging heterostructures or thin films by TEM: the cross-section and the planar view.

**A plan-view**: in this configuration the cut is parallel to the sample surface (perpendicular to the 00l planes). The thickness is reduced and a hole with non-vertical walls is etched in order to create a wedge .The thinnest part of the wedge is the one that can be imaged by TEM (see sketch in Fig A.5 (a)).

**A cross-section**: consists in an extremely thin slice of the sample cut in the direction perpendicular to the substrate plane. In this orientation, the substrate, the thin film layers, and the interfaces between them can be imaged either simultaneously or individually. The information from each of these regions remains distinct from that obtained from the others, eliminating the problems of superimposition that are a consequence of viewing a layered structure in the conventional manner (i.e., parallel to the surface normal). The most common preparation consists in cutting two slices of the sample and joining them by the surface. After that, the joint slice's thickness is reduced as much as possible. The substrate and different layers of the sample are resolved, and information is extracted about the quality of the interfaces, the in-plane and out-of-plane crystallographic/lattice parameters, the defects in the film, etc (see sketch in Fig A.5 (b)). If we need to probe a very small, specific region of the

sample, a focused ion beam (FIB) is used to cut the very small cross-section slice of sample directly, without distroying the rest of the sample. The advantage is that it is equipped with an electron gun (like in a SEM), so that we can image in-situ the part we are cutting with the ion beam.

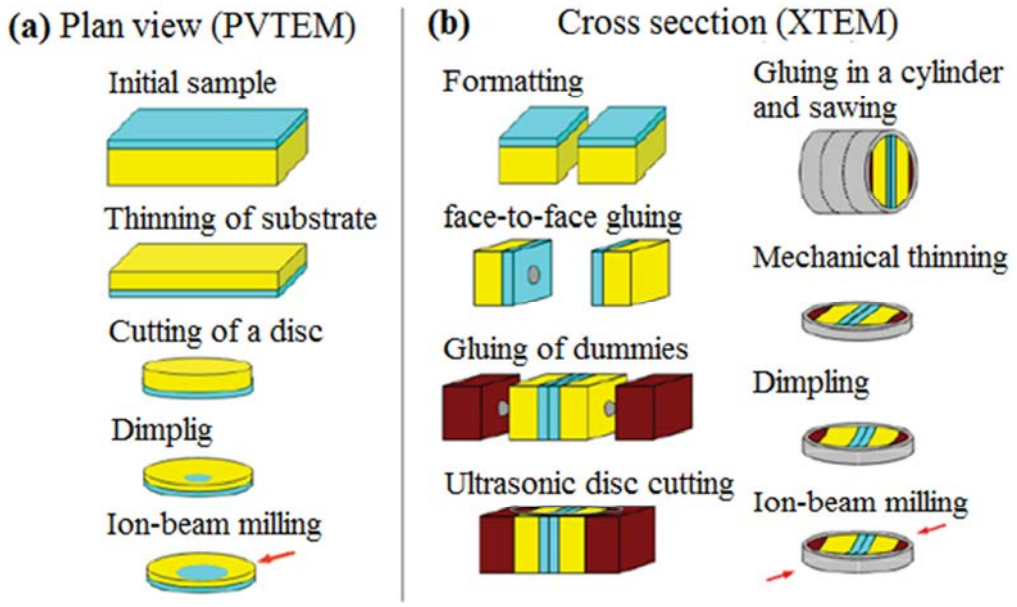


Figure A.5. Sketch of the preparation process of a plan view and cross section to be imaged by TEM. Figure taken from ref [318].

Finally, special TEM techniques can also be performed such as: First, Scanning Transmission Electron Microscopy (STEM), which no longer consists of a static electron beam but, instead, the condenser lenses concentrate the beam on a small spot size that can be scanned on the sample by means of scan coils. STEM images have better contrast than conventional TEM images and they can also be obtained either in dark field or in bright field mode. Second, High Resolution Transmission Electron Microscopy (HRTEM), in which TEM images are formed by a process called phase contrast. The contrast is formed by constructive and destructive interference from the electron waves passing through a material showing a certain periodicity (crystalline material). This phase-contrast technique allows obtaining much information about the crystal structure of the material.

In this work, High-Resolution Transmission Electron Microscopy (HRTEM) was used to study the microstructure of Cross-Section specimens and Plan View of the RNMO (R= La, Pr) thin films on a FEI Tecnai G2F20 S-TWIN HR(S) TEM operated at 200 kV with a point-to-point resolution of 0.19 nm, located at the *ICN2*.Cross section specimens were prepared by focus ion beam (FIB).

# A.3.3 Electron Probe Microanalysis

Electron probe microanalysis (EPMA) is a nondestructive analytical technique widely used for quantitative analysis of the elemental composition of solid specimens at a micrometer scale. The technique is based on the measurement of characteristic X-ray intensities emitted by the elements present in the sample when the latter is bombarded with a focused electron beam. The results are commonly displayed as weight percentages of elements. For each element, the ratio of the characteristic x-ray intensity emitted from the sample to that emitted from a standard of known composition (k-ratio) is measured. The transformation from measured k-ratios to concentrations is performed by analytical algorithms, which assume that the sample region from which x rays emerge has a homogeneous composition. For keV electron beams, this region is typically about 1 μm, depending on the density of the material and the analytical conditions. Accordingly, EPMA is suitable for the analysis of samples that are homogeneous on the micron scale. EPMA also couples quantitative analytical capabilities with imaging capabilities, allowing detailed mapping of compositional contrast [319].

Figure A.6. Electron microprobe CAMECA SX-50 at the CCiTUB (4 WD spectrometers + 1 EDS), Figure taken from ref [319].

Using wavelength-dispersive spectrometers, elements from Be to U can be analyzed by EPMA with detection limits for most elements down to 100 ppm or lower, accuracy of 2% for major element concentrations and a spatial resolution of few microns. EPMA also couples quantitative analytical capabilities with the imaging capabilities of a scanning electron microscope, allowing detailed x-ray mapping of composition contrast. Moreover, EPMA can also be used to determine the thickness and composition of thin films and multilayers with

thickness in the sub-micron range, providing information on the lateral variation in thickness and composition at the micrometer scale. At the same time, EPMA is extensively used in many fields and has been central for the microanalysis of ceramic, metallurgical, geological, biological, and other materials [319].

In this thesis, the chemical composition and stoichiometry ratio of RNMO (R= La, Pr) thin films were determined by wavelength dispersive spectrometer (WDS) electron probe microanalysis (EPMA) using a CAMECA SX-50 electron microprobe equipped with four wavelength-dispersive Xray spectrometers, located at the CCiTUB - Scientific and technological Centers UB.

# A.4 Structural Characterization Techniques

In this thesis work, different techniques based on X-rays were used to determine the crystalline quality of the samples, the film thickness and the lattice parameters of the films with respect to the substrate. These techniques will be briefly explained in this section.

## A.4.1. X-ray diffraction

X-ray diffraction (XRD) is a useful technique to identify crystal structure of materials since the X-ray wavelengths (between 0.2 and 10 nm) are comparable to the interatomic spacing of crystalline solids. The technique measures the average spacing between layers or rows of atoms. It provides information on structures, phase's identification, crystal orientations (texture) and other structural parameters, such as average grain size, crystallinity, strain, crystal defects, lattice parameters, epitaxial relation with the substrate, etc [320]. Diffraction is a coherent and elastic scattering phenomenon of an incident electromagnetic wave, where the periodic lattice of a crystal diffuses in a coherent way the X-rays. Providing that the X-ray fulfill the Bragg condition, we will have a constructive interference and observe a diffraction peak. Bragg's law describes the diffraction of X-rays by a crystal.

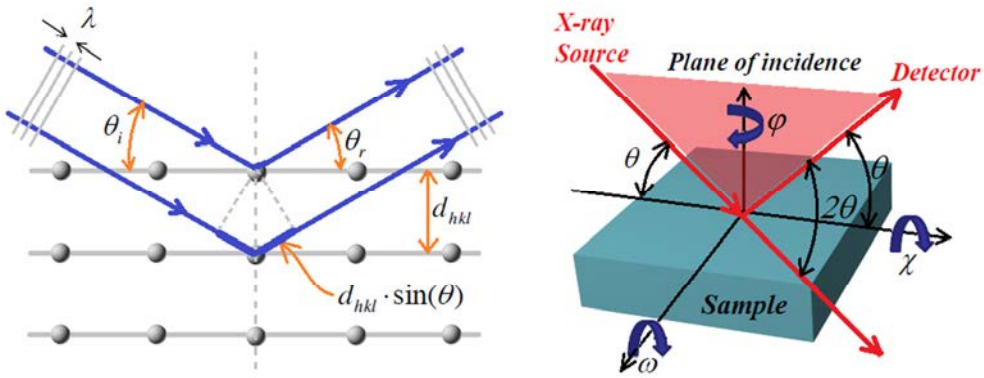


Figure A.7. Schematic representation of the Bragg's law.

In Fig A.7, Constructive interference occurs when the path difference of two waves equals a multiple of the wavelength of the incoming radiation, the so-called diffraction condition of the Bragg's law:

$$2d_{hkl}\,sin\theta = n\lambda \qquad \text{(A.1)}$$

where interplanar distance $d_{hkl}$ is the distance between adjacent crystal plane for a given family (*hkl*), $\theta$ is the Bragg angle at which one observes a diffraction peak, $n$ is the order of diffraction and $\lambda$ is the wavelength of the incoming X-ray radiation. In our case, the wavelength used is the $K\alpha_1$ line of copper: $\lambda$ =1.5406 Å [321]. Different configurations of X-ray source, thin film sample and detector can be performed in order to get different information, including θ-2θ scans, rocking curve or ω scans, reciprocal space maps (RSMs) or Q-plots and X-ray reflectivity (XRR).

At the ICMAB, structural characterization was made by means of X-ray diffraction (XRD) and reflectivity techniques using a D5000 (Siemens) diffractometer, an X`Pert MRD (PANalytical) four-angle diffractometer (Cu-$K\alpha_1$ radiation).

## A.4.2. θ-2θ scan

In this geometry, the scan motion of the detector ($2\theta$ angle) and the rotation of the sample plane around the ω axis are coupled in the condition $\omega=2\theta/2$. It provides information about the crystal orientation, the lattice mismatch between the film and the substrate and the out-of-plane lattice parameters. Thin film samples with a mixture of single crystal, random polycrystalline layers and highly textured layers can be measured with all the features appearing simultaneously in diffraction frames by using GADDS with 2D detector.

As an example, STO single crystals with (001) orientation are one of the most employed substrates for epitaxial thin film growth. Therefore, the out-of-plane direction is perpendicular to the sample surface, and thin films grow epitaxially on top of the substrate. This indicate that in the θ-2θ diffractogram, only peaks corresponding to the (00l) reflections will appear, and only the out-of-plane cell parameter (c) will be determined from the angular position of the peaks. From this geometry, no information about the in-plane parameters (a, b) can be extracted.

## A.4.3. Rocking curve or ω scans

In this scan the 2θ angle of a given reflection peak is maintained fixed while the ω angle is swept around ω =θ within a short range. Thus, narrow Rocking curve peaks, characterized by full width at half maximum (FWHM), become a figure of merit of the crystal quality of the films.

## A.4.4. Reciprocal space maps (RSMs) or Q-plots

The reciprocal space maps allow determination of in-plane and out-of-plane lattice parameters of the Bragg spots of the film and the substrate. In order to determine the in-plane parameter and the out-of-plane parameter is useful to define corresponding $q_{parallel}$ and $q_{perp}$ as the parallel and perpendicular component of $\vec{q}_{hkl}$ in reciprocal space (see Fig A.8) [322].

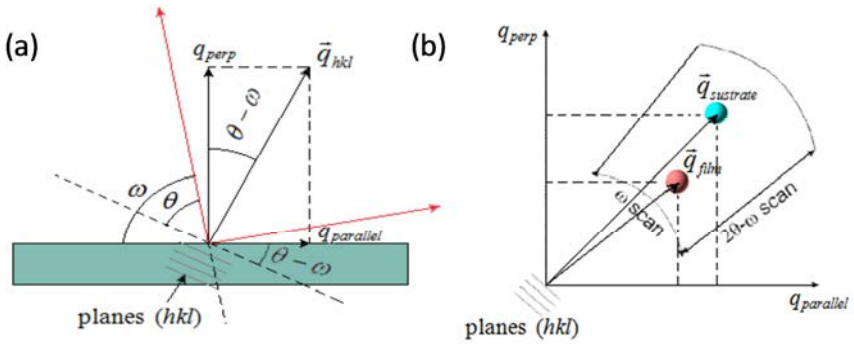


Figure A.8. (a) Reciprocal space vector $\vec{q}_{hkl}$ and the relationship with the angles $(\theta, \omega)$. (b) Schematic description of a *q*-plot scan.

If we consider $a$ and $b$ the in-plane parameters and $c$ the out-of-plane parameter in an orthogonal base, then next expressions are fulfilled:

$$q_{parallel} = \sqrt{\frac{h^2}{a^2} + \frac{k^2}{b^2}} \qquad q_{perp} = \frac{l}{c} \tag{A.2}$$

A reflection of the type (*h0l*) tends to be used. Then, the expressions are simplified:

$$q_{parallel} = \frac{h}{a} \qquad q_{perp} = \frac{l}{c} \tag{A.3}$$

The determination of $q_{hkl}$ is carried out by the so-called *q-plot scan*, which consists of doing a $2\theta - \omega$ scan for different values of $\omega$ of a given asymmetric reflection (otherwise only $q_{perp}$ could be determined), as depicted in Fig. A.8 (b). It is necessary to relate the angles $(\theta, \omega)$ to $q_{paral}$ and $q_{perp}$. From the Bragg law, $2d_{hkl} \sin\theta = \lambda$, and from Fig. A.8 (a), next expressions can easily be deduced:

$$\begin{aligned} q_{parallel} &= \frac{2}{\lambda} \sin\theta \sin(\theta - \omega) \\ q_{perp} &= \frac{2}{\lambda} \sin\theta \cos(\theta - \omega) \end{aligned} \tag{A.4}$$

RMSs were carried out in a Bruker-AXS General Detector Diffraction System (GADDS) model D8 Advance with a 2D detector (located at the icmab), with a step size of $0.01^o$ in 2θ and $0.034^o$ in $\omega$.

## A.4.5. X-ray reflectivity (XRR)

X-ray reflectivity (XRR) is a well-established and powerful technique for thin film characterization. The XRR pattern is measured in the same geometry as the θ-2θ scan but with a much smaller angle of incidence, from 0.3 to $5^o$. This technique allows determining the thickness of the films (2 – 200 nm), the roughness and the density of the film or even multilayers [323].

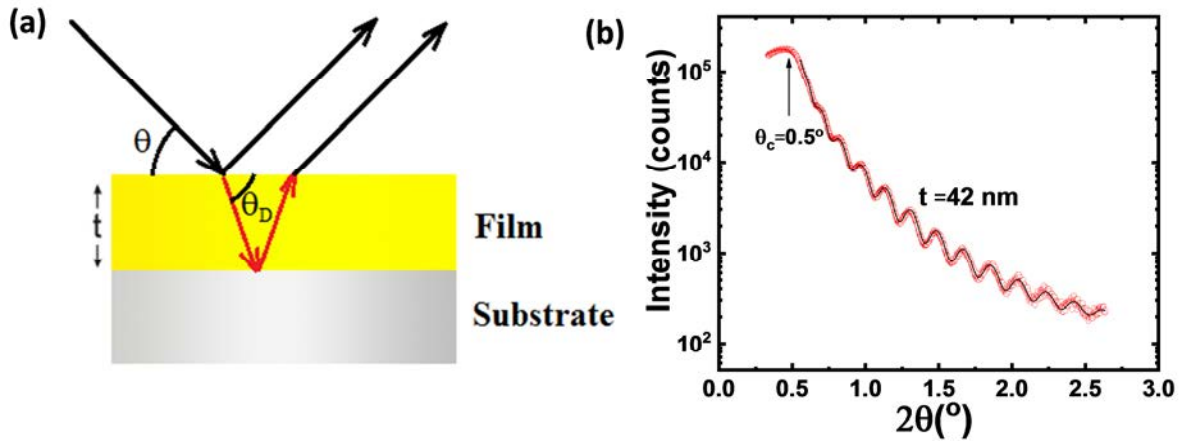


Figure A.9 (a) Sketch of the XRR experiment, where $\theta$ the incident angle, $\theta_D$ the diffracted angle and $t$ is the thickness of the film. (b) XRR spectrum of a 42 nm-LNMO thin film on an STO substrate showing the oscillations of the interference pattern. The fitting to the data (black line) was done using X-Ray utilities library [215].

XRR consists of irradiating the sample with an incident X-ray at grazing angles (small ω angle, Fig. A.7) and collecting the reflected beam in a detector (placed at 2θ angle, Fig . A.7), very much a like to Fig. A.7, accomplishing the condition $\omega = \theta$ and $\psi = 0$. As incident grazing angles are used much of the intensity of the X-ray beam is reflected, being $\theta_c$ the critical incident angle, below which total external reflection occurs. Above $\theta_c$ part of the incident radiation penetrates the film (see Fig. A.9), with a diffracted angle, $\theta_D$, that is given by the Snell's law, $\cos\theta/\cos\theta_D = n = \cos\theta c$, where $n$ is the refraction index of the film. $\theta_c$ depends on the electronic density of the material, with typical values below 0.5º. Due to the different electronic density of film and substrate, reflection of the diffracted beam occurs at the interface. Thus, the incident beam is reflected from both the top of the film (surface) and the bottom of the film (interface), giving rise to constructive and destructive interference pattern depending on the difference in the optical path (Fig. A.9 (a)). In contrast to XRD, the refractive effects are significant at low incident angle solely, becoming negligible for high θ. Thus, XRR experiments are normally performed as a coupled θ/2θ scan up to $2\theta < 6º$, in which a pattern of interference fringes are recorded above $\theta_c$ [323].

For instance, an XRR curve of a LNMO film on STO substrate is shown in Fig.A9 (b). From XRR curve we can extract information about the thickness, the roughness and the density of the layer. XRR curve shows that bellow a threshold angle, the critical angle θc, all the incident radiation are reflected. Thus, the intensity measured by the detector is oscillatory with respect to the 2θ angle. The period of these oscillations, called Kiessig fringes, depends inversely on the film thickness [323]. Therefore, the thickness $d$ can be calculated through the periodicity of the oscillations, extracting the position of the minima (or, equivalently, the maxima) of the oscillations of interference, which is determined by the relation [324]:

$$\sin^2 \theta_n = \sin^2 \theta_p + n^2 \left(\frac{\lambda}{2d}\right)^2 \quad \text{(A.5)}$$

Where $\theta_n$ corresponds to the maxima of the reflected intensity, $\theta_p$ is the lowest angle for which there is detection, $n$ is the order of the peak and $\lambda$ is the wavelength of the incident radiation. Finally, XRR measurements were done at ICMAB using a Siemens D-5000 diffractometer, ranging from 0.5 to 5$^o$ in 2θ and a step of 0.002$^o$. The analysis of the thickness was performed using the program XRR-thickness.

# A.5 Magnetic Characterization

Magnetic measurements were performed using Magnetic Property Measurements System (MPMS XL-7T) from Quantum Design, with a radio frequency superconducting quantum interference device (RF SQUID). This technique provides information about a sample's overall magnetic moment in absolute units. It enables to measure magnetic moments over a wide range of temperatures (from 2 to 400 K) and magnetic fields (from -7 to 7 T). SQUID uses Josephson effect phenomena to measure extremely small variations in magnetic flux. Typically, a SQUID is a ring of superconductor interrupted by one or more Josephson junctions [325] (see Fig.A.10 (a)). SQUID magnetometers usually detect the change of magnetic flux created by mechanically moving the sample through a superconducting pick-up coil which is converted to a voltage $V_{SQUID}$. For the MPMS, the position is denoted as the x direction which is parallel to the external magnetic field $B_{ext}$ so that one obtains raw data, the so-called "lastscan," where $V_{SQUID}$ is plotted versus x-pos. as appreciated in Fig. A.10 (b). To reliably suppress the influence of all kinds of external magnetic fields, the pick-up coil is made as second order gradiometer. The entire detection system is sketched in Fig. A.10 (b) and the inset exemplarily shows a single SQUID scan where the maximum of $V_{SQUID}$ at x-pos. of 2 cm corresponds to the sample directly positioned in-between the double coil of the pick-up gradiometer. Highly magnetized samples must be moved very slowly through the pick-up coils in order not to exceed the maximum slewing rate of the electronic system [326] [327].

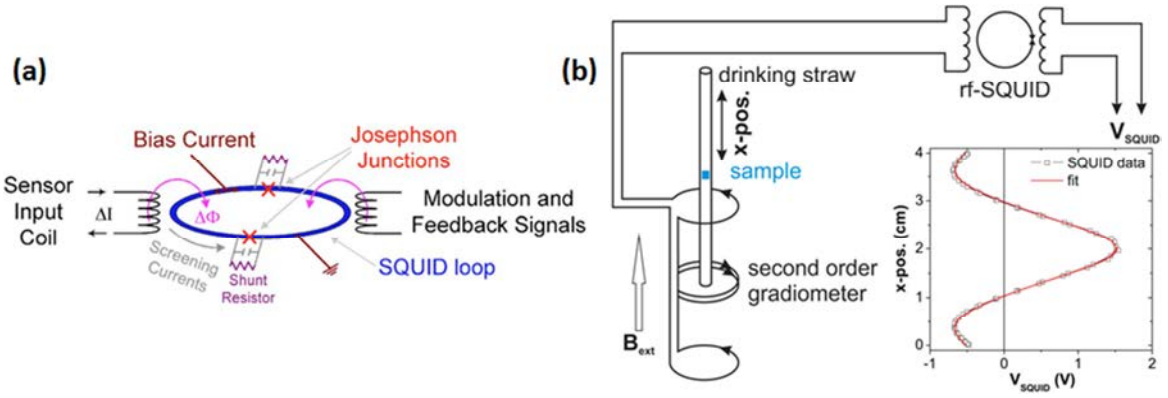


Figure A.10 (a) Dual junction (dc) SQUID loop. The capacitor represents the self-capacitance of the junction. (b) Schematic setup of a SQUID magnetometer with 2nd order gradiometer. The inset shows the SQUID response VSQUID versus sample position (x-pos.). Figs taken from refs [325] [326].

The magnetic properties of our materials are determined by measurements of magnetization vs. temperature and magnetic field (in units of emu/cm$^3$ or $\mu_B$/f.u.). The sample volume is a crucial parameter to determine the magnetization of the sample. This value is obtained from the film thickness (by XRR) and sample area. For instance, the magnetization of a LNMO sample as a function of temperature [M (T)] or an applied magnetic field [M (H)] is shown in Fig A.11 [(a) and (b) - (c)]. From the curve M (T), we can determine the Curie temperature Tc of the sample (Fig A.11 (a)).The raw data of M(H) is shown in Fig A.11 (b), the signal for thin films is generally weak (of the order of $10^{-5}$ emu), which it has a diamagnetic contribution coming from the substrate which must also be taken into account (it is not negligible). When measuring hysteresis loops, the negative slope at high magnetic fields indicates a diamagnetic contribution of the substrate (Fig A.11 (b)). This slope should be subtracted by adjusting the slope of the cycle at high fields. In Fig A.11 (a) and (c), the diamagnetic contribution of the substrate has been corrected, estimated from the linear high field slope of the raw data of the M(H) curve in (b).

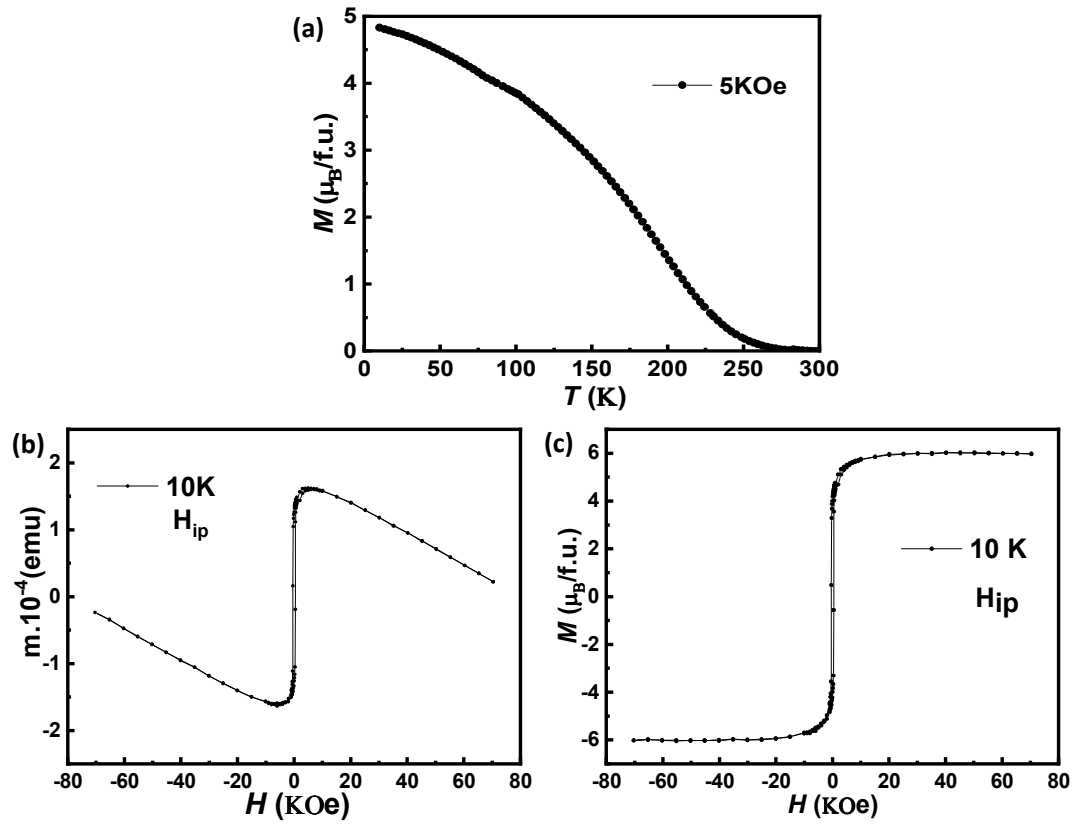


Figure A.11 (a) Magnetization as a function of temperature to determine the $T_C$ of a LNMO film on STO substrate (the field (5 KOe) is applied in-plane). (b) Raw data for magnetization as a function of applied magnetic field (in-plane) measured at 10K, showing the strong diamagnetic contribution at high fields coming from the STO substrate of the same LNMO film. (c) In-plane hysteresis loop M(H) at 10K after removing the diamagnetic contribution of the STO substrate of the same sample. Film was grown at 900°C under 140 mTorr $O_2$.

In this thesis, we have carried out two types of experimental procedures to measure the M (T) curves. The first procedure consists of field-cooled to determine the $T_C$. In this case, a magnetic field (in-plane) usually of 5 kOe ($\mu_0 H$= 0.5 T) is applied to the film while cooling from RT to 10K, thus the magnetic moment of the film is measured while temperature increases from 10 K to 300 K, above the $T_C$. The other procedure is the zero-field-cooled/field-cooled (ZFC-FC) process. The ZFC process consists on cooling the sample down to low temperature (from above $T_C$ down to 10 K) in zero applied field and once the low temperature value is stable, an external magnetic field of 1kOe is applied and the ZFC branch is measured while increasing temperature. After reaching the high temperature value above $T_C$, the sample is cooled down once more up to 10K keeping the same magnetic field of 1 KOe. After reaching the low temperature value again the FC branch is measured while increasing temperature. M(H) is the measurement of the magnetization of the sample while sweeping the magnetic field (from positive high magnetic field to high negative magnetic field and back to positive fields), for a fixed temperature. On the other hand, M(H) hysteresis

loops were usually measured at 10 K, for H applied in-plane and out-of plane, in a range field of ± 7 T. The hysteresis loops (IP and OP) allow determining the magnetic anisotropy of the films on different substrates.

Magnetic measurements were carried out at the ICMAB using Magnetic Property Measurements System (MPMS XL-7T) from Quantum Design, with a radio frequency superconducting quantum interference device (RF SQUID).

# A.6 Electrical transport characterization

To probe the transport properties, electrical characterization has been done using Keithley multimeters in a 4-point probe station. This consists in the positioning of direct tips (needles) on the sample, that no wiring to an external sample holder is required. These needles are connected to the multimeter, therefore I(V) curves can be easily carried out. These measurements are limited to room temperature and not applied magnetic field. On the other hand, electrical transport measurements have also been performed using a Physical Properties Measurements System (PPMS) from Quantum Design located at the ICMAB. The system has a 9T superconducting magnet and a helium cryostat which allows a precise temperature control between 1.9 K and 400 K. The system incorporates a nano-voltmeter and a dc/ac current source which provides currents down to 1μA and up to 2A with a resolution of 0.1μA.

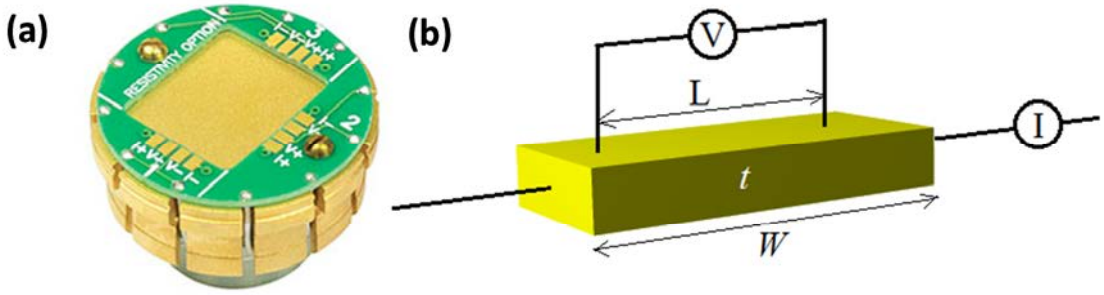


Figure A.12 (a) Standard puck for DC resistance measurement. (b) Schematic view of the four-point configuration.

In order to determine in-plane transport properties of the films we have used the four-point configuration. The 4-point method is used with 4-inline bar geometry. In this geometry, four parallel Pt stripes are deposited on sample by sputtering using a shadow mask. Then, the sample is mounted on a sample holder, called “puck”, which has three multiplexed four-probe measurement channels accessible on a single puck and an optional fourth channel for

customized measurements (see Fig. A.12 (a)). In a single channel there are four contacts are involved: current flows through the outer bars $I_+$ and I-, and the voltage drop between the inner bars, $V_+$ and V-. is measured. The electric contacts are done by silver paint. Thus, the resistivity has been obtained avoiding the contribution of contact resistivity. To compute the quantitative data, the geometry of the sample has to be considered; in this case the electrical resistivity of a film is calculated by:

$$\rho = R\frac{A}{L} = R\frac{Wt}{L} \tag{A.6}$$

where R is the resistance measured and derived from the difference between voltages of two separated points of the sample and the current *I* that through between them. The cross sectional area "A" is defined as the product of the width (w) and the thickness (t) of the film; *L* is the length of the bridge where the voltage drop is measured in the sample. A sketch of this configuration is displayed in Fig A.12 (b). The resistivity is always measured from 10K to a temperature higher than Tc, with zero field or a field of 9T respectively.

Physical Properties Measurements System (PPMS) from Quantum Design located at the ICMAB allows the option of AC current. The maximum resistance that can be measure by the equipment is 20 MΩ, therefore the measurements were done using an external multimeter Keithley 2601.

# A.7 Synchroton-based X-ray techniques

In order to determine the valence states and the ferromagnetic character in our RNMO compounds, X-ray absorption spectroscopy (XAS) and X-ray magnetic circular dichroism (XMCD) measurements were carried out, which will be briefly described in this section.

## A.7.1 X-ray absorption spectroscopy

X-ray Absorption Spectroscopy (XAS) is a powerful technique with which to probe the properties of matter, which allows studying the local electronic and atomic structure of solids, liquids or gases. XAS experiments require an intense and polychromatic source. This is the reason it needs the use of synchrotron radiation (SR) which is an electromagnetic field radiated by relativistic accelerated charged particles (electrons in general). When the charged

particle trajectory is subjected to a steady acceleration perpendicular to its velocity, as is the case in a bending magnet, radiation is emitted tangentially along the particle's trajectory. The SR is a very intense, collimated i.e. with high emittance and polarized X-ray source, having a continuous band of wavelengths from around the mm (infrared) to the pm (hard X-ray) range [328]. XAS is nowadays increasingly used for the speciation analysis of chemical elements owing to the development of new synchrotron radiation facilities worldwide. Modern synchrotron light sources not only enable standard XAS measurements with extremely high data quality, they also facilitate studies on the subsecond or nanometer scale. The main advantages of the XAS method are its subatomic (angstrom) resolution, the ability to analyze almost any type of samples including amorphous (non-crystalline) materials, the possibility to analyze such materials in situ requiring minor or no sample preparation [329] [328].

A generic experimental set-up of the optics and instrumentation used in an XAS experiment is shown in Fig. A.13. A monochromator is used to select and vary the incident energy around the threshold energy ($E_0$) of the probed element according to the Bragg law, $n\lambda=2d_{hkl}=\sin\theta$. The most commonly used is a double crystal monochromator to keep the beam propagating parallel to the initial direction following two reflections. Usually, XAS beamlines are installed on a bending magnet that provides a divergent flux. Thus to increase the photon flux on the sample and decrease the beam size, the second crystal of the monochromator is usually cylindrically curved to perform a dynamic sagittal focalization of the beam on the sample. The higher harmonic reflections (n > 1 in the Bragg law) are suppressed by the reflections on 2 curved mirrors on either side of the monochromator which are also used to collimate the X-ray beam on the monochromator (1st mirror) and to focus it on the sample (2nd mirror). The beam size range available for a normal XAS beamline is typically between 0.1 and 1 mm and can be controlled depending on the size of the sample [329].

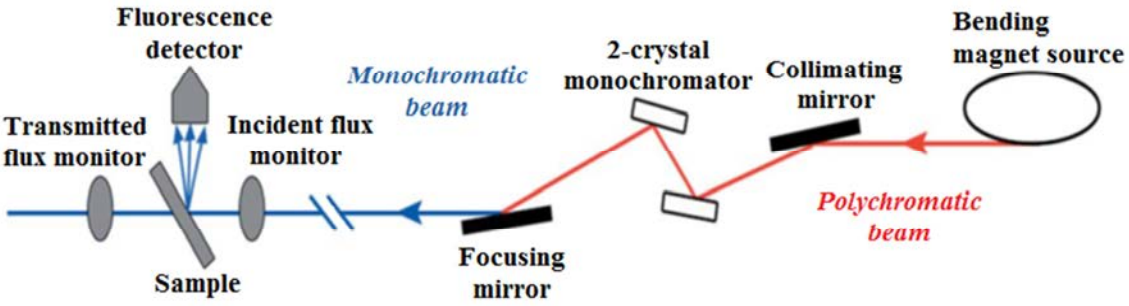


Figure A.13 Sketch of a generic X-ray absorption experiment using synchrotron radiation. Taken from ref [329].

XAS measures the probability of transition from an internal electronic state to an empty state above the Fermi level. Allowed transitions are mainly governed by the dipole selection rules, only transitions which change the angular momentum *l* of the excited electron by one can

occur ($\Delta l = \pm 1$). The spin momentum s is conserved ($\Delta s = 0$), so the z-component of the orbital momentum m must obey $\Delta m = 0, \pm 1$. In this case, $\Delta m = \pm 1$ corresponds to left- and right-hand circularly polarized light, while $\Delta m = 0$ corresponds for linearly polarized light.

If X-rays of intensity $I_0$ are incident on a sample, (see Fig. A.14 (a)), the extent of absorption depends on the photon energy $E$ and sample thickness $t$ [328].

According to Beer's Law, the transmitted intensity $It$ is

$$I_t(t) = I_0 e^{-\mu(E)t} \tag{A.7}$$

where $\mu(E)$ is the energy-dependent X-ray absorption coefficient. Over large energy regions, $\mu(E)$ is a smooth function of the photon energy, varying approximately as $\mu(E) \sim dZ^4/mE^3$. Here $d$ denotes the target density while $Z$ and $m$ are the atomic number and mass, respectively. Thus, $\mu(E)$ decreases with increasing photon energy. If the latter equals or exceeds the binding energy of a core electron, however, a new absorption channel is available in which the photon is annihilated thereby creating a photoelectron and a core-hole. This leads to a sharp increase in absorption coefficient as shown schematically in Fig.A.14 (b). Above the absorption edge, the difference between the photon energy and the binding energy is converted into kinetic energy of the photoelectron and $\mu(E)$ continues to decrease with increasing photon energy. After a short time of the order of $10^{-15}$ s, the core-hole is filled by an electron from a higher energy state. The corresponding energy difference is released mainly via fluorescence X-ray or Auger electron emission [328].

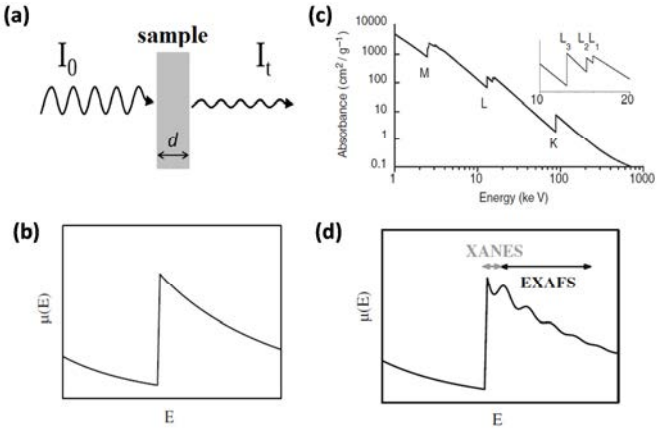


Figure A.14 (a) Schematic of incident and transmitted X-ray beam and (b) absorption coefficient $\mu(E)$ versus photon energy $E$ around an absorption edge and (c) Low-resolution X-ray absorption spectrum for Pb. Three major transitions are seen (K, L, and M edges), corresponding to excitation of an electron from n=1, 2, and 3 shells, respectively. (d) Absorption coefficient $\mu(E)$ versus photon energy $E$ including the fine structure above the edge divided into the XANES and EXAFS regions. Figures taken from refs [328] [330].

On the other hand, when an incident monochromatic X-ray beam impinging on a sample is scanned in energy, one can observe an abrupt increase in the measured absorption coefficient, the so-called ‘‘absorption edge’’ of the element (Fig. A.14 (c)). An absorption edge corresponds to the binding energy of core electrons. When the incident beam has sufficient photon energy to eject electrons from this core level to an unoccupied valence state, one can observe a sharp rise in the absorption spectrum. The edges are named according to the principle quantum number of the electron that is excited: K for n=1, L for n=2, M for n=3, etc. If we closely examine Fig. A.14 (c) (see inset) shows that the *L* edge is in fact three distinct *L* edges, named $L_1$, $L_2$, and $L_3$ in order of decreasing energy $L_1$ edge corresponds to excitation of a 2s electron (into 3*p* levels). The 2*p* excitation is split into two edges, $L_2$ and $L_3$, (transition from the 2*p* levels into 3*d* levels) as a consequence of the spin‑orbit coupling energy of the $2p^5$ configuration that is created when a 2*p* electron is excited. The higher energy of the $2p^5$ excited states is the $2P_{1/2}$ term; this gives rise to the $L_2$ edge. At lower energy is the $L_3$ edge, corresponding to the $2P_{3/2}$ excited state. Due to degeneracy, the $L_3$ edge has twice the edge jump of the $L_2$ and $L_1$ edges [328] [330]. Fig.A.14 (d) schematically shows the $\mu(E)$ fine structure as a function of photon energy. The XAS spectrum provides us with a valuable information on the partial density of the unoccupied states in the excited levels. Two regions are commonly distinguished:

(i) X-ray Absorption Near Edge Structure (XANES):

The structure in the vicinity of the edge is sometimes referred to as X-ray absorption near-edge structure (XANES). The region very close to the absorption edge is characterized by transitions of the photoelectron to unoccupied bound states. Therefore, XANES spectra provide detailed information about the oxidation state and coordination environment of the metal atoms (Fig. A.14 (d)) [330].

(ii) Extended X-ray Absorption Fine Structure (EXAFS):

The oscillations above the edge i.e., the oscillations beyond the XANES region, are often referred to as extended X-ray absorption fine structure (EXAFS). For photon energies higher than ∼30eV above the edge, the photoelectron is scattered by the nearest neighbors of the excited atom, and builds up interference patterns that contain structural information. EXAFS is thus independent of chemical bonding and depends on the atomic arrangement around the absorber. It contains quantitative information about the coordination number, interatomic distances and structural and thermal disorder around a particular atomic species [330].

The direct way to perform x-ray absorption spectroscopy is the transmission mode. In transmission mode both the incoming and the transmitted beam, $I_0$ and $I_t$ , respectively, are measured by ion chambers and the absorption coefficient can be obtained (see Fig. A.14 (a)). Transmission mode is a standard measurement technique for the hard x-ray range. In the soft x-ray range, owing to the strong interaction between soft x-rays and the sample, it is almost impossible to perform absorption measurements in the transmission mode. Instead, in the soft x-ray range, we usually use total electron yield (TEY) mode and total fluorescence yield (TFY) mode [328]. In this thesis work, XAS experiments were performed using two different detection modes: total electron yield (TEY) and total fluorescence yield (TFY).

**Total Electron Yield (TEY):** is the most widely used detection technique. The energy of the outgoing electrons is not selected and simply all the escaping electrons are counted. The signal is dominated by secondary electrons which are created in the cascade process of the Auger decay electrons. To that end the sample is situated inside the detector and the electrons are collected by suitable electrodes. Given the relatively short mean free path of the electrons this technique is extremely surface-sensitive with a probing depth of 2-5 nm. Therefore, the TEY method does not suffer from the "selfabsorption" effects as it happens for the fluorescence mode [328].

**Total fluorescence yield (TFY):** the FY mode is another general technique used for absorption measurements. The idea behind the FY mode is measuring the emission of the fluorescence photon. The photons created in the fluorescent process have a mean free path of the same order of magnitude as the incident x-rays. Consequently, the FY mode has a large probing depth (> 1000Å in the soft x-ray region), and is particularly suitable for studying bulk electronic structures [331]. Nevertheless, TFY measurements in thin films suffer from the "selfabsorption" effects, thus it is important to apply correction procedures to the spectra to recover the real signal of absorption coefficient [217].

## A.7.2 X-ray magnetic circular dichroism

Magnetic circular dichroism in the $L_{2,3}$ absorption spectra of the magnetically interesting 3*d* transition metals is readily measurable using synchrotron radiation. X-ray magnetic circular dichroism (XMCD) spectroscopy uses light with different circular polarization to create spin-polarized "photoelectrons" in the absorption process, which is proportional to the probability of electronic transitions into empty states. The right circularly polarized beam ($\mu^+$) mainly excites the spin-up electrons, while the left circularly polarized beam ($\mu-$) mainly excites the spin-down electrons [332]. This allows us to measure the intensity difference between the number of spin-up and spin-down holes in a magnetic material. Thus, XMCD is obtained

from the difference spectrum of two X-ray absorption spectra with the circular polarization vector parallel and antiparallel to the external magnetic field, i.e., one applying left circularly polarized light (positive helicity, (+$\hbar$)), and one with right circularly polarized light (negative helicity, (-$\hbar$)) with respect to the majority spin [333] [332].
In Fig. A.15 XMCD can be described as a two-step process. The 2*p* core state of a 3*d* metal is split in a j = 3/2 level ($L_3$ edge) and j = 1/2 level ($L_2$ edge), where spin and orbit are coupled parallel and antiparallel, respectively. In the first step, the emission with the light helicity vector parallel (antiparallel) to the 2*p* orbital moment results in excited electrons of preferred spin up (down) direction. Thus, a circularly polarized photon excites a spin-polarized electron from the spin–orbit split 2*p* level (Fano-effect). From the $2p_{3/2}$ level ($L_3$ edge) X-rays with positive helicity (q = +1) excite 62.5% spin up electrons and those with negative helicity (q = −1) excite 37.5% spin-up electrons, while the $2p_{1/2}$ level ($L_2$ edge) q = +1 gives 25% spin-up and q = −1 gives 75% spin-up. In the second step the excited electron has to find its place in the unoccupied 3d valence band, and if there are less spin-up than spin-down holes available, the XMCD spectrum has a net negative $L_3$and positive $L_2$ peak [333].

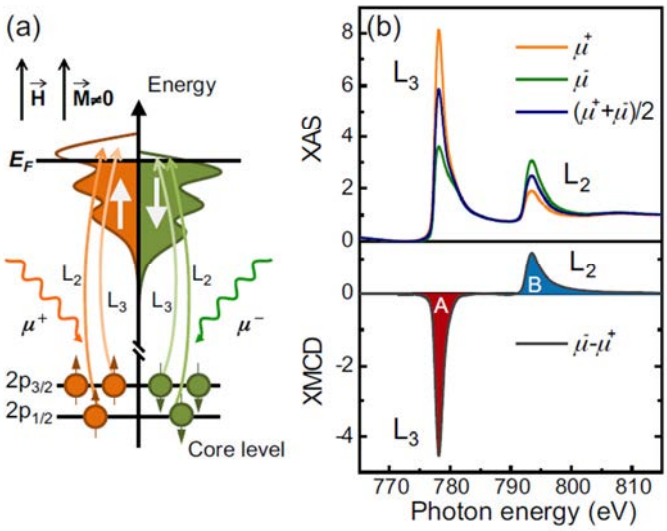


Figure A.15 (a) Diagram of the two-step picture of XMCD for a single-electron in the resonant excitation process for a 3d magnetic material. (b) XAS at the Co $L_{2,3}$ for right ($\mu_+$) and left ($\mu_-$)circular polarization together with the difference spectrum: the XMCD (bottom graph). Figure taken from ref [333].

The analysis of the XMCD spectrum enables to estimate the orbital and spin magnetic moment ($\mu_L$ and $\mu_S$) of a ferromagnetic (or) ferrimagnetic material. Thole *et al* [220] and Carra *et al.* [219] described a number of sum rules for x-ray absorption. It was shown that the integral over the XMCD signal of a given edge allows the determination of the ground state expectation values of the orbital moment ($L_z$) and the effective spin moment ($S_{eff}$). The sum

rules apply to one specific transition, that is, the transition from a 2*p* core state to 3*d* valence states in transition metal systems. For the transitions from the initial $2p_{3/2}$ and $2p_{1/2}$ into the 3*d* valence band. On the other hand, the integrated circular dichroism spectrum is defined as the absorption of + helicity x-rays ($\mu_+$) minus the absorption of – helicity x-rays ($\mu_-$). Therefore the orbital ($m_L$) and spin magnetic moment ($m_S$) can be determined from the integration of $\mu^+$-$\mu^-$ (XMCD spectra) and $\mu^+$+$\mu^-$ (XAS spectra). The XMCD sum rules for orbital ($m_L$) and spin magnetic moments ($m_S$), are given by [332]:

$$m_L = -\frac{4\int_{L_3+L_2}(\mu^+-\mu^-)dE}{3\int_{L_3+L_2}(\mu^++\mu^-)dE}(10-n_{3d}) \tag{A.8}$$

$$m_S = -\frac{6\int_{L_3}(\mu^+-\mu^-)dE-4\int_{L_3+L_2}(\mu^+-\mu^-)dE}{\int_{L_3+L_2}(\mu^++\mu^-)dE}(10-n_{3d})\left(1+\frac{7\langle T_Z\rangle}{2\langle S_z\rangle}\right)^{-1} \tag{A.9}$$

Where $m_L \equiv -\langle L_z\rangle\,\mu_B/\hbar$ and $m_S \equiv -2\langle S_z\rangle\,\mu_B/\hbar$ represent, the orbital and spin magnetic moment along the X-rays propagation axis; $n_{3d}$ is the 3*d* electron occupation number of the transition-metal ion under consideration; $L_3$ and $L_2$ denote the integrated area of $L_3$ and $L_2$. $\langle Tz\rangle$ is the spin-quadrupole coupling (also called the magnetic-dipole coupling operator), this operator could be neglected in octahedral symmetry [219] and at room temperature the $T_z$ values are generally very small and can be neglected. $\langle Sz\rangle$ is equal to half of $m_{spin}$ in Hartree atomic units [334] [332].

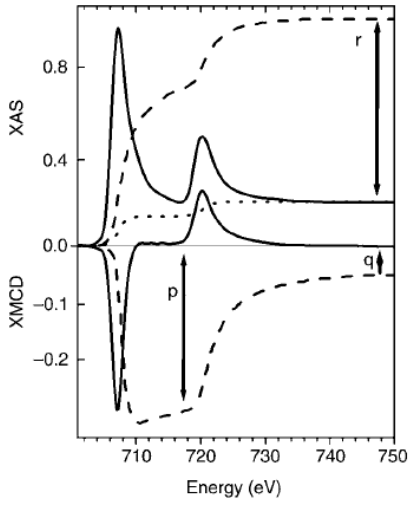


Figure A.16 $L_{2,3}$ XAS (upper panel) and XMCD (lower panel) spectra of Fe metal (Fe/parylene thin films measured in transmission). The solid lines give the XAS spectrum and its XMCD. The dotted line indicates the background and the dashed lines show the integrated value of the XAS and the XMCD, respectively, where *r*, *q* indicate their values after the $L_{2,3}$ edge and *p* after the $L_3$ edge. Taken from Ref [335].

Fig A.16 shows an example of the results of $L_{2,3}$ XAS and XMCD spectra of Fe/parylene thin film. From these spectra, the $\mu^+ - \mu^-$ (XMCD spectra) and $\mu^+ + \mu^-$ (XAS spectra) are determined. By dividing Equation (A.8) by Equation (A.9), we can obtain $m_L/m_s$ only from the XMCD spectra with no additional information. Fig. A.16 shows, by the dashed curve, the energy-integration of the XMCD spectrum and the values of the integrations for the $L_3$ region, and the whole $L$ edge range is indicated by $p$ and $q$, respectively [335] [332]. In order to verify the applicability of the individual orbital and spin sum rules, Chen et al. [335] adopted the edge jumps of $L_{2,3}$ XAS as shown with the dotted curve in Fig.A.16, where the height of the $L_3$ ($L_2$) step was set at 2/3(1/3) of the average intensity at high energy end of the XAS spectrum. The value $r$ indicated the XAS integral after the edge-jump removal. Then, taking into account the notation in Fig.A.16,the $m_{orb}$ and $m_{spin}$ can be also expressed as [332]:

$$m_L = -\frac{4q}{3r}(10 - n_{3d}) \tag{A.10}$$

$$m_s = -\frac{6p-4q}{3}(10 - n_{3d}) \tag{A.11}$$

Where $q$ is the XMCD integration of the $L_{2,3}$ edges, $p$ is the XMCD integration of the $L_3$ edge, $n_{3d}$ is the $3d$ electron occupation number, and $r$ is the XAS integration at the $L_{2,3}$ edges, in order to calculate the total XAS integral r, the background must be carefully corrected [332].

We have performed X-ray absorption spectroscopy (XAS) and X-ray magnetic circular dichroism (XMCD) experiments in BL29-BOREAS beamline at ALBA Synchrotron Light Source (Barcelona, Spain). The spectra were measured in both the total electron yield (TEY) and total fluorescence yield (TFY) modes, under ultrahigh vacuum conditions ($2 \cdot 10^{-10}$ mbar).

# List of publications

The publications related to the content presented in this thesis are:

- M Bernal-Salamanca, Z Konstantinović, L Balcells, E Pannunzio-Miner, F Sandiumenge, L Lopez-Mir, B Bozzo, J Herrero-Martín, A Pomar, C Frontera, and B Martínez. Nonstoichiometry Driven Ferromagnetism in Double Perovskite $La_2Ni_{1-x}Mn_{1+x}O_6$ Insulating Thin Films. *Crystal Growth & Design,* 19(5), 2765−2771, (2019).

- M Bernal-Salamanca, Z Konstantinović, C Frontera, V Fuentes, A Pomar, L Balcells and B Martínez. Formation of Nickel Oxide Nanocuboids in Ferromagnetic $La_2Ni_{1-x}Mn_{1+x}O_6$. *Nanomaterials*, 11(3), 804 (2021).

- M. Bernal-Salamanca, Z. Konstantinović, Ll. Balcells, M. Šćepanović, S. Valencia, E. Pannunzio-Miner, C. Frontera, A. Pomar, B. Martinez. Fractal polymer islands on top of ferromagnetic $La_2Ni_{0.6}$ $Mn_{1.4}O_6$ thin films. *Journal of Magnetism and Magnetic Materials*, 537, 168203 (2021).

# Bibliography


[1] N. S. Rogado, J. Li, A. W. Sleight, and M. A. Subramanian. Magnetocapacitance and Magnetoresistance Near room temperature in a Ferromagnetic Semiconductor: $La_2NiMnO_6$. *Adv. Mater.* 17, 2225 (2005).

[2] Igor Zutic, J. Fabian, and S. Das Sarma. Spintronics: Fundamentals and applications. *Rev. Mod. Phys.,* 76, 323 (2004).

[3] Baibich M N, Broto J M, Fert A, Dau F N V, Petroff F, Eitenne P, Creuzel G, Friedrich A and Chazelas. Low field magnetotransport in manganites. J *Phys. Rev. Lett.* 61 2472, (1988).

[4] Parkin S S P, Li Z G and Smith D.J. Giant magnetoresistance in antiferromagnetic Co/Cu multilayers. *Appl. Phys. Lett.* 58 2710 (1991).

[5] Parkin S S P, Bhadra R and Roche K P. Oscillatory Magnetic Exchange Coupling through Thin Copper Layers. *Phys. Rev. Lett.* 66 2152 (1991).

[6] Liu Chang, Min Wang, Lei Liu, Siwei Luo, Pan Xiao. A brief introduction to Giant Magnetoresistance. *arXiv preprint arXiv:1412.7691* (2014).

[7] M. Bibes and A. Barthélémy. Oxide spintronics. *IEEE transactions on electron devices* 54 (5): 1003-1023, (2007).

[8] J. Coey and M. Venkatesan. Half-metallic ferromagnetism: Example of $CrO_2$ (invited). *J. Appl. Phys.* 91, 8345 (2002).

[9] J.M.D. Coey and S. Sanvito. Magnetic semiconductors and half-metals. *J. Phys. D: Appl. Phys.* 988, (2004).

[10] P K Siwach, H K Singh and O N Srivastava. Low field magnetotransport in manganites. *J. Phys.: Condens. Matter* 20-273201, (2008).

[11] Zsolt Marton, Sung Seok A.Seo, Takeshi Egami, Ho Nyung Lee. Growth control of stoichiometry in $LaMnO_3$ epitaxial thin films by pulsed laser deposition. *Journal of Crystal Growth* 312, 2923–2927 (2010).

[12] Y. Tokura. Critical features of colossal magnetoresistive manganites. *Reports on Progress in Physics*. 69:797–851, (2006).

[13] Matthias Opel. Spintronic oxides grown by laser-MBE. *J. Phys. D: Appl. Phys.* 45 (3), 033001 (2012).

[14] Martin, L. W., Chu, Y. H., & Ramesh, R. J. M. S. Advances in the growth and characterization of magnetic, ferroelectric, and multiferroic oxide thin films. *Materials Science and Engineering: R: Reports*, 68(4-6), 89-133 (2010).

[15] Bibes, M., Villegas, J. E., & Barthelemy, A. Ultrathin oxide films and interfaces for electronics and spintronics. *Advances in Physics*, *60* (1), 5-84 (2011).

[16] J. Longo, R. Ward, J. Am. Magnetic Compounds of Hexavalent Rhenium with the Perovskite-type Structure. Chem. Soc. 83, 2816 (1961).

[17] López, C. A., Pedregosa, J. C., Lamas, D. G. & Alonso, J. A. The strongly defective double perovskite $Sr_{11}Mo_4O_{23}$: crystal structure in relation to ionic conductivity. J. *Appl. Crystallogr.* 47, 1395–1401 (2014).

[18] Rubel, M. H. K. et al. Superconducting double perovskite bismuth oxide prepared by a low-temperature hydrothermal reaction. *Angew. Chem.* 126, 3673–3677 (2014).

[19] Hashisaka, M.; Kan, D.; Masuno, A.; Takano, M.; Shimakawa, Y.; Terashima, T.; Mibu, K. Epitaxial growth of ferromagnetic $La_2NiMnO_6$ with ordered double-perovskite structure. *Appl. Phys. Lett. 89*(3), 032504 (2006).

[20] Chakraborty, T. et al. Disordered ferromagnetism in $Ho_2NiMnO_6$ double perovskite. J. Phys. Condens. *Matter Mater. Phys*. 29, 025804 (2017).

[21] Fukushima, T., Stroppa, A., Picozzi, S. & Perez-Mato, J. M. Large ferroelectric polarization in the new double perovskite $NaLaMnWO_6$ induced by non-polar instabilities. *Chem. Phys.* 13, 12186–12190 (2011).

[22] Shimakawa, Y., Azuma, M. & Ichikawa, N. Multiferroic compounds with double perovskite structures. *Materials* 4, 153–168 (2011).

[23] E. Fertitta *et al.* Study of disorder in pulsed laser deposited double perovskite oxides by first-principle structure prediction. *npj Computational Materials* 92, (2021).

[24] Moodera, Jagadeesh S.; Gallagher,Elizabeth F.; Keziah Robinson; Nowak, Janusz. Optimum tunnel barrier in ferromagnetic–insulator–ferromagnetic tunneling structures. *Appl. Phys. Lett.* 70, 3050 (1997).

[25] Itoh, H.; Ozeki, J.; Inoue, J. Electronic structure and spin-filter effect of ferromagnetic insulators with double perovskite structure *Journal of Magnetism and Magnetic Materials* 310, 1994–1996 (2007).

[26] Li, P.; Xia, C.; Zhu, Z.; Wen, Y.; Zhang, Q.; Alshareef, H.N.; Zhang, X.-X. Ultrathin Epitaxial Ferromagnetic γ-$Fe_2O_3$ Layer as High Effi ciency Spin Filtering Materials for Spintronics Device Based on Semiconductors. *Advanced Functional Materials* 26, 5679 (2016).

[27] López-Mir, L.; Frontera, C.; Aramberri, H.; Bouzehouane, K.; Cisneros-Fernández, J.; Bozzo, B.; Balcells, L.; Martínez, B. Anisotropic sensor and memory device with a ferromagnetic tunnel barrier as the only magnetic element. *Scientific Reports*. 8, 861 (2018).

[28] R. I. Dass, J.-Q. Yan, J.B. Goodenough. Oxygen stoichiometry, ferromagnetism and transport properties of $La_{2-x}NiMnO_{6+\delta}$. *Phys. Rev. B* 68 (6), 064415 (2003).

[29] M. P. Singh, K. D. Truong, S. Jandl, and P. Fournier. Magnetic properties and phonon behavior of $Pr_2NiMnO_6$ thin films. *Appl. Phys. Lett.* 98 (16), 162506 (2011).

[30] Booth R J, Fillman R, Whitaker H, Nag A, Tiwari A M, Ramanujachary K V, Gopalakrishnan J and Lofland S E. An investigation of structural, magnetic and dielectric properties of $R_2NiMnO_6$ (R= rare earth, Y). *Mater. Res. Bull.* 44(7), 1559 (2009).

[31] W. Prellier, M.P. Singh, P. Murugavel. Effects of Er doping on Raman spectra and on the structural properties of $YbMnO_3$. *J. Phys.: Condens. Matter* 17 R803 (2005).

[32] W. Eerenstein, N.D. Mathur, J.F. Scott. Multiferroic and magnetoelectric materials. *Nature (London)* 442 759 (2006).

[33] J.S. Moodera, X. Hao, G.A. Gibson, R. Meservey. Electron-Spin Polarization in Tunnel Junctions in Zero Applied Field with Ferromagnetic EuS Barriers. *Phys.Rev. Lett.* 61 637 (1988).

[34] P. LeClair, J.K. Ha, H.J.M. Swagten, C.H. van de Vin, J.T. Kohlhepp, W.J.M. de Jonge. Large magnetoresistance using hybrid spin filter devices. *Appl. Phys. Lett.* 80 625 (2002).

[35] H.R. Fuh, Y.P.Liu , Z.R.Xiao , Y.K.Wang. New type of ferromagnetic insulator: Double perovskite $La_2NiMO_6$ (M= Mn, Tc, Re, Ti, Zr, and Hf). *Journal of Magnetism and Magnetic Materials* 357, 7–12 (2014).

[36] Devi Chandrasekhar, K.; Das, A K.; Mitra, C.; Venimadhav, A. The extrinsic origin of the magnetodielectric effect in the double perovskite $La_2NiMnO_6$. *J. Phys.: Condens. Matter* 24, 495901 (2012).

[37] M. Nasir, et al. Role of Antisite Disorder, Rare-Earth Size, and Superexchange Angle on Band Gap, Curie Temperature and Magnetization of $R_2NiMnO_6$ Double Perovskites. *ACS Appl. Electron. Mater*. 1(1), 141−153 (2019).

[38] Goodenough J.B. An interpretation of the magnetic properties of the perovskite-type mixed crystals $La_{1-x}Sr_xCoO_{3-\lambda}$. *J. Phys. Chem. Solids* 6, 287 (1958).

[39] Goodenough, J. B.; Wold, A. ; Arnott, R. J.; Menyuk, N. Relationship Between Crystal Symmetry and Magnetic Properties of Ionic Compounds Containing $Mn^{3+}$. *Phys. Rev.* 124, 373 (1961).

[40] S. Majumder, M. Tripathi, R. Raghunathan, P. Rajput, S. N. Jha, D. O. de Souza, L. Olivi, R. J. Choudhary, D. M. Phase. Tailoring the magnetic states by controlling octahedral cation arrangement in double perovskite. Arxiv (2020).

[41] Guo, H. Z.; Burgess, J.; Ada, E. ; Street, S.; Gupta, A.; Iliev, M.N.; Kellock, A.J.; Magen, C.; Varela, M.; Pennycook, S.J. Influence of defects on structural and magnetic properties of multifunctional $La_2NiMnO_6$ thin films. *Phys.Rev. B* 77, 174423 (2008).

[42] Truong, K.D.; Singh, M.P.; Jandl, S.; Fournier, P. Influence of Ni/Mn cation order on the spin-phonon coupling in multifunctional $La_2NiMnO_6$ epitaxial films by polarized Raman spectroscopy. *Phys. Rev. B* ***80,*** 134424 (2009).).

[43] Zhao, Shuangyi.; Shi, Lei.; Zhou, Shiming.; Zhao, Jiyin.; Yang, Haipeng.; Guo,Yuqiao. Size-dependent magnetic properties and Raman spectra of $La_2NiMnO_6$ nanoparticles. *J. Appl. Phys*. 106, 123901 (2009).

[44] C. L. Bull, D. Gleeson, and K. S. Knight. Determination of B-site ordering and structural transformations in the mixed transition metal perovskites $La_2CoMnO_6$ and $La_2NiMnO_6$. *J. Phys.: Condens. Matter* 15, 4927 (2003).

[45] J. H. Ngai, F.J. Walker, and C.H. Ahn. Correlated Oxide Physics and Electronics. *Annu. Rev. Mater. Res.* 44:1–17, (2014).

[46] S.A. Wolf, D.D. Awschalom, R.A. Buhrman, J.M. Daughton, S. von Molnar, M.L. Roukes, A.Y. Chtchelkanova, D.M. Treger. Spintronics: a spin-based electronics vision for the future. *Science* 294 1488–1495, (2001).

[47] X. Yu, T.J. Marks, A. Facchetti. Metal oxides for optoelectronic applications, *Nat. Mater*. 15 383–396, (2016).

[48] M. A. Peña, J.L.G. Fierro. Chemical structures and performance of perovskite oxides. *Chem. Rev*. 101(7): 1981–2018, (2001).

[49] G. King and P. M. Woodward. Cation ordering in perovskites. *J. Mater. Chem*. 20 (28), 5785-5796, (2010).

[50] Tatsumi Ishihara. Perovskite Oxide for Solid Oxide Fuel Cells. *Springer Science & Business Media* (2009).

[51] M. B. Salamon and M. Jaime, Rev. Mod. The physics of manganites: Structure and transport. *Phys.* 73(3), 583 (2001).

[52] G. J. Bowden. A Review of the Low Temperature Properties of the Rare Earth Vanadates. *Australian Journal of Physics* 51(2) 201 – 236 (1998).

[53] G. H. Jonker, and J. H. Van Santen, Ferromagnetic compounds of manganese with perovskite structure. *Physica* 16 (3), 337-349, (1950).

[54] A. Urushibara, Y. Moritomo, T. Arima, A. Asamitsu, G. Kido, and Y. Tokura. Insulator-metal transition and giant magnetoresistance in $La_{1-x}Sr_xMnO_3$. *Phys. Rev. B* 51, 14103 (1995).

[55] Tanusri Saha-Dasgupta. Double perovskites with 3d and 4d/5d transition metals: compounds with promises. *Mater. Res. Express* 7 (1), 014003 (2020).

[56] Y. Zhang, V. Ji and K.-W. Xu. The structural, electronic, and magnetic properties of the stoichiometric (001) surface of double perovskite $Sr_2FeMoO_6$. *Surf. Interface Anal.,* 48, 1040–1047 (2016).

[57] M. W. Lufaso, P. W. Barnes and P. M. Woodward. Structure prediction of ordered and disordered multiple octahedral cation perovskites using SPuDS. *Acta Crystallogr., Sect. B: Struct. Sci.,* 62 (3), 397–410, (2006).

[58] C. J. Howard, B. J. Kennedy and P. M. Woodward. Ordered double perovskites–a group-theoretical analysis. *Acta Crystallogr., Sect. B: Struct. Sci.,* 59 (4), 463–471 (2003).

[59] S. Vasala, M. Karppinen. $A_2B'B''O_6$ perovskites: *A review. Progress in Solid State Chemistry* 43 (1-2) 1-36 (2015).

[60] D.E. Cox, A.W. Sleight, Crystal structure of $Ba_2Bi^{3+}Bi^{5+}O_6$, *Solid. State. Commun*. 19(10) 969–973 (1976).

[61] H. Kato, T. Okuda, Y. Okimoto, Y. Tomioka, Y. Takenoya, A. Ohkubo, M. Kawasaki, Y. Tokura. Metallic ordered double-perovskite $Sr_2CrReO_6$ with maximal Curie temperature of 635 K. *Appl. Phys. Lett.* 81 (2), 328–330 (2002).

[62] D. Serrate, J.M.D. Teresa, M.R. Ibarra. Double perovskites with ferromagnetism above room temperature. *J. Phys.: Condens. Matter* 19 (2), 023201 (2006).

[63] T. Kimura, T. Goto, H. Shintani, K. Ishizaka, T. Arima, Y. Tokura. Magnetic control of ferroelectric polarization. *Nature* 426 (6962) 55–58, (2003).

[64] W. Z. Yang, M.M. Mao, X.Q. Liu, X.M. Chen. Structure and dielectric relaxation of double-perovskite $La_2CuTiO_6$ ceramics. *J. Appl. Phys*. 107 (12), 124102 (2010).

[65] Mark T. Anderson, Kevin B. Greenwood, Gregg A. Taylor and Kenneth R. Poeppelmeier, B-Cation arrangements in double perovskites. *Prog. Solid State Chem*. 22 (3), 197-233 (1993

[66] Yi Tian, Zhizhong Ge, An Sun, Zhipeng Zhu, Quan Zhang, Shuhui Lv, Hongping Li. The impact of crystal structures on the magnetic and electronic properties in double perovskite $Sr_2NiTeO_6$. *Chemical Physics Letters* 754, 137776 (2020).

[67] Ortega-San Martin L, Chapman JP, Hernández-Bocanegra E, Insausti M, Arriortua MI, Rojo T. Structural phase transitions in the ordered double perovskite $Sr_2MnTeO_6$. *J Phys Condens Matter* 16 (23), 3879 (2004).

[68] T Tilley, R.J.D. Perovskites: Structure-Property Relationships, John Wiley & Sons. 330 (2016).

[69] Lufaso, Michael W. and Woodward, Patrick M., "Jahn-Teller Distortions, Cation Ordering and Octahedral Tilting in Perovskites". *Acta Cryst B* 60(1), 10-20 (2004).

[70] Woodward PM. Octahedral Tilting in Perovskites. I. Geometrical Considerations. Acta Crystallogr Sect B Struct Sci *53*(1), 32-43 (1997).

[71] Glazer AM. The classification of tilted octahedra in perovskites. *Acta Crystallogr Sect B Struct Crystallogr Cryst Chem 28* (11), 3384-3392 (1972).

[72] Goldschmidt, V. M. Goldshmidt tolerance factor. *Die Nature wissenschaften*, 14, 477-485 (1926).

[73] Kakarla, D. C.; Jyothinagaram, K. M.; Das, A. K.; Adyam, V. Dielectric and Magnetodielectric Properties of $R_2NiMnO_6$ (R = Nd, Eu, Gd, Dy, and Y). *J. Am. Ceram. Soc.* 97 (9), 2858−2866 (2014).

[74] Rutuparna Das, R.N.P. Choudhary. Studies of structural, dielectric relaxor and electrical characteristics of leadfree double Perovskite: $Gd_2NiMnO_6$. *Solid State Sciences* 87, 1–8 (2019).

[75] Fu WT, Akerboom S, IJdo DJW. Crystal structures of the double perovskites $Ba_2Sr_{1-x}Ca_xWO_6$. J *Solid State Chem* 180:1547 (2007).

[76] Day BE, Bley ND, Jones HR, McCullough RM, Eng HW, Porter SH, et al. Structures of ordered tungsten- or molybdenum-containing quaternary perovskite oxides. *J Solid State Chem* 185, 107-116 (2012).

[77] Philipp Ksoll,Christoph Meyer , Leonard Schüler , Vladimir Roddatis and Vasily Moshnyaga. B-Site Cation Ordering in Films, Superlattices, and Layer-by-Layer-Grown Double Perovskites. *Crystals 11,* 734 (2021).

[78] Zhou Q, Blanchard P, Kennedy BJ, Reynolds E, Zhang Z, Miiller W, et al. Synthesis, Structural and Magnetic Studies of the Double Perovskites $Ba_2Ce\mathit{M}O_6$ (*M* = Ta, Nb).*Chem Mater 24*(15), 2978-2986 (2012).

[79] Fu WT, IJdo DJW. New insight into the symmetry and the structure of the double perovskites $Ba_2LnNbO_6$ (Ln = lanthanides and Y). *J Solid State Chem 179*(4), 1022-1028 (2006).

[80] Lufaso MW, Woodward PM. Prediction of the crystal structures of perovskites using the software program *SPuDS. Acta Crystallogr Sect B Struct Sci 57*(6), 725-738 (2001).

[81] Das, H.; Waghmare, U. V.; Saha-Dasgupta, T.; Sarma, D. D. Electronic Structure, Phonons, and Dielectric Anomaly in Ferromagnetic Insulating Double Perovskite $La_2NiMnO_6$. *Phys. Rev. Lett. 100* (18), 186402 (2008).

[82] Monirul Shaikh, Aafreen Fathima, M. J. Swamynadhan, Hena Das, and Saurabh Ghosh. Investigation into Cation-Ordered Magnetic Polar Double Perovskite Oxides. *Chem. Mater.* 33(5), 1594-1606 (2021).

[83] Guo, H.; Gupta, A.; Varela, M.; Pennycook, S.; Zhang, J.; Local valence and magnetic characteristics of $La_2NiMnO_6$. *Phys. Rev. B 79* (17), 172402 (2009).

[84] Takata K, Azuma M, Shimakawa Y, Takano M. New ferroelectric ferromagnetic bismuth double-perovskites synthesized by high-pressure technique. *J Jpn Soc Powder Powder Metall* 52, 913 (2005).

[85] J. Blasco, J. García, M.C. Sánchez, J. Campo, G. Subías, and J. Pérez-Cacho. Magnetic properties of $LaNi_{1-x}MnxO_{3+\delta}$ perovskites. *Eur. Phys. J. B 30* (4), 469-479 (2002).

[86] M. W. Lufaso et al. Structural studies of $Sr_2GaSbO_6$, $Sr_2NiMoO_6$, and $Sr_2FeNbO_6$ using pressure and temperature. *J. Phys.: Condens. Matter* 18, 8761–8780 (2006).

[87] M. W. Lufaso et al. Pressure-induced phase transition and octahedral tilt system change of $Ba_2BiSbO_6$. Journal of Solid State Chemistry 179, 917–922 (2006).

[88] Gateshki M, Igartua JMM, Hern_andez-Bocanegra E. X-ray powder diffraction results for the phase transitions in $Sr_2MWO_6$ (M = Ni, Zn, Co, Cu) double perovskite oxides. *J Phys Condens Matter 15* (36), 6199 (2003).

[89] Zhang, G.; Li, G.; Liao, F.; Fu, Y.; Xiong, M.; Lin, J. Crystal Growth and Magnetic Properties of the Double Perovskites $R_2NiMnO_6$ (R = Pr, Sm and Ho) by a Hydrothermal Route. *J. Cryst. Growth 327* (1), 262-266 (2011).

[90] Sayed, F.N.; Achary, S.N.; Jayakumar, O.D.; Deshpande, S.K.; Krishna, P.S.R.; Chatterjee, S.; Ayyub, P.; Tyagi, A.K. Role of annealing conditions on the ferromagnetic and dielectric properties of $La_2NiMnO_6$. *J. Mater. Res.* 26, 567–577 (2011).

[91] R. I. Dass and J. B. Goodenough. Multiple magnetic phases of $La_2CoMnO_{6-\delta}$ ($0<\delta<0.05$), *Phys. Rev. B* 67 (1), 014401 (2003).

[92] Davies PK, Wu H, Borisevich AY, Molodetsky IE, Farber L. Annu. Crystal chemistry of complex perovskites: new cation-ordered dielectric oxides. *Rev Mater Res 38*, 369-401 (2008).

[93] Goodenough JB. Electronic and ionic transport properties and other physical aspects of perovskites. *Rep Prog Phys 67* (11), 1915 (2004).

[94] Eriksson AK, Eriksson S-G, Ivanov SA, Knee CS, Eriksen J, Rundlöf H, et al. High temperature phase transition of the magnetoelectric double perovskite $Sr_2NiMoO_6$ by neutron diffraction. *Mater Res Bull* 41:144, (2006).

[95] Serrate D, De Teresa JM, Ibarra MR. Magnetoelastic coupling in $Sr_2(Fe_{1-x}\ Cr_x)ReO_6$ double perovskites. *Journal of Physics: Condensed Matter*, *19*(43), 436226 (2007).

[96] Singh M. P., Grygiel C, Sheets W. C., Boullay Ph, Hervieu M, rellier W, Mercey B, Simon C, Raveau B. Absence of long-range Ni/Mn ordering in ferromagnetic $La_2NiMnO_6$ thin films. *Appl Phys Lett* 91(1), 012503 (2007).

[97] Boullay P, Grygiel C, Rautama EL, Singh MP, Kundu AK. Structure/microstructure versus properties in strongly correlated electronic oxides: "Quenched disorder" and non-CMR oxides. Mater Sci Eng B 144:49 (2007).

[98] D. Choudhury, P. Mandal, R. Mathieu, A. Hazarika, S. Rajan, A. Sundaresan, U.V. Waghmare, R. Knut, O. Karis, P. Nordblad and D. D. Sarma. Near-room-temperature colossal magnetodielectricity and multiglass properties in partially disordered $La_2NiMnO_6$. *PRL* 108 (12), 127201 (2012).

[99] Blasco, J., Sanchez, M. C., Perez-Cacho, J. & Campo. J. Synthesis and structural study of $LaNi_{1-x}Mn_xO_{3+\delta}$ perovskites. *J. Phys. Chem. Solids.* 63, 781–792 (2002).

[100] P. Sanyal, S. Tarat, and P. Majumdar. Structural ordering and antisite defect formation in double perovskites. *Eur. Phys. J. B.* *65*(1), 39-47 (2008).

[101] Viswanathan M, Kumar PSA, Bhadram VS, Narayana C, Bera AK, Yusuf SM. Influence of lattice distortion on the Curie temperature and spin–phonon coupling in $LaMn_{0.5}Co_{0.5}O_3$. *J Phys Condens Matter 22* (34), 346006 (2010).

[102] Kyômen T, Yamazaki R, Itoh M. Correlation between Magnetic Properties and Mn/Co Atomic Order in $LaMn_{0.5}Co_{0.5}O_{3+\delta}$: I. Second-Order Nature in Mn/Co Atomic Ordering and Valence State. Chem Mater *15* (25), 4798-4803 (2003).

[103] J.B. Goodenough, R.I. Dass. Comment on the magnetic properties of the system $Sr_{2-x}\ Ca_xFeMoO_6$ , $0 \leq x \leq 2$. *International Journal of Inorganic Materials* 2(1), 3–9 (2000).

[104] S. Pal, G. Sharada, M. Goyal, S. Mukherjee, B. Pal, R. Saha, A. Sundaresan, S. Jana, O. Karis, J.W. Freeland, D.D. Sarma. Effect of anti-site disorder on magnetism in $La_2NiMnO_6$, Phys. Rev. B 97 *97*(16), 165137 (2018).

[105] Meneghini C, Ray S, Liscio F, Bardelli F, Mobilio S, Sarma DD. Nature of ‘‘Disorder’’ in the Ordered Double Perovskite $Sr_2FeMoO_6$. *Phys Rev Lett* 103:46403 (2009).

[106] M. Nasir, et al. The effect of high temperature annealing on the antisite defects in ferromagnetic $La_2NiMnO_6$ double perovskite. *J. Magn. Magn. Mat.* 483; 114–123 (2019).

[107] Tokura Y and Nagaosa N. Orbital Physics in Transition-Metal Oxides. *288* (5465), 462-468, (2000)

[108] Jahn, H. A., Teller, E. Stability of polyatomic molecules in degenerate electronic states I−orbital degeneracy. *Proc. R. Soc. Lond. A* 161, 220-235 (1937).

[109] Goodenough, J. B. Jahn-Teller phenomena in solids. *Annual review of materials science* 28, 1:27 (1998).

[110] Warren E. Pickett and David J. Singh. Electronic structure and half-metallic transport in the $La_{1-x}Ca_xMnO_3$ system. *Physical Review B*, 53:1146, (1996).

[111] Bongjae Kim, Jieun Lee, Beom Hyun Kim, Hong Chul Choi, Kyoo Kim, J.-S. Kang, and B. I. Min. Electronic structures and magnetic properties of a ferromagnetic insulator: $La_2MnNiO_6$. *J. Appl. Phys*. **105**, 07E515 (2009).

[112] J. B. de Azevedo Filho et al. Theoretical and experimental investigation of the structural and magnetic properties of $La_2NiMnO_6$. *Journal of Magnetism and Magnetic Materials* 527, 167770 (2021).

[113] Kang et al. Temperature-dependent magnetic circular dichroism study of ferromagnetic double perovskite $La_2MnNiO_6$. *J. Appl. Phys*. 107, 09D721 (2010).

[114] Goodenough, J. B. Theory of the role of covalence in the perovskite-type manganites [La,*M*(II)]$MnO_3$. *Physical Review* 100, 564 (1955).

[115] Kanamori, J. Superexchange interaction and symmetry properties of electron orbitals. *Journal of Physics and Chemistry of Solids*, *10* (2-3), 87-98 (1959).

[116] Anderson, P. W. Antiferromagnetism. Theory of superexchange interaction. *Physical Review*, *79*(2), 350 (1950).

[117] Y. Shimakawa, M. Azuma, and N. Ichikawa. Multiferroic compounds with double-perovskite structures. *Materials*, 4 (1), 153–168 (2011).

[118] Tirmali, P. M., Mane, S. M., Patil, S. K. & Kulkarni, S. B. Effects of partial site substitution on magnetic and dielectric behavior of $La_2NiMnO_6$ double perovskite. *J. Mater. Sci. - Mater. Electron.* 27, 4314–4320 (2016).

[119] Cao, Z. Z. *et al*. Extrinsic and intrinsic contributions for dielectric behavior of $La_2NiMnO_6$ ceramic. *Physica B*. 477, 8–13 (2015).

[120] K D Truong, M P Singh, S Jandl and P Fournier. Investigation of phonon behavior in $Pr_2NiMnO_6$ by micro-Raman spectroscopy. *J. Phys.: Condens. Matter* 23 052202 (2011).

[121] M. Retuerto, et al. Magnetic Interactions in the Double Perovskites $R_2NiMnO_6$ (R = Tb, Ho, Er, Tm) Investigated by Neutron Diffraction. *Inorg. Chem.* 54, 10890−10900, (2015)

[122] A. Hossain, P. Bandyopadhyay, S. Roy. An overview of double perovskites $A_2BB'O_6$ with small ions at A site: Synthesis, structure and magnetic properties. *Journal of Alloys and Compo*unds 740, 414-427 (2018).

[123] Xiao-Wei Jin, Lu Lu, Shao-Bo Mi, Ming Liu, and Chun-Lin Jia. Phase stability and B-site ordering in $La_2NiMnO_6$ thin films. *Appl. Phys. Lett*. 109, 031904 (2016).

[124] Yang et al. Role of spontaneous strains on the biphasic nature of partial B-site disorder double perovskite $La_2NiMnO_6$. *APL Materials* 6, 066102 (2018).

[125] Y. Sakurai, I. Ohkubo, Y. Matsumoto, H. Koinuma, and M. Oshima. Influence of substrates on epitaxial growth of B-site-ordered perovskite $La_2NiMnO_6$ thin films. *J. Appl. Phys*. 110, 063913 (2011).

[126] Aslam Hossain, A. K. M. Atique Ullah, Partha Sarathi Guin, Sanjay Roy. An overview of $La_2NiMnO_6$ double perovskites: synthesis, structure, properties, and applications. *Journal of Sol-Gel Science and Technology* 93:479–494, (2020).

[127] M. C. Sánchez, J García, J Blasco, G Subías and J. Perez-Cacho. Local electronic and geometrical structure of perovskites determined by X-ray-absorption spectroscopy. *Physical Review B* 65, 144409 (2002).

[128] S. Chikazumi Physics of Ferromagnetism, Clarendon Press, Oxford (1997).

[129] M T Johnson, P J H Bloemen, F J A den Broeder and J J de Vries. Magnetic anisotropy in metallic multilayers. *Rep. Prog. Phys*. 59, 1409–1458 (1996).

[130] M. I. Darby and E. D. Isaac, "Magnetocrystalline anisotropy of ferro- and ferrimagnetics," vol. Mag-10, No. 10 (1974).

[131] R. Skmoski. Simple Models of Magnetism. Oxford University Press, 2008.

[132] P.J. Grundy. Encyclopedia of Materials: Science and Technology (2001)

[133] Katsuaki Suganuma.Wide Bandgap Power Semiconductor Packaging: Materials, Components, and Reliability. 1st Edition (2018).

[134] M. I. Darby and E. D. Isaac, "Magnetocrystalline anisotropy of ferro- and ferrimagnetics," vol. Mag-10, No. 10 (1974)

[135] C. Kittel. Physical theory of ferromagnetic domains. Rev. Mod. Phys., 21(4):541, (1949).

[136] H. Brune. "Epitaxial Growth of Thin Films". *Surface and Interface Science: Solid-Solid Interfaces and Thin Films,* First Edition, (2014).

[137] Kiyotaka Wasa, Makoto Kitabatake, Hideaki Adach. Thin film materials technology: sputtering of control compound materials, William Andrew, Inc., USA ( 2004).

[138] Bauer, E. Phanomenologische. Theorie der Kristallabscheidung an Oberflachen. I. *Z. Kristallogr.*, **110**, 372, (1958).

[139] Frank, F.C. and van der Merwe, J.H. One-dimensional dislocations. II. Misfitting monolayers and oriented overgrowth. *Proc. R. Soc. London, Ser. A*, 198, 216 (1949).

[140] Volmer, M. and Weber, A. Keimbildung in ¨ubers¨attigten Gebilden. *Z. Phys. Chem.*, 119, 277 (1926).

[141] Stranski, I.N. and Krastanov, L. Zur Theorie der orientierten Ausscheidung von Ionenkristallen aufeinander. *Sitzungsber. Akad. Wiss. Wien, Math.- naturwiss. Kl. IIb*, 146, 797 (1938).

[142] Y. Fang, V.R. Sakhalkar, J. He, H.Q. Jiang, Jiechao Jiang, Efstathios I. Meletis. Growth, Microstructure and Properties of Epitaxial $La_{1-X}Sr_xMnO_3$ thin films on various substrates using RF Magnetron Sputtering. *JNanoR* 14, 83–92 (2011).

[143] Kitamura, M.; Ohkubo, I.; Kubota, M.; Matsumoto, Y.; Koinuma, H.; Oshima, M. Ferromagnetic properties of epitaxial $La_2NiMnO_6$ thin films grown by pulsed laser deposition. *Appl. Phys. Lett.*, 94, 132506 (2009).

[144] Guo, H.; Burgess, J.; Street, S.; Gupta, A.; Calvarese, T. G.; Subramanian, M. A. Growth of epitaxial thin films of the ordered double perovskite $La_2NiMnO_6$ on different substrates. *Appl. Phys. Lett.* 89 (2), 022509 (2006).

[145] Singh, M. P.; Truong, K. D.; Jandl, S.; Fournier, P. Long-range Ni/Mn structural order in epitaxial double perovskite $La_2NiMnO_6$ thin films. *Physical Review B*, *79* (22), 224421 (2009).

[146] Steven R. Spurgeon, Yingge Du, Timothy Droubay, Arun Devaraj, Xiahan Sang, Paolo Longo, Pengfei Yan, Paul G. Kotula, Vaithiyalingam Shutthanandan, Mark E. Bowden,James M. LeBeau, Chongmin Wang, Peter V. Sushko, and Scott A. Chambers. Competing Pathways for Nucleation of the Double Perovskite Structure in the Epitaxial Synthesis of $La_2MnNiO_6$. *Chem. Mater.*, 28, 3814−3822 (2016).

[147] Zhiqing Zhang , Hongbin Jian, Xianwu Tang, Jie Yang, Xuebin Zhu, Yuping Sun. Synthesis and characterization of ordered and disordered polycrystalline $La_2NiMnO_6$ thin films by sol-gel. *Dalton Trans*. 41(38), 11836-40 (2012).

[148] Egoavil, R. et al. Phase problem in the B-site ordering of $La_2CoMnO_6$: impact on structure and magnetism. *Nanoscale*. 7, 9835–9843 (2015).

[149] H Wang, C Frontera, J Herrero-Martin, A Pomar, P Roura, B Martinez, and N Mestres. Aqueous Chemical Solution Deposition of Functional Double Perovskite Epitaxial Thin Films. *Chem. Eur. J*. 26, 9338 – 9347, (2020).

[150] R. Galceran, C. Frontera, Ll. Balcells, J. Cisneros-Fernandez, L. Lopez-Mir, J. Roqueta, J. Santiso, N. Bagues, B. Bozzo, A. Pomar, F. Sandiumenge, and B. Martınez. Engineering the microstructure and magnetism of $La_2CoMnO_{6-\delta}$ thin films by tailoring oxygen stoichiometry. *Appl. Phys. Lett.* 105, 242401 (2014).

[151] S. K. Singh, S. B. Palmer, D. McK. Paul, and M. R. Leesa. Growth, transport, and magnetic properties of $Pr_{0.67}Ca_{0.33}MnO_3$ thin films. *Appl. Phys. Lett*. 69, 263 (1996).

[152] P. H. Wagner, V. Metlushko, L. Trappeniers, A. Vantomme, J. Vanacken, G. Kido, V. V. Moshchalkov, and Y. Bruynseraede. Magnetotransport in epitaxial thin films of the magnetic perovskite $Pr_{0.5}Sr_{0.5}MnO_3$. *Phys. Rev*. B 55, 3699, (1997).

[153] Co**e**y J.M.D., Viret M., von Molnar S.; "Mixed-valence manganites". *Adv. Phys*. 48(2), 1999: 167–293 (1999).

[154] J T Gudmundsson. Physics and technology of magnetron sputtering discharges. Plasma Sources Sci. Technol. *29* (11), 113001 (2020).

[155] Rossnagel S M. Sputter deposition for semiconductor manufacturing. IBM J. Res. Dev. 43 163–79, (1999).

[156] Nadel S J, Greene P, Rietzel J and Strumpfel J. Equipment, materials and processes: a review of high rate sputtering technology for glass coating. *Thin Solid Films* 442 (1-2), 11–4 (2003).

[157] Stefan Wrehde, Marion Quaas, Robert Bogdanowicz, Hartmut Steffen, Harm Wulff, Rainer Hippler, Optical and chemical characterization of thin TiNx films deposited by DC magnetron sputtering, *Vacuum*, 82, 1115–1119, (2008).

[158] A.M.K. Dagamseh , B. Vet , F.D. Tichelaar , P. Sutta , M. Zeman. ZnO: Al films prepared by rf magnetron sputtering applied as back reflectors in thin-film silicon solar cells. *Thin Solid Films* 516 (21) 7844–7850, (2008).

[159] Hanns-Ulrich Habermeier. Thin films of perovskite-type complex oxides. *Materials Today*, *10* (10), 34-43 (2007).

[160] D.G. Schlom, L.-Q. Chen, X. Pan, A. Schmehl, M.A. Zurbuchen, A. Thin film approach to engineering functionality into oxides. *J. Am. Ceram. Soc*. 91 2429–2454, (2008).

[161] J.M. Phillips, Substrate selection for high-temperature superconducting thin films. *J. Appl. Phys*. 79, 1829 (1996).

[162] Abhijit Biswas, Chan-Ho Yang, Ramamoorthy Ramesh, Yoon H. Jeong. Atomically flat single terminated oxide substrate surfaces. *Progress in Surface Science* 92 117–141, (2017).

[163] T. Gagnidze et al. Structural properties of ultrathin SrO film deposited on $SrTiO_3$. *Sci. Technol. Adv. Mater*. 20 457 (2019).

[164] G. Koster et al. Surface morphology determined by (0 0 1) single-crystal $SrTiO_3$ termination. *Physica C* 339 215-230 (2000).

[165] Z.L. Wang , A.J. Shapiro. Studies of $LaAlO_3$ (100) surfaces using RHEED and REM II: 5 X 5 surface reconstruction. *Surface Science* 328, 159-169 (1995).

[166] K. Krishnaswamy, C. E. Dreyer, A. Janotti, and C. G. Van de Walle. Structure and energetics of $LaAlO_3$ (001) surfaces. *Physical Review B* 90, 235436 (2014).

[167] J.E. Kleibeuker, G. Koster, W. Siemons, D. Dubbink, B. Kuiper, J.L. Blok, C.-H. Yang, J. Ravichandran, R. Ramesh, J.E. ten Elshof, D.H.A. Blank, G. Rijnders. Atomically defined rare-earth scandate crystal surfaces. *Adv. Funct. Mater*. 20 (20), 3490–3496 (2010).

[168] M. Kawasaki, K. Takahashi, T. Maeda, R. Tsuchiya, M. Shinohada, O. Ishiyama, T. Yonezawa, M. Yoshimoto, H. Koinuma. Atomic control of the $SrTiO_3$ crystal surface. *Science* 266 (2190), 1540–1542 (1994).

[169] M. Kawasaki, A. Ohtomo, T. Arakane, K. Takahashi, M. Yoshimoto, H. Koinuma. Atomic control of $SrTiO_3$ surface for perfect epitaxy of perovskite oxides. *Appl. Surf. Sci.* 107, 102–106 (1996).

[170] C. Raisch, T. Chassé, Ch. Langheinrich, A. Chassé, Preparation and investigation of the A-site and B-site terminated $SrTiO_3$ (001) surface: A combined experimental and theoretical x-ray photoelectron diffraction study. *J. Appl. Phys.* 112, 073505 (2012).

[171] J.G. Connell, B.J. Isaac, G.B. Ekanayake, D.R. Strachan, S.S.A. Seo, Preparation of atomically flat $SrTiO_3$ surfaces using a deionized-water leaching and thermal annealing procedure. *Appl. Phys. Lett.* 101, 251607 (2012).

[172] R.C. Hatch, K.D. Fredrickson, M. Choi, C. Lin, H. Seo, A.B. Posadas, A.A. Demkov, Surface electronic structure for various surface preparations of Nb-doped $SrTiO_3$ (001). *J. Appl. Phys*. 114 103710 (2013).

[173] R.C. Hatch, M. Choi, A.B. Posadas, A.A. Demkov. Comparison of acid- and non-acid-based surface preparations of Nb-doped $SrTiO_3$ (001). *J. Vac. Sci. Technol*. B 33 061204 (2015).

[174] K. Iwahori, S. Watanabe, M. Kawai, K. Mizuno, K. Sasaki, and M. Yoshimoto. Nanoscale composition analysis of atomically flat $SrTiO_3$ (001) by friction force microscopy. *Journal of Applied Physics* 88, 7099 (2000).

[175] Z. L. Wang and A. J. Shapiro. Studies of $LaAlO_3$ "100" surfaces using RHEED and REM. II: 5× 5 surface reconstruction. *Surface science*, *328*(1-2), 159-169 (1995).

[176] D.-W. Kim, D.-H. Kim, B.-S. Kang, T. W. Noh, D. R. Lee, and K.-B. Lee. Roles of the first atomic layers in growth of $SrTiO_3$ films on $LaAlO_3$ substrates. *Appl. Phys. Lett 74*(15), 2176-2178 (1999).

[177] J. Yao, P. Merrill, and S. Perry. Thermal stimulation of the surface termination of $LaAlO_3${100}. *J. Chem. Phys. 108*(4), 1645-1652 (1998).

[178] H. Kawanowa, H. Ozawa, M. Ohtsuki, Y. Gotoh, and R. Souda. Structure analysis of $LaAlO_3$ (001) surfaces by low energy neutral scattering spectroscopy. *Surf. Sci. 506*(1-2), 87-92 (2002).

[179] R. Gunnarsson, A. S. Kalabukhov, and D. Winkler. Evaluation of recipes for obtaining single terminated perovskite oxide substrates. *Surf. Sci.* 603, 151 (2009).

[180] C. H. Lanier, J. M. Rondinelli, B. Deng, R. Kilaas, K. R. Poeppelmeier, and L. D. Marks. Surface Reconstruction with a Fractional Hole:(5× 5) R 26.6° $LaAlO_3$(001). *Phys. Rev. Lett. 98* (8), 086102 (2007).

[181] A.J.H. van der Torren, S.J. van der Molen, J. Aarts, Formation of a mixed ordered termination on the surface of $LaAlO_3$ (001). *Phys. Rev B* 91, 245426 (2015).

[182] G.B. Cho, Y. Kamada, M. Yamamoto. Studies of self-organized steps and terraces in inclined. $SrTiO_3$ (001) substrate by atomic force microscopy. *Jpn J. Appl. Phys*. 40, 4666 (2001).

[183] Aufderheide B.E.; Sputtered Thin Film Coatings. In: Tracton AA, editor. COATINGS Technol. Handb. Third Edit, Taylor and Francis Group, LLC, CRC Press; 2006.

[184] Lufaso MW, Gemmill WR, Mugavero SJ, Lee Y, Vogt T, zur Loye H-C. Compression mechanisms of symmetric and Jahn–Teller distorted octahedra in double perovskites: $A_2CuWO_6$ (A= Sr, Ba), $Sr_2CoMoO_6$, and $La_2LiRuO_6$. J Solid State Chem;179:3556 (2006).

[185] P. Padhan, H. Z. Guo, P. LeClair, and A. Gupta. Dielectric relaxation and magnetodielectric response in epitaxial thin films of $La_2NiMnO_6$. *Appl. Phys. Lett*. 92 (2), 022909 (2008).

[186] Gregoire, J. M.; Lobovsky, M. B.; Heinz, M. F.; DiSalvo, F. J.; van Dover, R. B. "Resputtering phenomena and determination of composition in codeposited films". *Physical Review B*. 76 (19): 195437 (2007).

[187] K. Wasa, "Sputtering Phenomena," in Handbook of Sputtering Technology (Second Edition), William Andrew Publishing, pp. 41 – 75, (2012).

[188] Lin, Y. Q., Wu, S. Y. & Chen, X. M. Effects of ordering domain structure on dielectric properties of double perovskite $La_2NiMnO_6$. *J Adv Dielectr.* 01, 319–324 (2011).

[189] M.P. Singh, K.D. Truong, S. Jandl, and P. Fournier. Multiferroic double perovskites: Opportunities, issues, and challenges. *J. Appl. Phys*. 107(9),09D917 (2010).

[190] M. N. Iliev, M. M. Gospodinov, M. P. Singh, J. Meen, K. D. Truong, P. Fournier, and S. Jandl. Growth, magnetic properties, and Raman scattering of $La_2NiMnO_6$ single crystals. *J. Appl. Phys.* 106, 023515 (2009).

[191] V. L. Joseph Joly, P. A. Joy, S. K. Date, and C. S. Gopinath. Two ferromagnetic phases with different spin states of Mn and Ni in $LaMn_{0.5}Ni_{0.5}O_3$. *Phys. Rev. B* 65, 184416 (2002).

[192] Iliev, M. N.; Guo H.; Gupta. A. Raman spectroscopy evidence of strong spin-phonon coupling in epitaxial thin films of the double perovskite $La_2NiMnO_6$. *Appl. Phys. Lett*. 90, 151914 (2007).

[193] DJ Kester, R Messier. Predicting negative ion resputtering in thin films. *J. Vac. Sci. & Technol. A: Vacuum, Surfaces, and Films*, *4*(3), 496-499, (1986).

[194] Wu, SQ., Cheng, S., Lu, L. *et al.* B-site ordering and strain-induced phase transition in double-perovskite $La_2NiMnO_6$ films. *Sci Rep* 8, 2516 (2018).

[195] Guo, Yuqiao.; Shi, Lei.; Zhou, Shiming.; Zhao, Jiyin.; Liu, Wenjie. Near room-temperature magnetoresistance effect in double perovskite $La_2NiMnO_6$. *Appl. Phys. Lett.* 102, 222401 (2013).

[196] N. F. Mott. Conduction in non-crystalline materials: III. Localized states in a pseudogap and near extremities of conduction and valence bands. *Philos. Mag. 19* (160), 835-852 (1969).

[197] Renner, B.; Lunkenheimer, P.; Schetter, M.; Loidl, A.; Reller, A.; Ebbinghaus, S. G. Dielectric behavior of copper tantalum oxide. *J. Appl. Phys*. 96, 4400 (2004).

[198] R. N. Mahato, K. Sethupathi, and V. Sankaranarayanan. Colossal magnetoresistance in the double perovskite oxide $La_2CoMnO_6$. *J. Appl. Phys. 107*(9), 09D714 (2010).

[199] I Chaitanya Lekshmi, ArupGayen and M S Hegde. Electrical transport properties of $LaNi_{1-x}M_xO_3$ (M= Co, Mn) thin films fabricated by pulsed laser deposition. J. Phys.: Condens. Matter 17 (41) 6445–6458 (2005).

[200] Lin, Y.Q. ; Chen, X.M. ; Liu, X.Q. Relaxor-like dielectric behavior in $La_2NiMnO_6$ double perovskite ceramics. *Solid State Communications* 149 (19-20), 784-787, (2009).

[201] K. Yoshii, N. Ikeda, M. Mizumaki. Magnetic and dielectric properties of the ruthenium double perovskites $La_2MRuO_6$ (M = Mg, Co, Ni, and Zn). *Phys. Status. Solidi*. (a) 203(11), 2812-2817, (2006).

[202] Zhaoliang Liao et al. Origin of the metal-insulator transition in ultrathin films of $La_{2/3}Sr_{1/3}MnO_3$. *Physical review B* 92, 125123 (2015).

[203] M. Huijben, L. W. Martin,1 Y.-H. Chu, M. B. Holcomb, P. Yu, G. Rijnders, D. H. A. Blank, and R. Ramesh. Critical thickness and orbital ordering in ultrathin $La_{0.7}Sr_{0.3}MnO_3$ films. *Physical review B* 78, 094413 (2008).

[204] B. Cui, C. Song, G. Y. Wang, H. J. Mao, F. Zeng & F. Pan. Strain engineering induced interfacial self-assembly and intrinsic exchange bias in a manganite perovskite film. *Sci Rep* 3, 2542 (2013).

[205] J. Z. Sun and D. W. Abraham, R. A. Rao and C. B. Eom. Thickness-dependent magnetotransport in ultrathin manganite films. *Appl. Phys. Lett*. 74, 3017 (1999).

[206] T. Becker, C. Streng, Y. Luo, V. Moshnyaga, B. Damaschke, N. Shannon, and K. Samwer. Intrinsic Inhomogeneities in Manganite Thin Films Investigated with Scanning Tunneling Spectroscopy. *Phys. Rev. Lett.* 89, 237203 (2002).

[207] M. Bibes, Ll. Balcells, S. Valencia, J. Fontcuberta, M. Wojcik, E. Jedryka, and S. Naldoski. Nanoscale Multiphase Separation at $La_{2/3}Ca_{1/3}MnO_3/SrTiO_3$ Interfaces. *Phys. Rev. Lett*. 87, 067210 (2001).

[208] M. Bibes, S. Valencia, L. Balcells, B. Martinez, J. Fontcuberta, M. Wojcik, S. Nadolski, and E. Jedryka. Charge trapping in optimally doped epitaxial manganite thin films. *Phys. Rev. B* 66, 134416 (2002).

[209] A. Biswas *et al.*. Strain-driven charge-ordered state in $La_{0.67}Ca_{0.33}MnO_3$. *Phys. Rev. B* 63, 184424 (2000).

[210] F. Sandiumenge, J. Santiso, L. Balcells, Z. Konstantinovic, J. Roqueta, A. Pomar, J. Pedro Espinós and B. Martínez. Competing Misfit Relaxation Mechanisms in Epitaxial Correlated Oxides. *PRL* 110, 107206 (2013).

[211] E. Dagotto, T. Hotta, and A. Moreo. Colossal magnetoresistant materials: the key role of phase separation. *Phys. Rep*. 344, 1 (2001).

[212] Deepak Kumar, Davinder Kaur. Structural and magnetic properties of $La_2NiMnO_6$ thin films on $LaAlO_3$ substrate with varying thickness. *Journal of Alloys and Compounds* 554 277–283 (2013).

[213] Marie-Bernadette Lepetit, Bernard Mercey, and Charles Simon. Interface Effects in Perovskite Thin Films. *PRL* 108, 087202 (2012).

[214] A. Tebano, C. Aruta, S. Sanna, P. G. Medaglia, and G. Balestrino. Evidence of Orbital Reconstruction at Interfaces in Ultrathin $La_{0.67}Sr_{0.33}MnO_3$ Films. *PRL* 100, 137401 (2008).

[215] Kriegner, D.; Wintersberger, E.; Stangl, J. Xrayutilities: a versatile tool for reciprocal space conversion of scattering data recorded with linear and area detectors. *J. Appl. Cryst*. 46, 1162-1170 (2013).

[216] Stamenov, P.; Coey, J. M. D. Sample size, position, and structure effects on magnetization measurements using second-order gradiometer pickup coils. *Review of Scientific Instruments* 77, 015106 (2006).

[217] S. Eisebitt, T. Böske, J. E. Rubensson, and W. Eberhardt. Determination of absorption coeficients for concentrated samples by fluorescence detection. *Physical Review B*, 47(21):14103–14109, (1993).

[218] Medarde, M. ; Fontaine, A. ; Garcia-Munoz, J. L. ; Rodriguez-Carvajal, J. ; De Santis, M. ; Sacchi, M. ; Rossi, G. ; Lacorre, P. $RNiO_3$ perovskites (R =Pr,Nd): Nickel valence and the metal-insulator transition investigated by x-ray-absorption spectroscopy. *Phys. Rev. B* 46, 14975 (1992).

[219] Carra, P.; Thole, B. T.; Altarelli, M.; Wang, X. X-Ray Circular Dichroism and Local Magnetic Fields. *Phys. Rev. Lett*. 70, 694 (1993).

[220] Thole, B. T.; Carra, P.; Sette, F.; van der Laan, G. X-Ray Circular Dichroism as a Probe of Orbital Magnetization. *Phys. Rev. Lett*. 68, 1943 (1992).

[221] M. Nasir, M. Khan, S. Bhatt, A.K. Bera, M. Furquan, S. Kumar, S.M. Yusuf, N. Patra, D. Bhattacharya, S.N. Jha, S.-W. Liu, S. Biring, S. Sen. Influence of Cation Order and Valence States on Magnetic Ordering in $La_2Ni_{1-x}Mn_{1+x}O_6$. *Phys. Status Solidi* B 256 (11), 1900019 (2019).

[222] A. Ghosh,1 R. Batabyal, G. P. Das, and B. N. Dev. An extended fractal growth regime in the diffusion limited aggregation including edge diffusion. *AIP Adv.* 6, 015301. (2016).

[223] A.P. Kotula, M.W. Meyer, F. De Vito, J. Plog, A.R. Hight Walker, K.B. Migler, The rheo-Raman microscope: Simultaneous chemical, conformational, mechanical, and microstructural measures of soft materials. *Rev. Sci. Instrum*. 87, 105105 (2016).

[224] K.B. Migler, A.P. Kotula, A.R.H. Walker, Trans-rich structures in early stage of crystalization of polyethylene. *Macromolecules* 48, 4555 (2015).

[225] G. van der Laan and I.W. Kirkman, The 2*p* absorption spectra of 3d transition metal compounds in tetrahedral and octahedral symmetry, *J. Phys.: Condens. Matter* 4 4189 (1992).

[226] F. Kronast and S. Valencia Molina. SPEEM: The photoemission microscope at the dedicated microfocus PGM beamline UE49-PGMa at BESSY II. *J. Large-Scale Res. Facil. JLSRF*, *2*, 90 (2016).

[227] S. Valencia, A. Gaupp, W. Gudat, Ll. Abad, Ll. Balcells, A. Cavallaro, B. Martínez, F. J. Palomares. Mn valence instability in $La_{2/3}Ca_{1/3}MnO_3$ thin films. *Phys Rev B* 73 104402 (2006).

[228] S. Valencia, A. Gaupp, W. Gudat, Ll. Abad, Ll. Balcells, B. Martínez. Impact of microstructure on the Mn valence of $La_{2/3}Ca_{1/3}MnO_3$ thin films, *Phys.Rev.* B 75 184431, (2007).

[229] M. Bernal-Salamanca, Z. Konstantinovic, Ll. Balcells, E. Pannunzio-Miner, F. andiumenge, L. Lopez, B. Bozzo., J. Herrero-Martin, A. Pomar, C. Frontera, B. Martinez. Nonstoichiometry driven ferromagnetism in double perovskite $La_2Ni_{1-x}Mn_{1+x}O_6$ insulating thin films. *Crystal Growth & Design* 19 (5) 2765-2771 (2019).

[230] P.B. Messersmith, S.I. Stupp. High-Temperature Chemical and Microstructural Transformations of a Nanocomposite Organoceramic. *Chem. Mater.* (3), 454-460 (1995).

[231] Schneider C. A., Rasband W. S. and Eliceiri K. W., NIH Image to Image J: 25 years of image analysis*, Nat. Methods*, 9, 671-675 (2012).

[232] Spurgeon S.R., Sushko P.V., Devaraj A., Du Y., Droubay T. and Chambers S.A. Onset of phase separation in the double perovskite oxide $La_2MnNiO_6$. *Phys. Rev. B*, 97, 134110 (2018).

[233] Detemple, E.; Ramasse, Q.M.; Sigle, W.; Cristiani, G.; Habermeier, H.-U.; Benckiser, E.; Boris, V.; Frano, A.; Wochner, P.; Wu, M.; et al. Polarity-driven nickel oxide precipitation in $LaNiO_3$-$LSaAlO_3$ superlattices. *Appl. Phys. Lett*., 99, 211903 (2011).

[234] Pomar, A.; Konstantinovic, Z.; Bagués, N.; Roqueta, J.; López-Mir, L.; Balcells, L.; Frontera, C.; Mestres, N.; Gutiérrez-Llorente, A.; Ščepanovic, M.; et al. Formation of Self-Organized $Mn_3O_4$ Nanoinclusions in $LaMnO_3$ Films. *Front. Phys*., 4, 41 (2016).

[235] Prellier W., Rajeswari M., Venkatesan T. and Greene R. L. Effects of annealing and strain on $La_{1-x}Ca_xMnO_3$ thin films: A phase diagram in the ferromagnetic region, *Appl. Phys. Lett*., 75, 1446 (1999).

[236] Konstantinovic Z., Santiso J., Balcells Ll. and Martinez B. Strain-Driven Self Assembled Network of Antidots in Complex Oxide Thin Films. *Small*, *5*(2), 265-271 (2009).

[237] Kim M.K., Moon J.Y., Choi H.Y., Oh S.H., Lee N., Choi. Y.J., Effects of different annealing atmospheres on magnetic properties in $La_2CoMnO_6$ single crystals. *Current Applied Physics*, 15, 776-779 (2015).

[238] Orayech B., Urcelay-Olabarria I., Lopez G.A., Fabelo O., Faik A. and Igartua J.M., Synthesis, structural, magnetic and phase transition studies of the ferromagnetic $La_2CoMnO_6$ double perovskite by symmetry-adapted modes, *Dalton Trans*.,.44, 13867 (2015).

[239] L. López-Mir, Ll. Balcells, S. Valencia, F. Kronast, B. Martínez, J.J. de Miguel and C. Ocal "Growth Instabilities as a Source of Surface Chemical Structuration in Functional Perovskite Thin Films". *Crystal Growth & Design* 16(9), 5479- 5486 (2016).

[240] M. Azuma, K. Takata, T.Saito, S. Ishikawa, Y.Shimakawa, M.Takano, J. Designed Ferromagnetic, Ferroelectric $Bi_2NiMnO_6$. *Am. Chem. Soc*.127, 8889 (2005).

[241] Tirthankar Chakraborty, Hariharan Nhalil, Ruchika Yadav, Aditya A. Wagh, Suja Elizabeth. Magnetocaloric properties of $R_2NiMnO_6$ (R=Pr, Nd, Tb, Ho and Y) double perovskite family. *Journal of Magnetism and Magnetic Materials* 428, 59–63 (2017).

[242] J.M. Grace, D. B. McDonald, M.T. Reiten, J. O1son, R.T. Kam0wirth, and K.E. Gray. The effect of oxidant on resputtering of Bi from Bi-Sr-Ca-Cu-O films. *Journal of Vacuum Science and Technology. A, Vacuum, Surfaces and Films*, *10*(4), 1600-1603 (1992).

[243] Chenyang Shi, Yongmei Hao and Zhongbo Hu. Local valence and physical properties of double perovskite $Nd_2NiMnO_6$. *J. Phys. D: Appl. Phys*. 44 (24), 245405 (2011).

[244] P. Neenu Lekshmi, M. Vasundhara , Manoj Raama Varma , K.G. Suresh , M. Valant. Structural, magnetic and dielectric properties of rare earth based double perovskites $RE_2NiMnO_6$ (RE=La, pr, Sm, Tb). *Physica B : Condensed Matter* 448, 285–289 (2014).

[245] A. Wold, R. J. Arnott, and J. B. Goodenough. Some Magnetic and Crystallographic Properties of the System $LaMn_{1-x}Ni_xO_{3+\lambda}$. *J. Appl. Phys.* 29 (3), 387-389 (1958).

[246] Woodward PM, Hoffmann RD, Sleight A. Order-disorder in $A_2M^{3+}M^{5+}O_6$ perovskites. ***J** Mater Res* 9 (8), 2118-2127 (1994).

[247] T. Shimada, J. Nakamura, T. Motohashi, H. Yamauchi, and M. Karppinen. Kinetics and Thermodynamics of the Degree of Order of the B Cations in Double-Perovskite $Sr_2FeMoO_6$. *Chem. Mater. 15,* 4494-4497 (2003).

[248] P. Balasubramanian et al. Electronic structure of $Pr_2MnNiO_6$ from x-ray photoemission, absorption and density functional theory. *J. Phys.: Condens. Matter* 30 (43) 435603 (2018).

[249] M. Mouallem-Bahout , T. Roisnel , F. Bourée , G. André , C. Moure , O. Peña. Neutron diffraction evidence for a cationic order in the $REMn_{0.5}Ni_{0.5}O_3$ (RE= La, Nd) and $YMn_{0.5}Co_{0.5}O_3$ perovskites. *Prog. Solid State Chem*. 35, 257-264 (2007).

[250] B.R.K. Nanda, S. Satpathy. Effects of strain on orbital ordering and magnetism at perovskite oxide interfaces: $LaMnO_3/SrMnO_3$. *Physical Review B* 78, 054427 (2008).

[251] X. J. Chen, H.-U. Habermeier, H. Zhang, G. Gu, M. Varela, J. Santamaria, and C. C. Almasan. Metal-insulator transition above room temperature in maximum colossal magnetoresistance manganite thin films. *Physical review B* 72, 104403 (2005).

[252] C. Xie, L. Shi. Tuning of magnetic properties for epitaxial $Y_2NiMnO_6$ thin film: Substrate is crucial. *Applied Surface Science* 384, 459–465 (2016).

[253] K. Yadav, H. K. Singh, K. K. Maurya, G. D. Varma. Thickness-dependent magnetic and transport properties of $La_{0.5}Sr_{0.5}MnO_3$ thin films deposited by DC magnetron sputtering on the $LaAlO_3$ substrate. *Applied Physics* A 124, 66 (2018).

[254] H. Yamada, M. Kawasaki, T. Lottermoser, T. Arima, Y. Tokura, $LaMnO_3/SrMnO_3$ interfaces with coupled charge-spin-orbital modulation. *Appl. Phys. Lett*. 89 (2006).

[255] C. Ma, M. Liu, J. Liu, G. Collins, Interface effects on the electronic transport properties in highly epitaxial $LaBaCo_2O_{5+\delta}$ films. *Appl. Mater. Interfaces* 6–11 (2014).

[256] Somnath Pal, Somnath Jana, Sharada Govinda, Banabir Pal, Sumanta Mukherjee, Samara Keshavarz, Danny Thonig, Yaroslav Kvashnin, Manuel Pereiro, Roland Mathieu, Per Nordblad, John W. Freeland, Olle Eriksson, Olof Karis, and D. D. Sarma. Peculiar magnetic states in the double perovskite $Nd_2NiMnO_6$. *Physical Review B* 100 (4), 045122 (2019).

[257] Van Der Laan G, Zaanen J, Sawatzky G A, Karnatak R and Esteva J M. Comparison of x-ray absorption with x-ray photoemission of nickel dihalides and NiO *Phys. Rev.* B, 33(6) 4253 (1986).

[258] J. García, M. C. Sánchez, G. Subías, and J. Blasco, J. High resolution x-ray absorption near edge structure at the Mn K edge of manganites. *Phys.: Condens. Matter* 13 (14), 3229 (2001).

[259] C. H. Booth, F. Bridges, G. J. Snyder, and T. H. Geballe. Comparison of local structure measurements from c-axis polarized XAFS between a film and a single crystal of $YBa_2Cu_3O_{7-\delta}$ as a function of temperature. *Phys. Rev. B*, *54*(13), 9542 (1996).

[260] T. Burnus, Z. Hu, H. H. Hsieh, V. L. J. Joly, P. A. Joy, M. W. Haverkort, H. Wu, A. Tanaka, H.-J. Lin, C. T. Chen, and L. H. Tjeng. Local electronic structure and magnetic properties of $LaMn_{0.5}Co_{0.5}O_3$ studied by x-ray absorption and magnetic circular dichroism spectroscopy. *Phys. Rev. B* 77, 125124 (2008).

[261] H.Wu, T. Burnus, Z. Hu, C. Martin, A.Maignan, J. C. Cezar, A. Tanaka, N. B. Brookes, D. I. Khomskii, and L. H. Tjeng, Phys. Ising magnetism and ferroelectricity in $Ca_3CoMnO_6$. *Phys. Rev. Lett.* 102 (2), 026404 (2009).

[262] W. L. O'Brien, B. P. Tonner, G. R. Harp, and S. S. P. Parkin, J. Experimental investigation of dichroism sum rules for V, Cr, Mn, Fe, Co, and Ni: Influence of diffuse magnetism. *Appl. Phys*. 76, 6462 (1994).

[263] J. Hunter Dunn, D. Arvanitis, N. Mårtensson, M. Tischer, F. May, M. Russo, and K. Baberschke, J. An angle-dependent magnetic circular X-ray dichroism study of Co/Cu (100): experiment versus theory. *Phys.: Condens. Matter* 7, 1111 (1995).

[264] S. M. Heald and E. A. Stern, Phys. Anisotropic X-ray absorption in layered compounds. *Rev. B* 16, 5549 (1977).

[265] E. Stern and K. Kim. Thickness effect on the extended-X-ray-absorption-fine-structure amplitude. *Phys. Rev. B* 23, 3781 (1981).

[266] R. Nakajima, J. Stöhr and Y. U. Idzerda. Electron-yield saturation effects in *L*-edge x-ray magnetic circular dichroism spectra of Fe, Co, and Ni. *Phys. Rev. B* 59, 6421 (1999).

[267] S. Gota, M. Gautier-Soyer, M Sacchi. Fe 2*p* absorption in magnetic oxides: Quantifying angular-dependent saturation effects. *Phys. Rev. B* 62, 4187 (2000).

[268] A. Ruosi, C. Raisch, A. Verna, R. Werner, B. A. Davidson, J. Fujii, R. Kleiner, and D. Koelle. Electron sampling depth and saturation effects in perovskite films investigated by soft x-ray absorption spectroscopy. *Phys. Rev. B* 90, 125120 (2014).

[269] O. Toulemonde, F. Studer, A. Barnabe, B. Raveau, J.B. Goedkoop. Magnetic properties of chromium doped rare earth manganites $Ln_{0.5}Ca_{0.5}Mn_{1-x}Cr_xO_3$ (Ln= Pr, Nd, Sm and $0.05 \leqslant x \leqslant 0.10$) by soft x-ray magnetic circular dichroism. *J. Appl. Phys*. *86*(5), 2616-2621 (1999).

[270] Stavitski, E.; de Groot, F. M. F. The CTM4XAS Program for EELS and XAS spectral shape analysis of transition metal L edges. *Micron*, 41 (7), 687-694 (2010).

[271] Thole, B. T.; van der Laan, G.; Fuggle, J. C.; Sawatzky, G. A.; Karnatak, R. C.; Esteva, J. M. 3d X-ray-absorption Lines and the $3d^94f^{n+1}$ Multiplets of the Lanthanides. *Phys. Rev. B:* Condens. Matter Mater. Phys., 32, 5107−5118 (1985).

[272] Cowan, R. D. The Theory of Atomic Structure and Spectra; University of California *Press: Berkeley,* (1981).

[273] Butler, P. H. Point Group Symmetry Applications: Methods and Tables; Plenum Press: New York, (1981).

[274] F. M. F. de Groot, J. C. Fuggle, B. T. Thole, and G. A. Sawatzky. 2*p* x-ray absorption of 3*d* transition-metal compounds: An atomic multiplet description including the crystal field. *Phys. Rev. B*, 42, 5459 (1990).

[275] F.M.F. de Groot. Multiplet effects in X-ray spectroscopy. *Coord. Chem. Rev*., 249, 31(2005).

[276] Mahnaz Ghiasi, Mario Ulises Delgado-Jaime, Azim Malekzadeh, Ru-Pan Wang, Piter S. Miedema, Martin Beye, and Frank M. F. de Groot. Mn and Co Charge and Spin Evolutions in $LaMn_{1-x}Co_xO_3$ Nanoparticles. *J. Phys. Chem. C*, 120, 8167−8174 (2016).

[277] Hidekazu Ikeno, Frank M F de Groot, Eli Stavitski and Isao Tanaka. Multiplet calculations of $L_{2,3}$ x-ray absorption near edge structures for 3*d* transition-metal compounds. *J. Phys.: Condens. Matter* 21(10), 104208 (2009).

[278] A.E. Bocquet, T. Mizokawa, T. Saitoh, H. Namatame, and A. Fujimori. Electronic structure of 3*d*-transition-metal compounds by analysis of the 2*p* core-level photoemission spectra. *Phys. Rev. B* 46 (7), 3771 (1992).

[279] T. Mizokawa, H. Namatame, A. Fujimori, K. Akeyama, H. Kondoh, H. Kuroda and N. Kosugi. Origin of the Band Gap in the Negative Charge-Transfer-Energy Compound $NaCuO_2$. *Phys. Rev. Lett*. 70, 1565 (1993).

[280] J. Zaanen, G. A. Sawatzky, and J. W. Allen. Band-gaps and electronic-structure of transition-metal compounds. *Phys. Rev. Lett.*, 55, 418 (1985).

[281] R. J. O. Mossanek, G Domínguez-Cañizares, A Gutiérrez, M Abbate, D Díaz-Fernández and L Soriano. Effects of Ni vacancies and crystallite size on the O 1s and Ni 2p X-ray absorption spectra of nanocrystalline NiO. *J. Phys.: Condens. Matter* 25, 495506 (2013).

[282] Abbate M *et al.* Controlled-valence properties of $La_{1-x}Sr_xFeO_3$ and $La_{1-x}Sr_xMnO_3$ studied by soft-X-ray absorption spectroscopy. *Phys. Rev.* B 46 4511 (1992).

[283] J Padilla-Pantoja *et al.* Stability of the Cationic Oxidation States in $Pr_{0.50}Sr_{0.50}CoO_3$ across the Magnetostructural Transition by X-ray Absorption Spectroscopy. *Inorg. Chem*. 53, 8854−8858, (2014).

[284] M. Alexander, H. Romberg, N. Nucker, P. Adelmann, J. Fink, J. T. Markert, M. B. Maple, S. Uchida, H. Takagi, Y. Tokura, A. C. W. P. James, and D. W. Murphy. Electronic structure studies on the n-type doped superconductors $R_{2-x}M_xCuO_{4-\delta}$ (R= Pr, Nd, Sm; M= Ce, Th) and $Nd_2CuO_{4-x}F_x$ by electron-energy-loss spectroscopy. *Phys. Rev. B* 43(1), 333 (1991).

[285] Medarde M. L. Structural, magnetic and electronic properties of $RNiO_3$ perovskites (R= rare earth). *J. Phys.: Condens. Matter 9*(8), 1679 (1997).

[286] Ogasarawa, A. Kotani, K. Okada, and B.T. Thole. Theory of x-ray-absorption spectra in $PrO_2$ and some other rare-earth compounds. *Phys. Rev*. B43, 854 (1991).

[287] R. C. Karnatak, J.-M. Esteva, H. Dexpert, M. Gasgnier, P. E. Caro, and L. Albert. X-ray absorption studies of $CeO_2$, $PrO_2$, and $TbO_2$. I. Manifestation of localized and extended f states in the 3d absorption spectra. *Phys. Rev. B* 36, 1745 (1987).

[288] www.quanty.org.

[289] http://esrf.fr/computing/scientific/crispy.

[290] M. Abbate, H. Pen, M.T. Czyzyk, F.M.F. de Groot, J.C. Fuggle, Y.J. Ma, C.T. Chen, F. Sette, A. Fujimori, Y. Ueda, and K. Kosuge. Soft X-ray absorption spectroscopy of vanadium oxides. *J. Electron spectrosc relat phenom*, *62*(1-2), 185-195 (1993).

[291] M. Abbate, F.M.F. de Groot, J.C. Fuggle, A. Fujimori, O. Strebel, F. Lopez, M. Domke, G. Kaindl, G.A. Sawatzky, M. Takano, Y. Takeda, H. Eisaki, and S. Uchida. Controlled-valence properties of $La_{1-x}Sr_xFeO_3$ and $La_{1-x}Sr_xMnO_3$ studied by soft-x-ray absorption spectroscopy. *Phys. Rev. B* 46 (8), 4511 (1992).

[292] M. Abbate, J.C. Fuggle, A. Fujimori, L.H. Tjeng, C.T. Chen, R. Potze, G.A. Sawatzky, H. Eisaki, and S. Uchida. Electronic structure and spin-state transition of $LaCoO_3$. *Phys. Rev. B* 47 (24), 16124 (1993).

[293] M. Abbate, G. Zampieri, F. Prado, A. Caneiro, J. M. Gonzalez-Calbet, and M. Vallet-Regi. Electronic structure and metal-insulator transition in $LaNiO_{3-\delta}$. *Physical Review B*, 65 (15), 155101 (2002)

[294] P. Kuiper, J. v. Elp, J. G. A. Sawatzky, A. Fujimori, S. Hosoya, and D. M. Leeuw. Unoccupied density of states of $La_{2-x}Sr_xNiO_{4+\delta}$ studied by polarization-dependent x-ray-absorption spectroscopy and bremsstrahlung isochromat spectroscopy. *Phys. Rev*. B, 44(9), 4570 (1991).

[295] De Groot F. M. F, Grioni M, Fuggle J C, Ghijsen J, Sawatzky G A and Petersen H. Oxygen 1s x-ray-absorption edges of transition-metal oxides. *Phys. Rev.* B, 40(8) 5715 (1989).

[296] Amit Kumar Singh, Padmanabhan Balasubramanian, Ankita Singh, M K Gupta and Ramesh Chandra. Structural transformation, Griffiths phase and metal-insulator transition in polycrystalline $Nd_{2-x}Sr_xNiMnO_6$ (x = 0, 0.2, 0.4, 0.5 and 1) compound. *J. Phys.: Condens. Matter* 30 (35) 355401, (2018).

[297] J. Zaanen, C. Westra, and G. Sawatzky. Determination of the electronic structure of transition-metal compounds: 2p x-ray photoemission spectroscopy of the nickel dihalides. *Phys. Rev. B* 33 (6), 8060 (1986).

[298] Toulemonde, O., Millange, F., Studer, F., Raveau, B., Park, J. H., & Chen, C. T. Changes in the Jahn-Teller distortion at the metal-insulator transition in CMR manganites. *Journal of Physics: Condensed Matter*, *11*(1), 109 (1999).

[299] Park J H, Chen C T, Cheong S-W, BaoW, Meigs G, Chakarian V and Idzerda Y U. Electronic aspects of the ferromagnetic transition in manganese perovskites. *Phys. Rev. Lett.* 76 (22) 4215 (1996).

[300] Millange F, Maignan A, Caignaert V, Simon Ch and Raveau B *Z.* Influence of the size of the interpolatedncation upon the CMR properties of the perovskites $Nd_{0.7}Ca_{0.3-x}Sr_xMnO_{3-\delta}$. *Phys.* B 101 (2), 169-174 (1996).

[301] Gardiner, A. S. Parkins. *Phys. Rev. A*, *50*, 1782 (1994).

[302] D. Sarma, N. Shanthi, and P. Mahadevan. Electronic excitation spectra from ab initio band-structure results for $LaMO_3$ (M= Cr, Mn, Fe, Co, Ni). *Phys. Rev. B*, 54, 1622 (1996).

[303] S. Medling, Y. Lee, H. Zheng, J. F. Mitchell, J. W. Freeland, B. N. Harmon, and F. Bridges. Evolution of magnetic oxygen states in Sr-doped $LaCoO_3$.*Phys. Rev. Lett.,* 109, 157204 (2012).

[304] C.R. Weissmantel, Deposition of Metastable Films by Ion Beam and Plasma Techniques, Proc. 9th Int. Vacuum Congress and 5th Int. Conf. on Solid Surfaces (Madrid), p 229-308, (1983).

[305] Kelly, P.J.; Arnell, R.D. Magnetron sputtering: a review of recent developments and applications. Vaccum, 56, 159–172 (2000).

[306] Safi, I. Recent aspects concerning DC reactive magnetron sputtering of thin films: A review. Surf. Coat. Technol. 2000, 127, 203–219; Brauer, G.; Szyszka, B.; Vergohl, M.; Bandorf, R. Magnetron sputtering-Milestones of 30 years. Vacuum, 84, 1354–1359 (2010).

[307] Thin film preparation and characterization techniques. https://shodhganga.inflibnet.ac.in/bitstream/10603/54335/8/08_chapter%202.pdf

[308] Vilalta-Clemente A., Gloystein K.; "Principles of Atomic Principles Force Microscopy (AFM), based on lecture by Prof. Nikos Frangis". (2008).

[309] G. Kaupp, "Atomic Force Microscopy, Scanning Nearfield Optical Microscopy and Nanoscratching", Springer- Verlag Berlin Heidelberg (2006)

[310] S. Brivio, J. Frascaroli, and M. H. Lee, "Electrical AFM for the Analysis of Resistive Switching," in Electrical Atomic Force Microscopy for Nanoelectronics. Springer, pp. 205–229, (2019).

[311] M. Lanza, "A Review on Resistive Switching in High-k Dielectrics: A Nanoscale Point of View Using Conductive Atomic Force Microscope," Materials, 7 (7), 2155-2182, (2014

[312] Quantitative Data Processing in Scanning Probe Microscopy. Micro and Nano Technologies, Pages 265-293 (2013)

[313] A Textbook on Fundamentals and Applications of Nanotechnology. K.S.Subramanian, G.J. Janavi, S. Marimythu, M.Kannan, K.Raja, S.Haripriya, D.Jeya Sundara Sharmila, Pon Sathya Moorthy, (2018)..

[314] Eastman M.; "Scanning Electron Microscopy". *Univ. Texas El Paso*. http://materialsworld.utep.edu/Background/SCANNIN, ELECTRONMICROSCOPY/SccaningElectronMicroscopy.htm (2010).

[315] Azad Mohammed, Avin Abdullah. Scanning Electron Microscopy (SEM): A Review. In *Proceedings of the 2018 International Conference on Hydraulics and Pneumatics—HERVEX, Băile Govora, Romania* (pp. 7-9).

[316] Ma, et al. Study of transmission electron microscopy (TEM) and scanning electron microscopy (SEM). *Nat. Sci*, *4*(3), 14-22, (2006).

[317] Aberration-Corrected Analytical Transmission Electron Microscopy, First Edition. Edited by Rik Brydson. John Wiley & Sons, Ltd. Published (2011

[318] Kirmse H. (Humboldt U. of B.; "Sample Preparation for Transmission Electron Microscopy" http://crysta.physik.huberlin. de/~kirmse/pdf/VL.TEM Probenpreparation (2013).

[319] Xavier Llovet. Electron probe microanalysis: principles and applications. Handbook of instrumental techniques from CCiTUB. Unitat Microsonda Electrònica, CCiTUB, Universitat de Barcelona, (2012)..

[320] Rajiv Kohli and K.L. Mittal. Developments in Surface Contamination and Cleaning: Methods for Assessment and Verification of Cleanliness of Surfaces and Characterization of Surface Contaminants, Pags 23-105 (2019).

[321] Clementina Dilim, Igwebike-Ossi World's largest Science, Technology & Medicine. X-Ray Techniques. Chapter 10.

[322] Paul E Fewster. Reciprocal Space Mapping. Critical Reviews in Solid State and Materials Sciences, 22(2):69- I I0 ( 1997).

[323] Yasaka, Miho. "X-ray thin-film measurement techniques." The Rigaku Journal 26.2: 1-9 (2010).

[324] Chason, E., and T. M. Mayer. "Thin film and surface characterization by specular X-ray reflectivity." *Critical Reviews in Solid State and Material Sciences* 22.1: 1-67 (1997).

[325] R. L. Fagaly. Superconducting quantum interference device instruments and applications. *Rev. Sci. Instrum*. 77, 101101 (2006).

[326] M. Buchner, K. Höfler, B. Henne, V. Ney, and A. Ney. Tutorial: Basic principles, limits of detection, and pitfalls of highly sensitive SQUID magnetometry for nanomagnetism and spintronics. *J. Appl. Phys*. 124, 161101 (2018).

[327] K. Gramm, L. Lundgren and O. Beckman. SQUID Magnetometer for Magnetization Measurements. *Physica Scripta*. 13, 93-95 (1976).

[328] C.S. Schnohr and M.C. Ridgway (eds.), *X-Ray Absorption Spectroscopy of Semiconductors*, Springer Series in Optical Sciences 190 (2015).

[329] Richard Ortega, Asuncion Carmona, Isabelle Llorensc and Pier Lorenzo Solaric. X-ray absorption spectroscopy of biological samples. A tutorial. *J. Anal. At. Spectrom*, 27, 2054, (2012).

[330] JE Penner-Hahn . X-ray Absorption Spectroscopy. The University of Michigan, Ann Arbor, MI, USA. (2001).

[331] F. M. F. de Groot, J. Electron Spectrosc. X-ray absorption and dichroism of transition metals and their compounds. *Relat. Phenom.* 67, 529 (1994).

[332] F. De Groot and A. Kotani, "Core level spectroscopy of solids" CRC press (2008).

[333] G. van der Laan, A.I. Figueroa. X-ray magnetic circular dichroism—A versatile tool to study magnetism. *Coordination Chemistry Reviews* 277, 95–129 (2014).

[334] J.P. Crocombette, B. T. Thole and F. Jollet. The importance of the magnetic dipole term in magneto-circular x-ray absorption dichroism for 3*d* transition metal compounds. *J. Phys. Condens. Matter* 8, 4095–4105, (1996).

[335] Chen, C.T., et al. Experimental confirmation of the X-ray magnetic circular dichroism sum rules for iron and cobalt. *Phys. Rev. Lett.,* 75, 152, (1995).